THESIS

PRESENTED AT

NATIONAL GRADUATE SCHOOL OF CHEMISTRY OF MONTPELLIER

(ECOLE NATIONALE SUPERIEURE DE CHIMIE DE MONPELLIER)

DOCTORAL SCHOOL OF CHEMICAL SCIENCES

(ECOLE DOCTORALE DES SCIENCES CHIMIQUES)

BY

PRASHANT TYAGI

TO OBTAIN THE DEGREE OF

DOCTORATE

SPECIALITY: CHEMISTRY OF MATERIALS (CHIMIE DES MATERIAUX)

ELABORATION OF SELF-HEALING POLYMERIC MEMBRANES

(ELABORATION DES MEMBRANES POLYMERES AUTO-REPARABLES)

DEFENDED ON: 23 NOVEMBER 2012

IN ACCORD WITH

| M. H. CRAMAIL | PROFESSOR – UNIVERSITY OF BORDEAUX 1 | REVIEWER |
| M.F. TOURNILHAC | RESEARCH DIRECTOR – ENSPCI PARIS | REVIEWER |

IN FRONT OF THE ESTEEMED JURY COMPRISING OF:

M. HENRY CRAMAIL	PROFESSOR – University of Bordeaux 1	REVIEWER
M. FRANCOIS TOURNILHAC	RESEARCH DIRECTOR – ENSPCI PARIS	REVIEWER
M. DIDIER GIGMES	RESEARCH DIRECTOR – University of Aix – Marseille – i,ii,iii	EXAMINER
M. ANDRE DERATANI	RESEARCH DIRECTOR – CNRS	EXAMINER
M. SERGE LAGERGE	ASSOCIATE PROFESSOR – University of Montpellier – ii	THESIS DIRECTOR
M. DAMIEN QUEMENER	ASSOCIATE PROFESSOR – University of Montpellier – ii	THESIS DIRECTOR

ACKNOWLEDGEMENT…

GENERAL INTRODUCTION…

As the human civilization progress more and more each day, our demands for energy and material are growing at an exponential rate. Polymers and their composites hold an important and significant share in type of materials that drive the current global technology scenario. Millions of tonnes of different kinds of polymer are produced each year to meet the ever increasing need. At same time it has given rise to the problem of piling up of huge polymeric waste and degraded materials. On the other hand, if we look closely to nature, we can easily see that it produces complex chemicals and materials in such an efficient and clean manner that there are no wastages or after effects. It recycles the broken or damaged parts in an exquisite fashion by virtue of regeneration process. This regeneration process, i.e. the "Self-Healing" capability is one of the several interesting ideas from nature that humans have tried to replicate in their quest for novel technology.

The concept of Self-Healing materials can be considered as a resurrected one, which remained dormant for significant number of years even though being first discussed in the 50s and 60s. The domain of self-healing polymers has seen a tremendous advancement in last two 15 years, thanks to pioneering work of researchers at Illinois university, who developed the microcapsule based self-healing composites. The concept opened the door for new direction to develop such kinds of materials which could heal themselves in a more simplistic manner than the ones in nature. The success of this approach made others to develop their own strategies to impart self-healing property to polymeric materials. Some of these approaches involving dynamic covalent or non-covalent bonding led to the development of novel series of polymers and composites. As more and more advances are made in chemistry, there still exist a whole lot of possibilities to develop even better and more efficient self-healing polymeric systems.

The main aim of this thesis is to bring the self-healing concept within the domain of polymeric membranes and develop such kind of membranes which can repair themselves in an event of damage. Unlike their solid state counterparts, membranes being a porous material pose some challenges of their own kind when applying the same kind of self-healing techniques. One of the main objective and challenge is to develop a complete autonomous self-healing mechanism for a polymeric membrane without affecting its principal property of separation.

The first chapter of this manuscript provides an outlook towards the idea of self-healing right from its beginning till the current scenario. We begin by discussing about the characteristics of failure that occur in a polymer during the course of its lifetime. This is followed by the classification of the self-healing approaches developed so far, although there are also other possible ways to classify these materials. We have broadly classified the self-healing polymeric systems in autonomous and non-autonomous ones, which are further sub-classified. The chapter provides only those works that have

managed to show the self-healing behavior experimentally. Few exceptions have been made to this selection for certain approaches which have been considered novel and extremely ingenious.

The second chapter discusses the membrane that has been developed to exhibit the self-healing capability. The membrane is based on the in-situ 3D self-assembly of copolymer micelles giving rise to nano-porous superstructure. The copolymer used was synthesized in collaboration with researchers at the University of Aix-Marseilles. We have explored the effect of pressure on the morphology of the membrane which in turn affects its porosity. We have further explored the self-healing aspect of the membrane in terms of pressure sensitiveness and tried to correlate with simulated results. With the series of experiments, we have proved that the membrane is capable of healing itself autonomously from a substantial damage.

The third chapter deals with the implications of a self-healing membrane. We have tried to replicate the "direct mode translocation" of nanoparticles across a biological membrane to across a synthetic self-healing membrane. We have discussed various parameters that govern the process of translocation of nanoparticles while relating to the simulation studies carried out other researchers in this area.

The fourth chapter discusses the self-assembly of micelles of a diblock copolymer which shows a "zipper effect". This novel effect gave us the freedom to change the surface properties of a substrate in a reversible manner, but importantly in a facile way. This is in contrast with other methods which are often tedious in nature. We conclude the chapter with strong belief that the same "zipper effect" can be used effectively to prepare a non-autonomous "self-healing" coating and with slight tailoring, even a membrane.

The fifth chapter discusses very preliminary results regarding a different approach "nano-gel" taken to obtain a self-healing membrane. It discusses the motivation of the approach and the experiments done so far towards the achievement of the goal. The work remained incomplete due to unavailability of time however, we hope that it will be carried forward to validate the approach and employ it successfully.

TABLE OF CONTENTS…

BIBLIOGRAPHY...

1.   SELF-HEALING POLYMERIC SYSTEMS

Nature has been instrumental in inspiration for innovations and discoveries for human kind since the predawn era. One can find a whole range of materials ranging from the hardest known material to innumerable stimuli-responsive systems. These advance complex biological materials are result of an evolutionary process which started millions of years ago and still continuing. Of all the remarkable features exhibited by these biological systems, the ability to self-heal or regenerate in response to damage caused by an external factor is quite intriguing. Organisms like hydra, starfish can regenerate easily even if a large chunk of their body is cut away. In humans, healing process is self-evident when a small wound is healed over the course of time. Human liver is able to wholly regenerate itself from as less as 25%, demonstrating the level of advancement in nature. In biological systems, the healing process (Figure – 1.1) follows mainly three stages[1]: an inflammatory response to the injury characterized by healing material clotting followed by cell proliferation leading to matrix deposition and in the end remodeling of the matrix. The last two steps generally slow and may span over several months depending upon the extent of injury.
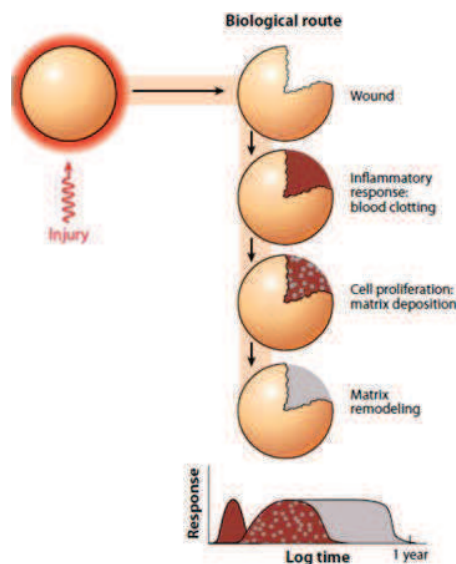
Figure– 1.1: Biological route for healing process[1]

Synthetic engineering materials in general do not have aforementioned healing ability. Most of these materials were developed and optimized by the constant need of more robustness, less cost and durability. However during the course of utilization, a material encounters various kinds of stresses leading to degradation, internal or external damages and finally a catastrophic failure. Consequently, research community has diverted its attention to develop such smart materials which are able to detect damages and repair themselves accordingly in an autonomous fashion. Such materials are expected to have longer life and reduced maintenance and life cycle costs. Different kinds of self-healing approaches have been developed for polymers, metals, concretes[2-6] and ceramics[7] with first class showing the maximum development related to self-healing. The scope of this chapter and work shall also be limited to polymers and composites in the same sense.

1.1 FRACTURE IN POLYMERIC SYSTEMS

Polymers used in engineering domain sustain damage *via* various external factors like thermal, chemical, biological and respective application related stresses. However, for such materials failures caused by cyclic fatigue and impact are most important and studied[8,9]. When a crack appears in a material, its further propagation inside the material is favored when the amount of energy released during cracking is larger or at least equal to the energy required to create new surfaces on the material[10]. The crack propagation modeling is often explained using a certain stress intensity parameter K_I[11,12]. This parameter depends on crack depth, geometry of both crack and material as well as the stress applied onto the material in case of crack opening type failure (Figure-1.2).
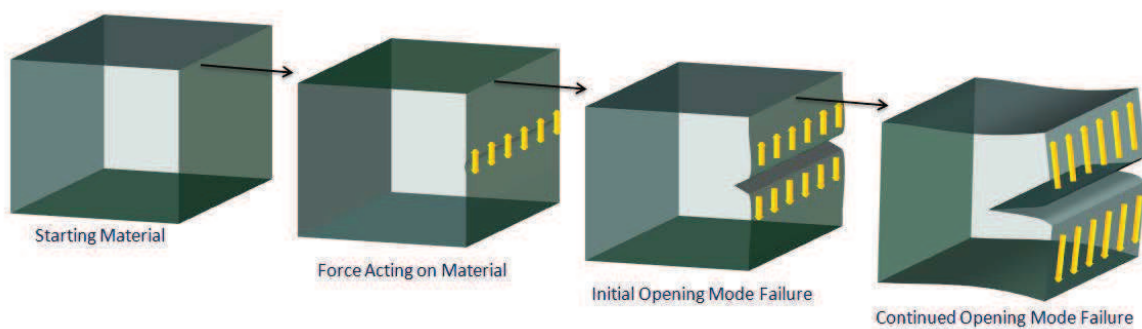
Figure– 1.2: Opening failure in a material of mode-I type[13]

The crack grows when K_I reaches a certain critical value, K_{IQ} due to change in the applied stress and geometry of the crack caused by cyclic or monotonic loads. During an impact damage incident (consisting of a monotonic load) the extent of crack propagation is related to the maximum stress

intensity factor (K_{IMax}) experienced. During fatigue-type damage crack propagation is related to both K_{IMax} and the change in K_I during cycling (ΔK). Either the fractured surfaces of the crack must be resealed or the growth of the crack must be stunted or checked to effectuate the healing process of the polymer. A number of so called extrinsic mechanisms[11,14] are proposed to mitigate the crack growth (Figure– 1.3)[13].
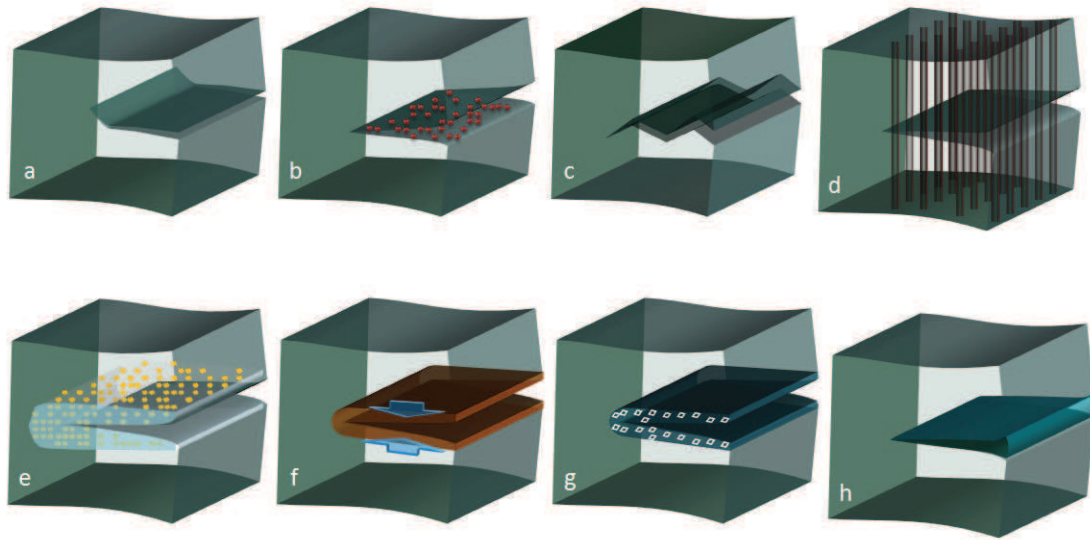
Figure– 1.3: The proposed extrinsic mechanisms for crack growth retardation in a material[13,14], a) Crack deflection, b) Wedging – debris induced crack retardation, c) Wedging – surface roughness induced crack deflection, d) Bridging – fiber toughening, e) Zone shielding – microcrack toughening, f) Zone toughening – transformation toughening, g) Zone shielding – crack field formation, h) Wedging and bridging – fluid pressure induced crack closure

All traditional and self-healing approaches are based on these mechanisms and generally involve dissipation of energy away from the propagating crack tip *via* a mechanical change behind the crack tip.

1.2 SELF HEALING MATERIALS IN GENERAL

An ideal self-healing material (polymeric) should have an in-built capability to repeatedly sense, respond and repair from damage it suffered while recovering most of its primal properties within a short timeframe. From here, healable polymeric materials can be broadly classified into two classes: *Autonomous self-healing materials* in which the healing process is triggered by the damage itself without need of any other external stimulus and the materials is able to attain pristine material's properties; *Non-Autonomous self-healing materials* in which healing is triggered and executed in

response to a specific external stimulus (related to intended application) other than damage. For both classes, the most important criteria to fulfill is to have inherent ability to create multiple new bonding interactions in and around the damage zone by using the components from within their existing structure[15]. Figure– 1.4 shows the classification of these polymeric systems based on the healing stimulus and chemistry involved that have been discussed in this chapter.
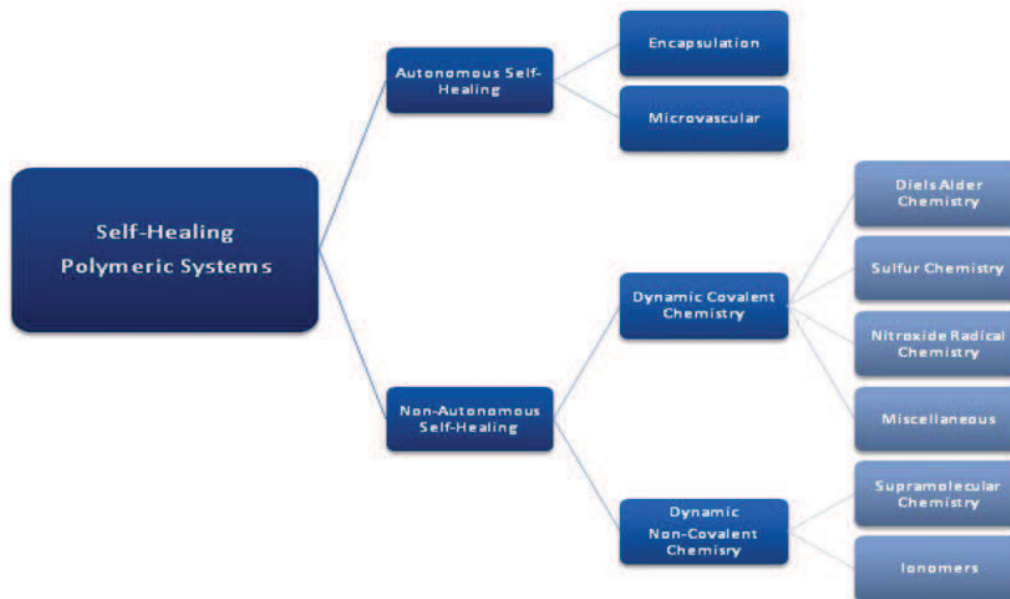
Figure– 1.4: Classification of self-healing polymeric systems based on the chemistry involved

Since the domain of applications for polymeric materials is large therefore the primal property differs with each application. Hence it is difficult to ascertain and compare the extent of healing. Also, in most of the cases, healed material is not able to recover all of the property as was of pristine material. In that case, it becomes pertinent to mention the efficiency of the healing method. A basic method proposed[16] to describe the extent of healing can be adopted. The equations used as depicted as below:

$$\text{(R) } Recovery\ Ratio = \frac{Property\ Value_{Healed}}{Property\ Value_{Initial}} \qquad \text{........ Eq.(1.1)}$$

$$\text{(}\eta\text{) } Healing\ Efficiency = 100\ X\ \frac{Property\ Value_{Healed}}{Property\ Value_{Initial}} \qquad \text{....... Eq.(1.2)}$$

Above equations have been used explicitly to explain various properties like fracture stress, elongation at break, fracture energy, molecular parameters and membrane resistance, etc in different polymeric systems. However it must be noted that the aforementioned equations give information only about that

particular property. They do not provide information about the extent of recovery of other properties of the material during the healing process unless explained separately. The healing efficiencies can be calculated either after healing of a single microscopic crack or after a material has been broken and the parts then separated and rejoined prior to the healing efficiency measurement[15]. Further factors like healing rate, number of times the material can be healed at the location and the extent of recovery of pristine properties should also be considered.

1.3 AUTONOMOUS SELF-HEALING POLYMERIC SYSTEMS

These polymeric systems, as defined in the previous section are characterized by their ability to undergo healing process initiated by the fracture itself. Such materials sometimes also referred as extrinsic self-healing materials rely on two quite comprehensively developed approaches namely: encapsulation and mechanoresponsive and will be discussed in this section.

1.3.1 Encapsulation

The encapsulation approach refers to the embedding of a self-repair fluid filled fibers or capsules or vesicles within the polymer matrix. In case of damage, the fluid holding reservoir would break thereby releasing the fluid in the damage plane thus healing the material autonomously. These materials closely mimic healing mechanism observed in nature (Figure-1.1) however unlike biological counterparts; it is much simpler and accelerated. This approach primarily has been used for thermoset polymers and their composites though applicability has been established for protective coatings and even for packaging films[17].
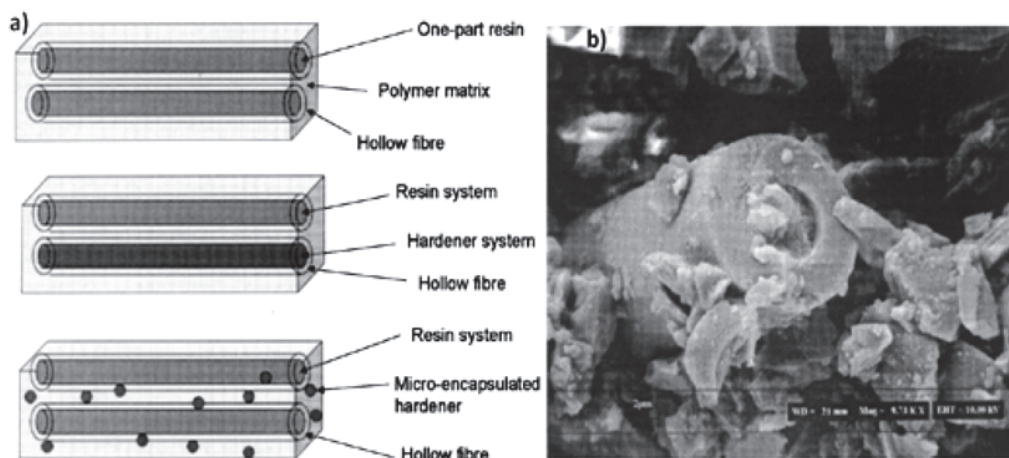
Figure– 1.5: Hollow fiber based repair systems, a) Different configurations considered, b) Scanning Electron Microscopy image of a resin filled fiber[18].

The first work based on this approach, reported way back in early 90s consisted of concrete reinforced with fibers filled with cyanoacrylate[19] and methylmethacrylate[20] adhesives. The idea was later replicated to polymeric system by embedding a two part epoxy crosslinking adhesive filled glass pipettes in a thermoset polymer matrix[21]. The technique was further investigated with different kind of hollow fibers and it was postulated that glass fibers were best suited for controlled fracture providing effective healing and also thicker composites were better in performance for healing studies[22]. In another work[18] by Bleay *et al.*, a two part system was investigated consisting either both epoxy resin & hardener contained in adjacent fibers or one of them (hardener) dispersed over in microencapsulated form while the resin was contained in the fiber embedded within the polymer matrix (Figure – 1.5). Although it was a onetime repair system however it validated the idea of controlled release of healing agent into a polymer matrix to stop the propagation of a crack, repair it and recover the mechanical properties.

An alternative novel approach was developed by White *et al.* in 2001, where healing agent was encapsulated in urea-formaldehyde microcapsules and embedded in a polymer matrix[23]. Upon crack intrusion, the healing agent would seep into the crack plane from ruptured capsules through capillary action where its polymerization takes place, triggered by contact with an embedded catalyst and thus leading to healing of the system (Figure– 1.6a).
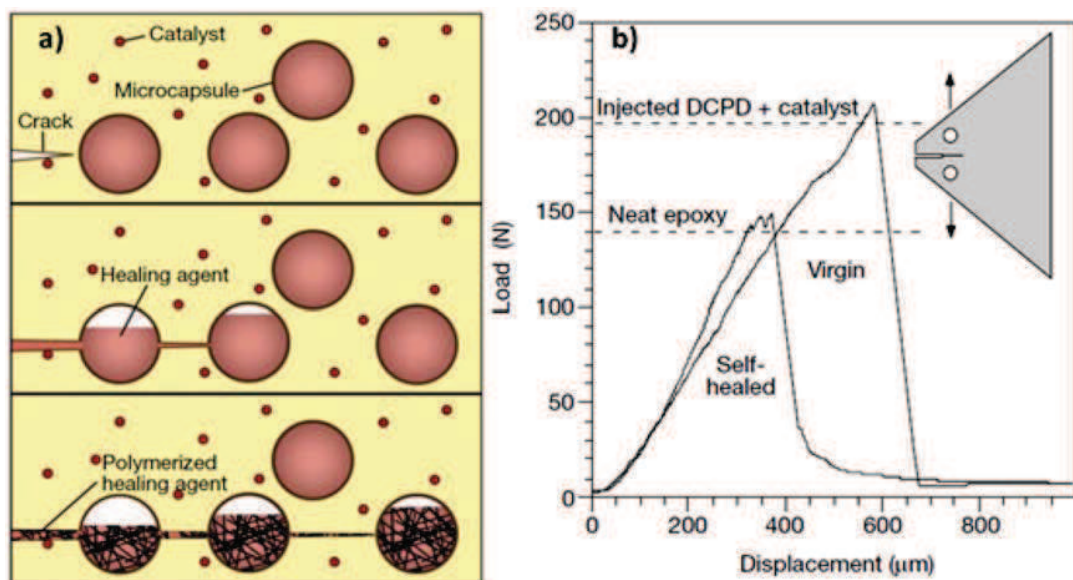
Figure– 1.6: The autonomic healing concept based on a microencapsulated healing agent embedded in a structural composite matrix containing a catalyst capable of polymerizing the healing agent, a) Cracks forms in the matrix wherever damage occurs thus releasing the healing agent into the crack plane through capillary action which

contacts the catalyst and undergoes polymerization thus filling the crack formed, b) Healing effciency is obtained by

fracture toughness testing of tapered double-cantilever beam (TDCB) specimens[23].

An almost 75% toughness recovery was obtained for the healed sample in a tapered double cantilever test where the load was applied perpendicular to the crack plane (Figure – 1.6b).

The healing agent used in this approach was the monomer known as dicyclopentadiene which would undergo ring-opening polymerization (ROMP) in the presence of a catalyst (Grubbs' catalyst) at room temperature (Figure– 1.8).
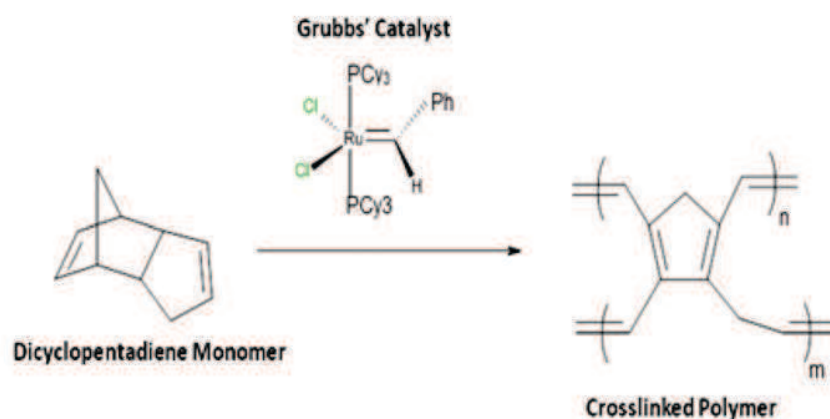
Figure – 1.7: The Ring Opening Metathesis Polymerization (ROMP) of dicyclopentadiene (DCPD) monomer by Ruthenium based Grubbs' catalyst

Another interesting feature of this work was the living nature of the polymer formed within the crack plane. The reason behind this was the usage of living polymerization catalyst. A direct consequence of this living nature is that if more monomer is added at the place further polymerization would occur giving the possibility of having multiple healings.

Due to novelty of this work and direction it provided, it is important at this point to discuss certain aspects of this approach. A significant number of parameters need to be considered and optimized to obtain good healing.

The first parameter is to ensure a so called "sequestration method"[1] for the healing agent and the catalyst. Various factors identified in this method are solubility, volatility, reactivity, viscosity and pH of the healing agent to be encapsulated. Generally a healing agent or catalyst soluble in oil, non-volatile, unreactive to inner wall of the capsule, having low viscosity is considered ideal for this approach though these requirements are not strict as per say.

The second parameter is the synthesis procedure of microcapsules and their physico-chemical properties. In most of the self-healing work involving encapsulation approach, the microcapsules have

been prepared from urea-formaldehyde[24-32]. However other polymers like melamine formaldehyde (MF) [33-36], recently melamine-urea-formaldehyde (MUF) [37,38], polyurethane (PU) [39,40] and acrylates[41] have also been investigated. In a slight modification to this approach, the microspheres were prepared by meltable dispersion encapsulation method in which dispersion of catalyst was carried out in molten wax[42]. An excellent toughness recovery was reported with tenfold reduction in catalyst concentration. However a non-linear fracture behavior was also observed for these microspheres. The most common technique for preparing microcapsules is by miniemusion polymerization technique[43] in which sub-micron oil soluble polymeric phase dispersion is carried out in water phase. During the in situ polymerization process, urea and formaldehyde react in the water phase to form a low molecular weight pre-polymer; as the weight of this pre-polymer increase, it deposits at the DCPD-water interface. This urea-formaldehyde polymer becomes highly cross-linked and forms the microcapsule shell wall. Nanoparticles of pre-polymer then deposit on the surface of the microcapsules providing a rough surface morphology that aide in the adhesion of the microcapsules with the polymer matrix during composite processing however it may also inhibit the deposition of the nanoparticles on the UF microcapsule surface thus affecting the wall thickness and ultimately the storability of DCPD for longer duration of time[44]. Barring the thickness of the microcapsule walls, other features like their surface morphology and size have been found to be influenced by manufacturing process variables[27]. While the thickness typically been found to be varying between 160 – 220 nm irrespective of what the process parameters are, the average diameter of the microcapsules could be varied between 10 – 10000 µm by varying the agitation rate between 200 – 2000 rpm. An increased agitation rate would decrease the average diameter of the microcapsules. The wall thickness range was found be optimum for robust microcapsules capable of surviving the manufacturing process of the polymer while still fragile enough to be ruptured in case of a crack formation[44]. Additionally, a capsule with higher elastic modulus than the matrix was shown to be deflecting the crack away from itself by generating a stress field (Figure – 1.8). Thus to ensure the triggering of the healing process, it is of primal importance that the capsule has lower elastic modulus[45].
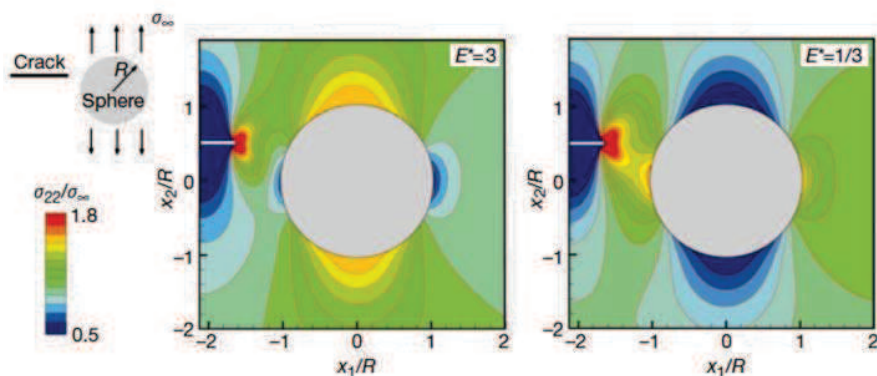
Figure – 1.8: Stress state in the vicinity of a planar crack as it approaches a spherical inclusion embedded in a linearly elastic matrix and subjected to a remote tensile loading perpendicular to the fracture plane[23].

The size of microcapsules further affects the healing efficiency at same weight fraction for a given crack volume. It was reported that larger microcapsules fared better than smaller due to amount to healing agent present in the polymer sample. A linear dependence was reported between the amount of healing agent delivered to the crack plane and the diameter of the microcapsule for a given weight fraction[46]. Earlier it was found that lower concentrations of smaller microcapsules would impart maximum toughening to the polymer specimen[47]. With the use of ultrasonification during capsule synthesis process, a further reduction in the size has been achieved. The lowest average diameter achieved was as small as 220 nm and as big as 1.65 µm. During fracture testing of the specimen, nearly all the capsules were found to be ruptured and a significant improvement in the fracture toughness per volume fraction of capsules was observed[24].

The third parameter is the properties of healing agent (monomer)/Catalyst system. The most studied system so far is Dicyclopentadiene (DCPD), a liquid healing agent/Grubbs' catalyst, a purple colored ruthenium (IV) catalyst system. Two isomeric form of DCPD have been identified in commercially available monomer (Figure – 1.9) containing more than 95 % of the "Endo" form. In situ NMR studies conducted for DCPD reactivity for ROMP showed that the "Endo" isomeric form is less reactive towards ROMP as compared to "Exo" isomeric form[48]. The reason behind this low reactivity was reported to be predominant entropic steric interactions. Ethylidene norbornene (ENB) (Figure – 1.9) is another potential monomer investigated[37,38,49-53] as an alternative of DCPD. ENB with lower freezing point has been found to be more reactive towards ROMP than DCPD[54]. However since the resulting polymer is linear in case of ENB hence its mechanical properties are inferior to that formed by DCPD polymerization. This problem was can be circumvented by using blend of these monomers as shown in one study[55], where a blend of DCPD/ENB (1:3) was found to show highest rigidity than individual

monomer systems. The addition of ENB not only enhanced the polymerization rate but also reduced the amount of catalyst needed.

Dicyclopentadiene (Endo)   Dicyclopentadiene (Exo)   Ethylidene Norbornene
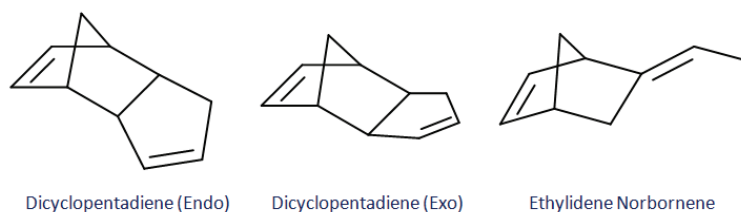
Figure – 1.9: Structure of Dicyclopentadiene isomers and Ethyliden Norbornene monomers

In the first work reporting microcapsule encapsulation self healing technique, the catalyst used was the first generation Grubbs' catalyst. Despite good healing observed, the catalyst showed inherent problems like deactivation upon exposure to air and moisture, reactivity loss to diethylenetriamine[56,57] (curing agent for epoxy matrix), and tendency to agglomerate within the polymer matrix leading to delamination. Also its decomposition starts just above 120°C in comparison to DCPD's temperature at 170°C[52,58]. This limitation renders this combination's healing usefulness for polymers requiring higher processing or usage temperatures. In most of the studies[44,47,59-63] carried out for DCPD/Grubbs' catalysts system, the loading of encapsulated DCPD varied between 10 – 25 wt% while typical catalyst concentration values were 2.5 wt% or 5 wt%. For effective healing to take place, the availability of activated catalyst in right amount is of very importance. However this availability has been found to be dependent upon factors like mixing order, matrix resin type, type of curing agent, particle size of the catalyst and the amount of catalyst[44]. Highest healing efficiency was obtained with catalyst particle size of 180 – 225 μm while concentrations greater than 2.5 wt% provided negligible gain in fracture toughness[44]. A fast dissolution of catalyst is important to obtain a good healing efficiency which would otherwise lead to heterogeneous polymerization to exposed catalyst particles locations. Smaller is the particle size; faster is the dissolution of the catalyst however this brings the problem of more catalyst exposure to curing agent mixed in the polymer matrix. The exposure can reduce the overall reactivity of the catalyst thus negating the effect of catalyst size and concentration[64]. As reported in an earlier work[65] about the ease of handling of Grubbs' catalyst and preservation of its reactivity by dispersion in paraffin wax, the amine deactivation problem was circumvented by encapsulating the catalyst in wax microspheres of size 50 – 150 μm before dispersing them into the polymer matrix[42]. The catalyst was found to retain 69% of its reactivity as well as was uniformly dispersed throughout the epoxy matrix without any sign of agglomeration. The system showed improved healing efficiency of 93% at comparatively very low amount of catalyst loading (0.75 wt%). Wax protected catalyst idea was further

used for a new epoxy polymer matrix having vinyl ester groups and superior mechanical properties[66]. The resin was cured *via* free radical polymerization techniques employing amine-peroxide initiator. As expected, the wax encapsulated catalyst retained its activity while being exposed to peroxide curing reactions. Larger size microspheres preserved highest catalyst activity[66]. As an alternative to first generation Grubbs' catalyst, different ruthenium catalysts have also been investigated. In one study[67], the first generation catalyst was compared with second generation Grubbs' and Hoveyda-Grubbs's catalysts. The three different catalysts were investigated for their ROMP initiation constants, stability curing agents, thermal stability and ROMP reactivity of alternative healing agents. The ROMP initiation constant of first generation Grubbs' catalyst was found be lowest in solution while higher in bulk in comparison to second generation catalyst. Hoveyda-Grubbs' catalyst showed an initiation too fast to be measured in both cases. During fabrication of the polymer specimens, the first generation Grubbs' catalyst turns from purple to brown indicating the deactivation of the catalyst. Second generation Grubbs' catalyst changed from brown to green but no color change was observed for catalyst of third kind. Due to complete deactivation, no healing was observed for first generation catalyst however despite showing healing activity, no significant improvement was observed in healing efficiency for the other two catalysts. Second generation Grubbs' catalyst exhibited best thermal stability in self-healing test at 125°C.

Despite good healing results and tremendous potential of newer generation of Grubbs' catalyst, the inherent temperature sensitivity, high cost and limited availability of these catalysts prompted the search for other cheaper alternatives. As one such cheaper alternative, Tungsten (VI) catalyst system (WCl_6) was explored for autonomous self-healing materials for large scale applications[68]. Being a catalyst precursor, WCl_6 needs to be activated for catalytic activity. In this work, WCl_6 was activated with a stable alkylating agent phenylacetylene even in air. Oxidation of WCl_6 also converts it into $WOCl_4$ which has also been reported as ROMP-active catalyst. Since solubility of catalyst is absolutely necessary for polymerization to occur, hence to address the insolubility of WCl_6 in DCPD, nonylphenol was also added as a dissolution agent. A 50% decrease was observed in fracture toughness for initially prepared samples, attributed to poor bonding between the matrix and the catalyst. The toughness value increased to 75 % of virgin epoxy when a silane coupling agent was employed. The healing efficiency dropped from 102 % for re-crystallized WCl_6 to 20 % as received but mechanically well dispersed WCl_6 in the polymer matrix. The probable reason for this decrease was the exposure of well dispersed catalyst particles to the surrounding polymer matrix leading to deactivation of larger surface area. Dispersion after wax protection gave better efficiency but the corresponding catalyst loading was as high as 7 %.

| | Composition [a] | | Fracture load [N] | Healing efficiency [%] |
PDMS [wt %]	Adhesion promoter [wt %]	Microcapsule [wt %]		
8	4	2.4	14 [3]	9 [2]
		5.0	9 [5]	6 [3]
12	2	3.6	14 [2]	9 [1]
	4	3.6	37 [7]	24 [4]
	8	3.6	28 [5]	19 [4]
15	4	2.4	21 [1]	14 [1]
		4.5	37 [3]	24 [3]
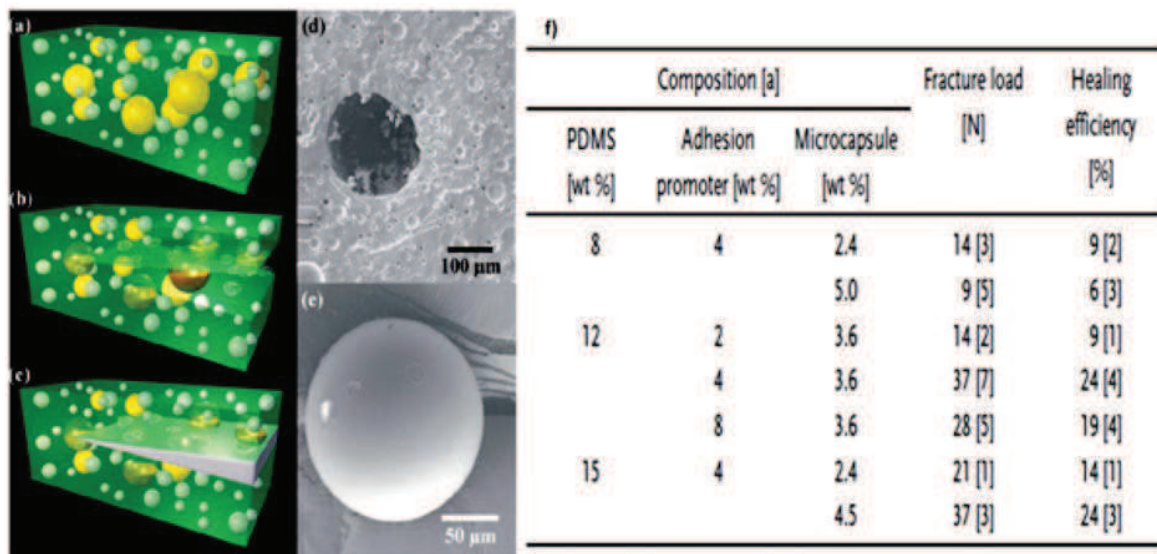
Figure – 1.10: Self-healing process based on siloxane and alkoxy siloxane systems, a) Composite consisting of microencapsulated catalyst (yellow) and phase-separated healing-agent droplets (white) dispersed in a matrix (green), b) Crack propagates into the matrix releasing the catalyst and healing agent into the crack plane, c) The crick is healed by polymerized PDMS, d-e) Scanning electron microscopy images of the fracture surface, showing an empty microcapsule and voids left by the phase-separated healing agent and a smooth surface microcapsule, f) Average maximum load of self-healed vinyl ester by the method and the corresponding healing efficiencies[39].

Moving away from DCPD/Grubbs' catalyst system due to their associated high cost and lower availability, in 2006 a new kind of healing system was introduced by Cho et al[39]. This system was based on the same healing principle as discussed above however the monomers were changed to hydroxyl-terminated siloxanes and alkoxysilanes while catalysts were changed to organotin compounds. Since this catalysts were found to be effective only in the presence of water, hence the proposed healing material was radical improvement over the DCPD/Grubbs' system in which the catalyst was highly susceptible to moisture. Additionally, the liquid phase healing agent, hydroxyl end functionalized poly(dimethylsiloxane) & poly(diethoxysiloxane), could be directly mixed with the polymer matix where they would remain as phase separated droplets having size between 1 – 20 μm. This left only the organotin catalyst (di-n-butyltin dilaurate) to be encapsulated along with a solvent (chlorobenzene). The size of the microcapsules could be varied from 50 μm – 450 μm by varying the stirring rate during the microcapsules formation (Figure-1.10)[39].

The reported η values are much lower than those for DCPD/Grubbs' catalyst based epoxy self-healing polymer system along with a bit higher catalyst loading however the observation is obvious given

the lower stiffness and fracture toughness of PDMS compared to matrix polymer. In a further modification to above work, PDMS was employed as the matrix polymer while containing two different sets of microcapsules[25]. One set of microcapsules contained a PDMS copolymer with active sites for crosslinking while the other kind contained a high molecular weight vinyl functionalized PDMS along with platinum catalyst (initiator capsule). Up to 75% healing efficiency was achieved with 10 wt% resin capsules and 5 wt% catalyst capsules.

Encapsulation of epoxy resin in microcapsules as healing agent is also one of the alternatives investigated[26,69-71]. However to accomplish healing, a latent hardener has to be incorporated into the matrix. Upon rupture of the microcapsule, the epoxy would seep into the crack and polymerizes due to contact with embedded hardener thus closing the crack. This approach shares the same advantage as the PDMS/catalyst system that the healing material generated during the healing process is identical as the matrix material itself chemically. This result in the de*via*tion of tear path in the healed sample from that of the virgin tear path, resulting in greater than 100 % healing efficiencies. The epoxy/hardener system, first reported in 2007[71] employed an imidazole-metal complex as a latent hardener. The solubility of $CuBr_2(2-MeIm)_4$ hardener complex in epoxy ensured a homogeneous distribution all over the matrix and thus capable of curing epoxy at any point in the matrix. The reported diameter range of the microcapsules was 30 – 70 μm with encapsulated epoxy resin. The incorporation of the hardener and the epoxy microcapsules did not impact the mechanical properties of the matrix as such though fracture toughness was found to be increased slightly. Using 10 wt% epoxy microcapsules and 2 wt% latent hardener, an impressive 111% healing efficiency was reported however the approach failed to qualify as a true autonomous healing system. The obvious reason is the inherent need to heat the samples between 130^oC – 170^oC to initiate the curing of the epoxy resin. To make this approach fully autonomous, the imidazole-metal complex hardener was replaced with low-temperature mercaptan hardener[34] in conjunction with a tertiary amine catalyst, encapsulated in microcapsules and embedded along with epoxy filled microcapsules in an epoxy matrix[35]. The microcapsules used for both components, were based on the melamine-formaldehyde due to instable nature of mercaptan hardener. The benzyldimethyl amine catalyst was infiltrated into mercaptan filled microcapsules in a secondary step, since being basic in nature the catalyst couldn't be incorporated during the microencapsulation procedure which is performed in acidic medium. A healing efficiency of 104.5% was reported for specimens containing 5 wt% (2.4 wt % each) capsules at 20^oC (Figure – 1.11a). It was observed that maximum healing occurred when the ratio of two microcapsules set is near 1:1. A minimum of 12 hours

was required to reach healing efficiency beyond 100 %. A novel feature of this work was the achievement of healing at temperature as low as -10°C with an efficiency of 86% (Figure – 1.11b).
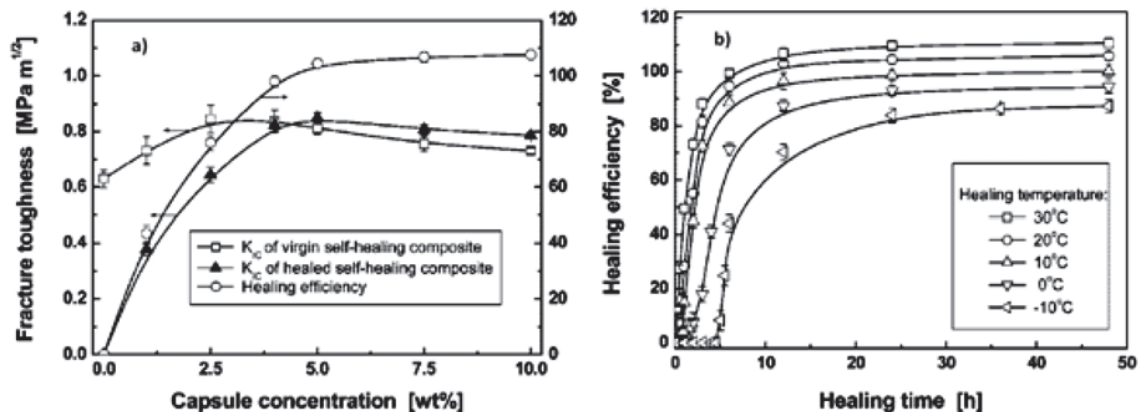
Figure – 1.11: Self-healing process based on epoxy/mercaptan system, a) Influence of capsules concentration on fracture toughness of the materials, b) Influence of temperature on healing efficiencies with time.

Solvent induced self-healing comprises the earliest known works in the field of self-healing. First reported in early 80s, the approach involved the heating of thermoplastic polymers (for example: PMMA) and simultaneous sealing of cracks with solvents like ethanol, methanol and carbon tetrachloride[72-77]. The healing mechanism involved wetting of the polymer surface and swelling of the bulk polymer material, which led to reptation and interlocking of the chains across the crack plane to recover mechanical properties of the virgin material and heal the crack. Immersion of polymer specimens in these solvents reduced the glass transition (T_g) of the polymer, thereby facilitating the healing procedure to occur at room temperature or slight heating. However due to high degree of swelling, the healed samples had lower strengths than the original ones. The solvent strategy was combined with encapsulation technique in 2007 by Caruso *et al.* in a work where the solvent was encapsulated and embedded into an epoxy matrix[78]. A significant number of solvents were investigated and first screened for their healing ability by manually injecting them onto a crack plane of a fractured epoxy specimen in reference tests mimicking the delivery of solvent to the crack by a ruptured capsule. The study showed a correlation between the healing efficiency and the solvent polarity (Figure – 1.12a). Five aprotic polar solvents exhibited the highest healing efficiencies namely: nitrobenzene, NMP, DMA, DMF, and DMSO. These solvents have dielectric constants ranging from 32 to 47. However, the relationship of polarity with healing efficiency could not be explained. On both extremes of the polarity spectrum, non polar solvents like cyclohexane, hexanes and protic polar solvents like formamide, and

water showed little or no healing. Encapsulation *via* Urea-formaldehyde encapsulation and reverse-phase encapsulation techniques remained problematic for aforementioned five solvents. The only solvent which could be encapsulated with relatively ease was
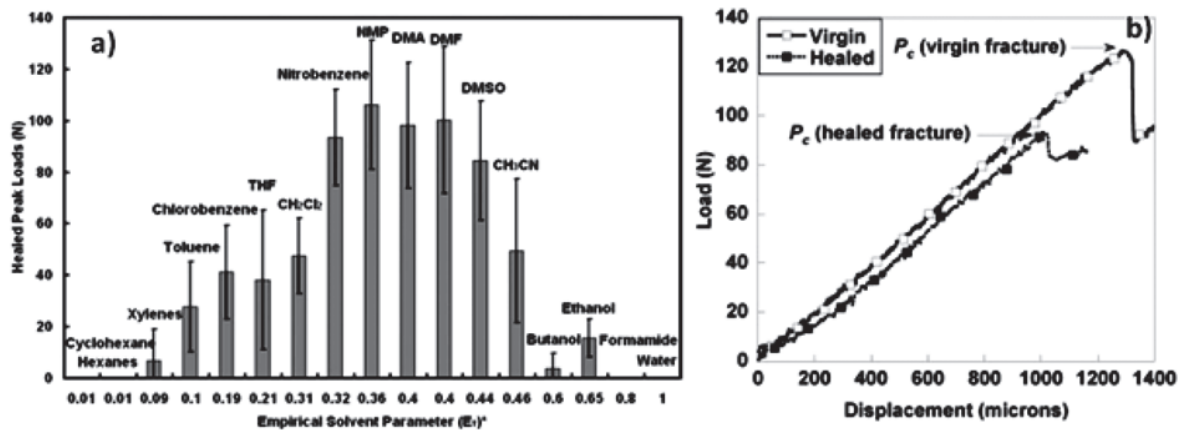
Figure – 1.12: Solvent based healing system, a) Influence of different solvents on healed peak fracture load, b) Load – displacement curve obtained for short – groove samples[78].

chlorobenzene, encapsulated into microcapsules having average diameter of 160 μm. However the maximum healing efficiency obtained was 82% with 20 wt% capsules loading (Figure – 1.12b). Correspondingly, xylene gave a 38% healing efficiency while that for hexane gave 0%, indicating a dependence of healing efficiency on the solvent polarity. In a continuation of the above work, further enhancements were reported for solvent-based self-healing of epoxy materials[79]. First, in place of microcapsules filled with solvent, a mixture of epoxy resin and solvent was used. This modification yielded a complete recovery of fracture toughness after crack propagation. Multiple healing events were also reported for this system. Second, less toxic solvents including aromatic esters giving efficient healing replaced more toxic chlorobenzene. A stable shelf-life of one month was also reported for epoxy-solvent system under ambient conditions for both chlorobenzene and phenyacetate. Similar encapsulation approach has been used in case of thermoplastic PMMA thin films where a plasticizer (Dibutylphthalate) was encapsulated in urea-formaldehyde microcapsules and dispersed into PMMA thin films[80]. Upon, rupture, the DBP is released into the crack where it plasticizes and swells surrounding polymer leading to the mending of the crack. The use of DBP helps in maintaining the optical properties of the prepared films and healed films also. Although no mechanical properties data was presented, the authors claimed to have recovered most of the protective properties of the virgin film along with certain portion of mechanical properties.

In addition to above works, some other novel reactive systems have also been investigated in conjugation with encapsulation technique. One of these systems is isocyanate encapsulated microcapsules[40], which is capable of performing healing in wet or humid conditions. This eliminates the need to use of a catalyst in the composite material. The isocyanate employed was isophorone diisocyanate encapsulated in polyurethane microcapsules prepared *via* interfacial polymerization of polyurethane prepolymer in an oil-in-water emulsion. The mean diameter of microcapsules and agitation rate followed an inverse power law relationship and isocyanate loss for a half year period was less than 10 wt%. In a more recent similar work[81], microcapsules containing a reactive amine with potential applications in self-healing polymers were prepared by interfacial polymerization of an isocyanate and an amine stabilized by an inverse pickering emulsion. The microcapsules were successfully isolated, dried, and redispersed in epoxy. Upon rupture, the capsules released the core material thereby able to cure the epoxy to form a polymer film. Click-chemistry has also been presented as a potential chemistry for healing materials. In one such work[31], a liquid azido-telechelic three-arm star poly(isobutylene) polymer and trivalent alkynes were encapsulated into micron-sized capsules and embedded into a high molecular weight poly(isobutylene) matrix. Using $(Cu(I)Br(PPh_3)_3)$ as low temperature catalyst for the azide/alkyne- "click"-reaction, crosslinking of the two components at $40^{o}C$ was observed within 380 min and as fast as 10 min at $80^{o}C$. Significant recovery of the tensile storage modulus was observed in a material containing 10 wt% capsules. Though promising, the approach still relies on the incorporation of a catalyst which is air sensitive, thus losing its activity over the surface of the material. Living polymerization techniques like ATRP[82] and RAFT[83,84] have also been explored where liquid monomer (glycidyl methacrylate) is encapsulated in microcapsules. Again, these systems though attractive, still posses inherent limitations. In case of ATRP, being air-sensitiveness of the catalysts used, the surface healing cannot occur as they get deactivated being in contact with humidity. Also, the metal ions are reported to accelerate the degradation of the material. Additionally, since the polymerization needs heating well above room temperature, hence it cannot be called an autonomous healing system. The RAFT approach although skips the problem of deactivation but still requires heating of the matrix for effective healing hence cannot be termed under autonomous healing systems. In place of microcapsules, use of carbon nanotubes as reservoirs has also been proposed *via* simulation studies[85,86] which will not only give healing ability but also boost mechanical and electrical properties for advanced applications.

1.3.2 Microvascular Networks

The microvascular approach is another novel approach which draws maximum inspiration from nature to create most biomimetic synthetic material. Although this methodology shares basics with the

hollow glass fibers and encapsulation techniques discussed in previous section, a striking advantage which differentiates it from these two techniques is the ability to heal at the same point multiple times. This healing multiplicity originates from the presence of an interconnected network of hollow capillaries filled with healing agent inside the polymer matrix. This healing system closely resembles the healing mechanism evident in humans, animals and even certain plants. For example, in human body (or an animal), blood circulates in an intricate network of arteries, veins and capillaries of varying diameter in a clot-free fluid state. When damage happens at a particular point, a localized solid clot of blood is created to fill the wound (Figure – 1.13). Designing of an efficient microvascular system similar to that in biological systems, it is primordially important to consider various factors like shape of vesicles, their dimensions, orientation, 3D spatial arrangement. In such a scenario, Murray's law can be considered, according to which the cube of the radius of the parent vessel should equal the sum of the cubes of the radii of the daughter vessels. It was postulated that minimization of associated energetic cost with optimum transport flow in a circulatory system could be achieved by maintaining this ratio[87].
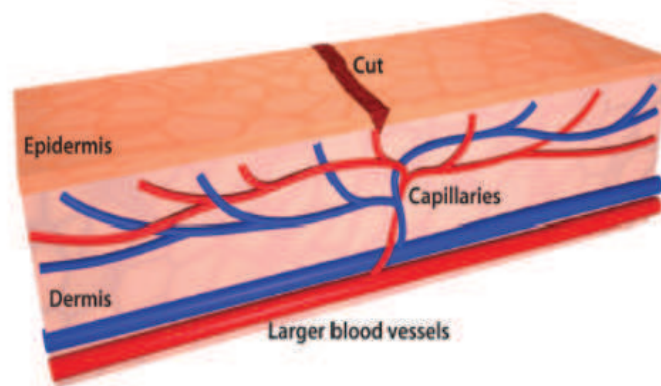
Figure – 1.13: Microvascular network of blood vessels and capillaries beneath the skin which supply the required materials for healing in case of damage to the skin.

A number of efficient network architectures have been proposed like a network of few large channels having large number of smaller sub-channels[88], looped channels[89], grid network[90,91], dual channels network[92] for optimum performance. In general, utilization of two segregated type of channels has been considered to be an optimal approach for the realization of vascular healing system. Under which, the main supply channels should be robust and strong enough to remain undamaged in case of mechanical impact thus maintaining the structural integrity of the material while the smaller channels should be capable of rupture and releasing the healing agent into the ruptured site[92]. Leakage of principal supply channel, closing of smaller channel due to cured healing agent, failure of smaller channel to rupture, degradation of healing agent and its improper cure are some of the additional parameters

that have been identified to be taken into consideration while designing materials based on microvascular approach[93]. Based on genetic algorithms, a modeling and optimization scheme was prepared for designing of 2D and 3D microvascular networks[94]. Various parameters like flow efficiency, homogeneity, network redundancy, network topology, microchannel diameter and void volume fraction were considered. The results showed that the addition of diagonal microchannels in the template improves flow efficiency, specifically at low values of the void volume fraction.
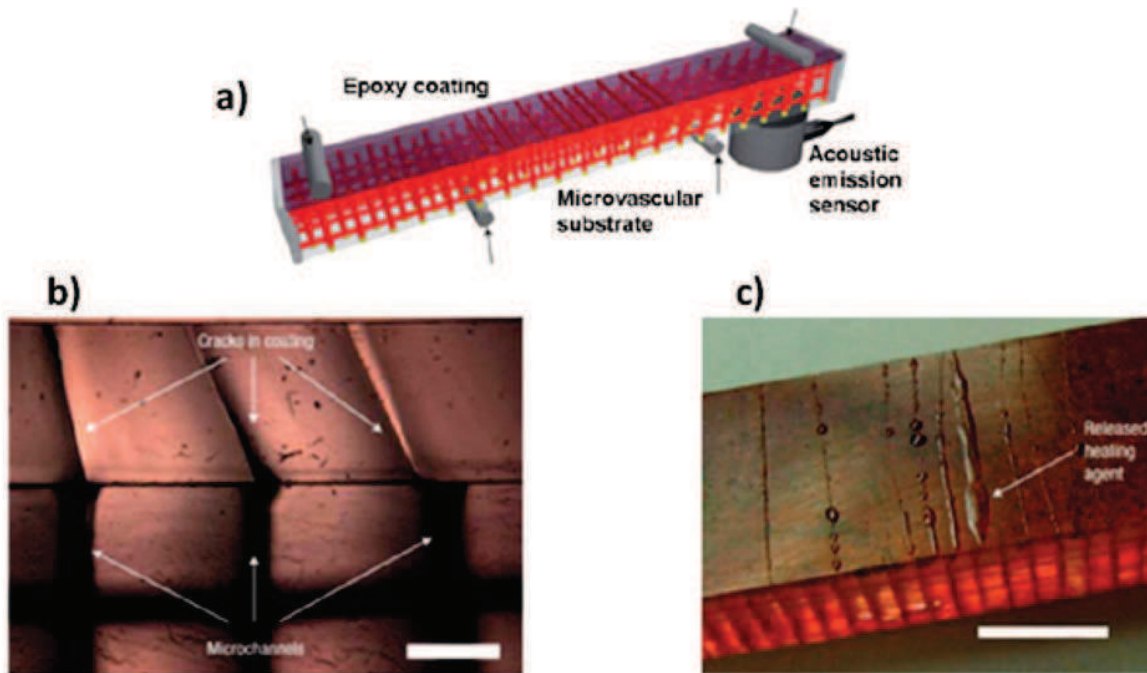
Figure – 1.14: a) Self-healing epoxy composite structure based on microvascular approach, b) Propagation of cracks towards the microchannel openings at the interface of the composite, c) Healed cracks with excess healing agent oozed out on the surface[95].

In a first practical work reported by Toohey *et al.* in 2007 demonstrating the above approach, epoxy composite materials were prepared and corresponding healing efficiencies were measured in number of healing cycles[95]. The work employed a 3-dimensional grid network substrate having 200 µm channels filled with dicyclopentadiene and embedded into a 700 µm epoxy coating which contained dispersed Grubbs' catalyst (Figure – 1.14). The interconnected nature of the channels was utilized to replenish the monomer reservoir enabling the healing of sample repeatedly up to 7 consecutive cycles. The system provided a 70% peak healing efficiency with 10 wt% catalyst in the top coating. It was remarked that the amount of catalyst (being a limited factor for a given sample) dictated the number of healing cycles that could be performed rather than healing efficiency for that sample. In following years, the number of healing cycles was augmented to 16 by using a two-part epoxy-amine healing chemistry

18

with dual isolated networks, holding each healing component[96]. A peak healing efficiency of 60 % was achieved. Although the system demonstrated clear advantages over DCPD/catalyst system, issues related to effective mixing of healing agents with successive healing cycles still persisted thereby limiting the maximum number of healing cycles that could be achieved.

In a parallel work[97] published in 2007 by Williams *et al.*, a microvascular-containing mechanically stimulated healable composite with sandwich structure was presented. The study found negligible influence of the network on the innate static mechanical properties of the host panel. The released healing agent (premixed epoxy/hardener) from ruptured channels was found to fill and repair the void resulted due to impact damage to the specimen leading to a full recovery of mechanical properties in a single healing cycle[97]. In a follow on study[98] consisting of dual network containing each component separately, showed significant recovery.

. In more recent work[99], dual complex and isolated 3-dimensional interpenetrating networks have been prepared to facilitate better stoichiometry and mixing at the damage point thus increasing the maximum number of healing cycles to more than 30 times. In a further refinement[100], a ternary interpenetrating network has been prepared where the third network is added to act as a conduit for circulating a temperature-controlled fluid that rapidly heats the locally damaged region leading to a sharp reduction in the time required for mechanical property restoration. The characteristic healing time is reported to be reduced by an order of magnitude by employing a third interdigitated microvascular network enabling *in situ* thermal regulation within the epoxy coating/substrate architectures.

1.4   NON-AUTONOMOUS SELF-HEALING POLYMERIC SYSTEMS

The autonomous healing polymer systems discussed so far have been remarkable for their performance and healing abilities for the particular applications they have been designed for. However despite their novelty, they still suffer from limited number of possible healing cycles and limitation to only certain type of polymer matrix. These limitations have prompted researchers to develop other strategies to obtain self-healing properties. The non-autonomous self-healing polymer materials rely on these strategies where the healing mechanism is triggered by certain stimulus, often integral part of the application for which the material has been designed. These materials are sometimes referred to as "intrinsic self-healing materials" because the inherent chemical nature of the polymer matrix is sufficient enough to undergo the healing process, negating the need of adding any external healing agent. This intrinsic nature imparts these materials a theoretical ability to heal unlimitedly though it comes as a trade-off for autonomic healing, relatively lower healing efficiency or low mechanical properties. In this

part of the chapter, these materials have been discussed based on the nature of bond chemistry they possess and the stimulus they require for the initiation of the healing process.

1.4.1 Dynamic Non-Covalent Bonding

1.4.1.1   *Supramolecular Chemistry*

The foremost dynamic non-covalent bond chemistry is represented basically by supramolecular chemistry involving non-covalent bonds such as hydrogen bonding, metal-ligand complexation, $\pi - \pi$ interactions which are reversible by nature and have been studied extensively[101]. Potential advanced functional applications for these interactions have been recently discussed[102,103]. Although reversible in nature, this dynamism however comes as a bargain with lower mechanical properties as compared to the materials with covalent bonding. To circumvent this problem, the number of such interactions was increased to get more robust materials in the form of linear polymer and reversible networks, copolymers[104-107]. These materials exploited the directional and cooperative effects of quadruple hydrogen bonding exhibited by 2-ureido-4-pyrimidone (UPy) functionalized monomers (Figure – 1.15).
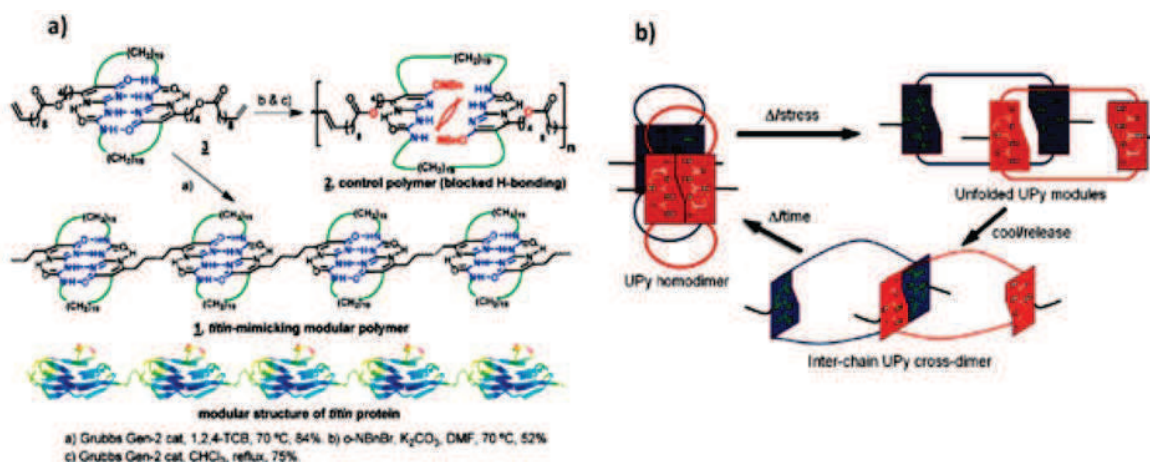
Figure – 1.15: Synthesis of biomimetic polymer prepared from, a) Assembly of 2-ureido-4-pyrimidone motifs having quadruple hydrogen bonding, b) The proposed mechanism of healing[107].

In 2008, a first supramolecular chemistry based material with decent mechanical properties and self-healing ability was introduced by Cordier *et al*[108]. It exhibited rubber like properties and harnessed the directionality and reversibility of hydrogen bonds as a tool to possess self-associated chains forming a network. The material was prepared from low molecular weight fatty di- and triacids functionalized with amido imidazolidones moieties which would then be mixed with urea derivatives in such a fashion

so as to have significant directional hydrogen bonding leading to network without crystalline regions (Figure – 1.16a).
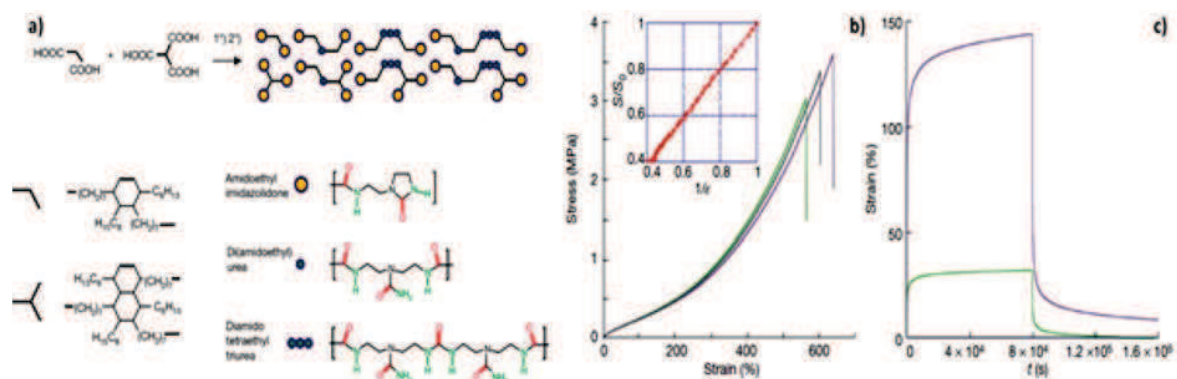
Figure – 1.16: Supramolecular chemistry based rubber, a) Mixture of oligomers obtained by reacting urea with condensed product of di- and triacids and diethylene triamine b) Stress-Strain curve obtained for the rubber, c) Creep recovery experiments conducted for the rubber[108].

The polymeric material with 11 % dodecane plasticization exhibited rubber like properties with strain at break exceeding 500 % while a residual strain of less than 5 % after elongated to more than 300 % (Figure – 1.16b,c). The other remarkable feature of this material making it relevant to the current discussion was its excellent self-healing ability and efficiency with a little mechanical stimulus. The mechanical stimulus was needed to bring the cut faces in contact with each other for the healing process to take place. When cut into two complete separate pieces, the material would mend itself completely with contact time of 15 minutes with elongation at break near 200 %. In elaborate series of experiments, it was shown that with longer contact time led to better recovery and longer is the elapsed time before bringing the cut faces together, lower is the recovery of strength (Figure- 1.17a,b,c). Another important feature of the healing ability of this system was its site specificity, i.e. healing could occur only between two fractured surfaces in contact with each other.
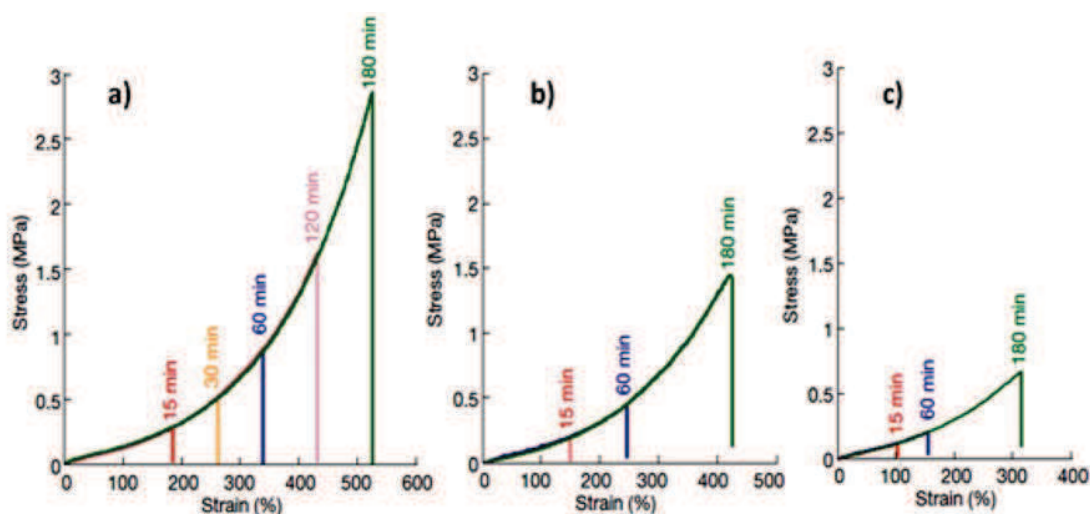
Figure – 1.17: Self-healing of the rubber at roome termperature, a) Stress – Strain curves until break obtained for healed sample at 40°C, b) Stress – Strain curves obtained at 20°C, c) Stress – Strain curves obtained for healed samples at 20oC but the two cut faces were joined after 18 hours time gap[108]

Metal-ligand coordination bonding is another approach that has been explored for the preparation of self-healing polymer systems. A preliminary work[109] in 2007, hybrid polymer gels were prepared with covalent cross-links creating a permanent, stiff network onto which reversible metal–ligand coordinative cross-links were added. It was shown, that reversible metal–ligand interactions bear mechanical stress within the hybrid gel thereby relieving the permanent network from stress. Upon removal of stress, these interactions would reform and reinstate the original strength of the material. Taking cue from nature, another novel self-healing polymer system has been proposed which mimics the catechol – iron complexation exhibited by mussel tissue. The rheological analysis of the system showed near covalent stiffness (G') of catechol-Fe^{3+} cross-linked networks at high strain rates proving that at a pH high enough to ensure good cross-linking; these transient coordination bonds can provide significant strength to bulk materials. Additionally, the catechol-Fe^{3+} cross-linked gels reestablished their stiffness and cohesiveness within minutes after through restoration of broken catecholato-Fe^{3+}cross-links thus showed near 100 % self-healing.

The dynamism of π – π stacking has also been exploited to obtain robust self-healing materials. In a first example of its kind[111], burattini et al prepared films from thermoresponsive polymer blends based on a low molecular weight polydiimide bearing multiple π - electron-poor receptor sites along its backbone and a siloxane polymer having p-electron-rich pyrenyl end-groups (figure- 1.18a). The system exhibited a rapid and reversible complexation in solution while solid state thermohealable

characteristics, due to presence of π-electron-rich and -poor receptors. Manual cuts made onto the films were shown to be healed completely at 90°C within a short time while at 115°C, healing was too fast to be observed (Figure – 1.18b,c,d).
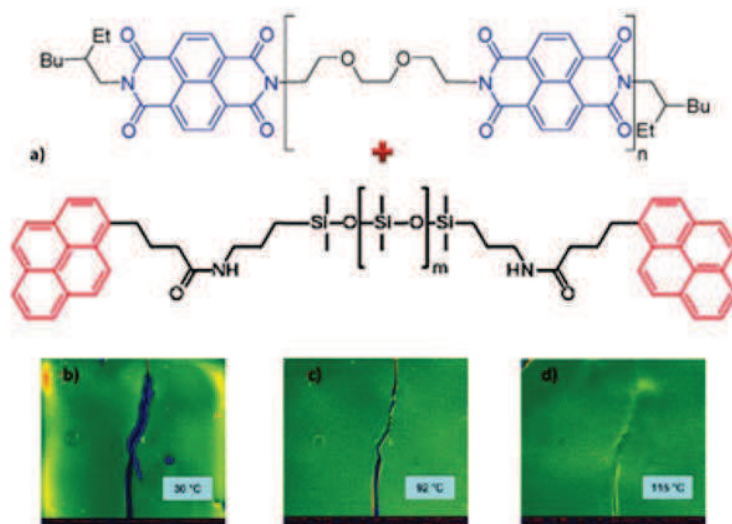
Figure – 1.18: Self-healing system based on π – π stacking, a) Chemical structure of low molecular weight polyimide and siloxane polymer bearing pyrenyl end groups, b-d) Unhealed and healed films at 30°C, 92°C and 115°C respectively[110].

In a further improved work, the authors capitalized on both interpolymer hydrogen bonding and π – π stacking modes of interaction to prepare robust, tough elastomeric thermally healable films. The system exhibited a nanophase separted morphology with well contrasted two different domains. The authors reported a reproducible regain of more than 95% of the tensile modulus, 91% of the elongation to break, and 77% of the modulus of toughness of the pristine material for fractured samples healed at 100°C.

1.4.1.2   Ionomers

Polymers consisting of upto 15 % of ionic content in their structure are classified as ionomers. Being thermoplastic in nature, these polymers contain carboxylic acid moieties as pendant groups which can either be in partially or completely neutralized state with either a metal or quaternary ammonium ions. Given the dynamic nature of the ionic bonds, it is not surprising that these polymer systems been explored recently for the preparation of self-healing materials. One of the most studied ionomers for self-healing application are based on poly(ethylene-co-methacrylic acid) (PEMAA). This ionomer is

commercialized under tradenames; *Nucrel®* having 5.4 mol% methacrylic acid, *Surlyn®* having 5.4 mol% methacyrlic acid but neutralized by metal ion in varying percentages. Both of these ionomers have shown self-healing behavior upon projectile impact, especially *Surlyn®* which shows an almost instantaneous healing. Earlier it was postulated that the healing phenomenon observed in these ionomers is due to their inherent thermally responsive ionic linkages. However this reasoning does not explains albeit small healing observed in case of *Nucrel®* which does not contain any ionic aggregates. Furthermore, the projectile puncture in these ionomers was circular in nature with diameter in millimeters. Therefore, while reptation motions responsible for chains interdiffusion in case of fractured surfaces in contact with each other, it is impossible for them to initiate large scale motions required to bring the surfaces together to heal the circular perforation. A later work[112] on the same ionomers showed that instead of ionic content, it is the presence of an ionic functionality (in the form of acid group) that is crucial for the healing process. The authors found that the incorporation of acid groups in the polymers, imparted thermoresponsive hydrogen bonding and unique viscoelastic response which were responsible for the promotion of the healing process. In follow on thermal studies[113], it was found that healing mechanism is strongly dependent upon the sharp increase in temperature at the puncture point after projectile impact however higher temperatures did not favored the healing process. The shape of projectile was also found to be important parameter for the healing response with pointed projectiles giving better results than blunt ones. In contribution to above findings, similar ballistic studies[114] combining a modified testing method[115] showed that while the outer impact regions exhibit ductile/elastic behaviour, the inner regions to the impact cavity exhibit elastomeric and viscous behaviour. The presence of ionic clusters imparts various properties from elastic, elastomeric and then molten behavior at different temperatures and thus playing a critical role during high-energy impact (Figure – 1.19). Additionally, healing cycles up to 6 were performed demonstrating the inherent nature of healing based on the chemical structure and morphology of the polymer system. Some more recent examples [116,117] using ionomers include their blends with ethylene-co-vinyl alcohol copolymer (EVA) and epoxidized natural rubber. Although in these works, healing efficiency has not been mentioned explicitly, nevertheless ionomers based materials can be considered highly efficient and completely autonomous in terms of healing given the rapid closure of hole created by very fast impact.
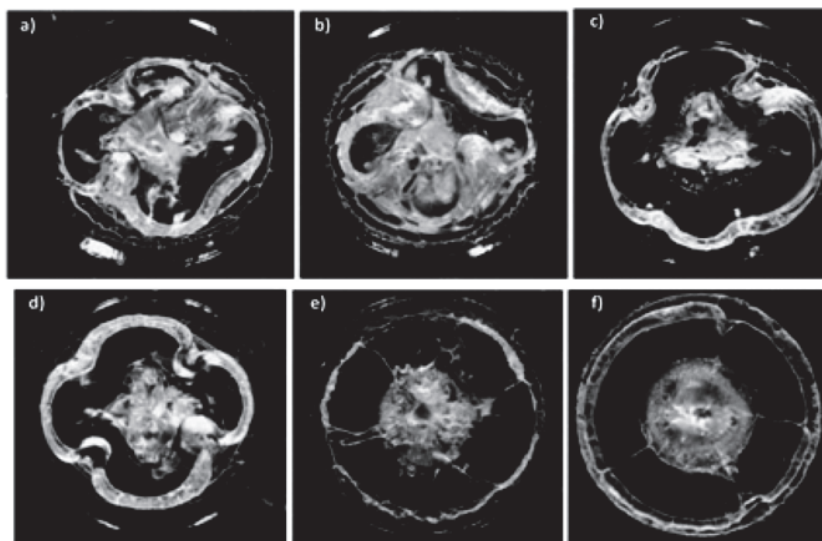
Figure – 1.19: Self-Healing in ionomer Surlyn 8940® upon projectile induced damage at, a) 20°C, b) 50°C, c) 90°C, d) 130°C, e) 170°C, f) 210°C[118]

1.4.1.3   Molecular Interdiffusion

The concept of molecular interdiffusion for self-healing was proposed in 1980s when a number of works on crack-healing were published for PSAN-PMMA[72], PSAN[119], PET[120,121], Polyamides[122], PS-PVPE[123], PS-PPO[123] and carbon fiber reinforced PEEK composites[124]. The healing observed in these polymer systems was attributed to molecular interdiffusion across the interface, facilitated by close contact between two surfaces at a temperature slightly higher than glass transition (T$_g$). At elevated temperatures, molecular chains entanglement would ensue the interdiffusion process leading to a swift disappearance of the interface and an increase in mechanical properties along with completion of the healing process. All of these works involved heating of specimens at temperatures above the T$_g$ of the polymer system, usually varying between -50°C to +100°C under certain pressure. Depending upon the kind and extent of fracture, temperature, pressure, sample geometry, the reported healing times would vary from few minutes to as long as years. In order to explain this healing phenomenon *via* interdiffusion, various models were considered; notably the reptation model of chain dynamics[125,126] and later a five stages model (Figure – 1.20) explaining the execution healing process in terms of surface rearrangement, surface approach, wetting, diffusion and randomization[16]. A mathematical microscopic theory was also presented to further explain the diffusion and randomization stages[127]. It was concluded that due to large presence of small chain segments (formed due to chain scission) at the fractured surfaces, the diffusion phenomenon is very different from that when two pieces of the same polymer are

joined together at temperature higher than the T_g since the latter has larger flat segmental distribution. Due to unavailability of a universal method to obtain the healing thereby varied healing times along with non-autonomous nature of the process, motivation for this approach almost ended by the beginning of 1990s. However the theory of interdiffusion and the models presented have been used to study and design encapsulation and microsvascular based healing approaches.
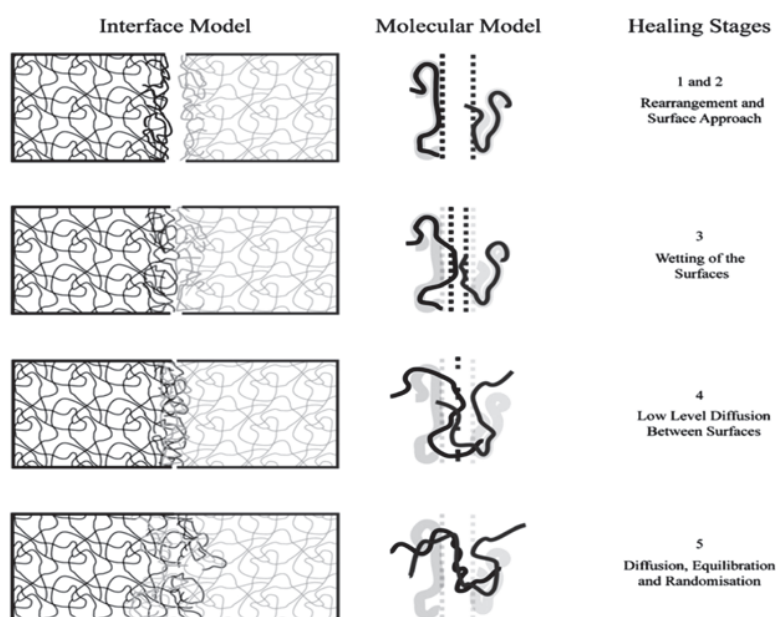
Figure – 1.20: Mechanisms involved in self healing via molecular interdiffusion.

1.4.2 Dynamic Covalent Bonding

Much like dynamic non-covalent bonding, dynamic covalent bond chemistry has also been extensively explored. Polymers incorporating these bonds do not suffer from low mechanical properties as their counterparts with non-covalent bonds. However again, this comes with less impressive self-healing ability and lower healing efficiencies. Moreover, most of these systems require a particular stimuli like heat, light, mechanical stress, pH fluctuations specific to the inherent dynamic chemistry of the material. In most of the cases, these materials have been designed in such a fashion that the required stimulus for the healing is encountered as a part of the sought application. Nevertheless, human intervention is still required in some way or another; hence these systems are categorized as non-autonomous self-healing systems.

1.4.2.1   Diels-Alder Chemistry

The diels-alder cycloaddition reaction was discovered in 1928 by Otto Diels and Kurt Alder (Figure – 1.21). The beauty of this reaction lies in its ability to form C – C bonds with little or no heat application. However the feature that makes it even more important for synthesis of self-healing materials is its thermal reversibility, also known as reversible diels-alder reaction (rDA). Generally the rDA reaction takes place at temperature higher than $100^{o}C$ and gives back the reaction precursors.
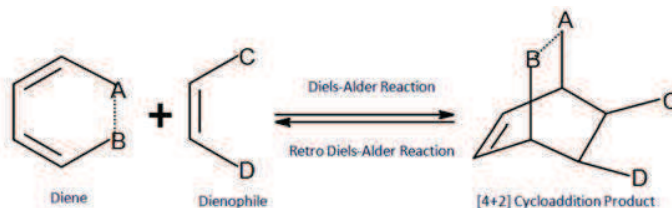
Figure – 1.21: The Diels-Alder reaction

A large number of publications have been published concerning the synthesis of polymer systems employing rDA chemistry, but their applicability for self-healing application and relevant data has been reported quite lately. In general, most of such polymer systems either incorporate dienophile/diene as a pendant groups to the backbone chain or the backbone chain itself is formed due to consecutive DA reactions between functionalized monomers. The Furan/Maleimide combination has been the most explored DA-rDA chemistry system for the fabrication of thermally self-healed polymers although other dienophile/diene combinations have also been explored.   In 1969, the earliest known work as a patent on the synthesis of a thermally reversible polymer incorporating Furan/maleimide moieties was reported. This was followed by a series of pioneering works[128-130], in which these moieties were incorporated as pendant groups onto the polymer chains (Figure – 1.22).
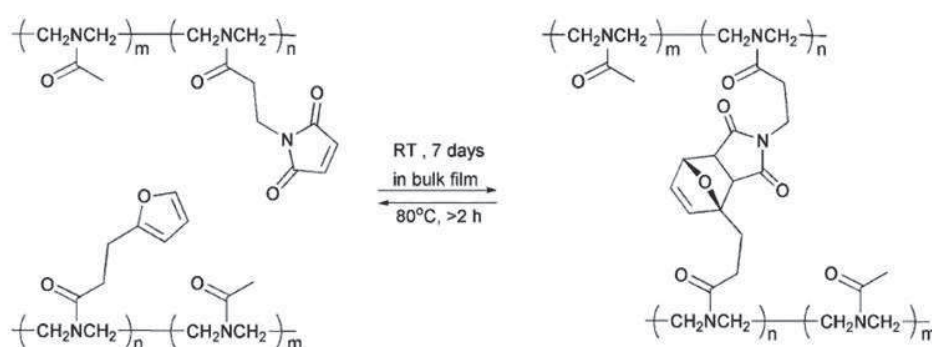
Figure – 1.22: Reversiblly crosslinked polymer via Diels–Alder cycloaddition reaction between pendent furan and maleimide moieties[129].

Inspired by these findings, the first thermally remendable polymer system based on DA-RDA chemistry was reported in 2002[131] by Chen et *al*.. A transparent and highly crosslinked solid polymer was prepared by diels-alder reaction between tris-maleimide and a tetra-furan (Figure – 1.23a). The polymer showed significant mechanical properties comparable to that of contemporary epoxy systems. The healing studies were conducted by completely fracturing the specimen followed by heating (90^oC – 120^oC) and cooling cycles and structural analysis by solid state C-NMR spectroscopy. The system was found to be able to heal multiple times although the healing efficiency was reported to be only 57 % (Figure – 1.23b)., the reason of which was attributed to the complete failure of the specimen leading to poor interfacial match-up between separated pieces.
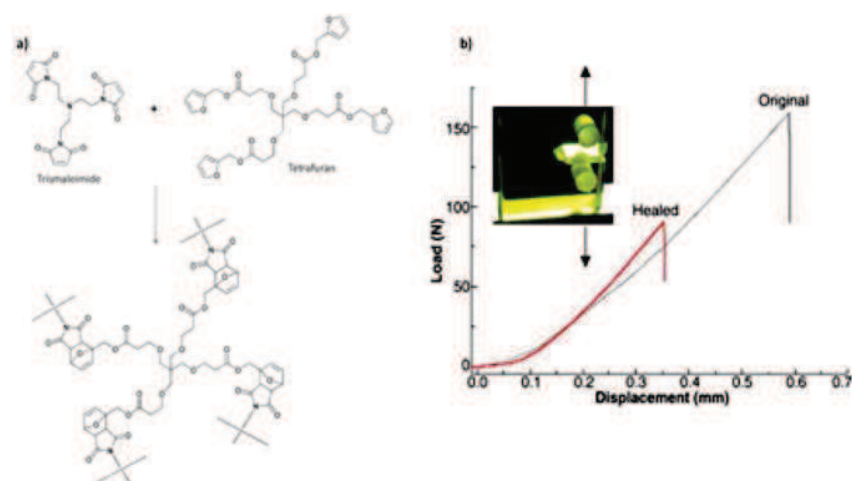
Figure – 1.23: Diels-Alder reaction based self-healing, a) Highly crosslinked polymer formed from trimaleimide and tetrafuran, b) Stress-Strain curve obtained for the healed specimen with only 57 % efficiency[131].

In a follow on work[132], several improvements were made to obtain a better healing efficiency. The new polymer was prepared in solvent-free conditions using a lower melting point bismaleimide in place of previous tris-maleimide. A better designed sample geometry for mechanical strength testing prevented complete specimen failure which permitted to have higher healing efficiencies of 80 % for first cycle while 78 % for second healing cycle. A series of works[133-138] have since been reported using the above approach to prepare thermally healable polymers and investigate their healing properties. Given the high crosslinking nature of these polymers and good mechanical strength thus obtained, the multifunctional furan/maleimide derivatives have also been explored for generating polymers for structural applications. In one of such recent works[139,140], carbon fibre reinforced polymer composite have been prepared using tetrafuran/bismaleimide based highly crosslinked polymer. In parallel to

above approach, the pendant group approach has also been extensively explored for the fabrication of thermally self-healing polymers. Most of the examples[140-142] are based on the incorporation of furan moiety as pendant groups (Figure – 1.24a) onto a thermoplastic or a thermoset polymer while a bis- or trismaleimide (Figure – 1.24b) compound is added as reversible crosslinking agent. Additionally, direct polymerization of furan based methacrylates with other methacrylates using atomic transfer radical polymerization to obtain controlled molecular architectures has also been performed[143,144]. In a recent work, a recyclable furan functionalized polyketone thermoset, crosslinked with bismaleimide was presented[145]. The reversible gelation as a function of temperature was used as an indicator for DA and rDA reactions demonstrating the thermal reversibility of the system. The recyclability of the system was proved by grinding a fractured sample and fabricating a new sample from it. The new sample performed as similar as the pristine sample in mechanical tests which led the authors to claim a 100 % healing efficiency in an otherwise different context.
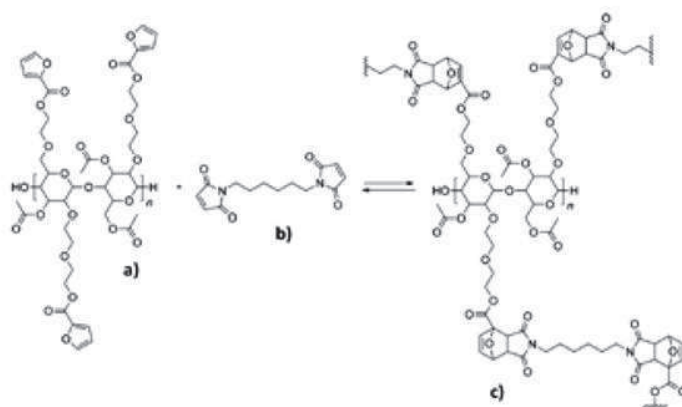
Figure – 1.24: Thermoreversible complex architectures made reaction of, a) Hydroxyethylcellulose furoate acetate with, b) Bismaleimide to form, c) Crosslinked polymer having flexible structure with liquid crystalline properties[141]

Besides furan/maleimide combination, there are also other compounds like dicyclopentadiene[146-148] and anthracene[149] which have been used recently to fabricate thermally reversible polymers. The advantages of dicyclopentadiene is its cyclic nature which provides a favorable s-cis conformation for Diels-Alder reaction and its ability to self-react to form DA adduct rendering the need to use maleimide as a dienophile. For instance, in one example, a biscyclopentadiene end-functionalized PMMA was synthesized and then crosslinked with a trifunctional pyridinyl dithioformate compound *via* hetero-DA reaction[150] (Figure – 1.25). Although no healing data in terms of mechanical properties or visual healing was presented, the so called "bonding" at room temperature in 10 minutes and "debonding" at

temperature greater than 80°C in less than 5 minutes of the system was demonstrated by size exclusion chromatography and ultra-violet spectroscopy.
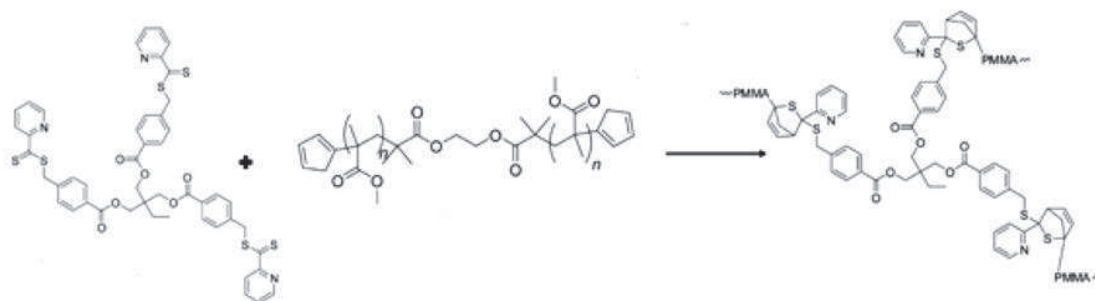
Figure – 1.25: Thermoreversible crosslinked Poly(methyl methacrylate) network formation via hetero Diels-Alder reaction[150].

The high temperatures associated with rDA reactions may sometimes generate undesirable byproducts due to decomposition of the polymer or any other reactant present in the system. Also a significant emphasis has been put towards the development of room temperature self-healing systems; therefore it is desirable to reduce the required temperature for rDA reaction as low as possible to minimize the need of energy for the healing process and if possible a complete replacement of heating procedure itself. In view of this constraint, use of ultrasound as a tool to facilitate rDA reaction has been proposed recently. In this work, poly(methyl acrylate)s (PMAs) of different molecular weights were prepared from a Diels-Alder adduct of maleimide with furan containing two polymerization initiators. When subjected to ultrasound at 0°C, the authors demonstrated the occurrence of rDA with gel permeation chromatography (GPC), ultra-violet visible spectroscopy and chromophore labeling of the liberated maleimide and furan moieties. However the no rDA reaction was observed for polymers with molecular weight greater than 60 KDa and lesser than 20 KDa. Similar results were obtained for analogous polymers that were prepared from a cycloaddition adduct initiators of maleimide with anthracene. Driven by the same constraint, new class self-healing polymer films have been successfully prepared by capitalizing over room temperature dynamic Diels-Alder chemistry[151]. In this novel work by Reutenauer et *al*, self standing thin films were casted from a mixture of bis(fulvene) and bis(tricyanoethylenecarboxylate) dynamers (Figure – 1.26a). To demonstrate the self-healing ability, the film was cut into two pieces and then the two pieces were pressed together with some overlapping. In less than 10 seconds, the pieces could no longer be separated (Figure – 1.26b). This is in contrast with the behavior shown by self-healing supramolecular elastomer which showed healing only between two

freshly cut surfaces. The reason behind the all surface healing feature has been attributed to the ability of the dynamers to constantly create new chain ends and form new connections.
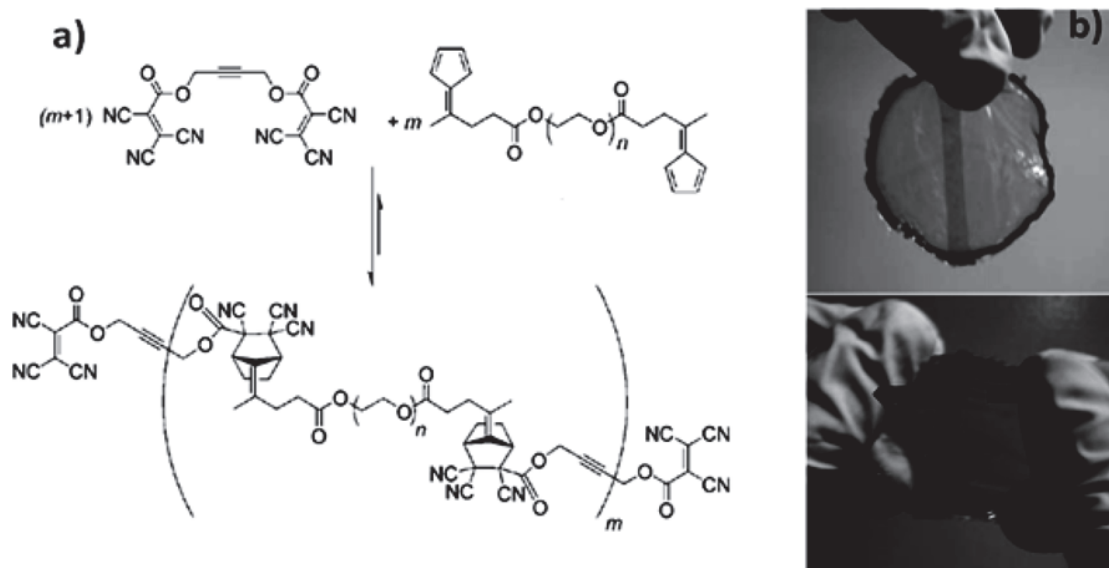
Figure – 1.26: Diels–Alder chemistry used to prepare, a) Reversibly cross-link fulvene functionalized glycol-based polymers with a cyanfumarate di-linker at room temperature, b) Room temperature healable film made from the crosslinked polymer[151].

1.4.2.2   Sulfur Chemistry

Sulfur chemistry is another emerging strategy for inducing self-healing ability in a polymeric system. The interesting feature which makes disulfide bonds important for this application is their cleavage under reducing conditions to give thiol groups which revert back to disulfide linkage in oxidizing conditions. Hence it is obvious from above feature that polymers consisting disulfide bridges can be reversibly crosslinked by effectively using reduction-oxidation conditions. Some notable works capitalizing above this chemistry include the very first example of a reversibly crosslinkable polyoxazoline hydrogel with disulfide bonds[152], ATRP derived polystyrene having disulfide bridge in the middle[153], ATRP derived poly(ethylene glycol diacrylate)$_m$-*co*-(poly(butyl acrylate)-*b*-poly(SS))$_n$ star copolymers[154](Figure – 1.27).
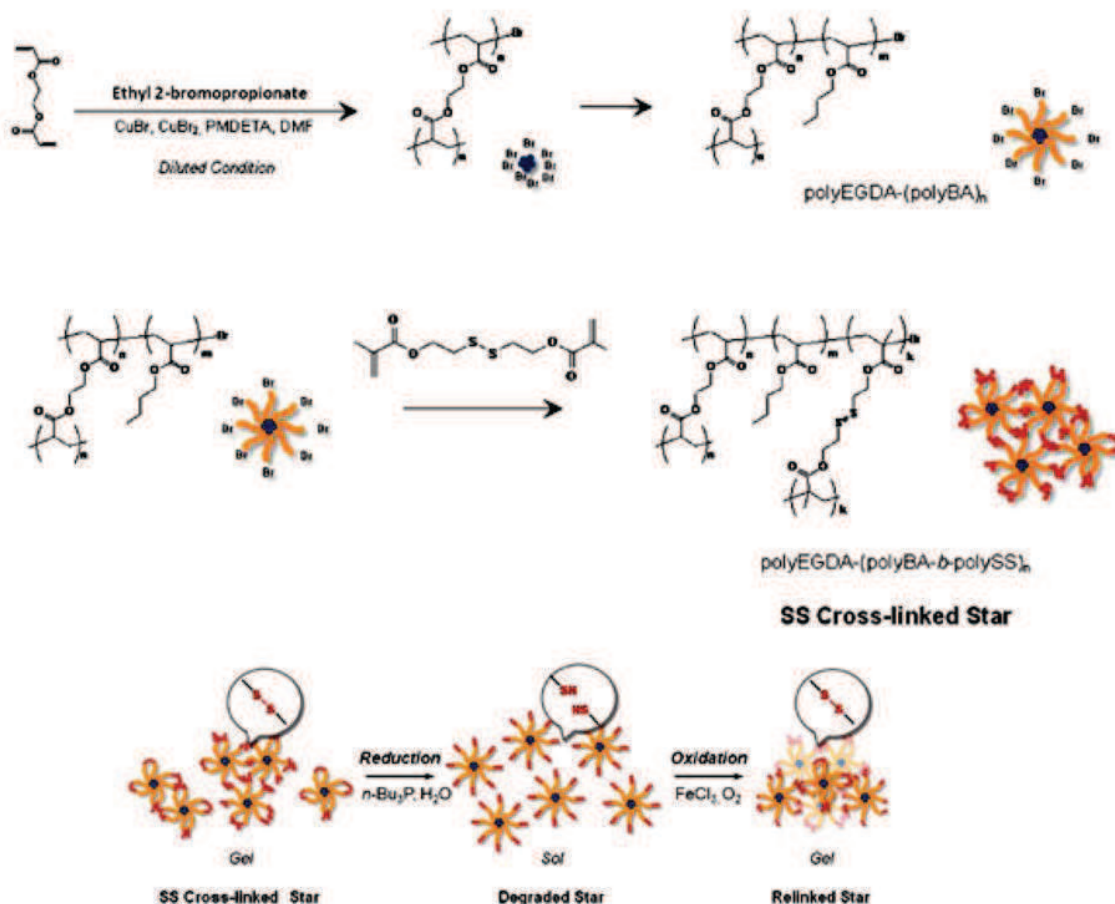
Figure – 1.27: Sulfur chemistry based synthesis of, a) Reversible cross-linked star polymers, b) Reduction and Oxidation of SH/SS-Functionalized Star Polymers[154].

In a slight different approach[155], a polymeric network was prepared from pentaerythritol tetra(3-mercaptopropionate) and triethyleneglycol divinyl ether along with a comonomer and instead of using reduction – oxidation for reversible crosslinking, light was used an agent for trigerring the cleavage of the allyl sulfide linkages. This photoinduced cleavage led to plasticity, actuation, and equilibrium shape changes without residual stress into the material.

Although none of these works reported any data regarding self-healing property, the relative ease of reversibility (especially in case of photoinduced cleavage) of these systems exhibited points towards the capability of thiol chemistry for a robust self-healing system in applications like functional coatings. In one such instance, poly(n-butyl acrylate) grafted star polymers were prepared by chain extension ATRP from cross-linked cores comprised of poly(ethylene glycol diacrylate). These polymers were further used as copolymerized with bis(2-methacryloyloxyethyl disulfide) (DSDMA), imparting

disulfide reversible cross-links (S-S) at branch peripheries (Figure – 1.27). The S-S cross-linked polymers were then cleaved under reducing conditions to form thiol (SH)-functionalized soluble star polymers, which were then deposited on silicon wafer substrates and oxidized into insoluble S-S re-cross-linked films. The self-healing of prepared polymer films was studied by continuous atomic force microscopy (AFM) imaging of cuts micromachined with the AFM tip and by optical microscopy. The re-cross-linked star showed a rapid spontaneous self-healing behavior, with the extent of healing dependent on the initial film thickness and the width of the cut. The self-healing behavior observed for this sample was attributed to the regeneration of S-S bonds *via* thiol - exchange reactions. Another recent work utilizing thermal disulfide exchange chemistry instead of disulfide redox chemistry and explicitly reporting self-healing ability involved epoxy resin crosslinked with a tetra thiol based crosslinker. The material showed rubbery behavior due to lower T_g and healing experiments were performed by making a knife cut into the sample followed by heating at 60^oC for certain time without application of any force. The initial cut in the sample disappeared completely after 1 hour at 60^oC as observed with microscopy (Figure- 1.28a). Additionally, the mechanical properties in terms of elongation at break were found to be fully restored at this temperature and in general better healing was observed with longer healing time and higher concentration of sulfide crosslinker. The system exhibited impressive healing efficiency in multiple healing cycles as evident by the very little change in elongation at break values observed for three successive healing cycles.
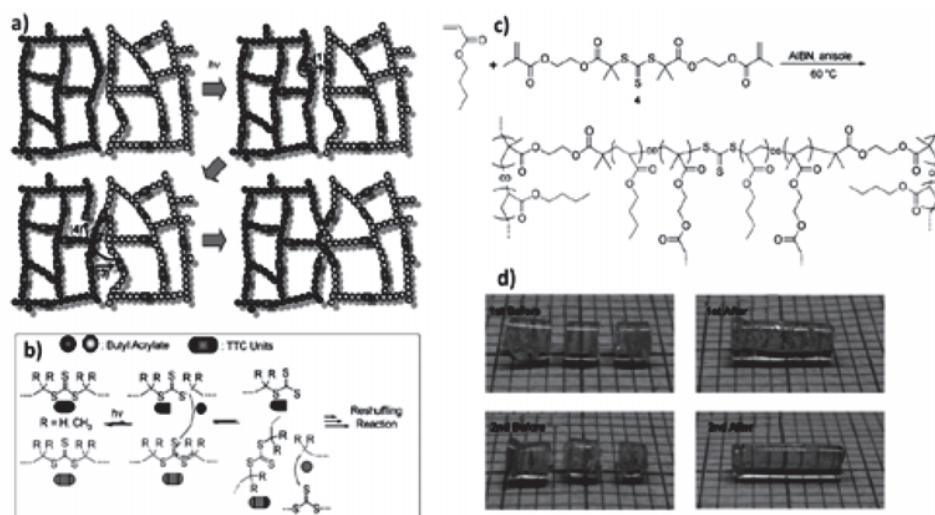
Figure – 1.28: Self-healing material based on reshuffling trithiocarbonate units, a,b) General mechanism of reshuffling under UV radiation, c) Preparation of a cross-linked polymer by RAFT copolymerization of Butyl Acrylate, d) Photographs of cross-linked polymers in repetitive self-healing reactions under UV irradiation in acetonitrile

A different kind of sulfur chemistry has also been investigated in the form of trithiocarbonates, which are capable to undergo reshuffling reactions when irradiated with UV light (Figure – 1.28a). A chemical simulation based proof of concept study[156] was reported on this in 2010 followed by practical examples in the following years[157,158]. In the most recent example based on this approach, self healing polymer gels were prepared from reversible addition fragmentation transfer (RAFT) copolymerization of n-butyl acrylate and a trithiocarbonate cross-linker to obtain Poly(n-butylacrylate) (PBA), a polymer with a low T_g value (~ —50°C) having high chain mobility at room temperature (Figure – 1.28b).

Healing was reported in terms of joining of pieces of monolithic polymer gel (in acetonitrile) when irradiated with UV light under nitrogen atmosphere with 10 g wt pressure with time duration varying between 4hrs – 12 hrs. The tensile modulus obtained for the healed monolith was 65±11 kPa while that for pristine monolith was 69±6 kPa indicating an almost complete recovery of mechanical strength.

1.4.2.3   *Miscellaneous Chemistries*

In addition to above discussed classical dynamic covalent chemistries, some novel chemistries have also been demonstrated of their potential for the synthesis of self-healing materials.
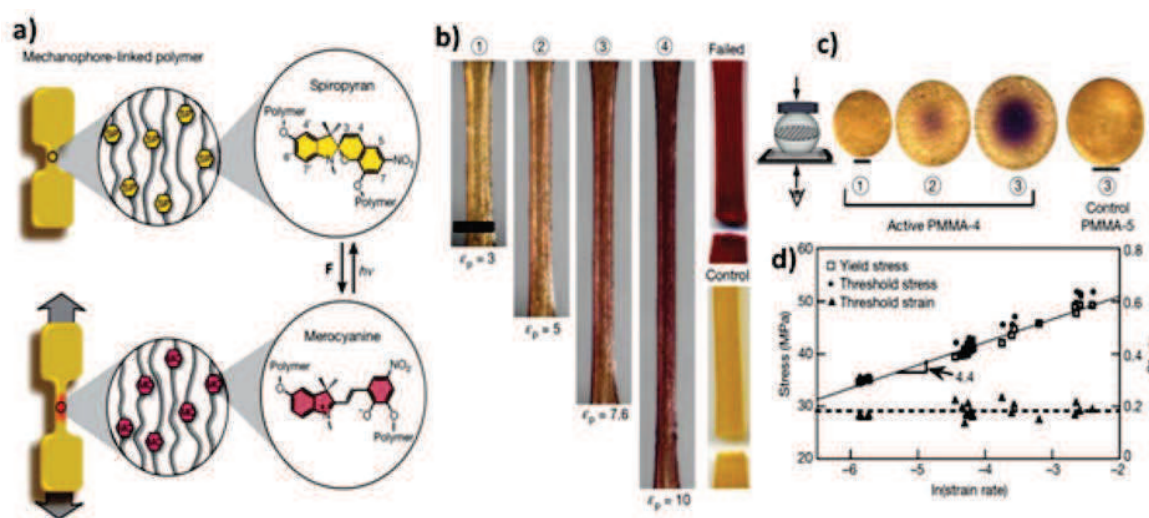
Figure – 1.29: Mechanoresponsive chemistry based Self-healing, a) Dog bone shaped specimens of poly(meth acrylate) (PMA) which changes from being colorless (spiropyran) to colored (merocyanine), b) Sample of PMA stretched until broken with corresponding change in color, the yellow colored controlled sample does not contain the mechanoresponsive moieties, c) Optical photos of PMMA beads containing mechanophore moieties under compression, d) Threshold stress and yield stress remain coincident for PMMA beads as a function of strain rate[159].

In first such example[159] by Davis et *al.*, mechanoresponsive chemistry[160] was employed for demonstrating mechanical force dependant color change in mechanophore-linked poly(methyl acrylate)(PMA) elastomers and mechanophore cross-linked poly(methyl methacrylate)(PMMA) glassy polymer specimen. The spiropyran mechanophore would undergo a stress-induced 6-π electrocyclic ring-opening reaction to give merocyanine form accompanied by a stark change in color (Figure – 1.28a). In a series of tensile stress tests conducted for mechanophore linked PMA and compression tests for mechanophore crosslinked PMMA beads, the authors were able to successfully visualize threshold stress for the specimens before failure (Figure – 1.28b). In case of PMMA bead compression tests (Figure 1.29c), that the threshold strain was found to be constant irrespective of strain rate while both yield stress and threshold stress increased linearly thus indicating that the mechanochemical reaction in the bulk polymer to be a strain-activated rate process(Figure – 1.28d).

Although no self-healing experiments were conducted in above work, novel self-healing material based on such mechanophoric building blocks can be visualized in which the mechanophore moieties would act as molecular "force sensor" to signal the effect of stresses and damage on polymer material thus providing a time window for effective repair or replacement before catastrophic failure.

In a second example, self-healing polymer gel was prepared using on a new kind of dynamic covalent bonding unit which imparted impressive healing properties under mild conditions regardless of the degree freshness of the cut surfaces[161], a restrictive feature observed with supramolecular self-healing rubber discussed earlier. In this work, 3-dimensional polymer gels were prepared using polypropylene glycol crosslinked with diarylbibenzofuranone (DABBF) units. Diarylbibenzofuranone can be cleaved easily at room temperature forming two oxygen tolerant radical unimers which again react with each other to reform the DABBF dimer (Figure – 1.29a).
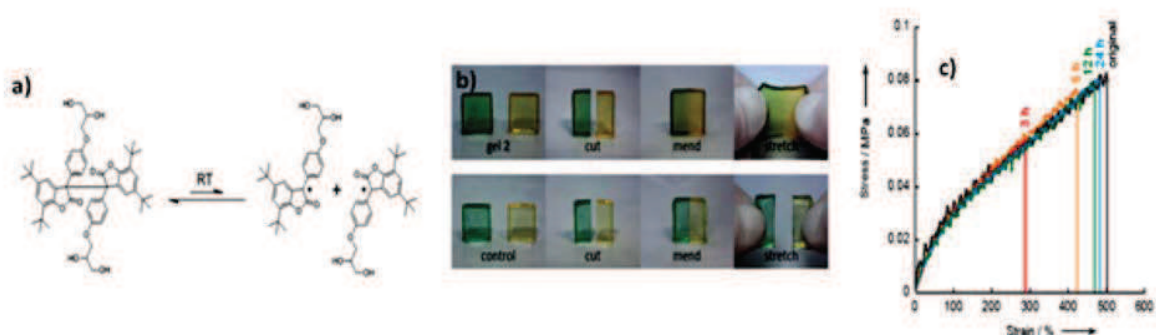
Figure – 1.29: Dynamic covalent chemistry based self-healing material, a) Chemical structure of diarylbibenzofuranone and its reversible fission at room temperature, b) Photographs of self-healing behavior of cross-linked polymer gels compared with conventional cross-linked polymer gels at room temperature stretchedstate, respectively, after 24 hours, c) Typical stress–strain (stress–stretch ratio) curves of cross-linked polymer gels before and after self-healing measured under air at room temperature.

Self-healing was demonstrated by slightly pressing together two pieces of polymer gel with faces slightly moistened in DMF (Figure – 1.29b). After 24 hours, the two pieces were impossible to separate by manual stretching. To quantify the healing, tensile tests were conducted for samples with different healed times (Figure – 1.29c). While the original sample showed an elongation at break at 500 MPa, a maximum 98 % recovery of elongation at break was obtained for samples healed for 24 hours. Samples healed for approximately 3 hours showed a maximum recovery of 55 %. The role of DMF was reported to be to prevent the hydrogen bonding between urethane units in the polymer.

Lately, nanoparticles have also been utilized to repair damaged sites in a fashion that very much mimics the movement of leucocytes and initiation of healing process at the wound or infection site in biological systems. This proposed "repair and go" approach was first validated using computer simulations in 2D[162] and later in 3D [163]space , modeling the rolling motion of a single fluid-driven, nanoparticles-filled microcapsule along a heterogeneous adhesive substrate. By combining the lattice Boltzmann model for hydrodynamics, lattice spring model for the micromechanics of elastic solids and a Brownian dynamics model for the release of nanoparticles, it was demonstrated that these microcapsules can move to the damaged sites to release the encapsulated particles for repair and then move further along the surface of the substrate. To obtain such an elaborate mechanism, the strength of the adhesive interaction between the capsule and the substrate, the rate of diffusion of the particles through the shell of the microcapsule and the Peclet number of the flow were found to be controlling variables. The effect of utilizing an alternate high and low shear rates (pulsatile shear) was also studied. Low shear rates enabled the microcapsule to be localized within the crack for a certain time and thus releasing the nanoparticles for repair. The capsule is then pushed further out of the crack by increasing the shear rate to carry out healing at other sites on the substrate, thus enabling a desired repair-and-go functionality. The above "repair and go" approach has further been validated experimentally by using polymer surfactant stabilized oil droplets containing CdSe nanoparticles[164] (Figure 1.30).
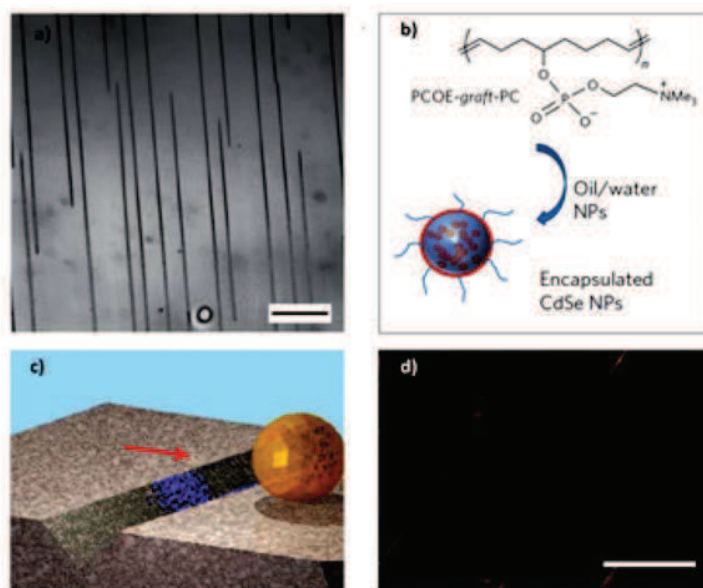
Figure – 1.30: The repair and go strategy, a) Optical image of a cracked, b) PCOE–g–PC polymer used for droplet stabilization and nanoparticle (NP) encapsulation, c) Frame from a simulation depicting nanoparticle deposition (blue particles) into a crack, followed by rolling of the capsule to the next crack (red arrow), d) Fluorescence micrograph of a substrate following nanoparticle deposition into the cracks[164].

Stable droplets mimicking the microspheres were prepared by sonicating an aqueous solution of poly(cyclooctene)–g–poly(phosphorylcholine) with trichlorobenzene containing fluorescent CdSe nanoparticles, to give polydisperse droplet samples (60±30 μm in diameter). This droplet solution was passed along an oxidized surface of poly(dimethyl siloxane) substrate at a flow rate of 0.5 ml/s, in 50 pulsed intervals, with 4 s of flow and 10 s of rest. It was noted that the 'rest' period was vitally significant for the desired deposition of nanoparticles with reduced deposition into the cracks was observed in case of short rest times whereas long rest periods resulted in more extensive particle deposition both in the cracks and surrounding areas. The substrate was rinsed thoroughly with pure water at the end of the experiment and analyzed with fluorescence microscopy. The observed fluorescence on the surface was largely confined to the crack planes indicating the presence of deposited CdSe nanoparticles.

The larger size of the droplets relative to cracks and the antifouling properties imparted to them by the hydrophilic PC-substituents of the PCOE–graft–PC polymer were noted to be contributing factors for their reversible deposition over the surface thus promoting the "repair and go" process. Further, the very thin polymer layer between the hydrophobic CdSe nanoparticles and crack surface enabled an easy translocation within the time frame in which the droplets are in contact with the

cracks. The recovered droplets after rinsing were found to be stable thus strengthening the fact that selective deposition of nanoparticles takes place without bursting the droplets *via* translocation across the thin polymer membrane.

REFERENCES

1   Blaiszik, B. J. *et al.* in *Annual Review of Materials Research, Vol 40* Vol. 40 *Annual Review of Materials Research* (eds D. R. Clarke, M. Ruhle, & F. Zok) 179-211 (Annual Reviews, 2010).

2   Yang, Z., Hollar, J., He, X. & Shi, X. A self-healing cementitious composite using oil core/silica gel shell microcapsules. *Cement & Concrete Composites* **33**, 506-512, doi:10.1016/j.cemconcomp.2011.01.010 (2011).

3   Wiktor, V. & Jonkers, H. M. Quantification of crack-healing in novel bacteria-based self-healing concrete. *Cement & Concrete Composites* **33**, 763-770, doi:10.1016/j.cemconcomp.2011.03.012 (2011).

4   Hager, M. D., Greil, P., Leyens, C., van der Zwaag, S. & Schubert, U. S. Self-Healing Materials. *Advanced Materials* **22**, 5424-5430, doi:10.1002/adma201003036 (2010).

5   Van Tittelboom, K., De Belie, N., De Muynck, W. & Verstraete, W. Use of bacteria to repair cracks in concrete. *Cement and Concrete Research* **40**, 157-166, doi:10.1016/j.cemconres.2009.08.025 (2010).

6   Jefferson, A. *et al.* A new system for crack closure of cementitious materials using shrinkable polymers. *Cement and Concrete Research* **40**, 795-801, doi:10.1016/j.cemconres.2010.01.004 (2010).

7   Yao, K., Tay, F. E. H. & Zhu, W. G. Self-mending of microcracks in barium titanate glass-ceramic thin films with high dielectric constant. *Journal of the American Ceramic Society* **85**, 496-498 (2002).

8   Baker, A. A., Jones, R. & Callinan, R. J. damage tolerance of graphite epoxy composites. *Composite Structures* **4**, 15-44, doi:10.1016/0263-8223(85)90018-2 (1985).

9   Wetzel, B., Rosso, P., Haupert, F. & Friedrich, K. Epoxy nanocomposites - fracture and toughening mechanisms. *Engineering Fracture Mechanics* **73**, 2375-2398, doi:10.1016/j.engfracmech.2006.05.018 (2006).

10   Kinloch, A. J. Mechanics and mechanisms of fracture of thermosetting epoxy polymers. *Advances in Polymer Science* **72**, 45-67 (1985).

11   Ritchie, R. O. Mechanisms of fatigue-crack propagation in ductile and brittle solids. *International Journal of Fracture* **100**, 55-83, doi:10.1023/a:1018655917051 (1999).

12   Sauer, J. A. & Richardson, G. C. Fatigue of polymers. *International Journal of Fracture* **16**, 499-532, doi:10.1007/bf02265215 (1980).

13   Wu, D. Y., Meure, S. & Solomon, D. Self-healing polymeric materials: A review of recent developments. *Progress in Polymer Science* **33**, 479-522, doi:10.1016/j.progpolymsci.2008.02.001 (2008).

14   Ritchie, R. O. Mechanisms of fatigue crack-propagation in metals, ceramics and composites - role of crack tip shielding. *Materials Science and Engineering a-Structural Materials Properties Microstructure and Processing* **103**, 15-28, doi:10.1016/0025-5416(88)90547-2 (1988).

15   Burattini, S., Greenland, B. W., Chappell, D., Colquhoun, H. M. & Hayes, W. Healable polymeric materials: a tutorial review. *Chemical Society Reviews* **39**, 1973-1985, doi:10.1039/b904502n (2010).

16   Wool, R. P. & Oconnor, K. M. A theory of crack healing in polymers. *Journal of Applied Physics* **52**, 5953-5963, doi:10.1063/1.328526 (1981).

17   Andersson, C. *et al.* Preparation and Incorporation of Microcapsules in Functional Coatings for Self-healing of Packaging Board. *Packaging Technology and Science* **22**, 275-291, doi:10.1002/pts.853 (2009).

18   Bleay, S. M., Loader, C. B., Hawyes, V. J., Humberstone, L. & Curtis, P. T. A smart repair system for polymer matrix composites. *Composites Part a-Applied Science and Manufacturing* **32**, 1767-1776, doi:10.1016/s1359-835x(01)00020-3 (2001).

19   Dry, C. Passive tunable fibers and matrices. *International Journal of Modern Physics B* **6**, 2763-2771, doi:10.1142/s0217979292001419 (1992).

20   Dry, C. & McMillan, W. Three-part methylmethacrylate adhesive system as an internal delivery system for smart responsive concrete. *Smart Materials & Structures* **5**, 297-300, doi:10.1088/0964-1726/5/3/007 (1996).

21   Dry, C. Procedures developed for self-repair of polymer matrix composite materials. *Composite Structures* **35**, 263-269, doi:10.1016/0263-8223(96)00033-5 (1996).

22   Motuku, M., Vaidya, U. K. & Janowski, G. M. Parametric studies on self-repairing approaches for resin infused composites subjected to low velocity impact. *Smart Materials & Structures* **8**, 623-638, doi:10.1088/0964-1726/8/5/313 (1999).

23   White, S. R. *et al.* Autonomic healing of polymer composites. *Nature* **409**, 794-797, doi:10.1038/35057232 (2001).

24   Blaiszik, B. J., Sottos, N. R. & White, S. R. Nanocapsules for self-healing materials. *Composites Science and Technology* **68**, 978-986, doi:10.1016/j.compscitech.2007.07.021 (2008).

25   Keller, M. W., White, S. R. & Sottos, N. R. A self-healing poly(dimethyl siloxane) elastomer. *Advanced Functional Materials* **17**, 2399-2404, doi:10.1002/adfm.200700086 (2007).

26   Yuan, L., Gu, A. J. & Liang, G. Z. Preparation and properties of poly(urea-formaldehyde) microcapsules filled with epoxy resins. *Materials Chemistry and Physics* **110**, 417-425, doi:10.1016/j.matchemphys.2008.02.035 (2008).

27   Brown, E. N., Kessler, M. R., Sottos, N. R. & White, S. R. In situ poly(urea-formaldehyde) microencapsulation of dicyclopentadiene. *Journal of Microencapsulation* **20**, 719-730, doi:10.1080/0265204031000154160 (2003).

28   Blaiszik, B. J. *et al.* Microcapsules filled with reactive solutions for self-healing materials. *Polymer* **50**, 990-997, doi:10.1016/j.polymer.2008.12.040 (2009).

29   Cosco, S., Ambrogi, V., Musto, P. & Carfagna, C. Properties of poly(urea-formaldheyde) microcapsules containing an epoxy resin. *Journal of Applied Polymer Science* **105**, 1400-1411, doi:10.1002/app.26263 (2007).

30   Jin, H. H. *et al.* Self-healing thermoset using encapsulated epoxy-amine healing chemistry. *Polymer* **53**, 581-587, doi:10.1016/j.polymer.2011.12.005 (2012).

31   Gragert, M., Schunack, M. & Binder, W. H. Azide/Alkyne-"Click"-Reactions of Encapsulated Reagents: Toward Self-Healing Materials. *Macromolecular Rapid Communications* **32**, 419-425, doi:10.1002/marc.201000687 (2011).

32   Yuan, L., Liang, G. Z., Xie, J. Q., Li, L. & Guo, J. Preparation and characterization of poly(urea-formaldehyde) microcapsules filled with epoxy resins. *Polymer* **47**, 5338-5349, doi:10.1016/j.polymer.2006.05.051 (2006).

33   Yuan, Y. C., Rong, M. Z. & Zhang, M. Q. Preparation and characterization of poly (melamine-formaldehyde) walled microcapsules containing epoxy. *Acta Polymerica Sinica*, 472-480 (2008).

34   Yuan, Y. C., Rong, M. Z. & Zhang, M. Q. Preparation and characterization of microencapsulated polythiol. *Polymer* **49**, 2531-2541, doi:10.1016/j.polymer.2008.03.044 (2008).

35   Yuan, Y. C. *et al.* Self-healing polymeric materials using epoxy/mercaptan as the healant. *Macromolecules* **41**, 5197-5202, doi:10.1021/ma800028d (2008).

36   Wang, H. P., Yuan, Y. C., Rong, M. Z. & Zhang, M. Q. Melamine resin-walled microcapsules containing styrene: Preparation and characterization. Part 1-2 (2008).

37   Liu, X., Sheng, X., Lee, J. K. & Kessler, M. R. Synthesis and Characterization of Melamine-Urea-Formaldehyde Microcapsules Containing ENB-Based Self-Healing Agents. *Macromolecular Materials and Engineering* **294**, 389-395, doi:10.1002/mame.200900015 (2009).

38   Liu, X., Lee, J. K. & Kessler, M. R. Microencapsulation of self-healing agents with melamine-urea-formaldehyde by the Shirasu porous glass (SPG) emulsification technique. *Macromolecular Research* **19**, 1056-1061, doi:10.1007/s13233-011-1009-3 (2011).

39   Cho, S. H., Andersson, H. M., White, S. R., Sottos, N. R. & Braun, P. V. Polydimethylsiloxane-based self-healing materials. *Advanced Materials* **18**, 997-+, doi:10.1002/adma.200501814 (2006).

40   Yang, J. L., Keller, M. W., Moore, J. S., White, S. R. & Sottos, N. R. Microencapsulation of Isocyanates for Self-Healing Polymers. *Macromolecules* **41**, 9650-9655, doi:10.1021/ma801718v (2008).

41   Xiao, D. S., Yuan, Y. C., Rong, M. Z. & Zhang, M. Q. Hollow polymeric microcapsules: Preparation, characterization and application in holding boron trifluoride diethyl etherate. *Polymer* **50**, 560-568, doi:10.1016/j.polymer.2008.11.022 (2009).

42   Rule, J. D., Brown, E. N., Sottos, N. R., White, S. R. & Moore, J. S. Wax-protected catalyst microspheres for efficient self-healing materials. *Advanced Materials* **17**, 205-+, doi:10.1002/adma.200400607 (2005).

43   Asua, J. M. Miniemulsion polymerization. *Progress in Polymer Science* **27**, 1283-1346, doi:10.1016/s0079-6700(02)00010-2 (2002).

44   Brown, E. N., Sottos, N. R. & White, S. R. Fracture testing of a self-healing polymer composite. *Experimental Mechanics* **42**, 372-379, doi:10.1177/001448502321548193 (2002).

45   Keller, M. W. & Sottos, N. R. Mechanical properties of microcapsules used in a self-healing polymer. *Experimental Mechanics* **46**, 725-733, doi:10.1007/s11340-006-9659-3 (2006).

46   Rule, J. D., Sottos, N. R. & White, S. R. Effect of microcapsule size on the performance of self-healing polymers. *Polymer* **48**, 3520-3529, doi:10.1016/j.polymer.2007.04.008 (2007).

47   Brown, E. N., White, S. R. & Sottos, N. R. Microcapsule induced toughening in a self-healing polymer composite. *Journal of Materials Science* **39**, 1703-1710, doi:10.1023/B:JMSC.0000016173.73733.dc (2004).

48   Rule, J. D. & Moore, J. S. ROMP reactivity of endo- and exo-dicyclopentadiene. *Macromolecules* **35**, 7878-7882, doi:10.1021/ma0209489 (2002).

49   Huang, G. C., Lee, J. K. & Kessler, M. R. Evaluation of Norbornene-Based Adhesives to Amine-Cured Epoxy for Self-Healing Applications. *Macromolecular Materials and Engineering* **296**, 965-972, doi:10.1002/mame.201100016 (2011).

50   Zhao, Y., Zhang, W., Liao, L. P., Li, W. J. & Xin, Y. in *Manufacturing Processes and Systems, Pts 1-2* Vol. 148-149 *Advanced Materials Research* (eds X. H. Liu, Z. Y. Jiang, & J. T. Han) 1031-1035 (Trans Tech Publications Ltd, 2011).

51   Aissa, B., Therriault, D., Haddad, E. & Jamroz, W. Self-Healing Materials Systems: Overview of Major Approaches and Recent Developed Technologies. *Advances in Materials Science and Engineering*, 17, doi:85420310.1155/2012/854203 (2012).

52   Lee, J. K., Liu, X., Yoon, S. H. & Kessler, M. R. Thermal analysis of ring-opening metathesis polymerized healing agents. *Journal of Polymer Science Part B-Polymer Physics* **45**, 1771-1780, doi:10.1002/polb.21089 (2007).

53   Sheng, X., Lee, J. K. & Kessler, M. R. Influence of cross-link density on the properties of ROMP thermosets. *Polymer* **50**, 1264-1269, doi:10.1016/j.polymer.2009.01.021 (2009).

54   Larin, G. E., Bernklau, N., Kessler, M. R. & DiCesare, J. C. Rheokinetics of ring-opening metathesis polymerization of norbornene-based monomers intended for self-healing applications. *Polymer Engineering and Science* **46**, 1804-1811, doi:10.1002/pen.20655 (2006).

55   Liu, X., Lee, J. K., Yoon, S. H. & Kessler, M. R. Characterization of diene monomers as healing agents for autonomic damage repair. *Journal of Applied Polymer Science* **101**, 1266-1272, doi:10.1002/app.23245 (2006).

56   Alcaide, B., Almendros, P. & Alonso, J. M. Ruthenium-catalyzed chemoselective N-allyl cleavage: Novel Grubbs carbene mediated deprotection of allylic amines. *Chemistry-a European Journal* **9**, 5793-5799, doi:10.1002/chem.200305236 (2003).

57   Fu, G. C., Nguyen, S. T. & Grubbs, R. H. Catalytic ring-closing metathesis of functionalized dienes by a ruthenium carbene complex. *Journal of the American Chemical Society* **115**, 9856-9857, doi:10.1021/ja00074a085 (1993).

58   Yuan, L., Liang, G. Z., Xie, J. Q., Guo, J. & Li, L. Thermal stability of microencapsulated epoxy resins with poly(urea-formaldehyde). *Polymer Degradation and Stability* **91**, 2300-2306, doi:10.1016/j.polymdegradstab.2006.04.026 (2006).

59   Brown, E. N., Moore, J. S., White, S. R. & Sottos, N. R. in *Bioinspired Nanoscale Hybrid Systems* Vol. 735 *Materials Research Society Symposium Proceedings* (eds U. Simon *et al.*) 101-106 (Materials Research Society, 2003).

60   Brown, E. N., White, S. R. & Sottos, N. R. Retardation and repair of fatigue cracks in a microcapsule toughened epoxy composite - Part 1: Manual infiltration. *Composites Science and Technology* **65**, 2466-2473, doi:10.1016/j.compscitech.2005.04.020 (2005).

61   Brown, E. N., White, S. R. & Sottos, N. R. Retardation and repair of fatigue cracks in a microcapsule toughened epoxy composite - Part II: In situ self-healing. *Composites Science and Technology* **65**, 2474-2480, doi:10.1016/j.compscitech.2005.04.053 (2005).

62   Kessler, M. R., Sottos, N. R. & White, S. R. Self-healing structural composite materials. *Composites Part a-Applied Science and Manufacturing* **34**, 743-753, doi:10.1016/s1359-835x(03)00138-6 (2003).

63   Sanada, K., Yasuda, I. & Shindo, Y. Transverse tensile strength of unidirectional fibre-reinforced polymers and self-healing of interfacial debonding. *Plastics Rubber and Composites* **35**, 67-72, doi:10.1179/174328906x79914 (2006).

64   Jones, A. S., Rule, J. D., Moore, J. S., White, S. R. & Sottos, N. R. Catalyst morphology and dissolution kinetics of self-healing polymers. *Chemistry of Materials* **18**, 1312-1317, doi:10.1021/cm051864s (2006).

65   Taber, D. F. & Frankowski, K. J. Grubbs' catalyst in paraffin: An air-stable preparation for alkene metathesis. *Journal of Organic Chemistry* **68**, 6047-6048, doi:10.1021/jo030005p (2003).

66   Wilson, G. O., Moore, J. S., White, S. R., Sottos, N. R. & Andersson, H. M. Autonomic healing of epoxy vinyl esters *via* ring opening metathesis polymerization. *Advanced Functional Materials* **18**, 44-52, doi:10.1002/adfm.200700419 (2008).

67   Wilson, G. O. *et al.* Evaluation of ruthenium catalysts for ring-opening metathesis polymerization-based self-healing applications. *Chemistry of Materials* **20**, 3288-3297, doi:10.1021/cm702933h (2008).

68   Kamphaus, J. M., Rule, J. D., Moore, J. S., Sottos, N. R. & White, S. R. A new self-healing epoxy with tungsten (VI) chloride catalyst. *Journal of the Royal Society Interface* **5**, 95-103, doi:10.1098/rsif.2007.1071 (2008).

69   Yin, T., Rong, M. Z., Zhang, M. Q. & Zhao, J. Q. Durability of self-healing woven glass fabric/epoxy composites. *Smart Materials & Structures* **18**, 7, doi:07400110.1088/0964-1726/18/7/074001 (2009).

70   Yin, T., Zhou, L., Rong, M. Z. & Zhang, M. Q. Self-healing woven glass fabric/epoxy composites with the healant consisting of micro-encapsulated epoxy and latent curing agent. *Smart Materials & Structures* **17**, 8, doi:01501910.1088/0964-1726/17/01/015019 (2008).

71   Yin, T., Rong, M. Z., Zhang, M. Q. & Yang, G. C. Self-healing epoxy composites - Preparation and effect of the healant consisting of microencapsulated epoxy and latent curing agent. *Composites Science and Technology* **67**, 201-212, doi:10.1016/j.compscitech.2006.07.028 (2007).

72   Jud, K., Kausch, H. H. & Williams, J. G. Fracture-mechanics studies of crack healing and welding of polymers. *Journal of Materials Science* **16**, 204-210, doi:10.1007/bf00552073 (1981).

73   Wu, T. & Lee, S. Carbon tetrachloride-induced crack healing in polycarbonate. *Journal of Polymer Science Part B-Polymer Physics* **32**, 2055-2064, doi:10.1002/polb.1994.090321212 (1994).

74   Wang, P. P., Lee, S. & Harmon, J. P. Ethanol-induced crack healing in poly(methyl methacrylate). *Journal of Polymer Science Part B-Polymer Physics* **32**, 1217-1227, doi:10.1002/polb.1994.090320709 (1994).

75   Lin, C. B., Lee, S. B. & Liu, K. S. Methanol-induced crack healing in poly(methyl methacrylate). *Polymer Engineering and Science* **30**, 1399-1406, doi:10.1002/pen.760302109 (1990).

76   Hsieh, H. C., Yang, T. J. & Lee, S. Crack healing in poly(methyl methacrylate) induced by co-solvent of methanol and ethanol. *Polymer* **42**, 1227-1241, doi:10.1016/s0032-3861(00)00407-9 (2001).

77   Shen, J. S., Harmon, J. P. & Lee, S. Thermally-induced crack healing in poly(methyl methacrylate). *Journal of Materials Research* **17**, 1335-1340, doi:10.1557/jmr.2002.0199 (2002).

78   Caruso, M. M. *et al.* Solvent-promoted self-healing epoxy materials. *Macromolecules* **40**, 8830-8832, doi:10.1021/ma701992z (2007).

79   Caruso, M. M., Blaiszik, B. J., White, S. R., Sottos, N. R. & Moore, J. S. Full recovery of fracture toughness using a nontoxic solvent-based self-healing system. *Advanced Functional Materials* **18**, 1898-1904, doi:10.1002/adfm.200800300 (2008).

80   Jackson, A. C., Bartelt, J. A. & Braun, P. V. Transparent Self-Healing Polymers Based on Encapsulated Plasticizers in a Thermoplastic Matrix. *Advanced Functional Materials* **21**, 4705-4711, doi:10.1002/adfm.201101574 (2011).

81   McIlroy, D. A. *et al.* Microencapsulation of a Reactive Liquid-Phase Amine for Self-Healing Epoxy Composites. *Macromolecules* **43**, 1855-1859, doi:10.1021/ma902251n (2010).

82   Wang, H. P., Yuan, Y. C., Rong, M. Z. & Zhang, M. Q. Self-Healing of Thermoplastics *via* Living Polymerization. *Macromolecules* **43**, 595-598, doi:10.1021/ma902021v (2010).

83   Yao, L., Yuan, Y. C., Rong, M. Z. & Zhang, M. Q. Self-healing linear polymers based on RAFT polymerization. *Polymer* **52**, 3137-3145, doi:10.1016/j.polymer.2011.05.024 (2011).

84   Yao, L., Rong, M. Z., Zhang, M. Q. & Yuan, Y. C. Self-healing of thermoplastics *via* reversible addition-fragmentation chain transfer polymerization. *Journal of Materials Chemistry* **21**, 9060-9065, doi:10.1039/c1jm10655d (2011).

85   Lanzara, G., Yoon, Y., Liu, H., Peng, S. & Lee, W. I. Carbon nanotube reservoirs for self-healing materials. *Nanotechnology* **20**, doi:33570410.1088/0957-4484/20/33/335704 (2009).

86   Liu, W. B., Liu, Y. & Wang, R. G. MD Simulation of Single-wall Carbon Nanotubes Employed as Container in Self-healing Materials. *Polymers & Polymer Composites* **19**, 333-337 (2011).

87   Sherman, T. F. ON CONNECTING LARGE VESSELS TO SMALL - THE MEANING OF MURRAY LAW. *Journal of General Physiology* **78**, 431-453, doi:10.1085/jgp.78.4.431 (1981).

88   Kim, S., Lorente, S. & Bejan, A. Vascularized materials: Tree-shaped flow architectures matched canopy to canopy. *Journal of Applied Physics* **100**, doi:06352510.1063/1.2349479 (2006).

89   Wechsatol, W., Lorente, S. & Bejan, A. Tree-shaped networks with loops. *International Journal of Heat and Mass Transfer* **48**, 573-583, doi:10.1016/j.ijheatmasstransfer.2004.08.020 (2005).

90   Bejan, A., Lorente, S. & Wang, K. M. Networks of channels for self-healing composite materials. *Journal of Applied Physics* **100**, doi:03352810.1063/1.2218768 (2006).

91   Wang, K. M., Lorente, S. & Bejan, A. Vascularized networks with two optimized channel sizes. *Journal of Physics D-Applied Physics* **39**, 3086-3096, doi:10.1088/0022-3727/39/14/031 (2006).

92   Williams, H. R., Trask, R. S., Knights, A. C., Williams, E. R. & Bond, I. P. Biomimetic reliability strategies for self-healing vascular networks in engineering materials. *Journal of the Royal Society Interface* **5**, 735-747, doi:10.1098/rsif.2007.1251 (2008).

93   Murphy, E. B. & Wudl, F. The world of smart healable materials. *Progress in Polymer Science* **35**, 223-251, doi:10.1016/j.progpolymsci.2009.10.006 (2010).

94   Aragon, A. M., Wayer, J. K., Geubelle, P. H., Goldberg, D. E. & White, S. R. Design of microvascular flow networks using multi-objective genetic algorithms. *Computer Methods in Applied Mechanics and Engineering* **197**, 4399-4410, doi:10.1016/j.cma.2008.05.025 (2008).

95   Toohey, K. S., Sottos, N. R., Lewis, J. A., Moore, J. S. & White, S. R. Self-healing materials with microvascular networks. *Nature Materials* **6**, 581-585, doi:10.1038/nmat1934 (2007).

96   Toohey, K. S., Hansen, C. J., Lewis, J. A., White, S. R. & Sottos, N. R. Delivery of Two-Part Self-Healing Chemistry *via* Microvascular Networks. *Advanced Functional Materials* **19**, 1399-1405, doi:10.1002/adfm.200801824 (2009).

97   Williams, H. R., Trask, R. S. & Bond, I. P. Self-healing composite sandwich structures. *Smart Materials & Structures* **16**, 1198-1207, doi:10.1088/0964-1726/16/4/031 (2007).

98   Williams, H. R., Trask, R. S. & Bond, I. P. Self-healing sandwich panels: Restoration of compressive strength after impact. *Composites Science and Technology* **68**, 3171-3177, doi:10.1016/j.compscitech.2008.07.016 (2008).

99   Hansen, C. J. *et al.* Self-Healing Materials with Interpenetrating Microvascular Networks. *Advanced Materials* **21**, 4143-+, doi:10.1002/adma.200900588 (2009).

100   Hansen, C. J., White, S. R., Sottos, N. R. & Lewis, J. A. Accelerated Self-Healing *Via* Ternary Interpenetrating Microvascular Networks. *Advanced Functional Materials* **21**, 4320-4326, doi:10.1002/adfm.201101553 (2011).

101   Seiffert, S. & Sprakel, J. Physical chemistry of supramolecular polymer networks. *Chemical Society Reviews* **41**, 909-930, doi:10.1039/c1cs15191f (2012).

102   Aida, T., Meijer, E. W. & Stupp, S. I. Functional Supramolecular Polymers. *Science* **335**, 813-817, doi:10.1126/science.1205962 (2012).

103   Rybtchinski, B. Adaptive Supramolecular Nanomaterials Based on Strong Noncovalent Interactions. *Acs Nano* **5**, 6791-6818, doi:10.1021/nn2025397 (2011).

104   Ohkawa, H., Ligthart, G., Sijbesma, R. P. & Meijer, E. W. Supramolecular graft copolymers based on 2,7-diamido-1,8-naphthyridines. *Macromolecules* **40**, 1453-1459, doi:10.1021/ma062317a (2007).

105   Sijbesma, R. P. *et al.* Reversible polymers formed from self-complementary monomers using quadruple hydrogen bonding. *Science* **278**, 1601-1604, doi:10.1126/science.278.5343.1601 (1997).

106   Rieth, L. R., Eaton, R. F. & Coates, G. W. Polymerization of ureidopyrimidinone-functionalized olefins by using late-transition metal Ziegler-Natta catalysts: Synthesis of thermoplastic elastomeric polyolefins. *Angewandte Chemie-International Edition* **40**, 2153-2156, doi:10.1002/1521-3773(20010601)40:11<2153::aid-anie2153>3.3.co;2-n (2001).

107   Kushner, A. M., Vossler, J. D., Williams, G. A. & Guan, Z. B. A Biomimetic Modular Polymer with Tough and Adaptive Properties. *Journal of the American Chemical Society* **131**, 8766-+, doi:10.1021/ja9009666 (2009).

108   Cordier, P., Tournilhac, F., Soulie-Ziakovic, C. & Leibler, L. Self-healing and thermoreversible rubber from supramolecular assembly. *Nature* **451**, 977-980, doi:10.1038/nature06669 (2008).

109   Kersey, F. R., Loveless, D. M. & Craig, S. L. A hybrid polymer gel with controlled rates of cross-link rupture and self-repair. *Journal of the Royal Society Interface* **4**, 373-380, doi:10.1098/rsif.2006.0187 (2007).

110   Burattini, S., Colquhoun, H. M., Greenland, B. W. & Hayes, W. A novel self-healing supramolecular polymer system. *Faraday Discussions* **143**, 251-264, doi:10.1039/b900859d (2009).

111   Burattini, S. *et al.* A self-repairing, supramolecular polymer system: healability as a consequence of donor-acceptor pi-pi stacking interactions. *Chemical Communications*, 6717-6719, doi:10.1039/b910648k (2009).

112   Kalista, S. J. Self-healing of poly(ethylene-co-methacrylic acid) copolymers following projectile puncture. *Mechanics of Advanced Materials and Structures* **14**, 391-397, doi:10.1080/15376490701298819 (2007).

113   Kalista, S. J. & Ward, T. C. Thermal characteristics of the self-healing response in poly (ethylene-co-methacrylic acid) copolymers. *Journal of the Royal Society Interface* **4**, 405-411, doi:10.1098/rsif.2006.0169 (2007).

114   Varley, R. J. & van der Zwaag, S. Towards an understanding of thermally activated self-healing of an ionomer system during ballistic penetration. *Acta Materialia* **56**, 5737-5750, doi:10.1016/j.actamat.2008.08.008 (2008).

115   Varley, R. J. & van der Zwaag, S. Development of a quasi-static test method to investigate the origin of self-healing in ionomers under ballistic conditions. *Polymer Testing* **27**, 11-19, doi:10.1016/j.polymertesting.2007.07.013 (2008).

116   Rhaman, M. A., Penco, M., Spagnoli, G., Grande, A. M. & Di Landro, L. Self-Healing Behavior of Blends Based on Ionomers with Ethylene/Vinyl Alcohol Copolymer or Epoxidized Natural Rubber. *Macromolecular Materials and Engineering* **296**, 1119-1127, doi:10.1002/mame.201100056 (2011).

117   Penco, M., Rhaman, A., Spagnoli, G., Janszen, G. & Di Landro, L. Novel system with damage initiated autonomous healing property based on heterogeneous blends of ethylene-methacrylic acid ionomer. *Materials Letters* **65**, 2107-2110, doi:10.1016/j.matlet.2011.05.008 (2011).

118   Varley, R. J. & van der Zwaag, S. Autonomous damage initiated healing in a thermo-responsive ionomer. *Polymer International* **59**, 1031-1038, doi:10.1002/pi.2841 (2010).

119   Nguyen, T. Q., Kausch, H. H., Jud, K. & Dettenmaier, M. CRACK-HEALING IN CROSSLINKED STYRENE-CO-ACRYLONITRILE. *Polymer* **23**, 1305-1310, doi:10.1016/0032-3861(82)90271-3 (1982).

120   Fakirov, S. Effect of the temperature on the chemical healing of poly(ethylene-terephthalate). *Makromolekulare Chemie-Macromolecular Chemistry and Physics* **185**, 1607-1611 (1984).

121   Fakirov, S. Chemical healing in poly(ethylene-terephthalate). *Journal of Polymer Science Part B-Polymer Physics* **22**, 2095-2104, doi:10.1002/pol.1984.180221208 (1984).

122   Fakirov, S. & Avramova, N. CHEMICAL HEALING IN PARTIALLY CROSS-LINKED POLYAMIDES. *Journal of Polymer Science Part B-Polymer Physics* **25**, 1331-1339, doi:10.1002/polb.1987.090250611 (1987).

123   Kausch, H. H., Petrovska, D., Landel, R. F. & Monnerie, L. Intermolecular interaction in polymer alloys as studied by crack healing. *Polymer Engineering and Science* **27**, 149-154, doi:10.1002/pen.760270209 (1987).

124   Davies, P., Cantwell, W. & Kausch, H. H. Healing of cracks in carbon-fiber peek composites. *Journal of Materials Science Letters* **8**, 1247-1248, doi:10.1007/bf00721480 (1989).

125   Degennes, P. G. Reptation of a polymer chain in presence of fixed obstacles. *Journal of Chemical Physics* **55**, 572-&, doi:10.1063/1.1675789 (1971).

126   Doi, M. & Edwards, S. F. Dynamics of concentrated polymer systems .1. BROWNIAN-MOTION IN EQUILIBRIUM STATE. *Journal of the Chemical Society-Faraday Transactions Ii* **74**, 1789-1801, doi:10.1039/f29787401789 (1978).

127   Kim, Y. H. & Wool, R. P. A theory of healing at a polymer polymer interface. *Macromolecules* **16**, 1115-1120, doi:10.1021/ma00241a013 (1983).

128   Stevens, M. P. & Jenkins, A. D. Crosslinking of polystyrene *via* pendant maleimide groups. *Journal of Polymer Science Part a-Polymer Chemistry* **17**, 3675-3685, doi:10.1002/pol.1979.170171123 (1979).

129   Chujo, Y., Sada, K. & Saegusa, T. A novel nonionic hydrogel from 2-methyl-2-oxazoline .4. Reversible gelation of polyoxazoline by means of diels-alder reaction. *Macromolecules* **23**, 2636-2641, doi:10.1021/ma00212a007 (1990).

130   Canary, S. A. & Stevens, M. P. Thermally reversible cross-linking of polystyrene *via* the furan-maleimide diels-alder reaction. *Journal of Polymer Science Part a-Polymer Chemistry* **30**, 1755-1760, doi:10.1002/pola.1992.080300829 (1992).

131   Chen, X. X. *et al.* A thermally re-mendable cross-linked polymeric material. *Science* **295**, 1698-1702, doi:10.1126/science.1065879 (2002).

132   Chen, X. X., Wudl, F., Mal, A. K., Shen, H. B. & Nutt, S. R. New thermally remendable highly cross-linked polymeric materials. *Macromolecules* **36**, 1802-1807, doi:10.1021/ma0210675 (2003).

133   Liu, Y. L. & Hsieh, C. Y. Crosslinked epoxy materials exhibiting thermal remendablility and removability from multifunctional maleimide and furan compounds. *Journal of Polymer Science Part a-Polymer Chemistry* **44**, 905-913, doi:10.1002/pola.21184 (2006).

134   Park, J. S. *et al.* Multiple healing effect of thermally activated self-healing composites based on Diels-Alder reaction. *Composites Science and Technology* **70**, 2154-2159, doi:10.1016/j.compscitech.2010.08.017 (2010).

135   Tian, Q. A., Rong, M. Z., Zhang, M. Q. & Yuan, Y. C. Synthesis and characterization of epoxy with improved thermal remendability based on Diels-Alder reaction. *Polymer International* **59**, 1339-1345, doi:10.1002/pi.2872 (2010).

136   Watanabe, M. & Yoshie, N. Synthesis and properties of readily recyclable polymers from bisfuranic terminated poly(ethylene adipate) and multi-maleimide linkers. *Polymer* **47**, 4946-4952, doi:10.1016/j.polymer.2006.05.036 (2006).

137   Polaske, N. W., McGrath, D. V. & McElhanon, J. R. Thermally Reversible Dendronized Step-Polymers Based on Sequential Huisgen 1,3-Dipolar Cycloaddition and Diels-Alder "Click" Reactions. *Macromolecules* **43**, 1270-1276, doi:10.1021/ma902180r (2010).

138   Jiang, B. B., Hao, J. J., Wang, W. Y., Jiang, L. X. & Cai, X. X. Synthesis and properties of novel polybismaleimide oligomers. *European Polymer Journal* **37**, 463-470 (2001).

139   Ghezzo, F. *et al.* Development and Characterization of Healable Carbon Fiber Composites with a Reversibly Cross Linked Polymer. *Journal of Composite Materials* **44**, 1587-1603, doi:10.1177/0021998310363165 (2010).

140   Peterson, A. M., Jensen, R. E. & Palmese, G. R. Room-Temperature Healing of a Thermosetting Polymer Using the Diels-Alder Reaction. *Acs Applied Materials & Interfaces* **2**, 1141-1149, doi:10.1021/am9009378 (2010).

141   Ax, J. & Wenz, G. Thermoreversible Networks by Diels-Alder Reaction of Cellulose Furoates With Bismaleimides. *Macromolecular Chemistry and Physics* **213**, 182-186, doi:10.1002/macp.201100410 (2012).

142   Toncelli, C., De Reus, D. C., Picchioni, F. & Broekhuis, A. A. Properties of Reversible Diels-Alder Furan/Maleimide Polymer Networks as Function of Crosslink Density. *Macromolecular Chemistry and Physics* **213**, 157-165, doi:10.1002/macp.201100405 (2012).

143   Kavitha, A. A. & Singha, N. K. Smart "All Acrylate" ABA Triblock Copolymer Bearing Reactive Functionality *via* Atom Transfer Radical Polymerization (ATRP): Demonstration of a "Click Reaction" in Thermoreversible Property. *Macromolecules* **43**, 3193-3205, doi:10.1021/ma902203r (2010).

144   Kavitha, A. A. & Singha, N. K. "Click Chemistry" in Tailor-Made Polymethacrylates Bearing Reactive Furfuryl Functionality: A New Class of Self-Healing Polymeric Material. *Acs Applied Materials & Interfaces* **1**, 1427-1436, doi:10.1021/am900124c (2009).

145   Zhang, Y., Broekhuis, A. A. & Picchioni, F. Thermally Self-Healing Polymeric Materials: The Next Step to Recycling Thermoset Polymers? *Macromolecules* **42**, 1906-1912, doi:10.1021/ma8027672 (2009).

146   Murphy, E. B. *et al.* Synthesis and characterization of a single-component thermally remendable polymer network: Staudinger and Stille revisited. *Macromolecules* **41**, 5203-5209, doi:10.1021/ma800432g (2008).

147   Park, J. S. *et al.* Towards Development of a Self-Healing Composite using a Mendable Polymer and Resistive Heating. *Journal of Composite Materials* **42**, 2869-2881, doi:10.1177/0021998308097280 (2008).

148   Park, J. S., Kim, H. S. & Hahn, H. T. Healing behavior of a matrix crack on a carbon fiber/mendomer composite. *Composites Science and Technology* **69**, 1082-1087, doi:10.1016/j.compscitech.2009.01.031 (2009).

149   Syrett, J. A., Mantovani, G., Barton, W. R. S., Price, D. & Haddleton, D. M. Self-healing polymers prepared *via* living radical polymerisation. *Polymer Chemistry* **1**, 102-106, doi:10.1039/b9py00316a (2010).

150   Inglis, A. J., Nebhani, L., Altintas, O., Schmidt, F. G. & Barner-Kowollik, C. Rapid Bonding/Debonding on Demand: Reversibly Cross-Linked Functional Polymers *via* Diels-Alder Chemistry. *Macromolecules* **43**, 5515-5520, doi:10.1021/ma100945b (2010).

151   Reutenauer, P., Buhler, E., Boul, P. J., Candau, S. J. & Lehn, J. M. Room Temperature Dynamic Polymers Based on Diels-Alder Chemistry. *Chemistry-a European Journal* **15**, 1893-1900, doi:10.1002/chem.200802145 (2009).

152   Chujo, Y., Sada, K., Naka, A., Nomura, R. & Saegusa, T. Synthesis and redox gelation of disulfide-modified polyoxazoline. *Macromolecules* **26**, 883-887, doi:10.1021/ma00057a001 (1993).

153   Tsarevsky, N. V. & Matyjaszewski, K. Reversible redox cleavage/coupling of polystyrene with disulfide or thiol groups prepared by atom transfer radical polymerization. *Macromolecules* **35**, 9009-9014, doi:10.1021/ma021061f (2002).

154   Kamada, J. *et al.* Redox Responsive Behavior of Thiol/Disulfide-Functionalized Star Polymers Synthesized *via* Atom Transfer Radical Polymerization. *Macromolecules* **43**, 4133-4139, doi:10.1021/ma100365n (2010).

155   Scott, T. F., Schneider, A. D., Cook, W. D. & Bowman, C. N. Photoinduced plasticity in cross-linked polymers. *Science* **308**, 1615-1617, doi:10.1126/science.1110505 (2005).

156   Nicolay, R., Kamada, J., Van Wassen, A. & Matyjaszewski, K. Responsive Gels Based on a Dynamic Covalent Trithiocarbonate Cross-Linker. *Macromolecules* **43**, 4355-4361, doi:10.1021/ma100378r (2010).

157   Amamoto, Y., Kamada, J., Otsuka, H., Takahara, A. & Matyjaszewski, K. Polymers through Reshuffling of Trithiocarbonate Units. *Angewandte Chemie-International Edition* **50**, 1660-1663, doi:10.1002/anie.201003888 (2011).

158   Amamoto, Y., Otsuka, H., Takahara, A. & Matyjaszewski, K. Changes in Network Structure of Chemical Gels Controlled by Solvent Quality through Photoinduced Radical Reshuffling Reactions of Trithiocarbonate Units. *Acs Macro Letters* **1**, 478-481, doi:10.1021/mz300070t (2012).

159   Davis, D. A. *et al.* Force-induced activation of covalent bonds in mechanoresponsive polymeric materials. *Nature* **459**, 68-72, doi:10.1038/nature07970 (2009).

160   Piermattei, A., Karthikeyan, S. & Sijbesma, R. P. Activating catalysts with mechanical force. *Nature Chemistry* **1**, 133-137, doi:10.1038/nchem.167 (2009).

161   Imato, K. *et al.* Self-Healing of Chemical Gels Cross-Linked by Diarylbibenzofuranone-Based Trigger-Free Dynamic Covalent Bonds at Room Temperature. *Angewandte Chemie-International Edition* **51**, 1138-1142, doi:10.1002/anie.201104069 (2012).

162   Verberg, R., Dale, A. T., Kumar, P., Alexeev, A. & Balazs, A. C. Healing substrates with mobile, particle-filled microcapsules: designing a 'repair and go' system. *Journal of the Royal Society Interface* **4**, 349-357, doi:10.1098/rsif.2006.0165 (2007).

163   Kolmakov, G. V. *et al.* Using Nanoparticle-Filled Microcapsules for Site-Specific Healing of Damaged Substrates: Creating a "Repair-and-Go" System. *Acs Nano* **4**, 1115-1123, doi:10.1021/nn901296y (2010).

164   Kratz, K. *et al.* Probing and repairing damaged surfaces with nanoparticle-containing microcapsules. *Nature Nanotechnology* **7**, 87-90, doi:10.1038/nnano.2011.235 (2012).

RESULTS & DISCUSSION…

2. SELF-HEALING DYNAMIC INTERACTIVE MEMBRANE

D ynamic Interactive Systems have received considerable interest from scientific community because of their promising novel properties not present at molecular level[1,2]. Understanding and controlling such up-scale propagation from molecular level toward nanoscale dimensions[3,4], might provide new insights into the basic features that control the design of emergent systems operating at the core of advance technologies: tissue engineering[5], artificial organs[6], catalysis[7], membrane filtration[8,9] or sensing[10]. *De novo* design of porous systems as mechanical supports, molecular capacitors/distributors or gating effectors by using self-healing[11,12], self-cleaning[13,14] or stimuli responsive strategies[15], has become an area of expanding interest. Classical membranes for water filtration are strongly subjected to compression depending on their structural behaviours and bulk porosity[16,17]. An irreversible compaction is usually undertaken in order to reach a steady state flux, giving the membrane a stable pore size. On the contrary, a responsive membrane can undergo a self-regulation of its performance according to the change in environmental conditions such as pH, temperature, light and ionic strength[18,19]. In this chapter, we shall discuss a novel dynamic interactive membrane based on copolymer micelles which responds to pressure and shows variable porosities accordingly and more importantly displays a self-mending ability.

2.1 THE COPOLYMER

The building blocks of the membrane are based on an ABA type triblock copolymer (PSAN-PEO-PSAN) consisting of Poly(ethylene oxide) as block "B" in between two "A" blocks of Poly(Styrene – *co* – Acrylonitrile) block copolymer (Figure – 2.1).
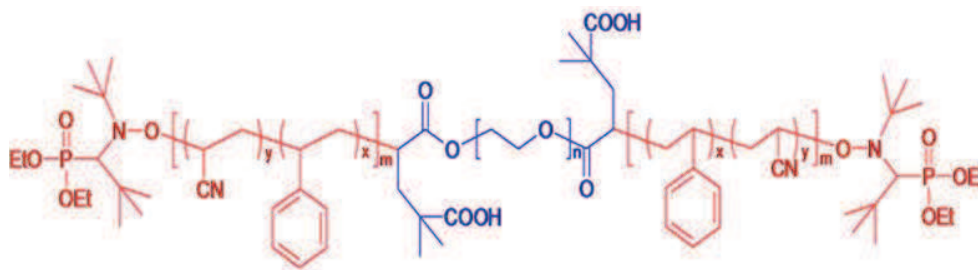

Figure – 2.1: Chemical structure of PSAN-b-PEO-b-PSAN copolymer used in this work

The value of subscripts "n", "x" and "y" are 795, 319 and 262 respectively. The synthesis of this copolymer is based on nitroxide mediated controlled radical polymerization, well described in an earlier work[20]. We used the copolymer synthesized in collaboration*, in as such form without any further modification. The copolymer can essentially be considered as amphiphilic in nature due to presence of hydrophobic PSAN block and hydrophilic PEO block in the middle. By varying the binary solvent mixture composition, nonergodic morphologies like spherical and spider-web were obtained in the previous work[20]. The relatively hard PSAN blocks ($T_g > 100^{\circ}C$) formed the core while the softer PEO ($T_g < -40^{\circ}C$; due to presence of oxygen in the main chain) formed corona of the spherical micelles. Amphiphilic Block copolymer like this are known to exhibit nonergodicity which leads to a large variety of micelles' locked-in morphologies in accordance to their initial preparation pathways[21,22]. Therefore, we decided to not change the molecular weight and block ratio.

2.2 MEMBRANE PREPARATION

The 3-dimensional superstructure was prepared from a homogeneous solution of PSAN-*b*-PEO-*b*-PSAN in DMF/toluene (50/50 v/v) at a concentration of 100 mg.ml^{-1}. Analysis carried out using Photon Cross Correlation Spectroscopy (PCCS) showed absence of micelles in the solution, even after increasing the concentration up to 200 mg.ml^{-1}. Beyond this concentration, the polymer solution was too viscous to be analyzed. The homogeneous solution of the copolymer in DMF/Toluene was then spin-coated onto thoroughly cleaned silicon wafers under argon atmosphere for certain duration of time with 20 droplets per wafer (Figure – 2.2).
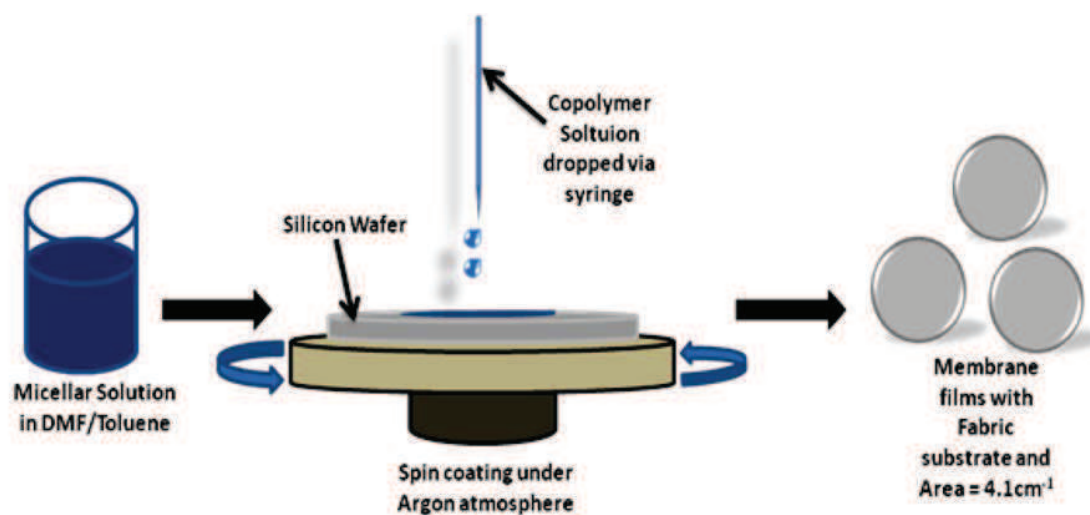

Figure – 2.2: General representation of preparation of PSAN-b-PEO-b-PSAN copolymer micelles' membrane films

The wafers thus obtained were then kept in vacuum for 24 hours to dry followed by immersion in ultrapure water for few hours. The immersion in water facilitates an easy separation of copolymer film from the wafer and loading onto a polyester non-woven fabric. Fabric supported membranes of 4.1 cm^2 area were cut from these films thereafter for further experiments.

2.3 MEMBRANE CHARACTERISTICS

The top surface analysis by Atomic Force Microscopy (AFM) of the films revealed a morphology marked by an assembly of spherical micelles having an average diameter of 50 nm with a narrow size distribution (Figure – 2.3a,b). Moreover, the surface of film seemed to be very flat as indicated by 3D AFM image (Figure – 2.3c) with a z value of 20 nm, which is approximately half of the diameter of the particles and indicates a rather dense packing of the micelles.
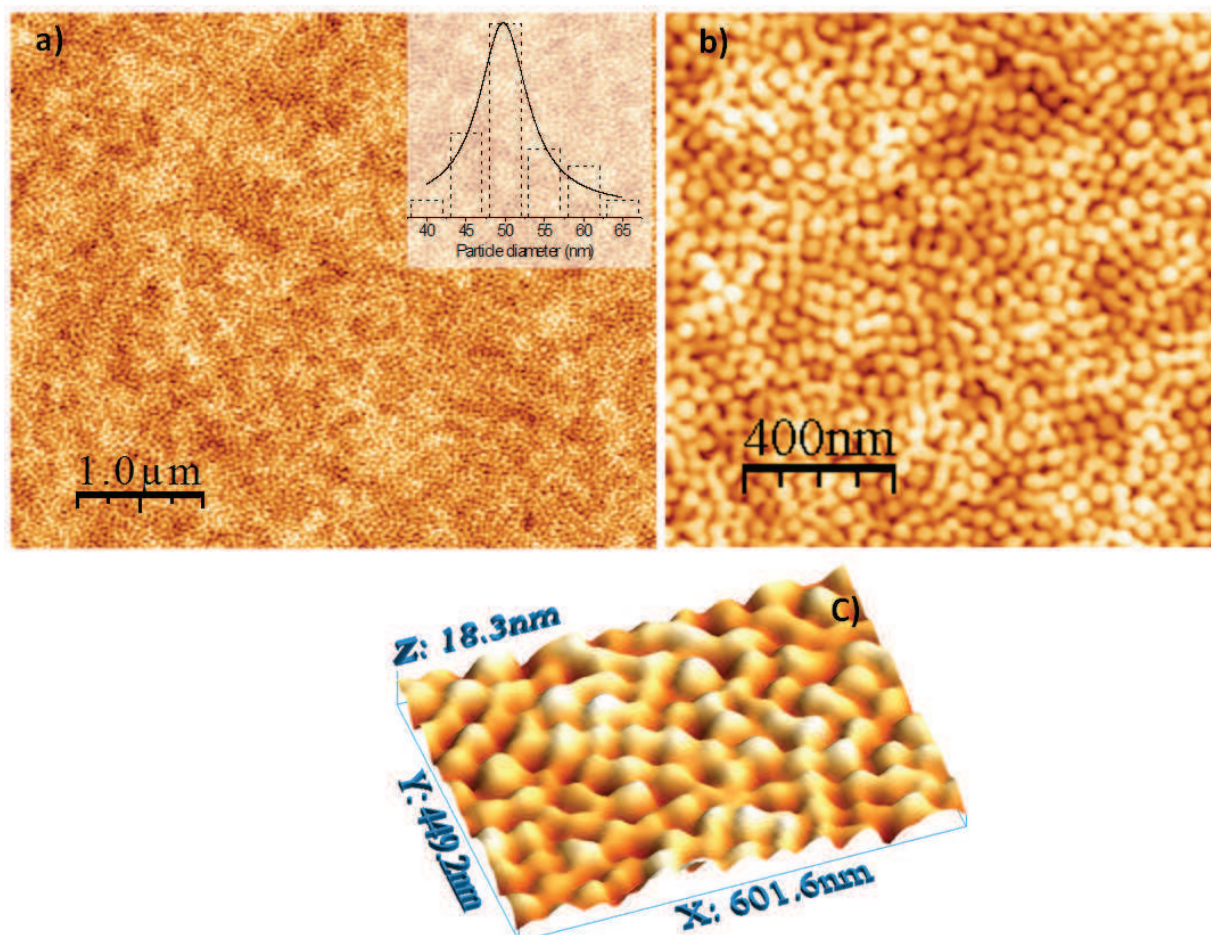

Figure – 2.3: Atomic Force Microscopy images obtained for the copolymer micelles assembly, a) closely packed micelles with monomodal size distribution (inset), b) enlarged view of the micelles, c) z-profile image for the surface showing a relative smooth topography and tight packing

The formation of spherical micelles can be attributed to the achievement of critical micelle concentration (cmc) during the solvent evaporation phase of spin coating process leading to the formation of flower like micelles with a hard PSAN core inside and relatively softer PEO corona outside. Once the micelles appear, the solvent evaporation leads to a progressive decrease in intermicellar distance. When the micelles are close enough to interact, dynamic association takes place through bridged conformations[23-25] of the ABA polymer chains (Figure – 2.4) giving birth to a kinetically frozen morphology that prevents the reorganization of micelles into gel like disordered network. These reversible non-covalent interactions between micelles mediate their dynamic self-assembly at macroscopic level as to have inter-micelle free volume thus imparting nanoporosity[20,26-29] to the membrane and play a crucial role in the self-healing behavior.
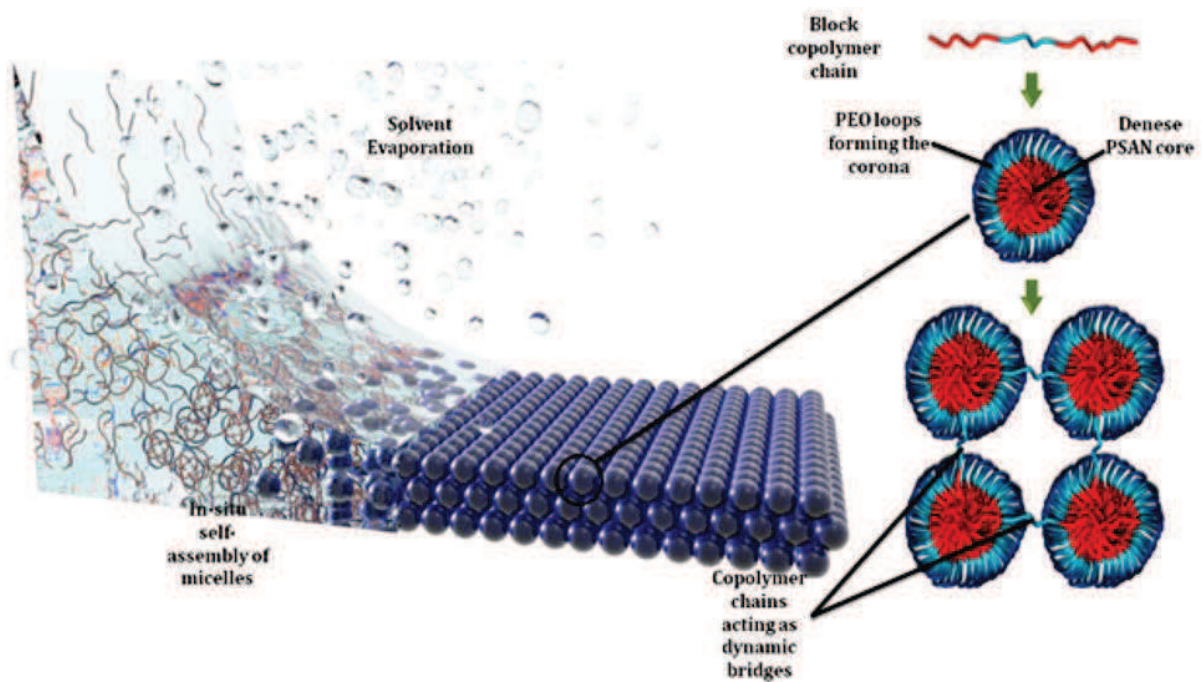

Figure – 2.4: In-situ formation of 3-dimensional assembly of micelles during spin-coating. The micelles are interconnected via copolymer chains acting as dynamic bridges.

The Scanning Electron Mircroscopy (SEM) analysis of the top and bottom surface of the casted films showed no defects whatsoever (Figure – 2.5a,d). The cross-section analysis gave an average thickness of 1.3 µm corresponding to an average of 35 stacked layers of nanoparticles taking the approximation of a hexagonal packing (Figure – 2.5b,c).
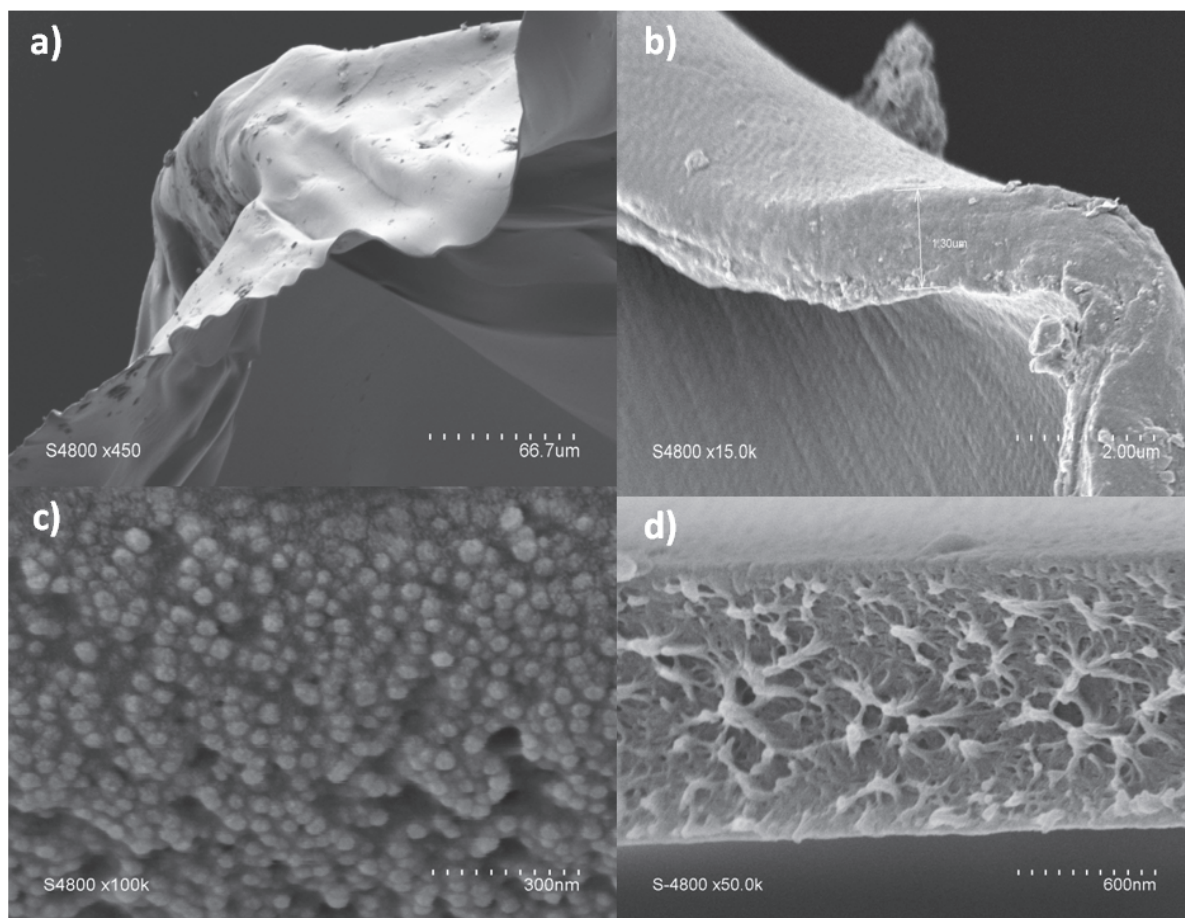
Figure – 2.5: Scanning Electron Microscopy images of copolymer film frozen in liqid nitrogen, a) Ondulated membrane film, b) Cross-section view of the film, c) Enlarged view of the cross-section showing micelles, d) Another cross-section view

2.4 INTERMICELLE BRIDGES AND THEIR INFLUENCE ON SELF-ASSEMBLY

The entropic penalty associated with the chain looping gives a possibility of having bridged conformations in associated micelles or even free micelles with chains providing a dangling end. A theoretical work, simulating potential morphological transitions reported that a fraction of bridge chains lies between 3 to 15% according to the block copolymer concentration and the reduced interaction energy between block A and the solvent. To have such kind of micelle association, the hydrophobic A block of a copolymer chain in one micelle has to cross the hydrophilic shell of another micelle in order to reach the hydrophobic core, thus linking the two. In order to evidence the presence of bridge chains as a vital key for the micelles cohesion and membrane tenacity, the length of block A was decreased from 47 kDa to 7.5 kDa while keeping the length of block B unchanged. SEM and AFM images (Figure – 2.6a,b) of

the micelle assembly showed the presence of multiple cracks, possibly due to weaker inter-micelle interactions. The AFM image of a crack is shows individual 50 nm micelles aligned in short rods along the cracks. It should be noted that decreasing dramatically the block A does not alter the possibility of generating flower-like micelles; however it seems to reduce bridge proportion. An explanation could be that a shorter block A is unable to reach the hydrophobic core of another micelle while crossing its hydrophilic shell.
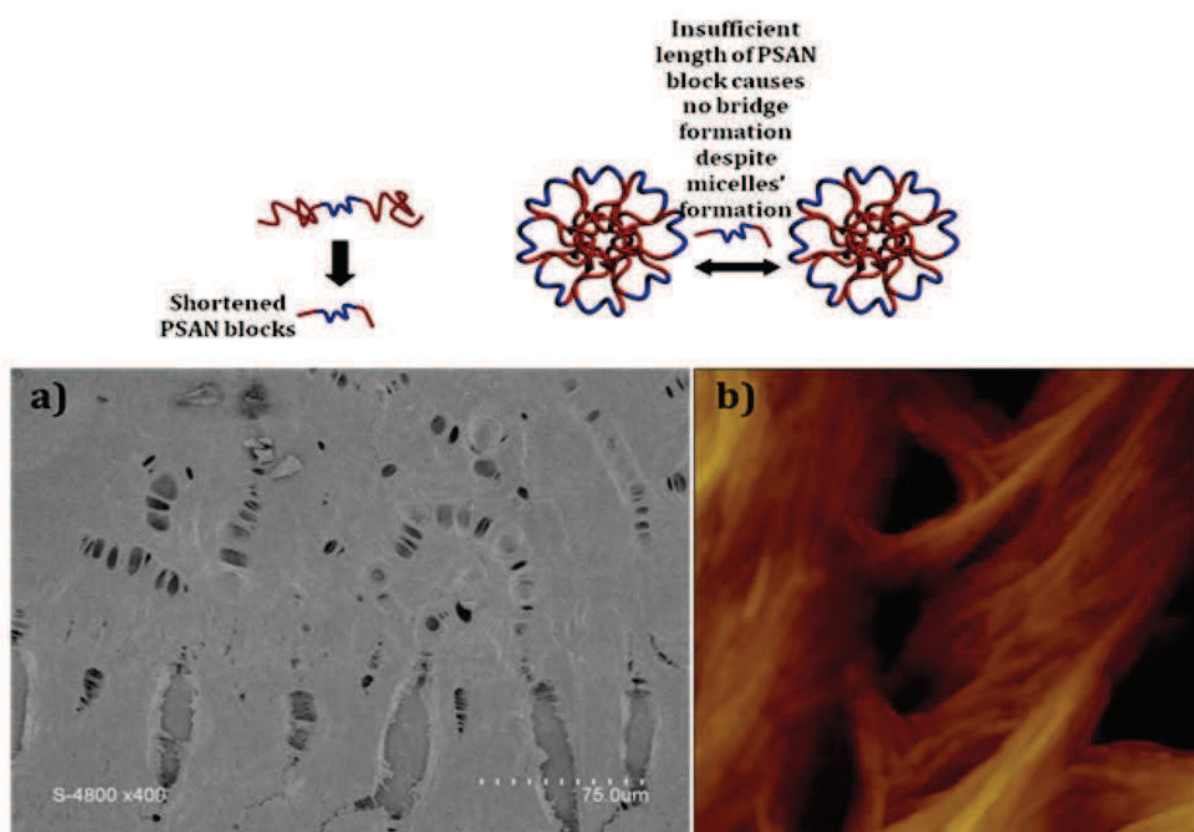

Figure – 2.6: Scanning Electron Microscopy image (a) and Atomic Force Microscopy image (b) for copolymer film prepared from PSAN(7.5k)-b-PEO(35k)-b-PSAN(7.5k). Despite successful assembly, the film suffers from large voids formation due to insufficient length of PSAN block which effects the formation of bridges in between the micelles

To detect the micelle assembly, Quartz Crystal Microbalance** (QCM) was used by injecting micellar solutions at different block copolymer concentrations onto gold-coated QCM electrodes. While the PSAN(47k)-*b*-PEO(35k)-*b*-PSAN(47k) showed a clear micelle adsorption after injection (Figure – 2.7a), the PSAN(7.5k)-*b*-PEO(35k)-*b*-PSAN(7.5k) micelle adsorption was found to be very low and unstable (Figure – 2.7b). Given the fact that the gold-coated electrode is highly hydrophobic therefore only the presence of dangling hydrophobic blocks can explain the adsorption through hydrophobic interactions.
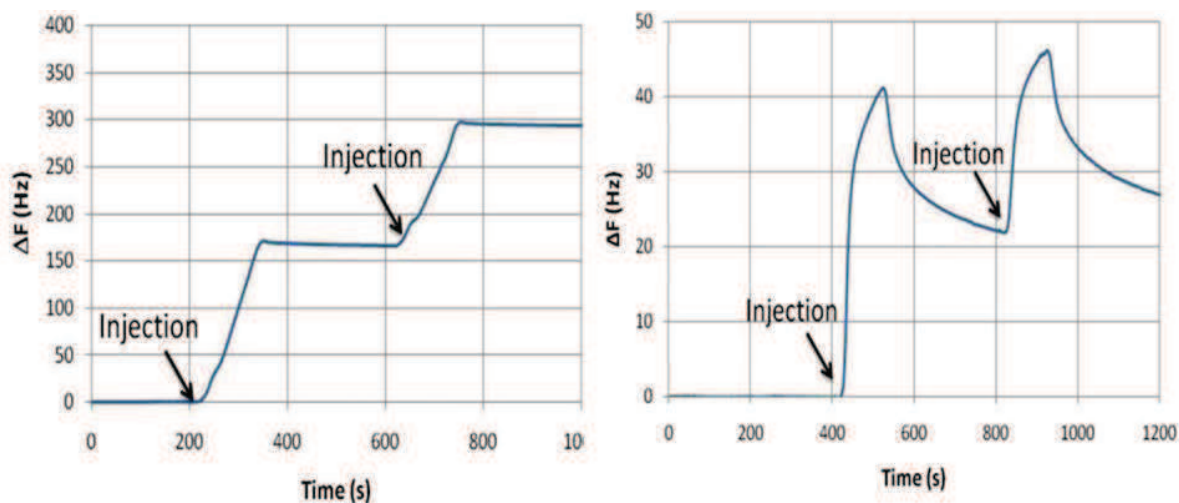
Figure – 2.7: Quartz Crystal Microbalance measurements for the two copolymers having different PSAN block length, a) PSAN(47k)-b-PEO(35k)-b-PSAN(47k) shows stable and strong bridging characteristics as can be seen by high increase in frequency, b) PSAN(7.5k)-b-PEO(35k)-b-PSAN(7.5k) shows very unstable assembly as the frequency gain is very low and unstable suggesting that despite micelles formation, they are not able to hold each other thus falling apart resulting in overall loss of mass.
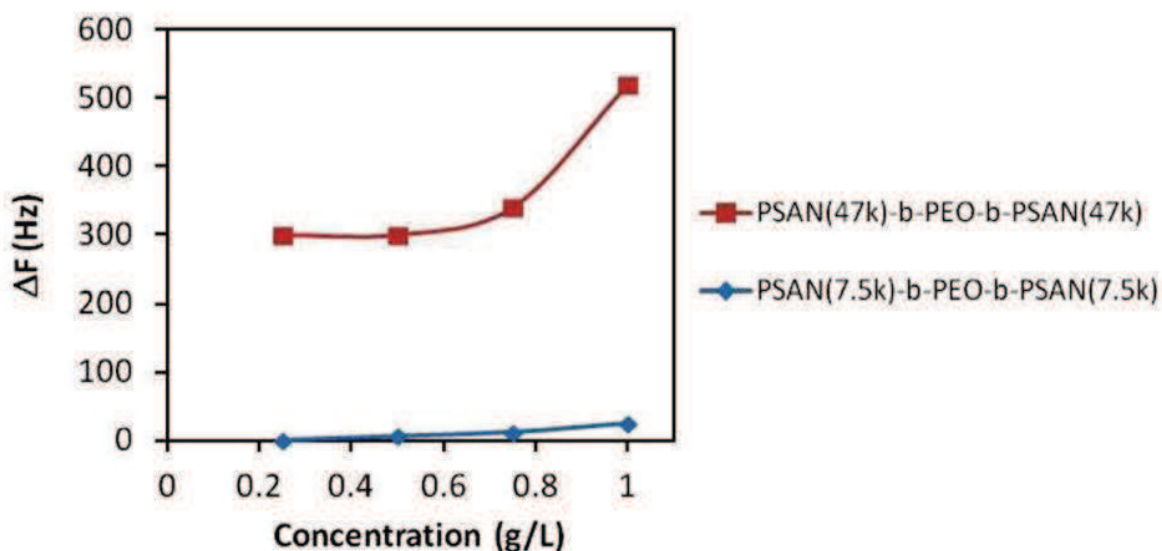
Figure – 2.8: Evolution of frequency in response to concentration change for the two copolymers.

For each concentration, injections were repeated (2-3 times) until reaching a maximum value of frequency ΔF (Figure – 2.8). An exponential increase in ΔF with the concentration was observed for PSAN(47k)-*b*-PEO(35k)-*b*-PSAN(47k) rather than a stable value. It can be explained by the micelle association through bridging conformations beyond a threshold concentration thus increasing the mass

gain onto the electrodes by building multilayers or reorganization of micelles into a more compact order. On the other hand, almost no ΔF increase is observed with PSAN(7.5k)-*b*-PEO(35k)-*b*-PSAN(7.5k) signifying a reduced proportion of block copolymer bridges.

2.5 FLUID FLOW EXPERIMENTS OF THE MEMBRANE

The term "fluid flow experiments" represent the water permeability experiments conducted for the membrane in a simple dead-end filtration cell at different pressure regimes. The amount of water permeated through the membrane at a given pressure was collected in a recipient. The increase in the recipient's weight was monitored using a balance while simultaneously recorded by the computer software. In this fashion, the evolution in the amount of water with respect to time could be plotted at given water pressure.
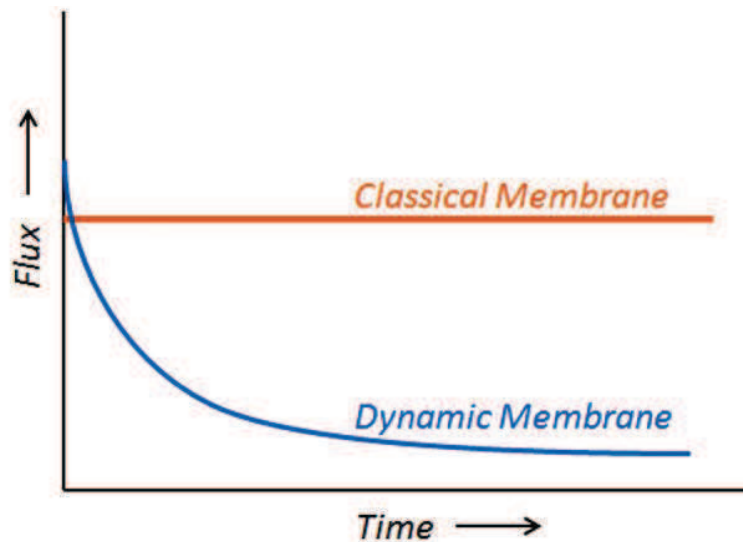

Figure – 2.9: Water flux response of a classical membrane with respect to a dynamic membrane

Unlike classical membranes which are first conditioned at high pressure before being subjected to permeability tests, a dynamic membrane like ours cannot be conditioned. This is due to ever changing flux values over the course of time exhibited by the membrane at each pressure value. Therefore, while the flux curve for a classical membrane is marked by a constant straight line in function of time, in case of a dynamic membrane it follows a polynomial trajectory (Figure – 2.9). In the present case, flux curves were obtained for the membrane at different pressure values (Figure – 2.10). As it can seen, the flux values rapidly decrease with time and approach near zero value for longer duration of time.
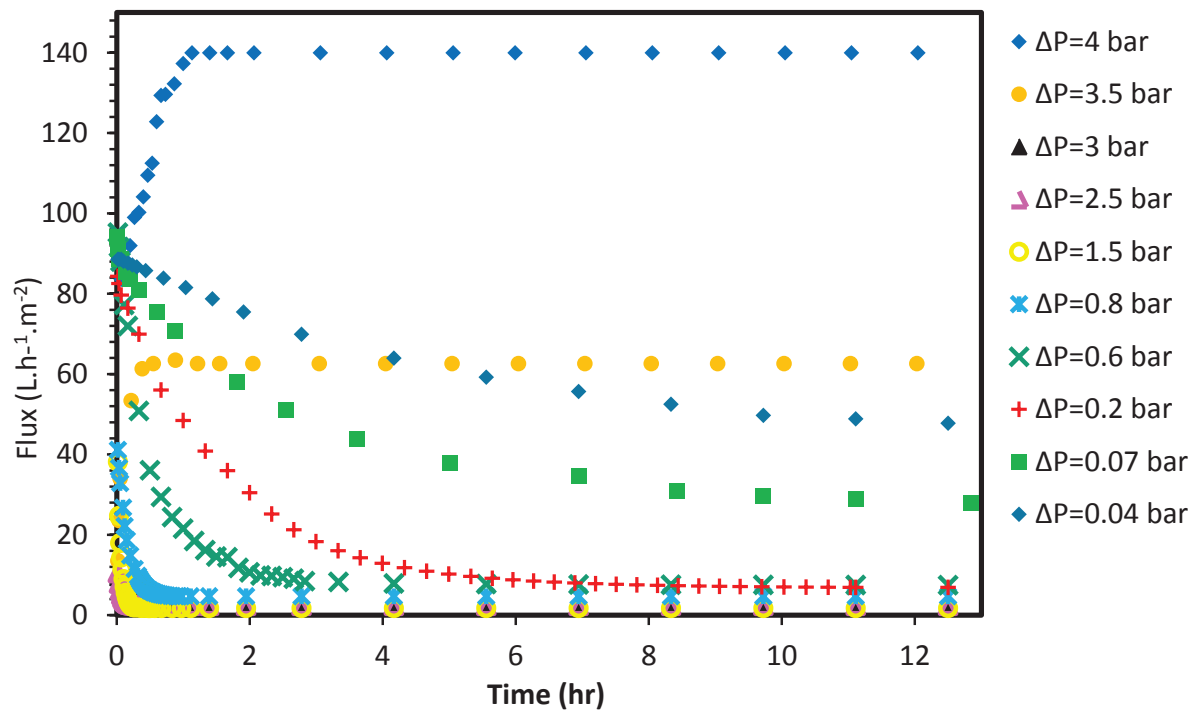
Figure – 2.10: Evolution of water flux with respect to time for the dynamic membrane at different pressure values.

Since the flux values tend to merge towards near zero values hence to have a significant measurable value for longer durations and for a better representation of the dynamics of the membrane, the quantity "fluid flow resistance" (R) was preferred instead of flux. The merit of using this quantity is that unlike flux, the value of resistance increases with time reaching infinity hence providing more meaningful and measurable values at all time period. Nonetheless, flux values are still needed to calculate the resistance values.

To obtain resistance values from flux, the membrane can be considered as a porous nanomaterial with cylindrical pores of constant diameter along length at a particular instant, for which the relationship between the empty tower velocity *U* and the pressure drop *ΔP* can be expressed using Darcy's law:

$$U = \frac{Q}{A} = \frac{\Delta P}{\mu R}$$

.... Eq. (2.1)

where *Q* represents the fluid flow rate through the section *A* and *R* is the fluid flow resistance of the porous material, and μ is the fluid viscosity. The empty tower velocity *U* is equivalent to the flux of the membrane, which is a measurable quantity.

The resistance R can be further expressed in terms of measurable parameters using the Kozeny-Carman equation which is based on the fact that the porous medium can be assimilated to a bundle of circular capillary tubes:

$$R = \frac{150 \, L}{\phi_s^2 d_p^2} \frac{(1-\varepsilon)^2}{\varepsilon^3}$$ .... Eq. (2.2)

where Φ_s, d_p and ε represent the sphericity of the particles, the particle diameter, and the bed porosity, respectively. L is the porous material thickness. The constant 150 includes classical values of the tortuosity and pore circularity in such porous material (spherical particles and porosity below 0.6).

Combining equations 1 and 2, the empty-tower velocity can be expressed as:

$$U = \frac{\phi_s^2 d_p^2}{150} \frac{\varepsilon^3}{(1-\varepsilon)^2} \frac{\Delta P}{\mu L}$$ .... Eq. (2.3)

Furthermore, the filtration characteristics of polymer particles under various conditions have been reported in the literature[30-33]; the instantaneous material porosity can be relied to the compression time as follow:

$$\frac{(\varepsilon_t - \varepsilon_0)}{(\varepsilon_t - \varepsilon_0)} = 1 - e^{-t/\tau}$$ .... Eq. (2.4)

Where ε_t is the material porosity at time t, ε_0 is the porosity before compression and ε_f the porosity at equilibrium after compression. The term τ represents the retardation time for compression. Finally, the empty-tower velocity can be written as:

$$U = \frac{\phi_s^2 d_p^2}{150} \frac{\left[\varepsilon_0 + (\varepsilon_f - \varepsilon_0)(1 - e^{-t/\tau})\right]^3}{\left[1 - \varepsilon_0 + (\varepsilon_0 - \varepsilon_f)(1 - e^{-t/\tau})\right]^2} \frac{\Delta P}{\mu L}$$ .... Eq. (2.5)

Following the aforementioned equation, the fluid flow resistance of the membrane was calculated at various pressure drops by following the water flux through the beds of polymer particles during time. All curves exhibited the same trend: a low resistance (high flux) at initial time eventually increasing (flux decreasing) with time as the compression of the bed begin (Figure – 2.11). The experiments were ended once an equilibrium state was reached. At constant pressure, the increase in resistance i.e., decrease of the water flux indicated that the permeability decreased during the filtration process due to the bed compression.
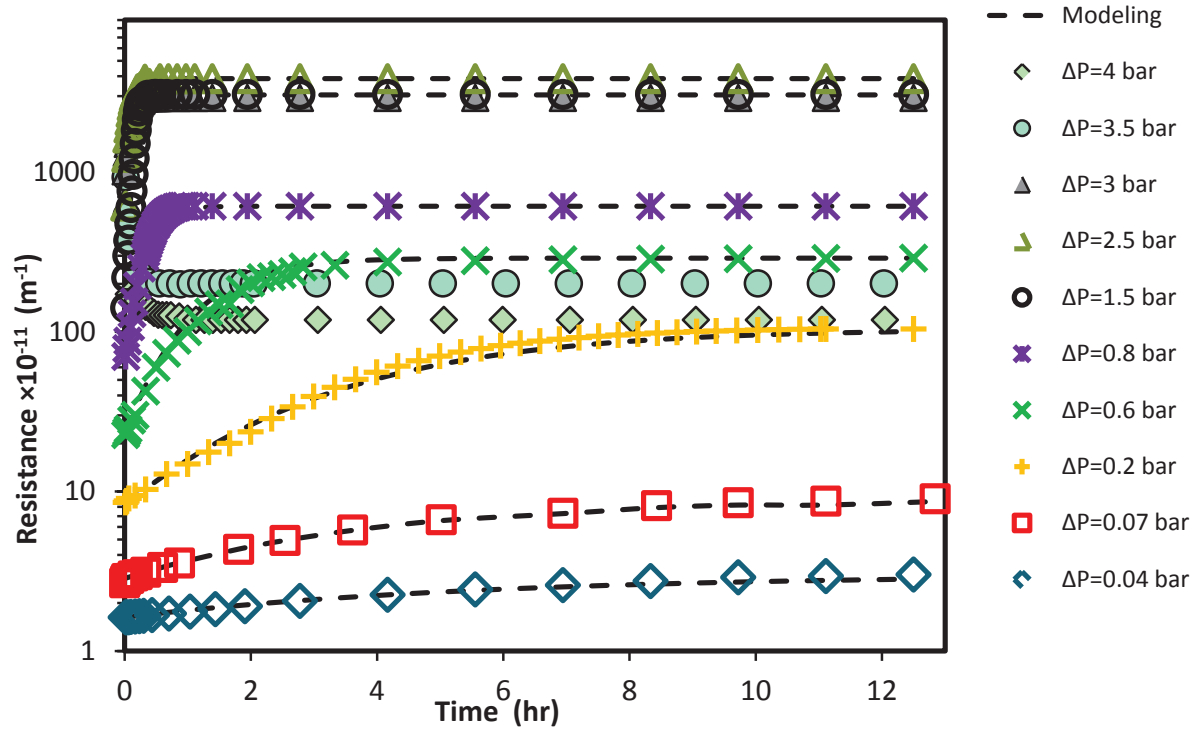
Figure – 2.11: Evolution of fluid flow resistance calculated from flux values with respect to time for the dynamic membrane at different pressure values. The dashed curves show the theoretical evolution of the resistance values.

Contributing to the experimental curves obtained for the resistance, we further modeled the fluid flow behavior of the membrane (Figure – 2.11). As can be seen, an excellent correlation was obtained between the experimental values and the theoretical ones (dashed lines). The theoretical calculations were performed using methodology as follows:

Using equation 1, the permeability of the membrane can be determined at initial time (K_0) and at equilibrium (K_∞). Then, equation 2 can be rearranged to express the porosity versus the permeability:

$$\frac{\varepsilon^3}{A} + A\varepsilon^2 + 2A\varepsilon - A = 0 \qquad .... \text{Eq. (2.6)}$$

where,
$$A = \frac{150\,K}{\phi_S^2 d_p^2} \qquad .... \text{Eq. (2.7)}$$

The third order equation 6 can be solved to determine the values of the porosity at initial time (ε_0) and at equilibrium (ε_∞) for each pressure drop. As an approximation, the particle diameter was considered to be constant during the experiments and the sphericity equal to unity. So, in Eq. 2.5, the

empty-tower velocity U only depends on the retardation time for a given experimental condition (pressure drop, particle bed thickness, temperature). The theoretical expression of the empty-tower velocity U_{theo} was then compared to the experimental data to determine the retardation time τ in each case.

At each time step, the function f_t was calculated:

$$f_t = U_{theo}(t) - U_{exp}(t)$$

.... Eq. (2.8)

And the objective function F was minimized using Newton's method:

$$F = \sum f_t^2$$

.... Eq. (2.9)

This left the retardation time τ as the only fitting parameter.

The dynamism of the membrane is further highlighted when the porosities and the fluid flow resistance of the membrane are plotted as a function of pressure (Figure – 2.12). As it can be seen, for relative water pressures from 0.04 to 3 bar, the water flow resistance R of the membrane increased, while the porosity ε decreased from 35 % to 5 %. The value 35 % is significant given the fact that the theoretical value reported in an earlier work for the random close packing of block copolymer micelles is 36 %. The pressure induces compression of micelles' soft corona thus leading to the decrease in the interstitial volume. Between 2 and 3 bar, the compression is at its maximum and a plateau for R and ε is observed. Beyond 3 bar, R decreases dramatically while porosity increases irreversibly.
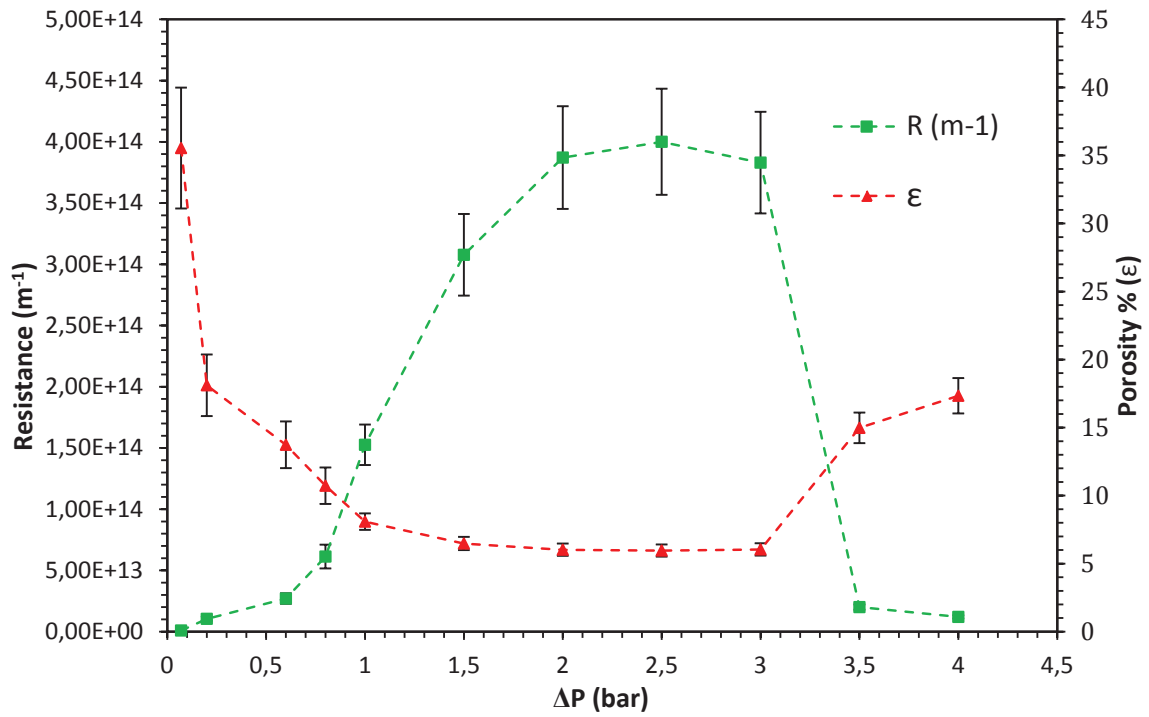
Figure – 2.12: Evolution of fluid flow resistance and porosity of the membrane with respect to pressure.
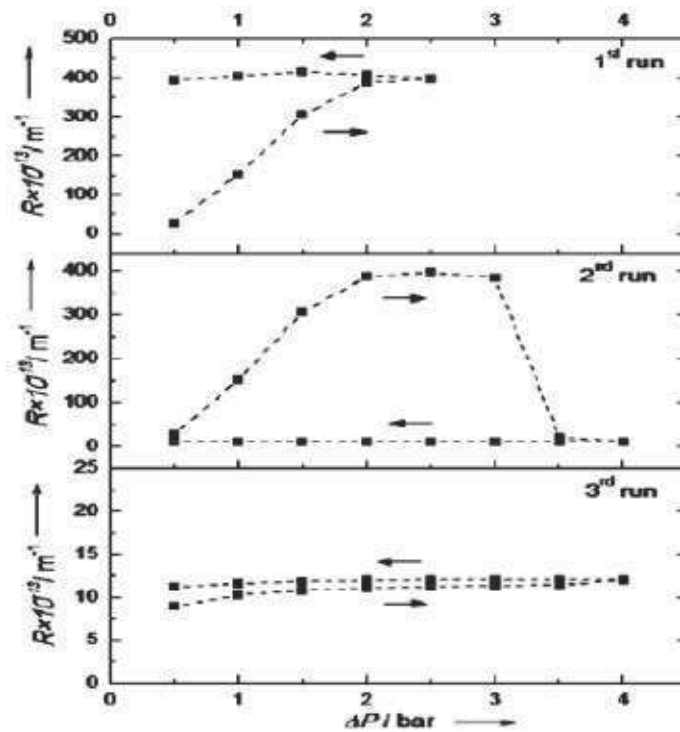

Figure – 2.13: Evolution of fluid flow resistance and porosity of the membrane with respect to pressure.

This apparent morphological switching can also be visualized via cyclic change in resistance values (Figure – 2.13), where three successive increasing/decreasing cycles of the transmembrane pressure have been carried out. The 1st run, stopped below the threshold pressure, showed a strong hysteresis, which can be due to an increase in the contact surface area between micelles during compression, thus facilitating PEO interactions. Novel copolymer bridges formation seems to be realistic since the resistance is maintained while decreasing the pressure, attesting the presence of strong links between the deformed micelles. However, with removal of water pressure, the 2nd run matches closely the 1st run during the pressure increase, in agreement with a good reversibility between sphere/spheroid morphologies. Interestingly, beyond 3.5 bar, the 3rd run shows almost no hysteresis being reliable to the large pores worm-like network of very low resistance, which is the usual behaviour of classical membranes.

2.6 ATOMIC FORCE MICROSCOPY EVIDENCE FOR MORPHOLOGY CHANGE

The perpetual changes in the porosity and resistance of the membrane with respect to pressure indicate clearly towards the morphological changes. To prove this, the membranes were analyzed using AFM after being subjected to water pressure followed by drying at room temperature in a dry chamber for 1 day. The Atomic Force Microscopy (AFM) images revealed that when subjected to a 4 bar water flow, there is rearrangement of the spherical particles into a more compact ordering (Figure – 2.14a, b, c, d). Till 2.5 bar, the films showed ability to retrace their original resistance value until a threshold pressure value is reached, indicating that the system's morphology was resilient enough to counter the pressure change in agreement with AFM observation. This resilience comes from the hard core-soft corona nature of the micelles and is also due to copolymer chains running through them interconnecting each other. At 3 bar, the micelles begin to irreversibly deform from spheres to spheroids (Figure – 2.14d). This deformation becomes much more pronounced at 3.5 bar (Figure – 2.14e) and further at 4 bar when the most of the micelles collapse to irreversibly give a "worm like" network with uneven large voids formation, leading to a significant porosity change (Figure – 2.14f). These large voids explain the sudden large increase in the porosity and thus decrease in resistance calculated at pressures 3 bar.
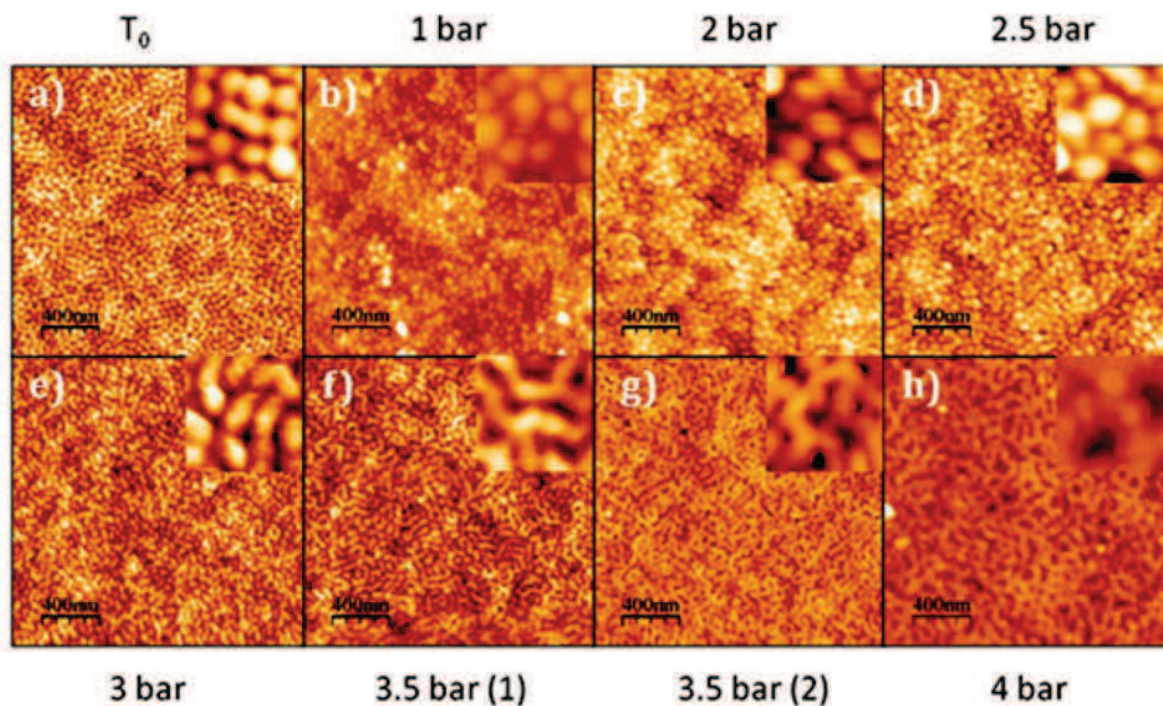
Figure – 2.14: Atomic Force Microscopy images obtained for different membranes showing the evolution of morphology with respect to pressure.
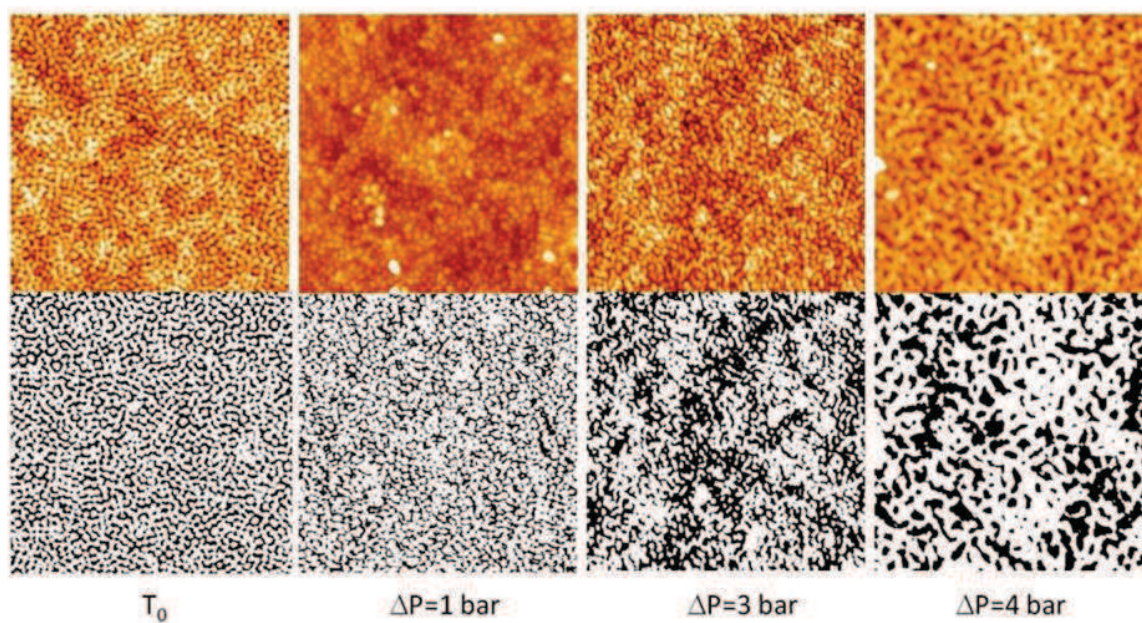

Figure – 2.15: Binary color images obtained from corresponding Atomic Force Microscopy images to obtain approximate pore size and their evolution with pressure.

In a further qualitative analysis, binary pictures (Figure – 2.15) were taken from AFM images in height-contrast mode and the pore area was calculated by a density analysis method for the pressure indicated (Table – 2.1).

Pressure (ΔP)	Number of Pores Detected	Total Pore Area (μm^2)	Average Pore Size (μm^2)	Pore Area Fraction (%)
0	793	0.971	1.00×10^{-3}	24.3
1	1124	0.782	6.96×10^{-4}	19.5
3	371	0.398	1.00×10^{-3}	9.9
4	200	0.990	5.00×10^{-3}	24.6

Table – 2.1: The approximate number of pores, total pore area, average pore size and pore area fraction calculated from binary images.

From T_0 to any pressure, the first step is a small reorganization of the micelle assembly into a more compact structure, then followed by deformation (reversible (ΔP <3bar) or irreversible (ΔP =3 bar)) or even morphology change (ΔP >3bar). When comparing the results at T_0 and 1 bar, it can be seen that the pore area decreased together with an increase in the number of pores detected and a decrease of the mean pore size, which is in agrees well with a slight compaction. At 3 bar, the micelles are irreversibly deformed into short rods made from the partial fusion of 2 to 3 micelles. In this situation, pore area decreased due to the disappearance of free interface caused by the decrease in the number of individual objects and thus the number of pores. At 4 bar, the short rods have fused into a worm-like network forming large pores.

2.7 APPLYING TUNABLE POROSITY FOR SELECTIVE FILTRATION

When compared with classical hydrophilic ultrafiltration membranes in which the pore size irreversibly decrease with the applied pressure[16], this pressure responsive membranes shows a very sharp change in filtration performances between ΔP=0 and 4 bar. Thus it might to possible to operate it in reversibly controlled "*open*" and "*closed*" states in response to applied pressures. To demonstrate this ability, a solution of five different poly(ethylene oxide)s ($M_{n,A}$=35 KDa; $M_{n,B}$=10 KDa; $M_{n,C}$=4.6 KDa; $M_{n,D}$=1.45 KDa; $M_{n,E}$=0.4 KDa) for a total concentration of 0.2 g.L^{-1} (0.04 g.L^{-1} each) was prepared and filtered through the membranes at pressures: ΔP=0.6, 1.5, 2.5 and 4 bar. In order to follow the membrane compression, the PEO solution in the permeate side was collected at different times from the dead-end filtration cell. The molecular weight distribution of PEOs in the permeates were analyzed by Size Exclusion Chromatography (SEC). At *ΔP*=0.6 bar, the retention of all PEGs were found to increase

over time due to the progressive compression of the micelles (Figure – 2.16a). Increasing ΔP=1.5 bar leads to a clear decrease of the pore size and a higher retention is observed as only D and E could significantly cross the membrane (Figure – 2.16b). The retention process is more selective at ΔP = 2.5 bar, where only E crosses the membrane (Figure – 2.16c). Finally, increasing ΔP to 4 bar leads to a clear increase of the pore size and any retention may be observed (Figure – 2.16d).
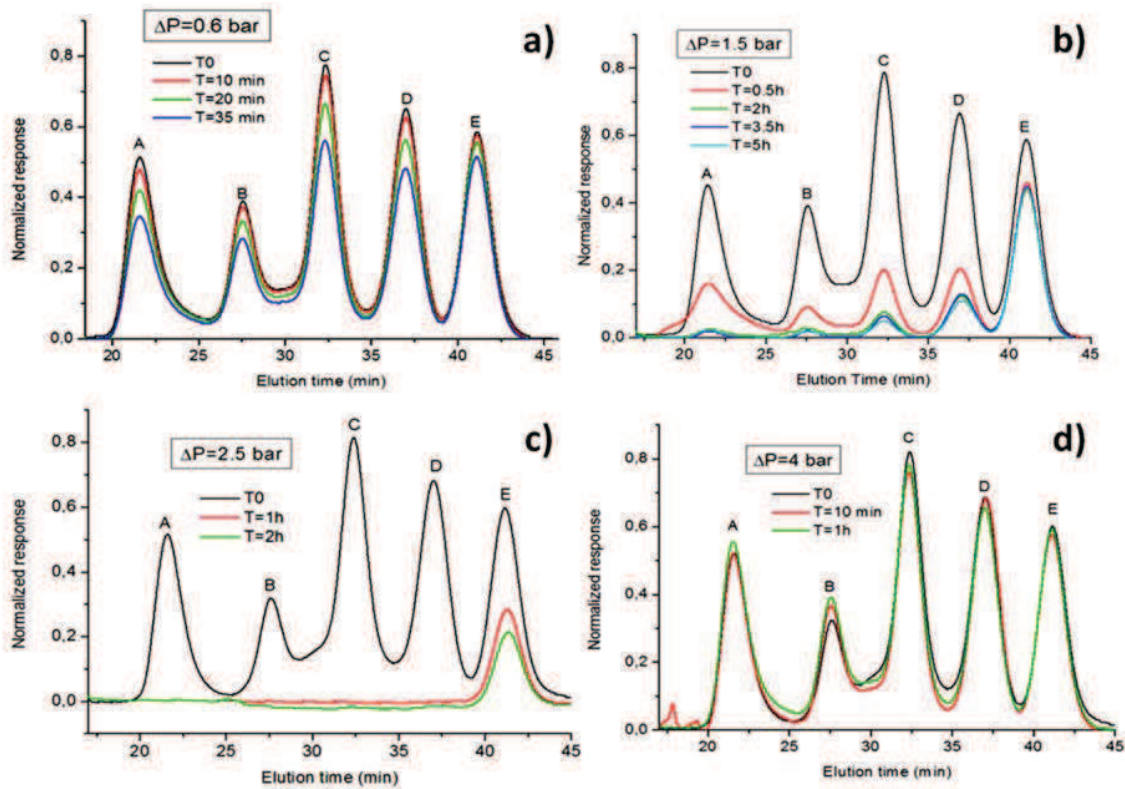

Figure – 2.16: Size Exclusion Chromatogram obtained for the permeates after PEG filtration experiments at different pressures.

These filtration tests concur well with the findings obtained using fluid flow resisting measurements and AFM images thereby not only establishing the progressive compression of the membrane albeit in a reversible manner but also pressure driven "gating" capability of the membrane.

2.8 SELF-HEALING

It could be presumed that by virtue of its dynamic behavior, a self-healing ability of this porous material would be highlighted at macroscopic level. Currently, the scope of self-healing materials is confined largely and specifically to dense systems[34-37]. Developing a self-healing porous material is

noteworthy and though its feasibility has been demonstrated theoretically[38,39], it still remains a challenge to be practically validated.

We studied the self-healing ability of the membranes by damaging them with a needle leaving a circular perforation of 110 µm in diameter, followed by the water permeation experiments (Figure – 2.17a). From the flux curves thus obtained, water flow resistance values were calculated at various pressures (Figure – 2.17 b, c, d, e, f, g and h).
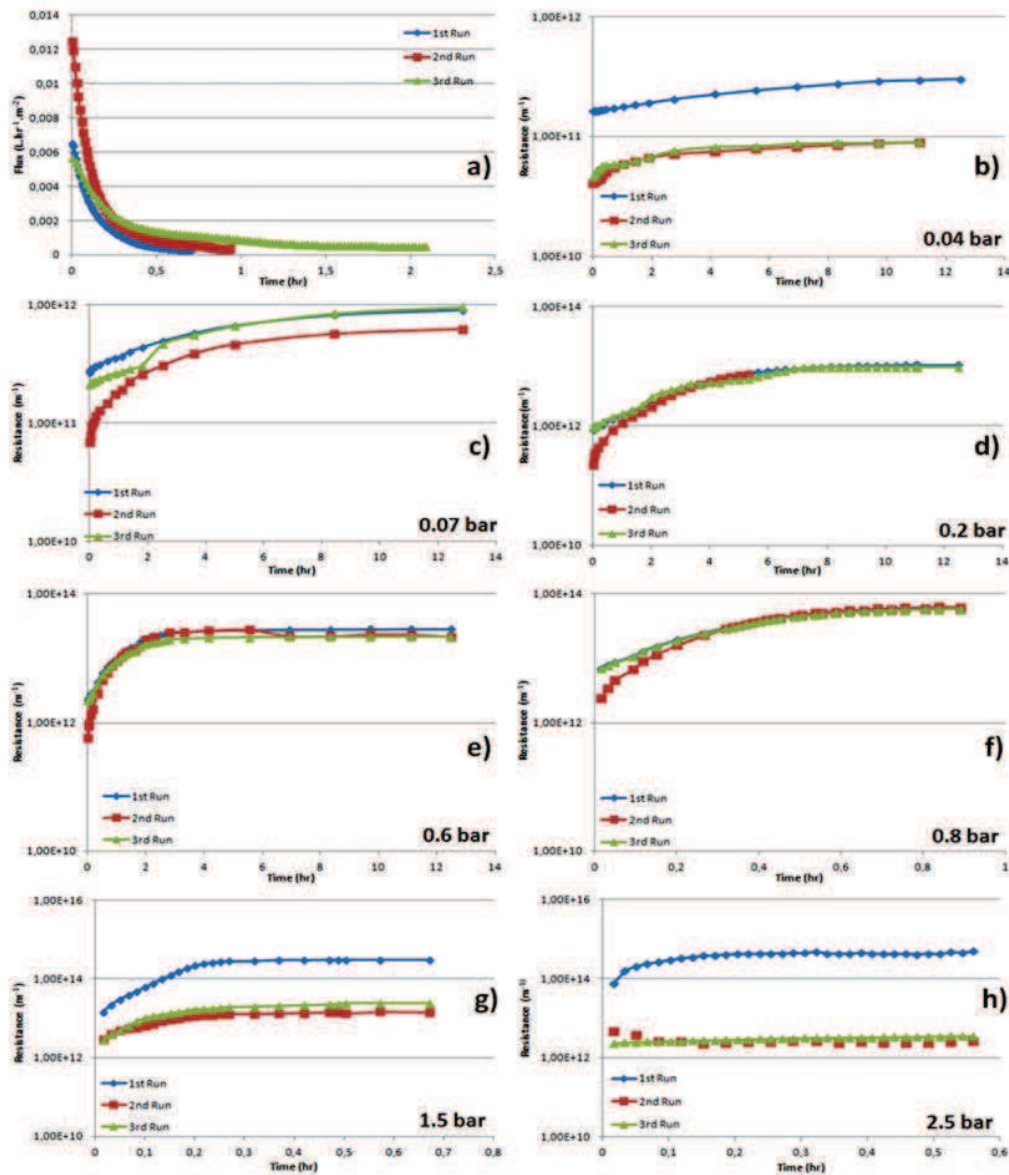

Figure – 2.17: Study of self-healing of the membranes by following the fluid flow resistance changes, a) A general change and evolution in flux before (blue), after perforation (red) and healed (green) membrane, b-h)the fluid flow

resistance curves obtained from flux curves before perforation (red), just after perforation (blue) and after healing process (green)

Given the film thickness of only 1.3 μm, the perforation represents almost 85 times the thickness, which is a major damage to the material. In general, the R value should converge over time to the 1st run curve of undamaged membrane, if healing has occurred. As expected, the initial *R* value of the virgin membrane (Red Curve, 1st run) dramatically decreases immediately after the perforation (Blue Curve, 2nd run). A third run (Green Curve, 3rd run) was carried out 24 hours later to verify the stability of the healing phenomenon. To verify the role of pressure as a necessary stimulus for self-healing, some of the perforated membranes were immersed for one month in water under static conditions as compared to other membranes subjected to water flux however no augmentation in resistance was observed. At very low pressure of 0.04 bar (Figure – 2.17b), very little resistance recovery was measured even after 15 hr while at 1.5 bar and beyond (Figure – 2.17g, h), the resistance again failed to achieve its original value. These results indicated that there is a pressure range (0.07-0.8 bar) (Figure – 2.17c-f) in which the healing process takes place effectively (Figure – 2.18).For a given perforation of 110 μm at 0.8 bar, 100 % recovery of resistance was achieved effectively within 40 minutes.
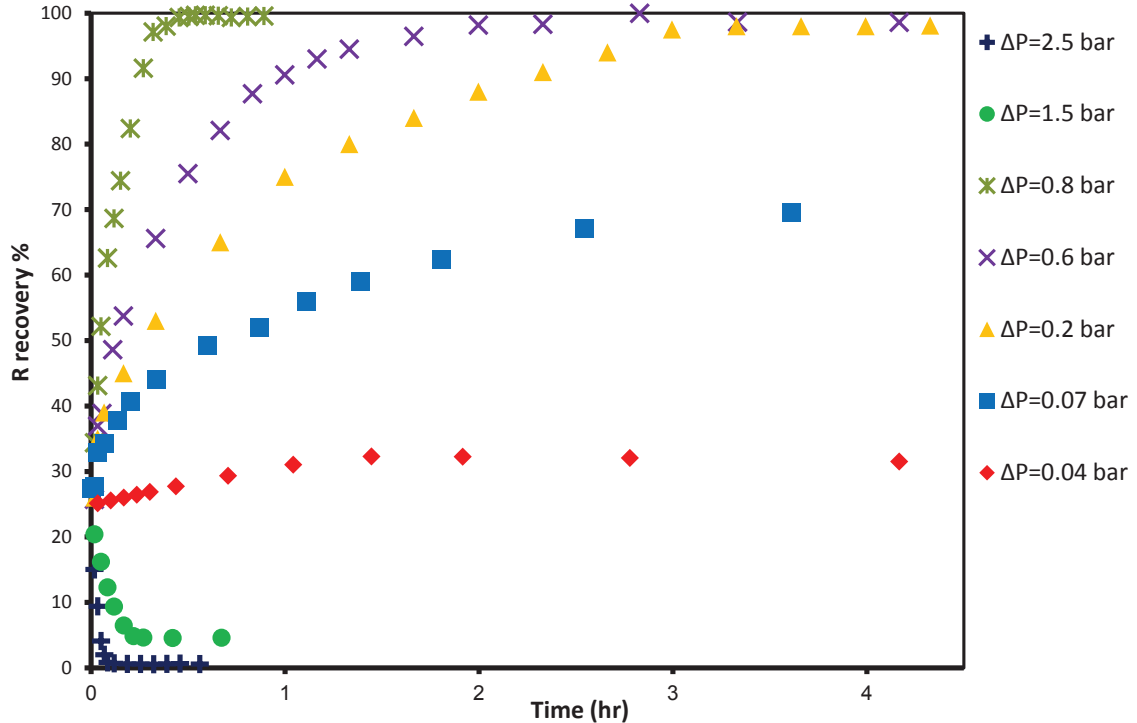
Figure – 2.18: % recovery of fluid flow resistance calculated with respect to time.

Furthermore within this range, lowering the pressure increased the time required for the effective healing and vice-versa as indicated by healing half time calculated at different pressures (Figure – 2.19). A perfect match between the 1st run curve and 3rd run curve observed in this range proved the permanent closure of the perforation (Figure – 2.20).

Figure – 2.19: Healing half rate calculated at different pressures.

Figure – 2.20: A composite graph showing that the once healed, the fluid flow resistance values reached their original values at the corresponding pressures.

Figure – 2.21: Evolution of healing rate with respect to perforation healing% at different pressures.

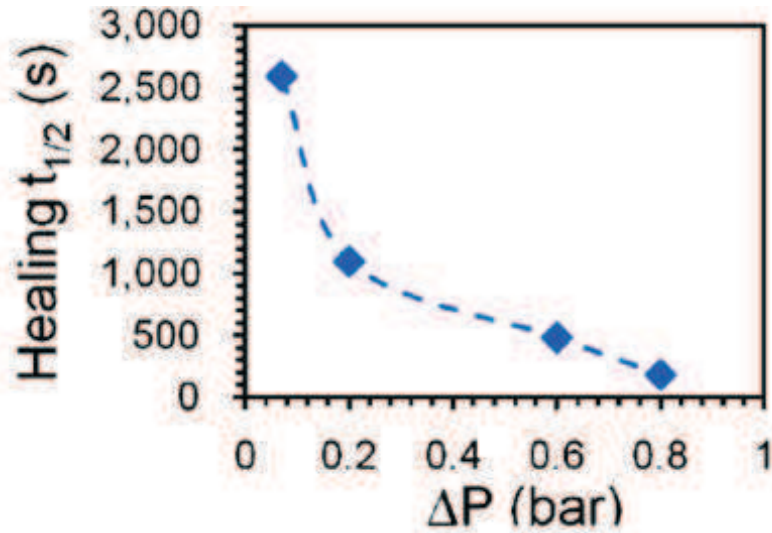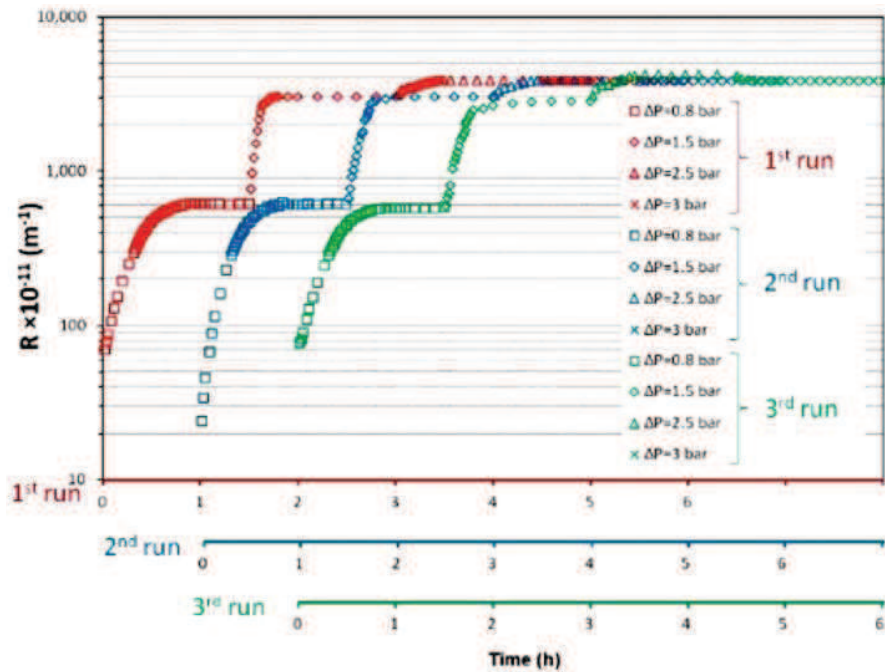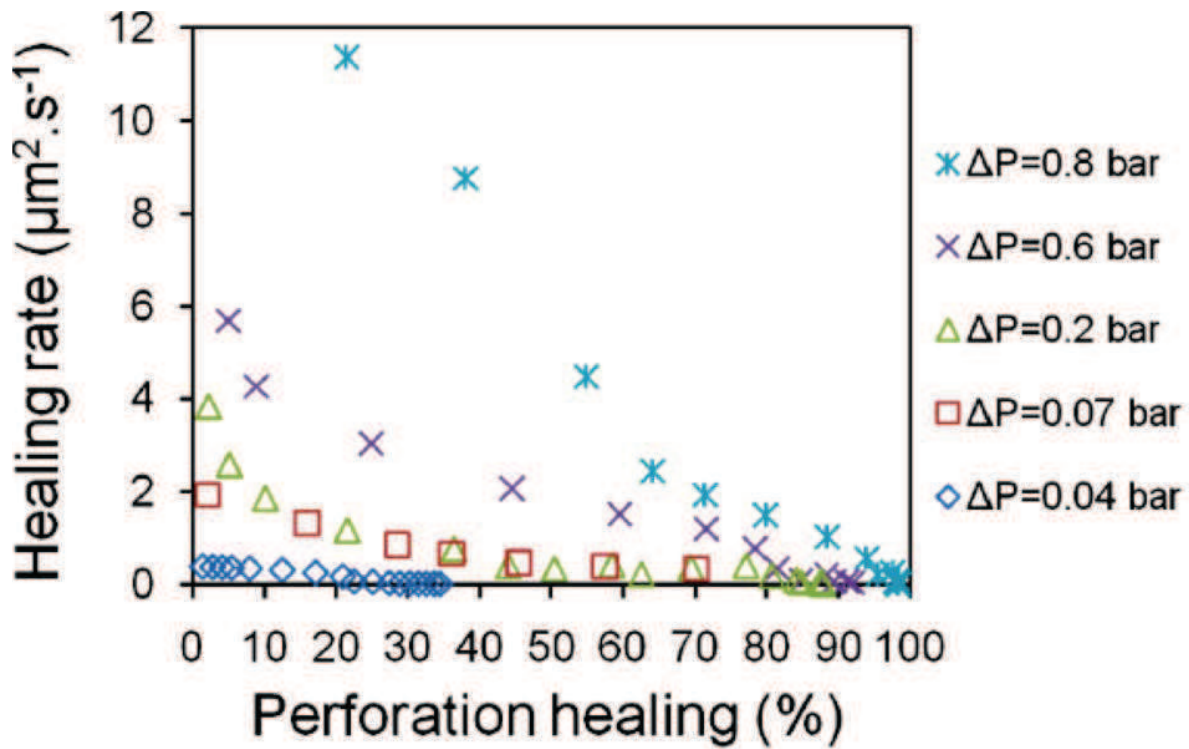Lastly, considering the perforation to be a perfectly circular in nature and healing phenomenon taking place evenly from all direction, the healing rate of the membrane could also calculated from resistance values (Figure – 2.21). The correlation between the healing rate and healing % reveals that rate of healing decreases rapidly with the increase in pressure. At 20% healing, a maximum healing rate of 12 $\mu m^2.sec^{-1}$ was observed at 0.8 bar although it decreased rapidly to 2 μm^2/sec once 70 % healing was achieved.

To complement the self-healing calculations based on flow resistance, Scanning Electron Microscopy (SEM) images were obtained for unhealed and healed membranes (Figure – 2.22a, b, c and d). Due to the piercing by the needle, the perforation is caused in such a manner that the broken fragments are aligned in the downward direction (Figure – 2.22a). From images of partially healed and fully healed membranes at 0.07 and 0.8 bar respectively, it can be seen that the fragments coming back onto the perforation plane and joining together to close the perforation (Figure – 2.22b, c). No healing was observed for pressures higher than 1.5 bar (Figure – 2.22d) which is in good agreement with water flow resistance recovery measurements.
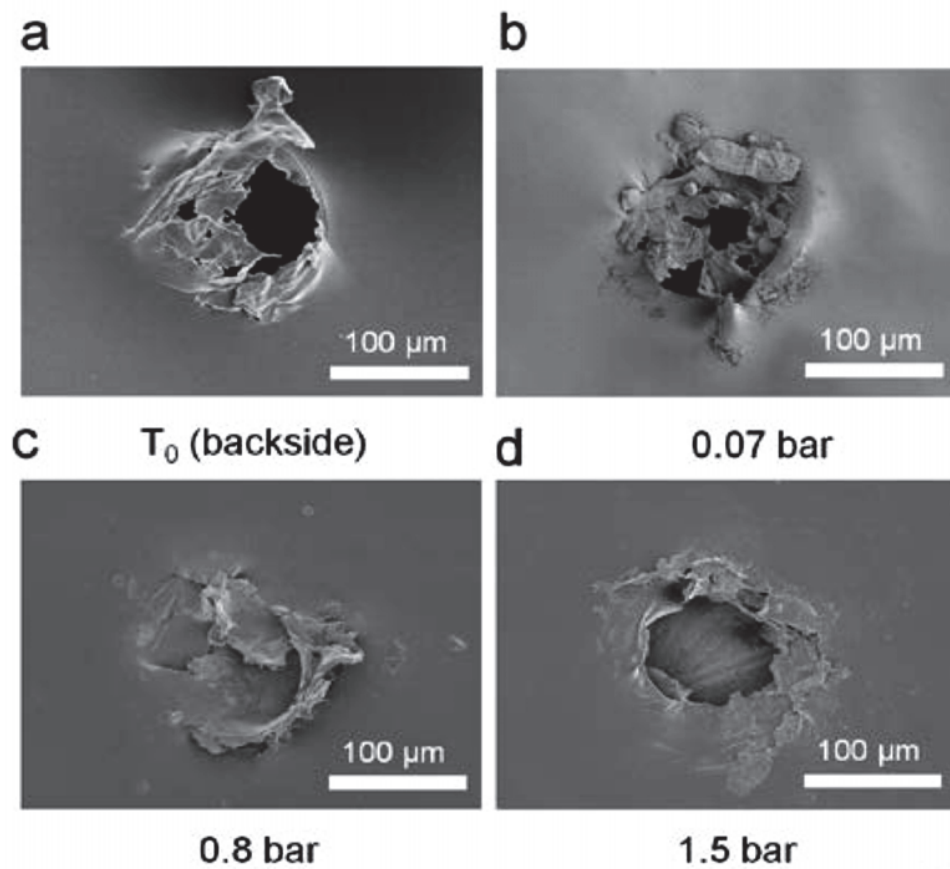
Figure – 2.22: Scanning Electron Microscopy images obtained for a) backside view of the perforation, b) a partially healed membrane at 0.07 bar, c) a completely healed membrane with scar formation, d) unhealed membrane with perforation intact.
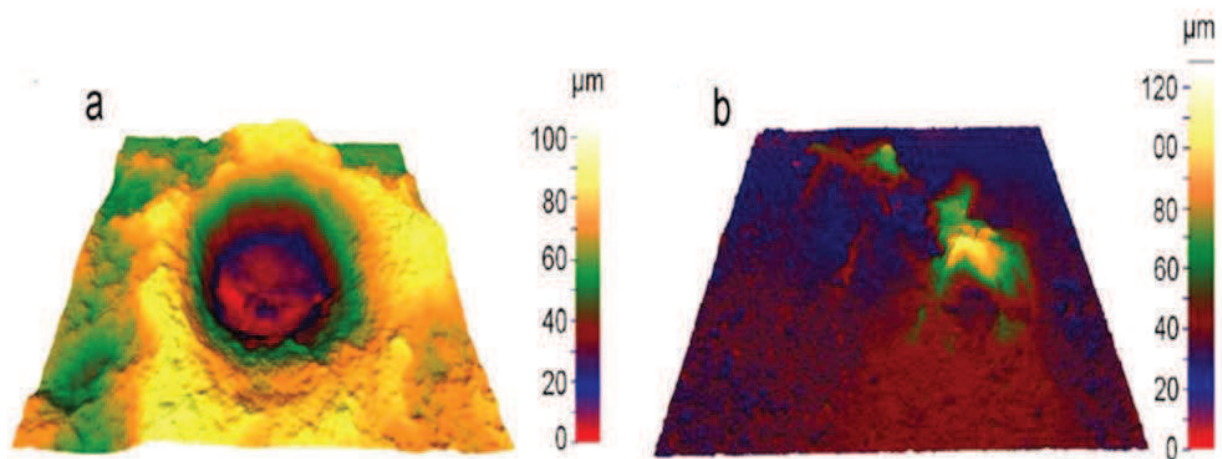

Figure – 2.23: False color 3-dimensional SEM images obtained for a) perforation, b) healed membrane with scar

To examine the topography of the perforation and completely healed membranes, 3D false color images were constructed by joining SEM images obtained from three different perspective angles ($90^{o}/80^{o}/70^{o}$) (Figure – 2.23a, b). As these images reveal, the perforation in the membrane causes an elevation of edges by 40 μm and a depression of film fragments by 60 μm with respect to the membrane surface plane. The healed membrane at 0.8 bar showed a scar above the surface plane due to the random overlapping and joining of the perforation fragments.

In order to verify the healing response with response to a catastrophic damage, a 2 mm cut was made into the membrane and was kept under water flux at 0.4 bar. Due to such a large damage, it was impractical to measure the flux since the amount of water permeated was huge. After 48 hours of continuous, although the amount of water decreased but it still remained substantial in amount. When examined using SEM, the cut was found to be closed at some points which explains the decreased water flow (Figure – 2.24a,b,c,d). Hence it can be inferred that the parameters like healing rate, effective healing pressure, healing time are influenced by the extent of damage to the membrane.
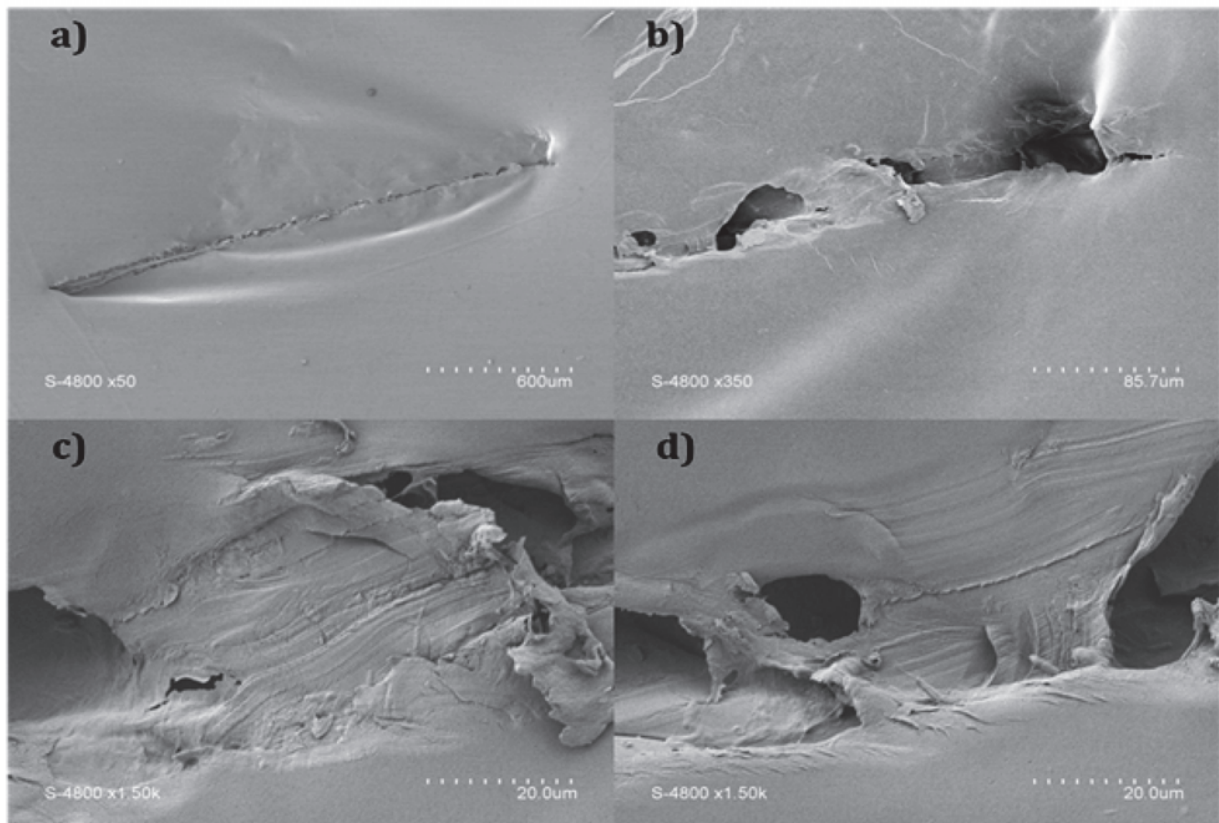

Figure – 2.24: Scanning Electron Microscopy images of a) Partially healed 2 mm cut, b-d) areas showing closure of the cut at 0.4 bar

While the resistance measurements give the values of appropriate pressure necessary for self-healing in particular time period, the SEM images provided an important aspect of the healing process: that is the movement of membrane fragments towards the membrane surface in the opposite direction of the water pressure. Based on this aspect, a mechanism for the observed self-healing may be explained on the basis of structure of the network of the micelles which are compressible under pressure in wet conditions. In case of perforation in the material, the micelles are drawn apart from each other with the ABA chains pulled out and consequently dangling in the perforation space. When pressure is exerted on the perforated film, the dynamic links between the micelles enable the network to rearrange (Figure – 2.25).
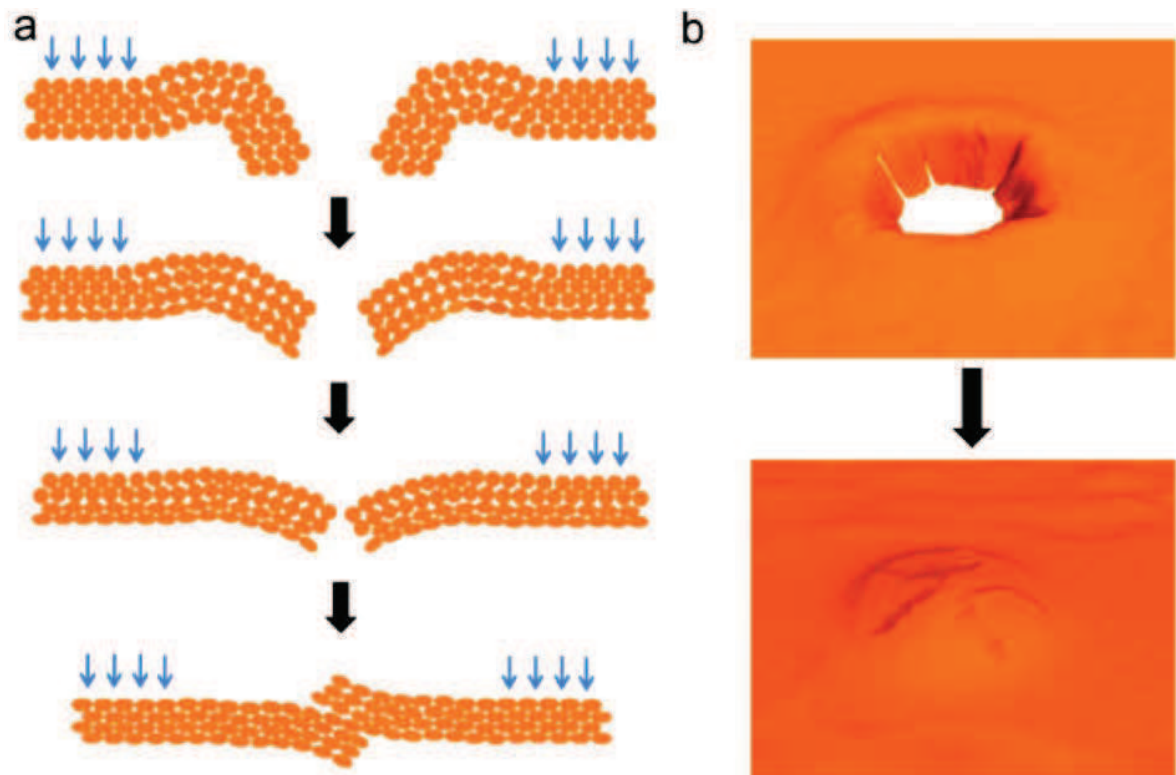
Figure – 2.25: Probable self-healing mechanism for the membrane

The deformation is neither instantaneous nor uniform as the bottom layer of micelles in contact with a rigid support get deformed first followed by subsequent upper layers[32]. Hence, the compression forces the deformed micelles to move towards the only available space, i.e. the perforation. Once the micelles of the two opposite fragments are in contact, the dangling ABA chains have enough mobility and time to penetrate into each other's micelle core thereby creating a bridge and ensuring the healing stability. At low pressure, the compression is too low to initiate this global movement of micelles while at

higher pressure end, the flow of the water restricts this concerted movement. It can be said that this fragmental contact is purely random filling up in nature rather than zipping up of the two opposite fragments as shown by the scarring observed for the healed samples in the SEM images (Figure – 2.22).
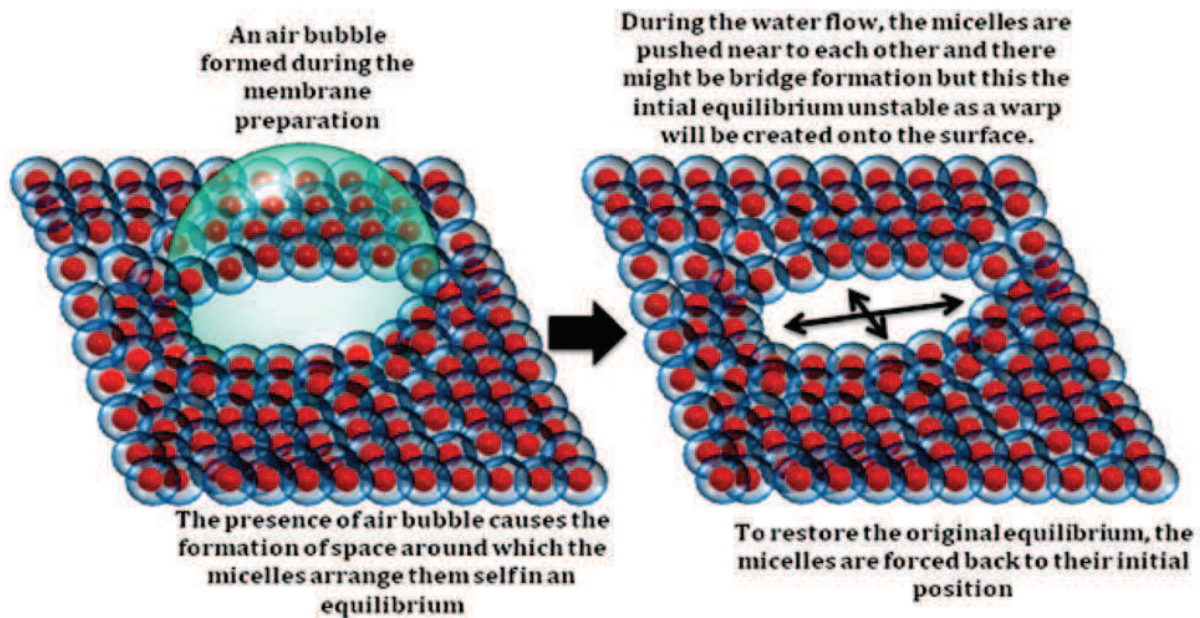
Figure – 2.26: No self-healing is possible in case of a perforation created by an air bubble or any other object present on the surface during the membrane process.

The presence of free dangling chains onto the created fragments is further strengthened by the fact that no stable healing was observed when a perforation was induced intentionally by creating a small air bubble during the film preparation. Consequently, block copolymer chains arrange themselves around bubble's periphery in such a way that the bridge formation between the two opposite sides of it is avoided. When compression takes place, even though the micelles are pushed towards each other, there are no dangling chains to create a bridge or even even if there are chains to create a bridge, it will not be stable since the closure will result in the destabilization of the micelles' equilibrium and create a physical warp onto its surface. Hence the closure is essentially temporary and once the pressure is relieved, the micelles are forced to retreat to their original positions to restore the original equilibrium thereby recreating the original space (Figure – 2.26).

2.9 CONCLUSION

In conclusion, a self-healing membrane with tunable porosity based on dynamic set of nanometric block copolymer micelles has been described. The membrane shows the capacity to self-regulate its performance in response to applied water pressure. The proof of the pore size tuning and most important its functional applicability is demonstrated by the filtration experiments of PEO polymers according to their size through membranes previously subjected to various water pressures. Despite the low permeabilities[27,29] (i.e. 13.4 $L.h^{-1}.m^{-2}$ bar^{-1} for the adaptive spherical-type membranes and 40 $L.h^{-1}.m^{-2}$ bar^{-1} for the very stable worm-like membranes), the reversible sharp change in the membrane performance controlled via operating conditions is quite remarkable. Moreover the membrane exhibits capacity to mend itself at the macroscopic level. The production of such self-healable films to be used in membrane science can prolong their usable life in a given application without any other external intervention. The use of block copolymer micelles with adaptive behaviors under compression shows some formal similarity with the functional complexity of natural systems for which the communication between different length scales is the central point of the natural selections of functions[2,40].

REFERENCES

1   Lehn, J.-M. From supramolecular chemistry towards constitutional dynamic chemistry and adaptive chemistry. *Chemical Society Reviews* **36**, doi:10.1039/b616752g (2007).

2   Rybtchinski, B. Adaptive Supramolecular Nanomaterials Based on Strong Noncovalent Interactions. *Acs Nano* **5**, 6791-6818, doi:10.1021/nn2025397 (2011).

3   Tauk, L., Schroeder, A. P., Decher, G. & Giuseppone, N. Hierarchical functional gradients of pH-responsive self-assembled monolayers using dynamic covalent chemistry on surfaces. *Nature Chemistry* **1**, doi:10.1038/nchem.400 (2009).

4   Mann, S. Self-assembly and transformation of hybrid nano-objects and nanostructures under equilibrium and non-equilibrium conditions. *Nature Materials* **8**, doi:10.1038/nmat2496 (2009).

5   Kim, B. S. *et al.* Design of artificial extracellular matrices for tissue engineering. *Progress in Polymer Science* **36**, 238-268, doi:10.1016/j.progpolymsci.2010.10.001 (2011).

6   Oda, T. *et al.* Effectiveness of near-infrared spectroscopy during surgical repair of tracheo-innominate artery fistula. *Journal of Artificial Organs* **14**, doi:10.1007/s10047-011-0565-9 (2011).

7   Kaur, P., Hupp, J. T. & Nguyen, S. T. Porous Organic Polymers in Catalysis: Opportunities and Challenges. *Acs Catalysis* **1**, doi:10.1021/cs200131g (2011).

8   Jackson, E. A. & Hillmyer, M. A. Nanoporous Membranes Derived from Block Copolymers: From Drug Delivery to Water Filtration. *Acs Nano* **4**, doi:10.1021/nn1014006 (2010).

9   Krieg, E., Weissman, H., Shirman, E., Shimoni, E. & Rybtchinski, B. A recyclable supramolecular membrane for size-selective separation of nanoparticles. *Nature Nanotechnology* **6**, doi:10.1038/nnano.2010.274 (2011).

10   Stein, A. Advances in microporous and mesoporous solids - Highlights of recent progress. *Advanced Materials* **15**, doi:10.1002/adma.200300007 (2003).

11   Guimard, N. K. *et al.* Current Trends in the Field of Self-Healing Materials. *Macromolecular Chemistry and Physics* **213**, 131-143, doi:10.1002/macp.201100442 (2012).

12   Wu, D. Y., Meure, S. & Solomon, D. Self-healing polymeric materials: A review of recent developments. *Progress in Polymer Science* **33**, 479-522, doi:10.1016/j.progpolymsci.2008.02.001 (2008).

13   Ma, M. & Hill, R. M. Superhydrophobic surfaces. *Current Opinion in Colloid & Interface Science* **11**, doi:10.1016/j.cocis.2006.06.002 (2006).

14   Ogawa, T., Ding, B., Sone, Y. & Shiratori, S. Super-hydrophobic surfaces of layer-by-layer structured film-coated electrospun nanofibrous membranes. *Nanotechnology* **18**, doi:10.1088/0957-4484/18/16/165607 (2007).

15   He, D., Susanto, H. & Ulbricht, M. Photo-irradiation for preparation, modification and stimulation of polymeric membranes. *Progress in Polymer Science* **34**, doi:10.1016/j.progpolymsci.2008.08.004 (2009).

16   Persson, K. M., Gekas, V. & Tragardh, G. STUDY OF MEMBRANE COMPACTION AND ITS INFLUENCE ON ULTRAFILTRATION WATER PERMEABILITY. *Journal of Membrane Science* **100**, doi:10.1016/0376-7388(94)00263-x (1995).

17   Ebert, K., Fritsch, D., Koll, J. & Tjahjawiguna, C. Influence of inorganic fillers on the compaction behaviour of porous polymer based membranes. *Journal of Membrane Science* **233**, doi:10.1016/j.memsci.2003.12.012 (2004).

18   Yang, Q., Adrus, N., Tomicki, F. & Ulbricht, M. Composites of functional polymeric hydrogels and porous membranes. *Journal of Materials Chemistry* **21**, doi:10.1039/c0jm02234a (2011).

19   Tokarev, I. & Minko, S. Multiresponsive, Hierarchically Structured Membranes: New, Challenging, Biomimetic Materials for Biosensors, Controlled Release, Biochemical Gates, and Nanoreactors. *Advanced Materials* **21**, doi:10.1002/adma.200801408 (2009).

20   Quemener, D. *et al.* Free-Standing Nanomaterials from Block Copolymer Self-Assembly. *Macromolecules* **43**, doi:10.1021/ma100809v (2010).

21   Jain, S. & Bates, F. S. Consequences of nonergodicity in aqueous binary PEO-PB micellar dispersions. *Macromolecules* **37**, doi:10.1021/ma035467j (2004).

22   He, Y. Y., Li, Z. B., Simone, P. & Lodge, T. P. Self-assembly of block copolymer micelles in an ionic liquid. *Journal of the American Chemical Society* **128**, doi:10.1021/ja058091t (2006).

23   Giacomelli, F. C., Riegel, I. C., Petzhold, C. L., da Silveira, N. P. & Stepanek, P. Aggregation Behavior of a New Series of ABA Triblock Copolymers Bearing Short Outer A Blocks in B-Selective Solvent: From Free Chains to Bridged Micelles. *Langmuir* **25**, doi:10.1021/la8026732 (2009).

24   Kong, W., Li, B., Jin, Q., Ding, D. & Shi, A.-C. Complex Micelles from Self-Assembly of ABA Triblock Copolymers in B-Selective Solvents. *Langmuir* **26**, doi:10.1021/la903292f (2010).

25   Giacomelli, F. C., Riegel, I. C., Petzhold, C. L., da Silveira, N. P. & Stepanek, P. Internal Structural Characterization of Triblock Copolymer Micelles with Looped Corona Chains. *Langmuir* **25**, doi:10.1021/la804254k (2009).

26   Ikkala, O. & ten Brinke, G. Hierarchical self-assembly in polymeric complexes: Towards functional materials. *Chemical Communications*, doi:10.1039/b403983a (2004).

27   Nunes, S. P. *et al.* Switchable pH-Responsive Polymeric Membranes Prepared via Block Copolymer Micelle Assembly. *Acs Nano* **5**, doi:10.1021/nn200484v (2011).

28   Nunes, S. P. *et al.* Ultraporous Films with Uniform Nanochannels by Block Copolymer Micelles Assembly. *Macromolecules* **43**, doi:10.1021/ma101531k (2010).

29   Peinemann, K.-V., Abetz, V. & Simon, P. F. W. Asymmetric superstructure formed in a block copolymer via phase separation. *Nature Materials* **6**, doi:10.1038/nmat2038 (2007).

30   Knipprath, C., McCombe, G. P., Trask, R. S. & Bond, I. P. Predicting self-healing strength recovery using a multi-objective genetic algorithm. *Composites Science and Technology* **72**, 752-759, doi:10.1016/j.compscitech.2012.02.002 (2012).

31   Hwang, K.-J., Wang, Y.-T., Iritani, E. & Katagiri, N. Effect of gel particle softness on the performance of cross-flow microfiltration. *Journal of Membrane Science* **365**, doi:10.1016/j.memsci.2010.08.043 (2010).

32   Hwang, K.-J., Wang, Y.-T., Iritani, E. & Katagiri, N. Effects of porous gel particle compression properties on microfiltration characteristics. *Journal of Membrane Science* **341**, doi:10.1016/j.memsci.2009.06.029 (2009).

33   Lu, W. M., Tung, K. L., Hung, S. M., Shiau, J. S. & Hwang, K. J. Compression of deformable gel particles. *Powder Technology* **116**, doi:10.1016/s0032-5910(00)00357-0 (2001).

34   White, S. R. *et al.* Autonomic healing of polymer composites. *Nature* **409**, 794-797, doi:10.1038/35057232 (2001).

35   Cordier, P., Tournilhac, F., Soulie-Ziakovic, C. & Leibler, L. Self-healing and thermoreversible rubber from supramolecular assembly. *Nature* **451**, 977-980, doi:10.1038/nature06669 (2008).

36   Bond, I. P., Trask, R. S. & Williams, H. R. Self-healing fiber-reinforced polymer composites. *Mrs Bulletin* **33**, 770-774, doi:10.1557/mrs2008.164 (2008).

37   Trask, R. S., Williams, G. J. & Bond, I. P. Bioinspired self-healing of advanced composite structures using hollow glass fibres. *Journal of the Royal Society Interface* **4**, 363-371, doi:10.1098/rsif.2006.0194 (2007).

38   Kolmakov, G. V. *et al.* Using Nanoparticle-Filled Microcapsules for Site-Specific Healing of Damaged Substrates: Creating a "Repair-and-Go" System. *Acs Nano* **4**, 1115-1123, doi:10.1021/nn901296y (2010).

39   Salib, I. G., Kolmakov, G. V., Gnegy, C. N., Matyjaszewski, K. & Balazs, A. C. Role of Parallel Reformable Bonds in the Self-Healing of Cross-Linked Nanogel Particles. *Langmuir* **27**, doi:10.1021/la104609t (2011).

40   Moulin, E., Cormosw, G. & Giuseppone, N. Dynamic combinatorial chemistry as a tool for the design of functional materials and devices. *Chemical Society Reviews* **41**, doi:10.1039/c1cs15185a (2012).

3. TRANSLOCATION ACROSS A SELF-HEALING MEMBRANE

Translocation of matter across biological membranes is one of the most crucial processes in nature, being essential for both delivery and signaling purposes[1]. Due to recent use of nanoparticles as potential drug carriers[2,3], sub-cellular sensors[4,5] and imagers[6,7], nanoinjectors[8], and gene carriers[9], their trafficking across lipid membranes has been studied extensively for better understanding of the process[10-13]. Translocation has been indentified to happen either by a "direct penetration" (diffusion) process in which a nanoparticle or nano-object diffuses through cellular membrane under the effect of an external force or by a much more prevalent "receptor mediated endocytosis"[14-16] process which involves internalization of the matter via three steps[17-19]: First being the adsorption of nanoparticle or nano-object over the surface of the cellular membrane via functional groups, second being their wrapping or engulfing by the membrane and third being the "pinching-off" of the lipid-particle complex from the membrane[20]. Usually, the direct mode of translocation (diffusion) is considered less attractive from practical applications point of view as compared to endocytosis process since the former involves the application of an external force[8,12] and in most cases the delicate membrane structure is disrupted by this force induced translocation. In recent works, although novel polymer architectures like dendrimers[21-23] have been used to create pore across the membrane across their passage way to facilitate the diffusion process but the permanent nature of the pores has detrimental effect on the membrane which in worst case can even lead to its complete destruction[24] and consequently cell death. The problem of permanent pore formation in the membrane and its structural failure can be circumvented if the membrane is able to close the created pores by itself while the particle moves across it.

In this chapter we have investigated the above scenario by carrying out the translocation of different nano-objects having different geometry, size and surface characteristics across a self-healing membrane (Figure – 3.1). We recall that this self-healing membrane[25] discussed in the previous chapter, is essentially a 3-dimensional network of a triblock copolymer micelles held together dynamically via copolymer chains acting as bridges. While the interstitial space between the spherical constituent

micelles enabled the membrane to separate objects, their compressible nature and dynamic bridges interconnecting them ensured a self-healing system.
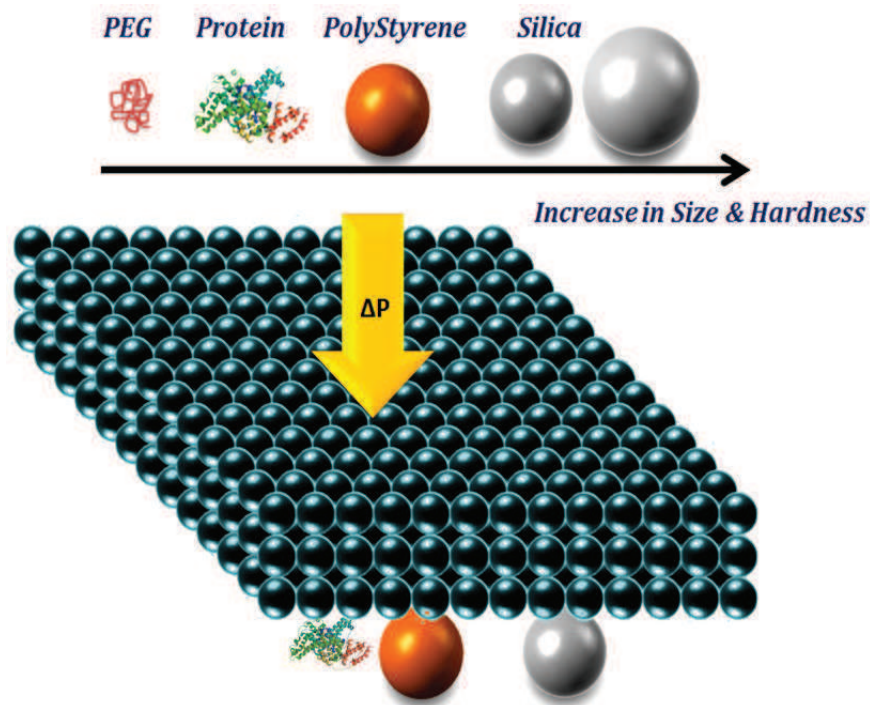

Figure – 3.1: General representation of translocation experiments of various nano-objects carried out across dynamic self-healing membrane. For simplicity, only three layers of micelles are shown.

The feeble and reversible bridging between the micelles presents the possibility of formation of an instantaneous pore followed by pressure induced self-healing and ultimately its closure. Therefore, it can be expected that an object translocating across this membrane would create a dynamic cavity along its passage, which would close immediately as the object moves further across the membrane.

3.1 THE MEMBRANE & THE EXPERIMENTAL SET-UP

The membranes used in this work had the same dimensions (4.1 cm^2 area and 1.3 µm thickness) as used for the fluid flow resistance experiments. The experimental set-up also remained essentially the same except the fact that a finite quantity of feed solution (10 ml) was introduced into the filtration cell and the compressed air supply was connected directly to it to have the required pressure changes. A small recipient was attached to the outlet of the cell to collect the permeates in sufficient quantities (1.5 ml) to be analyzed further by the gel permeation chromatography, UV-Visible spectroscopy, Photon Cross Correlation Spectroscopy or Scanning Electron Microscopy depending upon the type of nano-

object translocated. Given the sensitivity of the membrane with respect to pressure (porosity change from 35 % to 5 %), each membrane was compressed to its maximum at the corresponding pressure before carrying out the translocation experiment. To achieve this, water was permeated through the membrane at the given pressure for 2 hours quickly followed by the introduction of nano-object feed solution in the cell and switching of compressed air supply.

3.2 NANO-OBJECTS AND THEIR PREPARATION

In this work, we chose four classes of nano-objects to be translocated across the self-healing membrane. The first being represented by Poly(ethylene glycol)s (PEG)s as the smallest objects in terms of dimensions and softest in terms of nature and highly hydrophilic. A mixture of 3 PEGs (100 KDa, 200 KDa and 300 KDa) was prepared with a final concentration of 0.75 g.l^{-1}. This feed solution was analyzed by passing through a gel permeation chromatography column equipped with refractive index detector. The chromatogram of the feed solution (Figure – 3.2) was obtained in order to compare with retentates and permeates solution obtained after the translocation experiments. As it can be seen that the column was not able to resolve the peaks perfectly however this not important due to the fact that in this particular part of the experiment, the GPC chromatograms have been used only for qualitative analysis rather than quantitative.
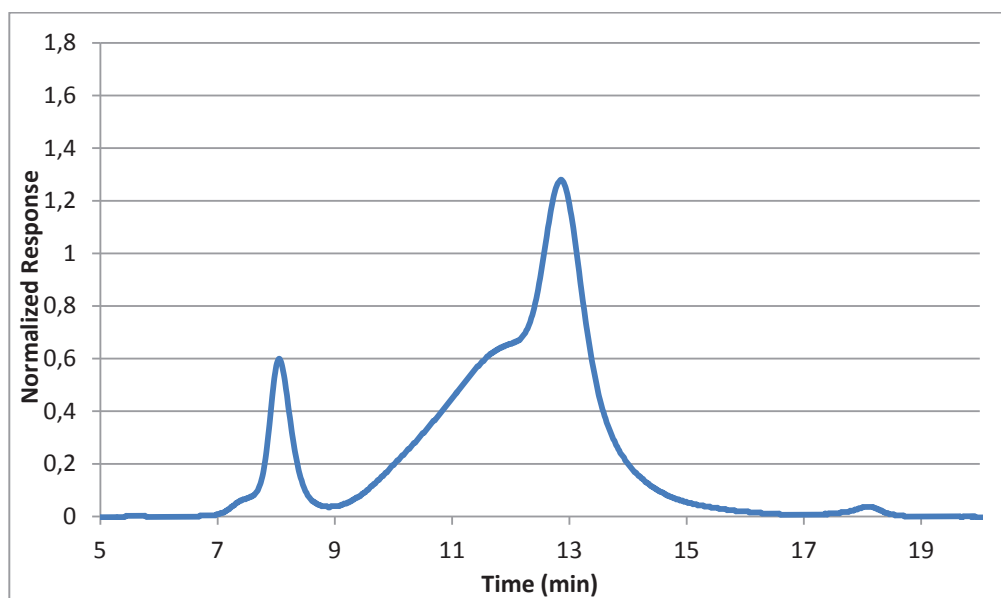

Figure – 3.2: Chromatogram obtained for the feed solution of mixture of PEGs using Gel Permeation Chromatography

The second class is represented by Bovine Serum Albumin protein (BSA) whose aqueous suspension was prepared at different concentrations and the absorbance at 276 nm was measured by UV-Visible spectroscopy to obtain a calibration graph (Figure – 3.3). As compared to the random structure of PEG chains in aqueous medium, BSA bears a much compact and well defined structure in the form of a prolate ellipsoid ($L_a = L_b < L_c$) as measured by transient electric birefringence[26] (Figure – 3.4a,b). It can be assumed that while passing through the membrane, the structural integrity of the protein will be maintained.
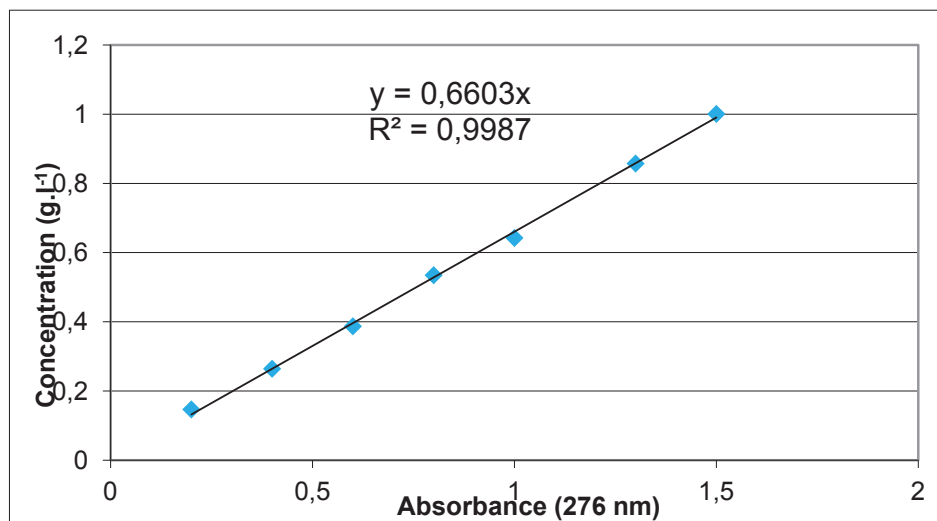
Figure – 3.3: Absorbance vs. concentration calibration graph obtained for BSA protein using UltraViolet – Visible Spectroscopy
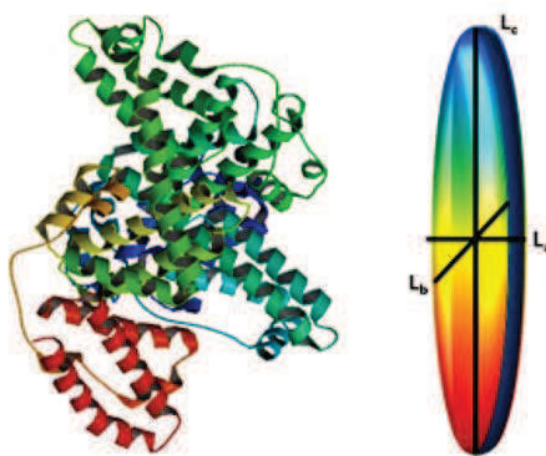
Figure – 3.4: 3-Dimenstional structure of Bovine Serum Albumin and it apparent shape as a prolate ellipsoid or a spheroid.

The third class of the nano-objects is represented by Poly(styrene) latex beads (PS) whose average mean diameter was calculated to be approx. 110 nm with a mono-modal size distribution (Figure – 3.5a) using Scanning Electron Microscopy images (Figure – 3.5b) and confirmed by Photon Cross Correlation Spectroscopy. The average mean diameter was calculated by measuring the diameter of individual particles in the SEM image and according to the following equation also known as De Brouckere Mean Diameter[27]:

$$D_{Av} = \frac{\sum_i^n D_i^4}{\sum_i^n D_i^3}$$ ……….. Eq. (3.1)
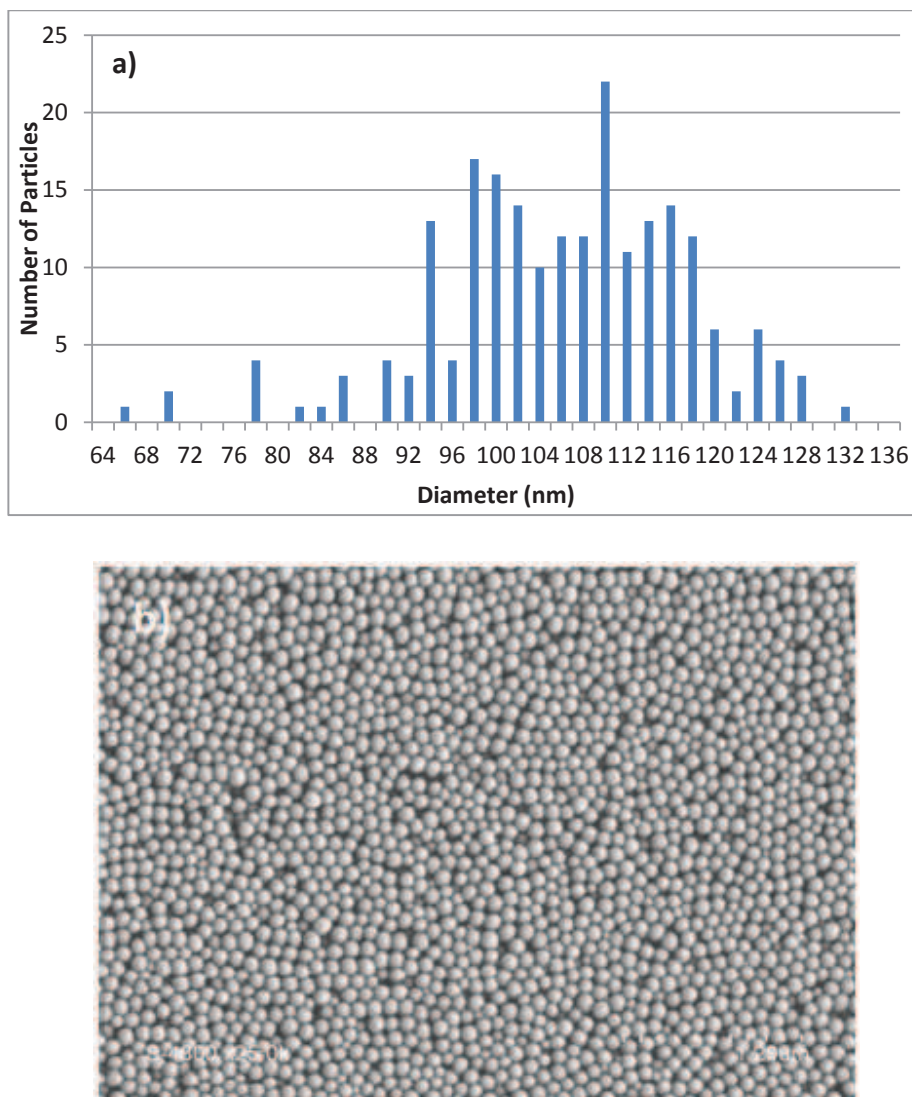
Figure – 3.5: a) Monomodal size distribution obtained for Poly(styrene), b) Scanning Electron Microscopy image

To avoid the probable clogging of the membrane by excess nanoparticles a minimum concentration value was obtained using PCCS while still lying within the detection limit of PCCS (Figure – 3.6). This is important since if the concentration is too low, it will be further lowered in the permeates due to which PCCS may not be able to detect enough nanoparticles in the solution.
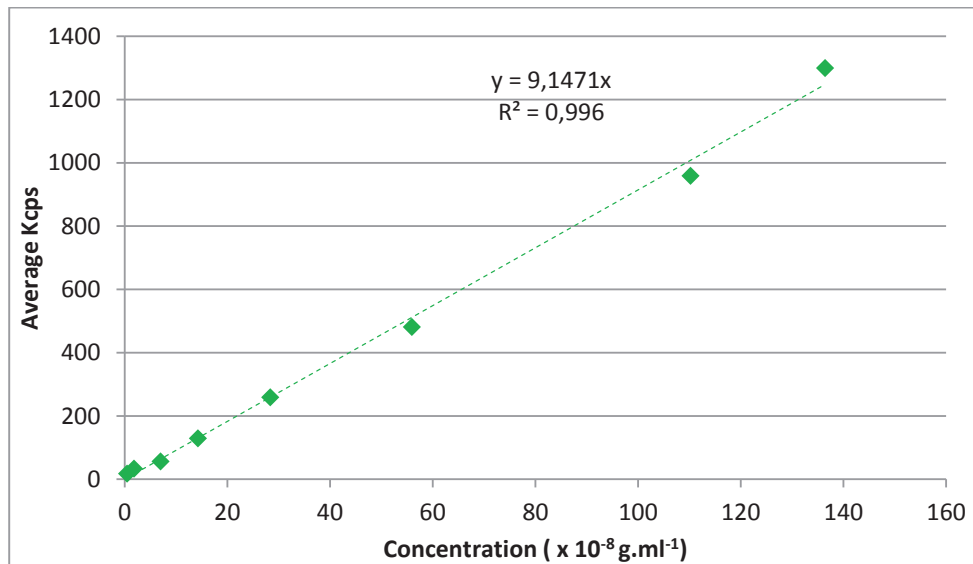
Figure – 3.6: Concentration vs Kcps calibration curve obtained for PS nanoparticles using Photon Cross Correlation Spectroscopy
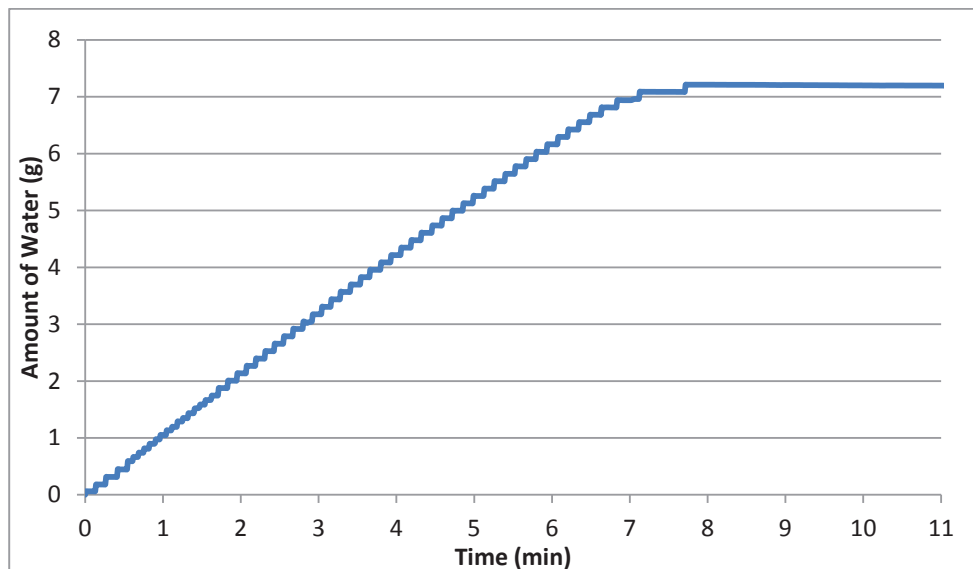
Figure – 3.7: Amount of water passed through the membrane over the course of time with increasing concentration of PS nanoparticles

The effect of concentration of particles on the permeation of water can be gauged from a simple experiment where the concentration of nanoparticles was increased over the course of filtration experiment. At a low pressure value of 0.2 bar, a maximum concentration of (1.43×10^{-7} g.ml^{-1}) was achieved beyond which the membrane was completely clogged (Figure – 3.7).

The final class of the nano-objects is represented by Silica nanoparticles which are the stiffest and biggest amongst the nano-objects studied in this work. Two series of silica NPs (SP1 & SP2) were prepared by a modified Stober process[28]. The synthesis was carried out in isopropanol at 20°C with the concentrations of various reactants governed by the following relation:

$$[NH_3] = 0.81[TEOS]), [H_2O] = 6.25[TEOS] \qquad \text{where, [TEOS] was taken to be 0.22 M}$$

An excess of water in the system facilitates thorough hydrolysis of Triethylorthosilicate (TEOS) which gives high mass fraction. Ammonia (NH$_3$) accelerates the hydrolysis and condensation of TEOS while supplying –OH ions adhering on the particles, thus stabilizing the suspension via repulsion against Van der Waals attractive force[28]. The reported optimum concentration of NH$_3$ with respect to TEOS was used as it was observed that a high concentration leads to coagulation while too low concentrations led to longer reaction time or even no silica particles formation.
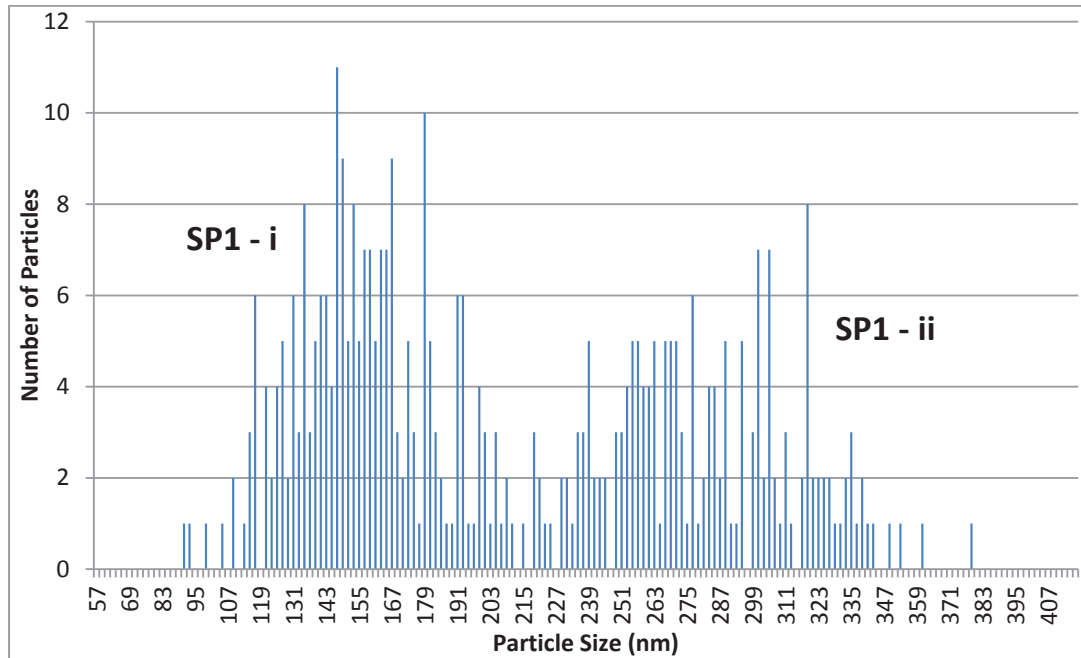
Figure – 3.8: Bimodal size distribution obtained for silica nanoparticles (SP1) showing two population of NPs
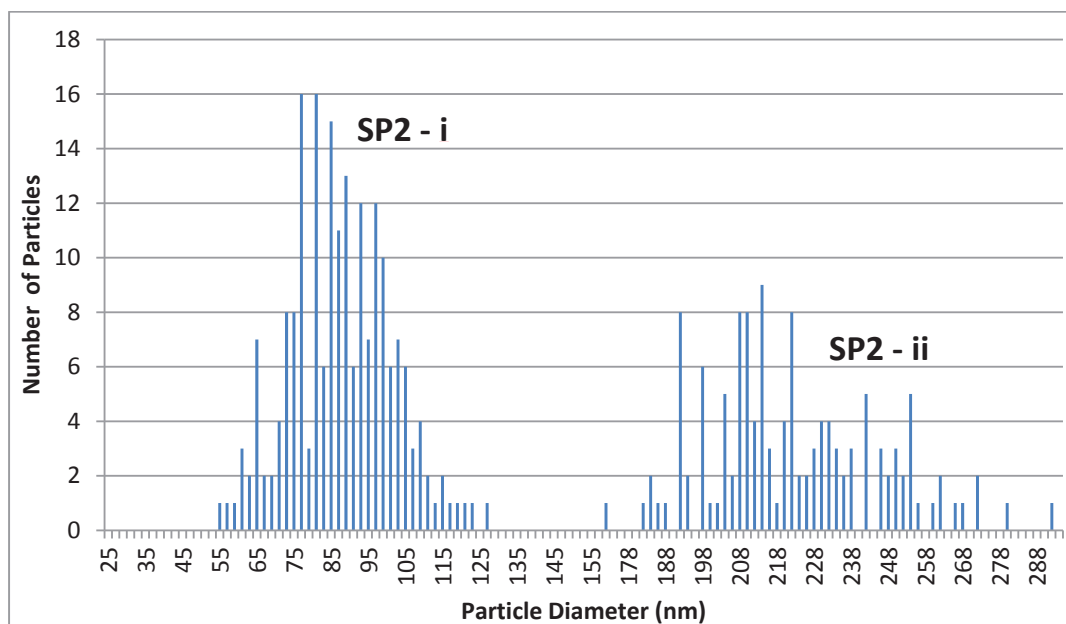
Figure – 3.9: Bimodal size distribution obtained for silica nanoparticles (SP2) showing two population of NPs

Unlike the monomodal distribution of poly(styrene) NPs, both series of silica NPs showed a bimodal distribution (Figure – 3.8 & 3.9). The average diameters of the NPs were calculated using equation – 3.1 by measuring the diameters of individual NPs in SEM images (Figure – 3.10a,b,c,d) obtained for both series. The average mean diameters thus obtained for two populations of both the series have been presented in the table – 3.1. The SP1 series silica particles comprised an approximate 56.7 % of smaller silica particles while SP2 series comprised 61 % of smaller NPs.

Nanoparticles	Average Mean Diameter (D_a) (nm)	De Brouckere Mean Diameter (D_b) (nm)	Dispersity Index (D_b/D_a)	Percentage of Nanoparticles
Silica SP1 – i	156	167	1,07	57
Silica SP1 – ii	279	293	1,05	43
Silica SP2 – i	88	94	1,07	61
Silica SP2 – ii	223	230	1,03	39

Table – 3.1: Various diameters, dispersity indices and relative % of silica nanoparticles calculated from Scanning Electron Microscopy images. 200 particles were counted for each type of population.
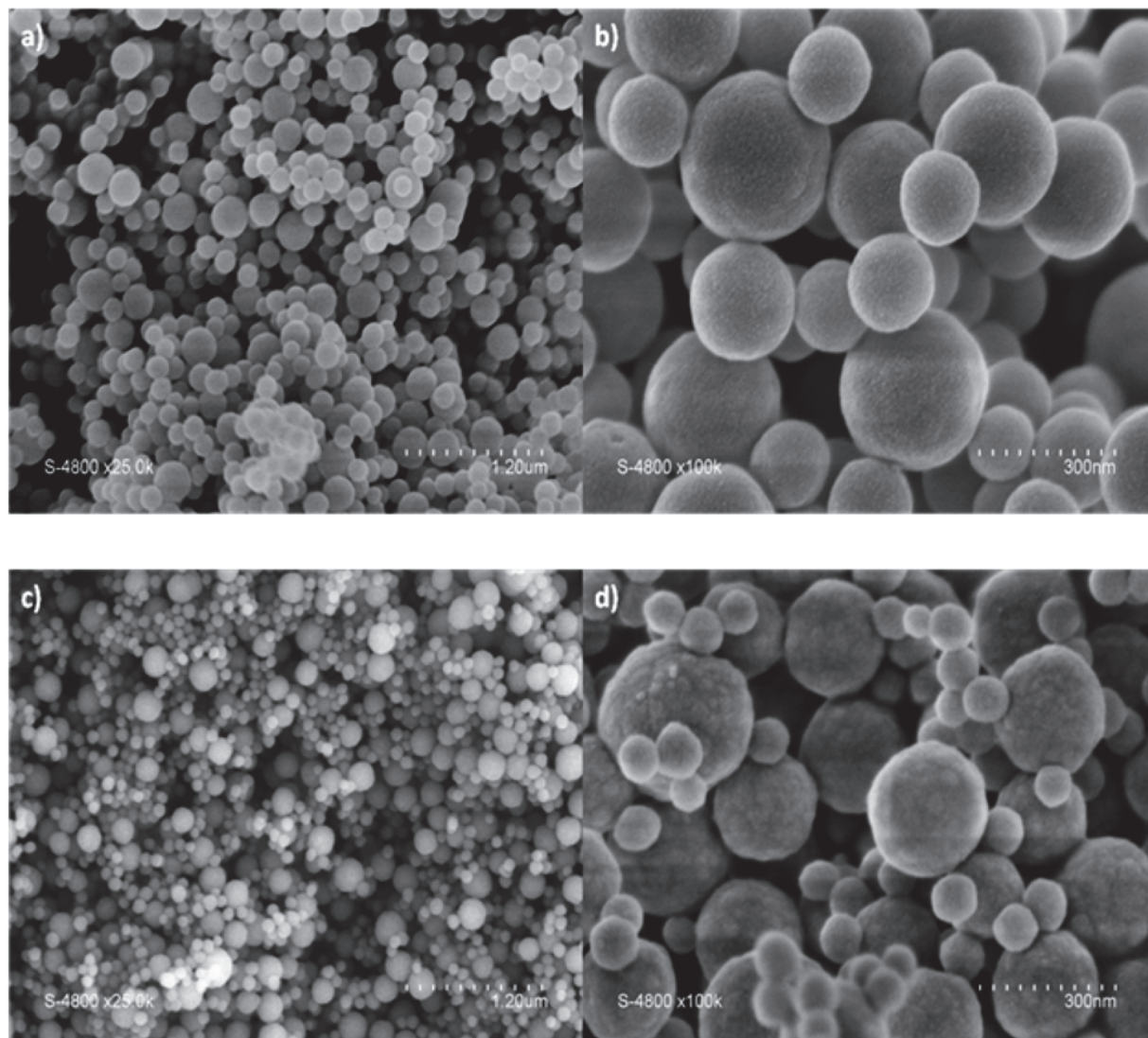
Figure – 3.10: Scanning Electron Microscopy images obtained for, a-b) Silica SP1 series with two populations of NPs, c-d) Silica SP2 series with two populations of NPs

Again as in case of Polystyrene NPs, an optimum concentration of silica particles was obtained in order to avoid clogging as well as to be able to detect translocated particles in the permeates by PCCS. Hence concentration calibration curves (Figure – 3.11) were obtained for both the series. Based on these curves, 2.4×10^{-4} g.ml^{-1} was taken to prepare the feed solution. As compared to Polystyrene NPs, Silica NPs tend to aggregate due to strong interparticle attraction and settle down to the bottom in a solvent like water which has high dielectric constant. Hence, their feed solutions as well as retentates and permeates were ultrasonicated prior to any analysis.
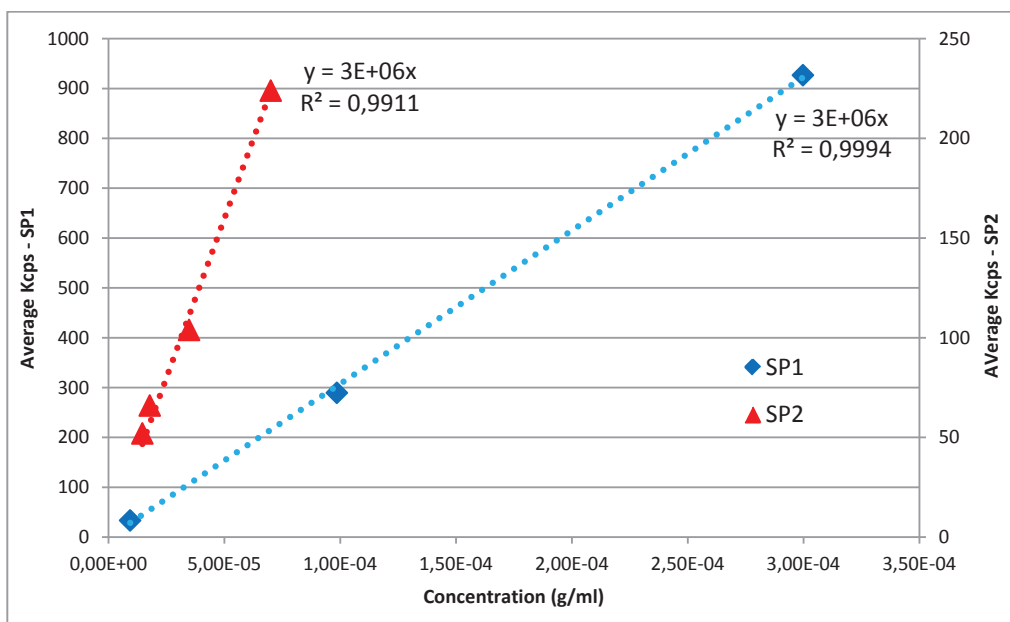
Figure – 3.11: Concentration vs Kcps calibration curve obtained for the two series of silica nanoparticles using Photon Cross Correlation Spectroscopy

3.3 TRANSLOCATION OF NANO-OBJECTS

The translocation of PEGs was carried out at pressure range of 0.2 bar to 1 bar. As the hydrodynamic radii of all PEG were all way above the maximum pore size of the membrane at the corresponding pressures hence any detection of PEG chains in the permeate would demonstrate their translocation across the membrane. In the previous studies[29-31], passage of single polymer chain across a nanopore has been studied in much detail establishing the fact that the individual chains having random coil confirmations translocate through chain stretching mechanism. The GPC analysis of the permeates obtained at different pressures, showed no peaks for any of the PEGs signifying that none of the four could pass through the membrane (Figure – 3.12). This is not surprising given the fact that being hydrophilic in nature and non-specific in shape, the PEG chains can undergo many conformational and orientation changes before migrating slowly to the interior of the membrane. However due to long chain length and strong interaction with PEO corona of the micelles, they are entangled within the membrane interior. Few such entanglements lead to a cascade effect of further entanglements leading to an ultimate fouling of the membrane despite continuous stirring of the solution inside the cell. It must be noted that in previous work, PEG chains having lower molecular weights and lower hydrodynamic radii than pore size were capable of transferring through the membranes at pressures as low as 0.2 bar. Given the absence of PEGs in the permeates and the presence and intensity of peaks observed in the

chromatogram for the retentates (Figure – 3.13) indicates that a most of the PEGs were retained completely by the membrane with small possible amount remaining entrapped over its surface. .

Figure – 3.12: Chromatograms obtained for permeates at different pressures using Gel Permeation Chromatography, indicating the absence of PEGs.

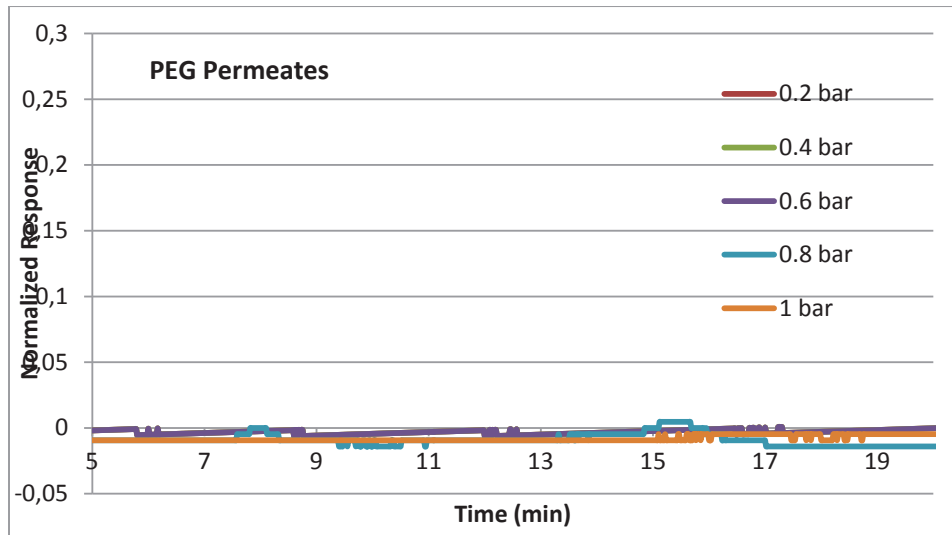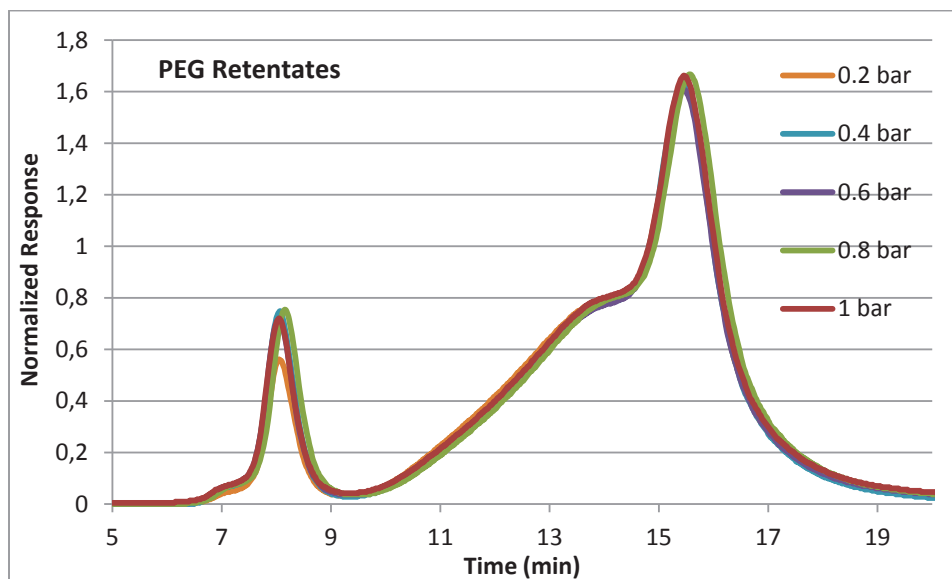*Figure – 3.13: Chromatograms obtained for retentates at different pressures using Gel Permeation Chromatography, indicating presence of PEGs.*

In case of BSA translocation, the results were completely reversed as all the protein molecules went through the membrane completely at all pressures until the feed solution concentration reached a

very high value of 1.5 g.l^{-1}. This is surprising as with an approximate molecular weight of 66,463 Da, BSA has almost twice the molecular weight of the lowest PEG used in the PEG mixture hence it should be retained in a more pronounced way and completely foul the membrane. The fouling of ultrafiltration membranes by BSA has been reported in the past where the fouling has been reported to occur by cake formation mechanism[32-34]. The interaction between protein-protein and protein-membrane influence the fouling process[35]. While the former type interaction influences the adsorption into the pores and over the surface of membrane, the   latter type interaction influences the cake structure and its formation. In the present case, one of the reasons for such inverse result can be attributed to the near absent interactions between the protein molecules and the PEO corona of the micelles of the membrane. Due to its hydrophilic nature, high excluded volume and coordination ability with water molecules, PEO is considered as an effective antifouling material[36,37]. Moreover, a neutrally charged polymer like PEO forms hydrogen bonds with water thereby generates an energetic barrier, thus preventing the adsorption of biomolecules[37-39]. The dense coronas of PEO reduce or even prevent initial adhesion of the first layer of protein molecules over the membrane, which act as a precursor to fouling. Another important reason can be attributed to the ellipsoidal shape of the protein and contact angle of the protein molecules with respect to the membrane surface which play a vital role in its translocation. A recent computer simulation study[12] conducted for ellipsoidal nanoparticles translocating through lipid membranes revealed that in general smaller is the volume of the particle, lesser is the driving force required leading to an easy penetration through the membrane. In the present case, although the volume of the ellipsoidal protein molecules is ~ 939 nm^3 with L_a/L_c = 3.5, the applied pressure in the cell compensates for the required high force for membrane penetration. Moreover, since most of the protein molecules were able to pass through the membrane, it can be assumed that a majority of these had an angle much lesser than 90° with respect to the line normal to the membrane surface. This is because the ellipsoidal particles in unconstrained state tend to align themselves in a position perpendicular to the surface of the membrane while rotating at a longer axis. Such preferential alignment of anisotropic nanoparticles while diffusing through a membrane has been proved by various techniques[40-44] and further substantiated by simulation studies[45,46].

Another important aspect of BSA translocation across the membrane was the arresting of morphology change at high pressure values. We recall from previous chapter that at pressure equal to 3 bar and beyond, the spherical micelles started to deformed considerably leading to large voids formation and thus a large porosity change. The AFM images (Figure – 3.14) show the surface state of the membranes after being subjected to BSA filtration at 3 different concentrations (0.5, 1 and 1.5 g.l^{-1}).

While at low concentration values (Figure – 3.14a,b), the membrane still contained pores even at 4 bar but at 1.5g.l^{-1} almost all the voids were completely filled with BSA (Figure – 3.14e,f) making it totally impermeable.
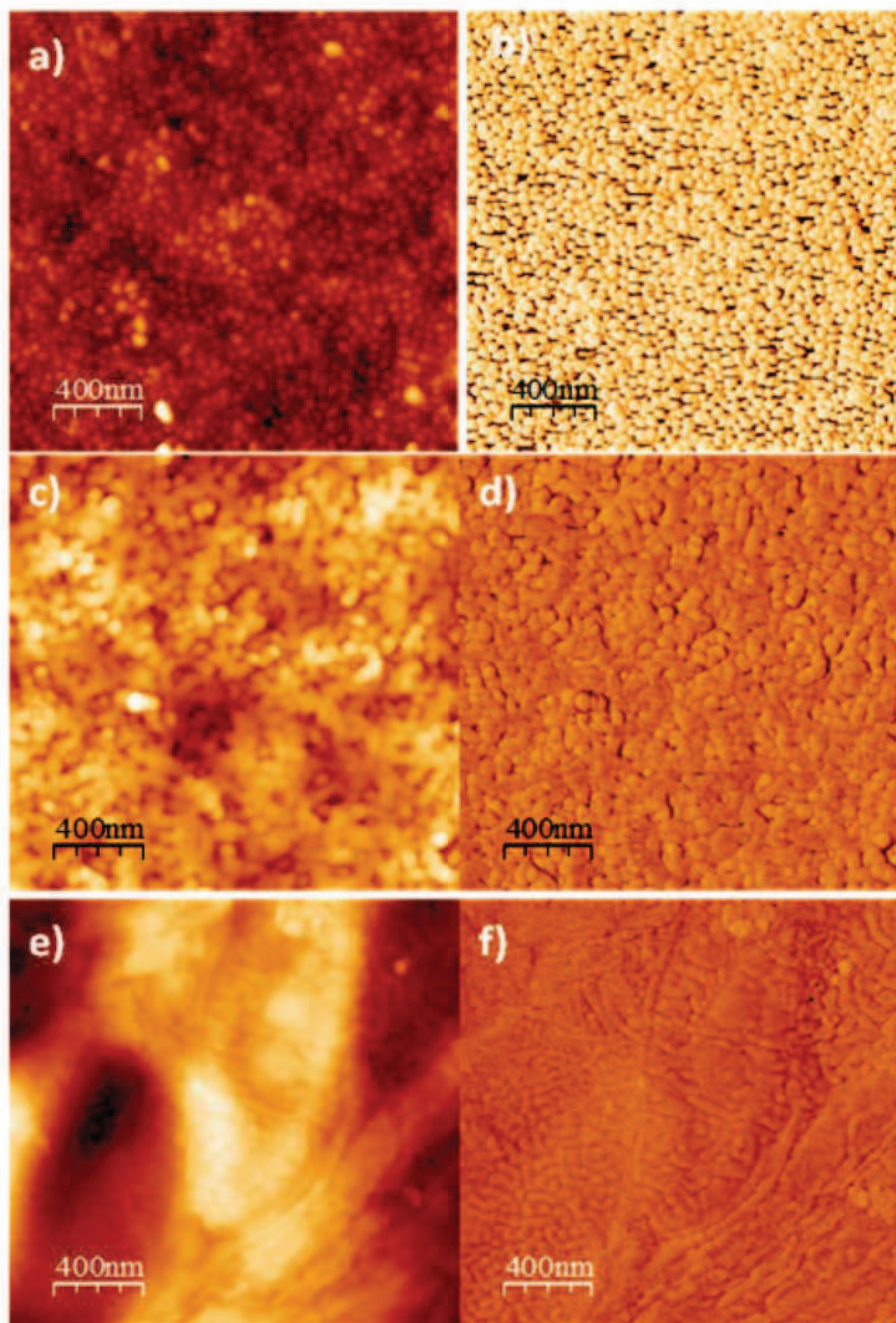
Figure –3.14: Atomic Force Microscopy images of the membrane obtained after BSA translocation, a-b) Translocation with 0.5 g.l^{-1} at 0.2 bar, c-d) Translocation with 1 g.l^{-1} at 2.5 bar, e-f) Fouled membrane with 1.5 g.l^{-1} at 4 bar

Since the only change in the membrane's morphology could come from the presence of protein molecules surrounding the micelles, hence their translocation is confirmed. Interestingly, the proteins in between the micelles seem to delay the morphological change at higher pressure value (as observed in 3rd chapter) since nothing happened at 4 bar. An explanation could be that the protein will avoid or delay the partial fusion of the micelles due to the low affinity between PEO and the BSA.

Moving further across the continuum, the response of stiffer and more voluminous polystyrene latex nanoparticles (NPs) showed unsurprising pressure dependence within the pressure range of 0.2 bar to 0.8 bar. For each given pressure, the respective collected permeates and retentates were analyzed using PCCS to determine the presence of NPs (Figure – 3.15a,b,c). The curves for 0.07 bar & 0.8 bar are not shown since 100 % retention and permeation were observed respectively for poly(styrene) NPs.
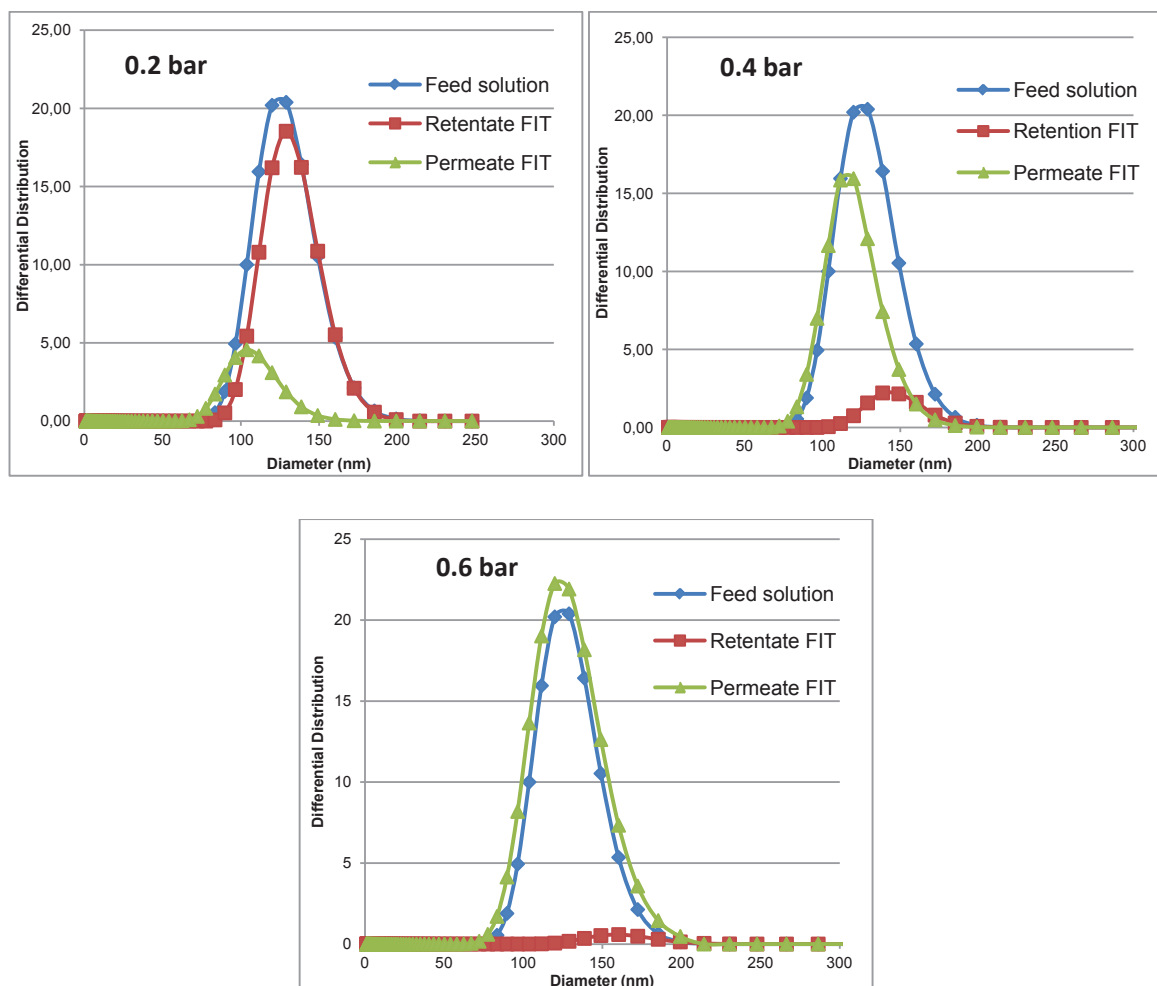
Figure – 3.15: Differential distribution curves observed for retentates and permeates obtained at different pressures using Photon Cross Correlation Spectroscopy.

The global retention values (Figure – 3.16) for the NPs were calculated from the area of the retentate and permeate curves. The values were also matched with that calculated from concentrations obtained from calibration curve equations.
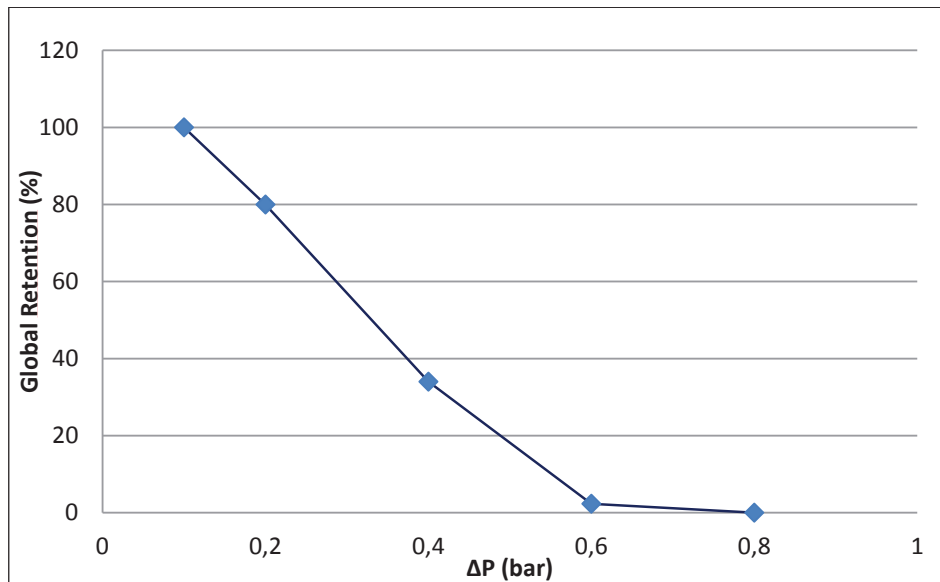
Figure – 3.16: The calculated global retention values for poly(styrene) NPs at different pressures

Nearly all the particles were retained at low pressure however as the pressure was increased, some of the particles managed to translocate across the membrane. At 0.8 bar, an almost negligible retention indicates that nearly all particles were able to pass through comfortably.

To further substantiate the effect of pressure on the retention in correlation with size dependence of the particles, the approximate retention percentage values were calculated mathematically at each pressure for a given particle size (Figure – 3.17) by normal fitting of PCCS differential distribution q3lg curves for permeates and the retentates.
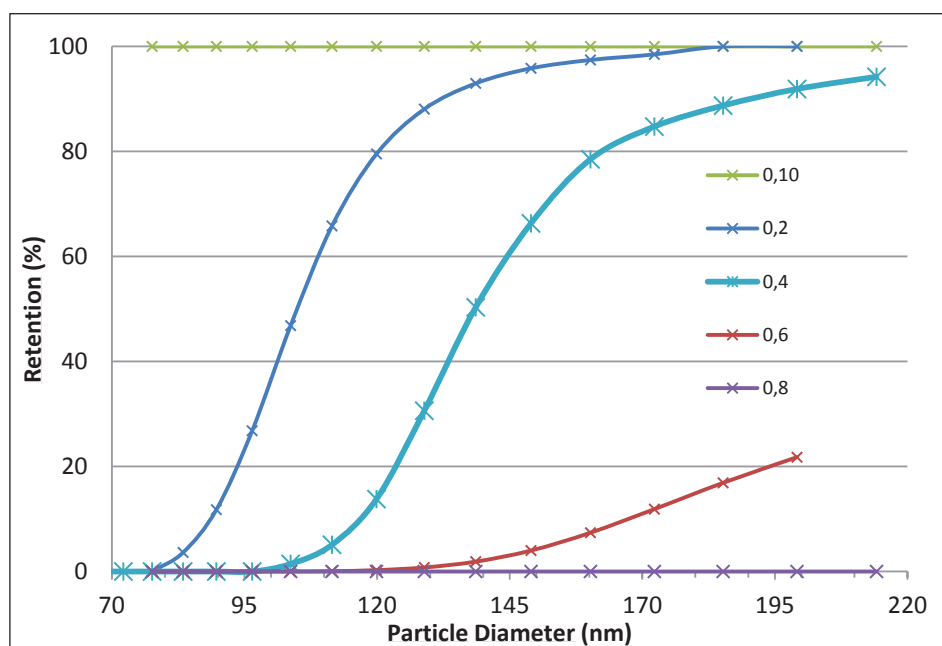
Figure – 3.17: The calculated retention values for poly(styrene) NPs at different pressures as a function of particle diameter.

At 0.1 bar, particles of all sizes were retained however at 0.8 bar all of them passed through. In between these two values, the retention of particles with higher diameter contributed principally to the observed global retention values at given pressure. Given the low porosity of the membrane only 6 % at 0.8 bar, it is remarkable though not surprising that nearly all the particles with such huge diameter were able to pass through the membrane without damaging it at all. At this point it can be concluded that due dynamic nature of the membrane, we were able to change the pore size with pressure to be able to translocate big nano-objects. To further prove this, top and bottom surface images of one such membrane was obtained by using Scanning Electron Microscopy (Figure – 3.18a,b,c), which showed the presence of NPs in significant amounts on both surfaces however no physical damage was observed to the membrane.

The reason for such non-damaging translocation can be explained by the self-healing nature of the membrane. At the onset of the translocation process, the particle is compressed against the surface of the membrane due to the water pressure. As more and more compression takes place, the particle tends to push itself more inside the membrane thus constraining the dynamic bridges between the micelles. Once these bridges are dislodged from one end, the particle enters inside and continues to be pushed further deep, dislodging the forward direction bridges. However behind the particle, the

dislodged bridges are again restored by the virtue of copolymer chains' mobility and micelles' compression thereby effectively closing the membrane. The healing scars (Figure – 3.18c) found on the back side of membrane having sizes approximate to that of translocated NPs reinforcing the above argument of self-healing.
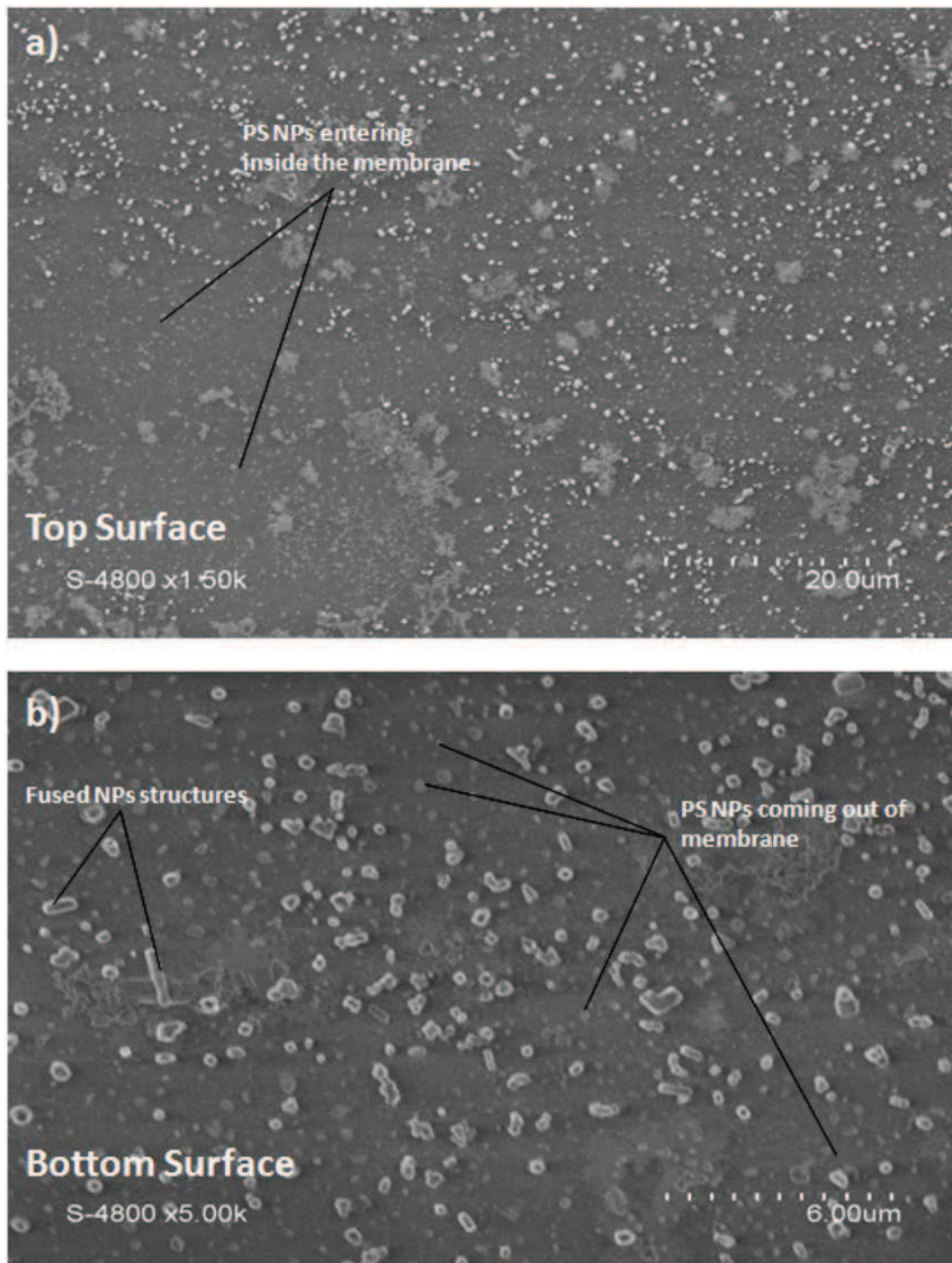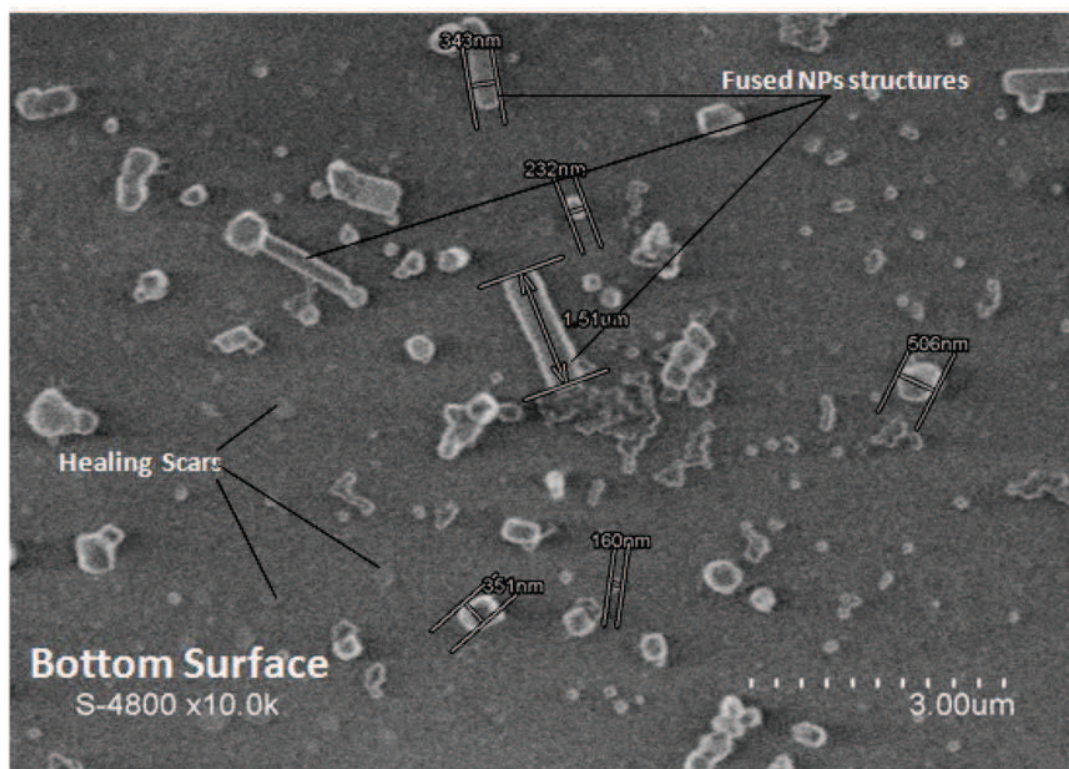
Figure – 3.18: Scanning Electron Microscopy images obtained of a membrane with translocated poly(styrene) NPs, a) Top surface, b) Bottom surface, c) Bottom surface showing the fused structures of NPs and the healing scars. The images are little distorted due to enlargement along width.

A variation to the healing event can be a situation where, this restoration of bridges is hindered by entrance of another particle into the perforation created by previous particle. This second particle can be followed by another and so on thus making a channel across the membrane thickness. Given the high compression encountered throughout the process, some of these particles can get fused together while still inside and leave the membrane in distorted shapes. Such fused structures were observed on the backside of the membrane used at 0.8 bar (Figure – 4.18b). The occurrence of such phenomenon within the membrane was proved by the presence of one such cylindrical structure having approximate length of be 1.51 µm which nearly corresponds to the thickness of the membrane.

Finally, the stiffest nano-objects represented by silica NPs were fed to the membrane and their translocation was found to be less when compared to Polystyrene NPs. For both series, the diffential distribution curves obtained for the retentates and permeates by PCCS showed the presence of nanoparticles however due to low concentration and aggregation due to surface charge in aqueous medium, it remains inconclusive to draw a general trend or conclusion. To have a general idea, the

curves for feed, retentate and permeate have been shown for two series fed to a membrane at 0.6 bar (Figure – 3.19).
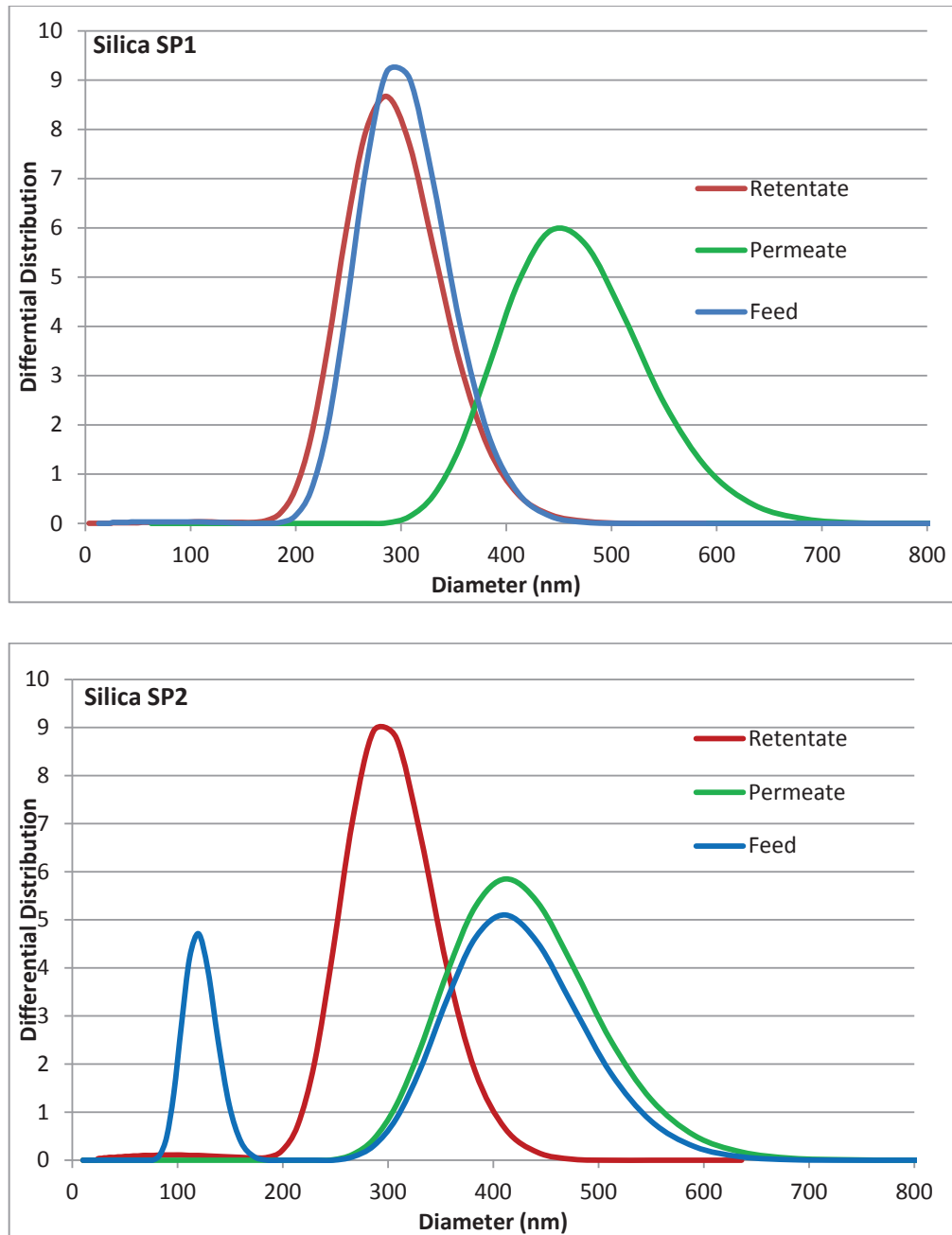
Figure – 3.19: Differential distribution curves obtained for silica nanoparticles (SP1 and SP2) in the feed, retentate and permeate of a membrane at 0.6 bar.

Since nothing conclusive could be drawn from the aforementioned curves, the global retention values were calculated from the concentrations which in turn obtained from the observed kcps values

(Figure – 3.20). A cursory look at the values shows that in case of SP1 represented by largest size NPs, the retentions values hovers between 86 % and 97 % indicating that most of the particles were either retained over the surface or possibly remain trapped within the membranes. In comparison, SP2 series NPs showed a visible decrease in retention values as the pressure increased however the decrease was less pronounced than that of polystyrene NPs. In case of SP2 series, the global retention of particles started from 90% at 0.2 bar and reached to a minimum retention of 62 % at 1 bar. These observed retention values might be the result of silica NPs of the second population having diameter lesser than 100 nm. It can be inferred from these observations that majority of silica NPs having diameter greater than 125 nm could not pass through the membrane. In case of polystyrene NPs, where 100 % permeation was observed at 1 bar, comparatively only 37.5 % silica NPs were able to pass through the membrane. Still, these findings need to verified since the distribution curve for the permeate shows only one population of particles having a much larger size distribution.
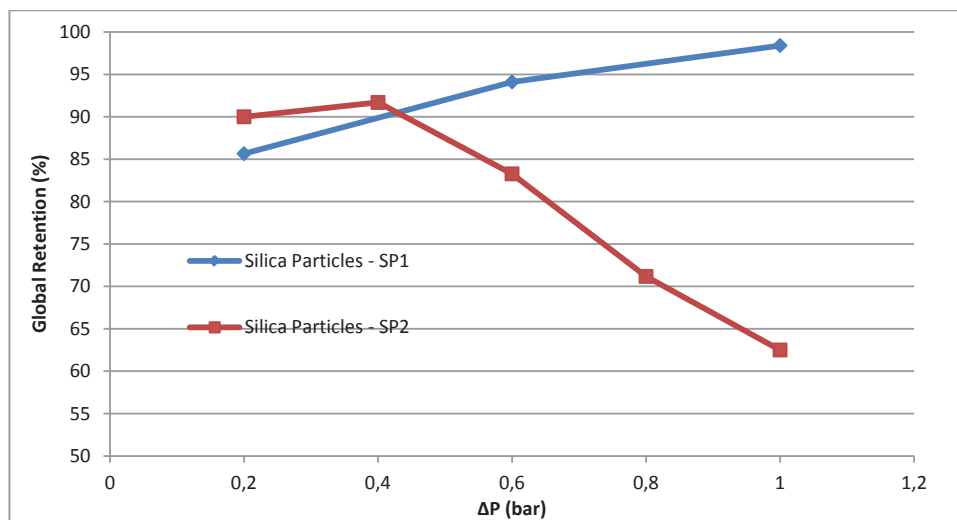
Figure – 3.20: Differential distribution curves obtained for silica nanoparticles (SP1 and SP2) in the feed, retentate and permeate of a membrane at 0.6 bar.

The Scanning Electron Microscopy images (Figure – 3.21) of the top and bottom surfaces of the membranes showed the nanoparticles entering and leaving the membranes for both series. Although unlike poly(styrene), the number of particles on the backside was markedly low.

The difference in global retention and aggregates formation can possibly be due to the presence of hydroxyl group over the surface of silica NPs which causes strong secondary interactions with PEO corona of the micelles as well as each other, leading to a retarded permeation thorough the membrane

and probable entrapment within the membrane. This gives enough time to these NPs to interact with each other to form small aggregates and leave in such form from the membrane.
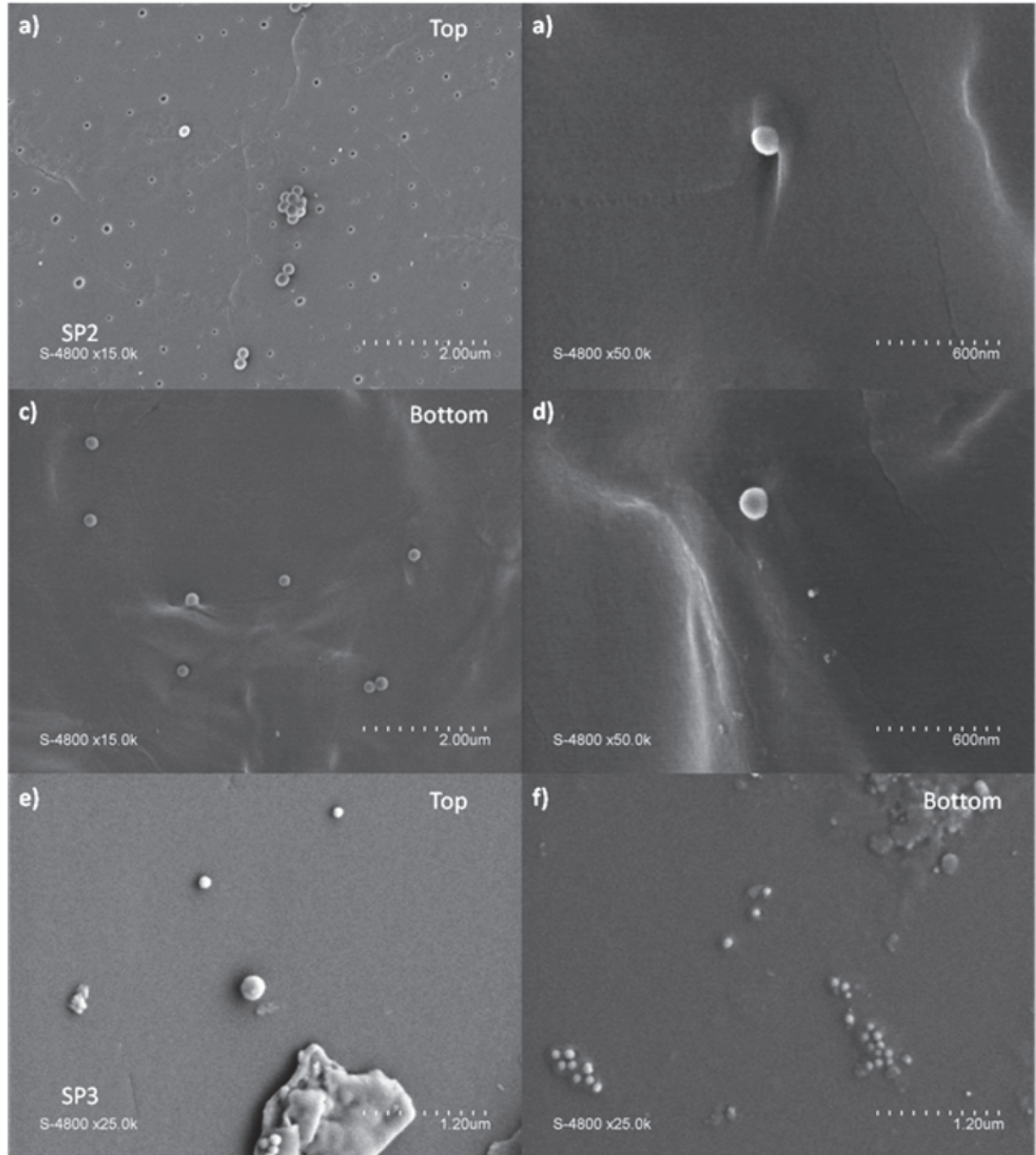
Figure – 3.21: Scanning Electron Microscopy images of translocated silica NPs, a-d) Top and bottom surface of membrane fed with SP1 series NPs. The unhealed perforations can be seen clearly on the surface which are absent on the back side, e-f) Top and bottom surface of membrane fed with SP2 series NPs. The aggregates of NPs alons with single NPs coming out can also be seen.

When compared to poly(styrene) NPs, the silica NPs are more stiffer and rigid in nature. Hence, when comparing the nanoparticles having same size of above two species, the poly(styrene) ones will pass through the membrane easily by easily undergoing deformation and thus lower retention. On the other hand, the silica ones can only form aggregates having much more irregular shapes thus further complicating their translocation and consequently giving a higher retention.

The perforations observed on the top surface of the membrane (Figure – 3.21a), does not mean that healing process has been hindered in case of a stiffer nano-object. When the size distribution of these perforations is compared with the size distribution of silica SP1 NPs, a significant difference can be seen (Figure – 3.22). The explanation of still opened pore can either be due to entrapment of silica NPs inside the membranes thus destabilizing the natural equilibrium of the micelles which would otherwise in usual case, force them to come back to their original position to heal the space created.
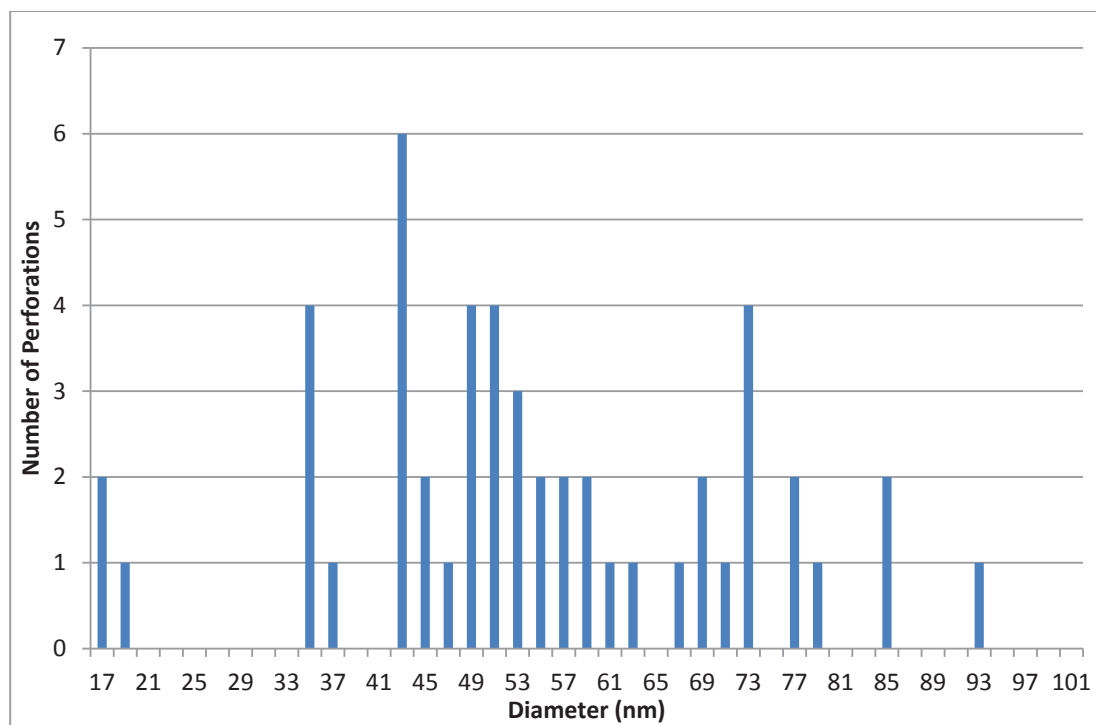
Figure – 3.22: Size distribution of perforations observed in the Scanning Electron Microscopy image of top surface of a membrane fed with silica SP1 NPs.

The transverse section SEM image of one such membrane fed with SP1 series NPs reveals a layer of agglomerated NPs within the membrane before they reached the end of the membrane (Figure – 3.23). Above this layer, other NPs can also be seen. The thickness of the membrane was found to be well

above that of normal value. This agglomeration of NPs within the membrane is perhaps responsible for negligible permeation observed SP1 series and also for the unhealed perforation observed on the top surface of the membrane.
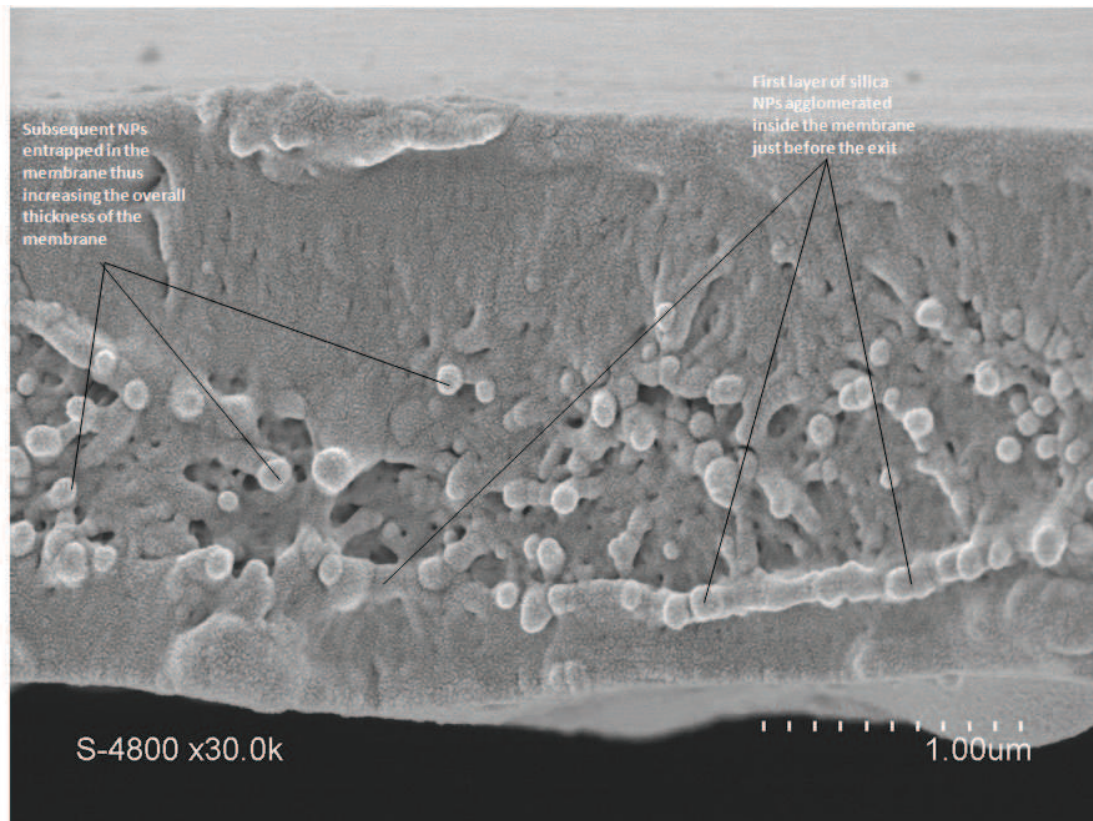
Figure – 3.23: Scanning Electron Microscopy images of transverse section of a membrane with entrapped silica NPs. The increased thickness can be observed easily due to the space occupied by the trapped NPs inside.

When a very high concentration of nanoparticles was used and the filtration time extended to 48 hours, an irreversible reorganization of the micelle assembly was observed, as revealed by the membrane autopsy (Figure – 3.24). It seems that at such high NP concentration, the pores remained open for an extended time and the continuous flow of solid silica NPs inside the pores induced an alignment of micelles along the direction of flow.
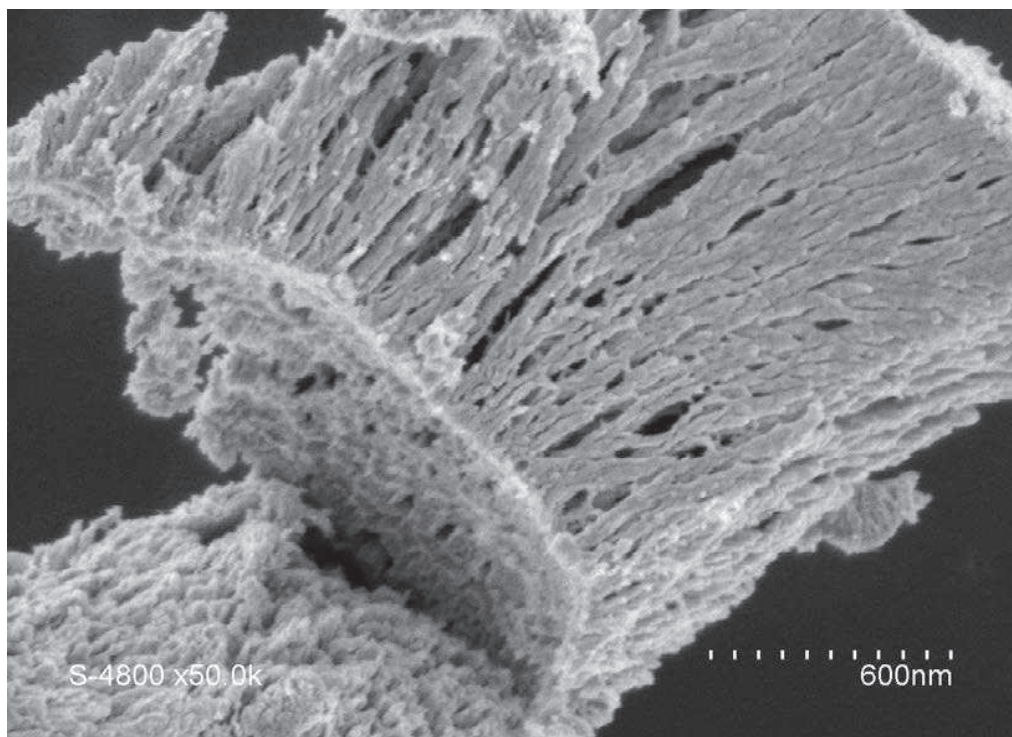
Figure – 3.24: Scanning Electron Microscopy image of a membrane with the aftereffects of high concentration of silica SP2 NPs.

3.4 CONCLUSION

In this work, we utilized the pressure sensitive variable porosity and self-healing ability of a synthetic membrane mimicking biological membranes to perform the translocation of four different types of nano-objects. Despite lowest hydyrodynamic size, PEG chains were able not to translocate the membrane due to their random coil conformations in solution form. The dynamic nature of the membrane enabled the direct penetration mode translocation of protein molecules, polystyrene & silica NPs having much larger diameters as compared to pore size flawlessly without damaging the membrane. However each nano-object showed different translocation characteristics. The BSA protein passed through easily at all pressures without any fouling of the membrane until very high concentration value, where due to cake formation made the membrane completely impermeable. In case of poly(styrene) NPs, the translocation was readily visible and strongly dependent upon the concentration of NPs and the applied pressure. As a perspective, translocation with bigger size NPs can also be carried out to obtain the maximum cut-off size. In case of silica NPs, the distribution curves from PCCS remained inconclusive regarding the population distribution however an approximation could be obtained from the kcps values

and SEM images. The translocation occurred in less pronounced fashion as compared to poly(styrene) but nevertheless certain number of NPs were able to pass through despite much bigger size. The strong interaction between the NPs and micelles of the membrane as well huge size of the former had a clear negative impact on the translocation as well as the healing process. The findings of this work are in contrast to the biological membranes whose structure is easily disrupted when nanoparticles diffuse through them due to formation of pores, which in some cases can even destroy the cells permanently. Using a novel non-biological system, we further showed experimentally that dimensions, shape of a nano-object, its interactions with the membrane and the external force govern its translocation across a membrane. These findings are in well accord with the simulation studies[12,20,47] done in the past involving lipid membranes and much smaller nano-particles.

REFERENCES

1   Metzler, R. & Klafter, J. When translocation dynamics becomes anomalous. *Biophysical Journal* **85**, 2776-2779, doi:10.1016/s0006-3495(03)74699-2 (2003).

2   Duncan, R. & Izzo, L. Dendrimer biocompatibility and toxicity. *Advanced Drug Delivery Reviews* **57**, 2215-2237, doi:10.1016/j.addr.2005.09.019 (2005).

3   Chavanpatil, M. D., Khdair, A. & Panyam, J. Surfactant-polymer nanoparticles: A novel platform for sustained and enhanced cellular delivery of water-soluble molecules. *Pharmaceutical Research* **24**, 803-810, doi:10.1007/s11095-006-9203-2 (2007).

4   Cao, Y. W. C., Jin, R. C. & Mirkin, C. A. Nanoparticles with Raman spectroscopic fingerprints for DNA and RNA detection. *Science* **297**, 1536-1540, doi:10.1126/science.297.5586.1536 (2002).

5   Elghanian, R., Storhoff, J. J., Mucic, R. C., Letsinger, R. L. & Mirkin, C. A. Selective colorimetric detection of polynucleotides based on the distance-dependent optical properties of gold nanoparticles. *Science* **277**, 1078-1081, doi:10.1126/science.277.5329.1078 (1997).

6   Jaiswal, J. K., Goldman, E. R., Mattoussi, H. & Simon, S. M. Use of quantum dots for live cell imaging. *Nature Methods* **1**, 73-78, doi:10.1038/nmeth1004-73 (2004).

7   Michalet, X. *et al.* Quantum dots for live cells, in vivo imaging, and diagnostics. *Science* **307**, 538-544, doi:10.1126/science.1104274 (2005).

8   Chen, X., Kis, A., Zettl, A. & Bertozzi, C. R. A cell nanoinjector based on carbon nanotubes. *Proceedings of the National Academy of Sciences of the United States of America* **104**, 8218-8222, doi:10.1073/pnas.0700567104 (2007).

9   Kam, N. W. S. & Dai, H. J. Carbon nanotubes as intracellular protein transporters: Generality and biological functionality. *Journal of the American Chemical Society* **127**, 6021-6026, doi:10.1021/ja050062v (2005).

10   Leroueil, P. R. *et al.* Nanoparticle interaction with biological membranes: Does nanotechnology present a janus face? *Accounts of Chemical Research* **40**, doi:10.1021/ar600012y (2007).

11   Roiter, Y. *et al.* Interaction of nanoparticles with lipid membrane. *Nano Letters* **8**, 941-944, doi:10.1021/nl0800801 (2008).

12   Yang, K. & Ma, Y. Q. Computer simulation of the translocation of nanoparticles with different shapes across a lipid bilayer. *Nature Nanotechnology* **5**, 579-583, doi:10.1038/nnano.2010.141 (2010).

13   Verma, A. *et al.* Surface-structure-regulated cell-membrane penetration by monolayer-protected nanoparticles. *Nature Materials* **7**, doi:10.1038/nmat2202 (2008).

14   Mukherjee, S., Ghosh, R. N. & Maxfield, F. R. Endocytosis. *Physiological Reviews* **77**, 759-803 (1997).

15   Kirchhausen, T. Three ways to make a vesicle. *Nature Reviews Molecular Cell Biology* **1**, 187-198, doi:10.1038/35043117 (2000).

16   Gao, H. J., Shi, W. D. & Freund, L. B. Mechanics of receptor-mediated endocytosis. *Proceedings of the National Academy of Sciences of the United States of America* **102**, 9469-9474, doi:10.1073/pnas.0503879102 (2005).

17   Smith, K. A., Jasnow, D. & Balazs, A. C. Designing synthetic vesicles that engulf nanoscopic particles. *Journal of Chemical Physics* **127**, doi:10.1063/1.2766953 (2007).

18   Lerner, D. M., Deutsch, J. M. & Oster, G. F. HOW DOES A VIRUS BUD. *Biophysical Journal* **65**, 73-79 (1993).

19   Zhang, S., Li, J., Lykotrafitis, G., Bao, G. & Suresh, S. Size-Dependent Endocytosis of Nanoparticles. *Advanced Materials* **21**, doi:10.1002/adma.200801393 (2009).

20   Ding, H.-m., Tian, W.-d. & Ma, Y.-q. Designing Nanoparticle Translocation through Membranes by Computer Simulations. *Acs Nano* **6**, 1230-1238, doi:10.1021/nn2038862 (2012).

21   Lee, H. & Larson, R. G. Multiscale Modeling of Dendrimers and Their Interactions with Bilayers and Polyelectrolytes. *Molecules* **14**, 423-438, doi:10.3390/molecules14010423 (2009).

22   Ting, C. L. & Wang, Z. G. Interactions of a Charged Nanoparticle with a Lipid Membrane: Implications for Gene Delivery. *Biophysical Journal* **100**, 1288-1297, doi:10.1016/j.bpj.2010.11.042 (2011).

23   Ginzburg, V. V. & Balijepailli, S. Modeling the thermodynamics of the interaction of nanoparticles with cell membranes. *Nano Letters* **7**, 3716-3722, doi:10.1021/nl072053l (2007).

24   Nel, A. E. *et al.* Understanding biophysicochemical interactions at the nano-bio interface. *Nature Materials* **8**, 543-557, doi:10.1038/nmat2442 (2009).

25   Tyagi, P. *et al.* Dynamic Interactive Membranes with Pressure-Driven Tunable Porosity and Self-Healing Ability. *Angewandte Chemie-International Edition* **51**, 7166-7170, doi:10.1002/anie.201201686 (2012).

26   Wright, A. K. & Thompson, M. R. Hydrodynamic structure of bovine serum-albumin determined by transient electric birefringence. *Biophysical Journal* **15**, 137-141 (1975).

27   Allen, T. & Khan, A. A. Critical evaluation of powder sampling procedures. *Chemical Engineer-London*, C108-& (1970).

28   Wang, X.-D. *et al.* Preparation of spherical silica particles by Stober process with high concentration of tetra-ethyl-orthosilicate. *Journal of Colloid and Interface Science* **341**, doi:10.1016/j.jcis.2009.09.018 (2010).

29   Kotsev, S. & Kolomeisky, A. B. Translocation of polymers with folded configurations across nanopores. *The Journal of chemical physics* **127**, doi:10.1063/1.2800008 (2007).

30   Muthukumar, M. Translocation of a confined polymer through a hole. *Physical Review Letters* **86**, 3188-3191, doi:10.1103/PhysRevLett.86.3188 (2001).

31   Slonkina, E. & Kolomeisky, A. B. Polymer translocation through a long nanopore. *Journal of Chemical Physics* **118**, doi:10.1063/1.1560932 (2003).

32   Palecek, S. P. & Zydney, A. L. Intermolecular electrostatic interactions and their effect on flux and protein deposition during protein filtration. *Biotechnology Progress* **10**, 207-213, doi:10.1021/bp00026a010 (1994).

33   Ho, C. C. & Zydney, A. L. Effect of membrane morphology on the initial rate of protein fouling during microfiltration. *Journal of Membrane Science* **155**, 261-275, doi:10.1016/s0376-7388(98)00324-x (1999).

34   Ho, C. C. & Zydney, A. L. A combined pore blockage and cake filtration model for protein fouling during microfiltration. *Journal of Colloid and Interface Science* **232**, 389-399, doi:10.1006/jcis.2000.7231 (2000).

35   Huisman, I. H., Pradanos, P. & Hernandez, A. The effect of protein-protein and protein-membrane interactions on membrane fouling in ultrafiltration. *Journal of Membrane Science* **179**, 79-90, doi:10.1016/s0376-7388(00)00501-9 (2000).

36   Wang, P., Tan, K. L., Kang, E. T. & Neoh, K. G. Plasma-induced immobilization of poly(ethylene glycol) onto poly(vinylidene fluoride) microporous membrane. *Journal of Membrane Science* **195**, 103-114, doi:10.1016/s0376-7388(01)00548-8 (2002).

37   Ostuni, E., Chapman, R. G., Holmlin, R. E., Takayama, S. & Whitesides, G. M. A survey of structure-property relationships of surfaces that resist the adsorption of protein. *Langmuir* **17**, 5605-5620, doi:10.1021/la010384m (2001).

38   Pasche, S., Voros, J., Griesser, H. J., Spencer, N. D. & Textor, M. Effects of ionic strength and surface charge on protein adsorption at PEGylated surfaces. *Journal of Physical Chemistry B* **109**, 17545-17552, doi:10.1021/jp050431+ (2005).

39   Rixman, M. A., Dean, D. & Ortiz, C. Nanoscale intermolecular interactions between human serum albumin and low grafting density surfaces of poly(ethylene oxide). *Langmuir* **19**, 9357-9372, doi:10.1021/la0340571 (2003).

40   Jacobs, R. E. & White, S. H. Behavior of hexane dissolved in dioleoylphosphatidylcholine bilayers - an nmr and calorimetric study. *Journal of the American Chemical Society* **106**, 6909-6912, doi:10.1021/ja00335a006 (1984).

41   Mulders, F., Vanlangen, H., Vanginkel, G. & Levine, Y. K. The static and dynamic behavior of fluorescent-probe molecules in lipid bilayers. *Biochimica Et Biophysica Acta* **859**, 209-218, doi:10.1016/0005-2736(86)90216-6 (1986).

42   Adler, M. & Tritton, T. R. Fluorescence depolarization measurements on oriented membranes. *Biophysical Journal* **53**, 989-1005 (1988).

43   McIntosh, T. J., Simon, S. A. & Macdonald, R. C. The organization of normal-alkanes in lipid bilayers. *Biochimica Et Biophysica Acta* **597**, 445-463, doi:10.1016/0005-2736(80)90219-9 (1980).

44   Salafsky, J. S. & Eisenthal, K. B. Second harmonic spectroscopy: detection and orientation of molecules at a biomembrane interface. *Chemical Physics Letters* **319**, 435-439, doi:10.1016/s0009-2614(00)00116-0 (2000).

45   Xiang, T. X. & Anderson, B. D. Liposomal drug transport: A molecular perspective from molecular dynamics simulations in lipid bilayers. *Advanced Drug Delivery Reviews* **58**, 1357-1378, doi:10.1016/j.addr.2006.09.002 (2006).

46   Bemporad, D., Luttmann, C. & Essex, J. W. Behaviour of small solutes and large drugs in a lipid bilayer from computer simulations. *Biochimica Et Biophysica Acta-Biomembranes* **1718**, 1-21, doi:10.1016/j.bbamem.2005.07.009 (2005).

47   Fiedler, S. L. & Violi, A. Simulation of Nanoparticle Permeation through a Lipid Membrane. *Biophysical Journal* **99**, 144-152, doi:10.1016/j.bpj.2010.03.039 (2010).

4.   BLOCK COPOLYMER MICELLES' ZIPPER ASSEMBLY

Coatings obtained from traditional methods like grafting of polymers[1], electrodeposition[2], or atomic layer deposition[3] are permanent in nature which prevent any further self-adjustment of the structure or surface properties. In contrast, a responsive coating can optimize dynamically the surface state of materials with respect to their environment. For example, polyelectrolyte multilayers display a reversible nanoporosity *via* a pH-induced swelling transition[4], whereas a polyelectrolyte-based sacrificial coating can be used in a controlled manner to ensure a continuous regeneration of the surface state[5]. However, their preparation employs an industrially fastidious and time consuming multistep strategy. Inspired by natural systems, synthetic materials having reversible connections between their constituting objects (molecules, macromolecules, dendrimers, particles…) demonstrate a certain dynamism leading to potential new applications[6]. The preparation of such materials is usually based on a self-assembly strategy with a bottom-up approach where small building blocks are assembled into larger edifices with a sharp control over local and global architecture[7]. Self-sorting constitution can be observed from complex systems following "natural" selection rules[8], but the need to target the final material properties is generally reached by designing the assembly stage with a predictable strategy[9].

The so called "Zipper effect" has been observed in several natural systems at all scales with an exceptional ability to form reversible assembly through a controlled zipping-unzipping process. For example, many transcription factors are known to contain leucine zippers[10,11]. In this case, the structure of the proteins contain a series of leucines every seven residues. This specific spacing enables the leucine moieties to be lined up on one side of an α-helix and to interact with a second analogous protein fragment *via* hydrophobic bonds. Molecular zippers have been used alone like in the preparation of DNA zippers and tweezers[12], reversibly opening organic tubes[13], one dimensional molecular assemblies[14], or in combination with layer-by-layer techniques or chemical reactions[15,16]. In polymer science, zipping has also been reported for example in molecularly imprinted polymers to control the access to the recognition pocket[17], to drive a crystallization process[18,19], or to prepare ultra-dense polymer brushes[20]. Zipper-assembly can be considered as a variant in the "self-assembly" family that combines (macro) molecular interactions and architectural cooperation[21].

In this chapter, preparation of 3D reversible zipper assembly of micelles based on a diblock copolymer poly(methyl methacrylate)-b-poly(n-octadecyl methacrylate) (PMMA-b-PODMA) has been discussed. The crystallization of pendant n-octadecyl chains along the PODMA backbone has been studied in the past, for example to prepare molecular brushes[22] or to study the dynamics of block copolymers under confinement[23]. The stark resemblance between the crystallization mechanism of PODMA chains and the interdigitated layers observed with molecular zippers prompted us to examine the possibility of using PODMA as a macromolecular zipper to achieve a controllable reversible assembly of block copolymer micelles.

4.1 THE COPOLYMER

The aforementioned copolymer was synthesized using the "Reverse Addition-Fragmentation Transfer" (RAFT) polymerization[24,25], a technique well established in order to achieve controlled radical polymerization for near monodisperse polymer chains.

In first stage, one of the monomers "n-octadecyl methacrylate" was first synthesized. Although this monomer is available commercially, the presence of 35 % cetyl methacrylate as impurity makes it unsuitable in the preparation of the copolymer. Therefore, the monomer was synthesized in the lab by reacting 1-octanol and methyacrylolyl chloride in dried THF (Figure – 4.1). Since the reaction between an acid chloride and alcohol produces acid molecules as leaving groups therefore it is important to capture these liberated molecules to minimize the side reactions. To prevent this, generally a tertiary amine like Triethylamine (TEA) is employed which neutralize acid molecules to form ammonium salt. This salt being insoluble in the organic solvent can be easily removed by simple filtration thus simplifying the purification process.
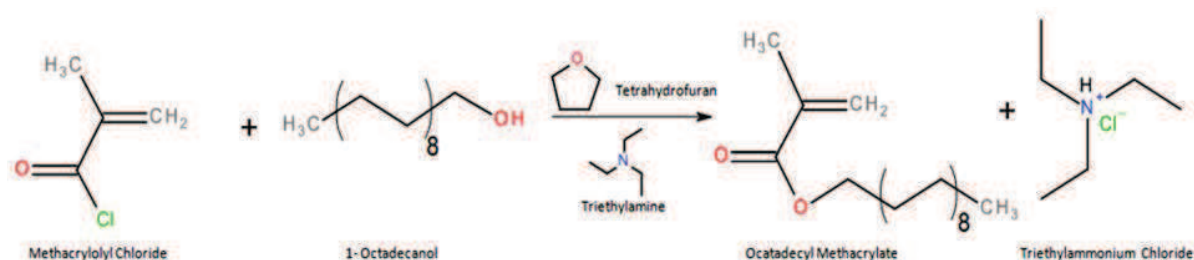
Figure – 4.1: General reaction for the synthesis of Octadecyl Methacrylate

The reaction between and acyl chloride and an alcohol is exothermic in nature hence maintaining the temperature of the reaction to very low value is important during the addition of

chloride. For low molecular weight alcohols, an ice bath can be used conveniently to bring the reaction temperature near 0°C however in case of 1-octanol; such low temperature causes it to crystallize out from THF solution which affects the reaction efficiency. Therefore, this particular reaction was carried out at relatively higher temperature of 20°C. After 24 hours of reaction followed by filtration, evaporation and crystallization in hexane, a pale white colored solid was obtained with a yield of 65 %. The structure of the monomer was verified using ^{1}HNMR (Figure – 4.2) spectrum. The relative proton shift observed for two protons attached to the carbon immediate to oxygen atom in 1-octanol (δ_{CH2-O} = 3.5 ppm) to (δ_{CH2-O} = 4.3 ppm) octadecyl methacrylate proved the successful condensation of methacrylolyl chloride with the alcohol.
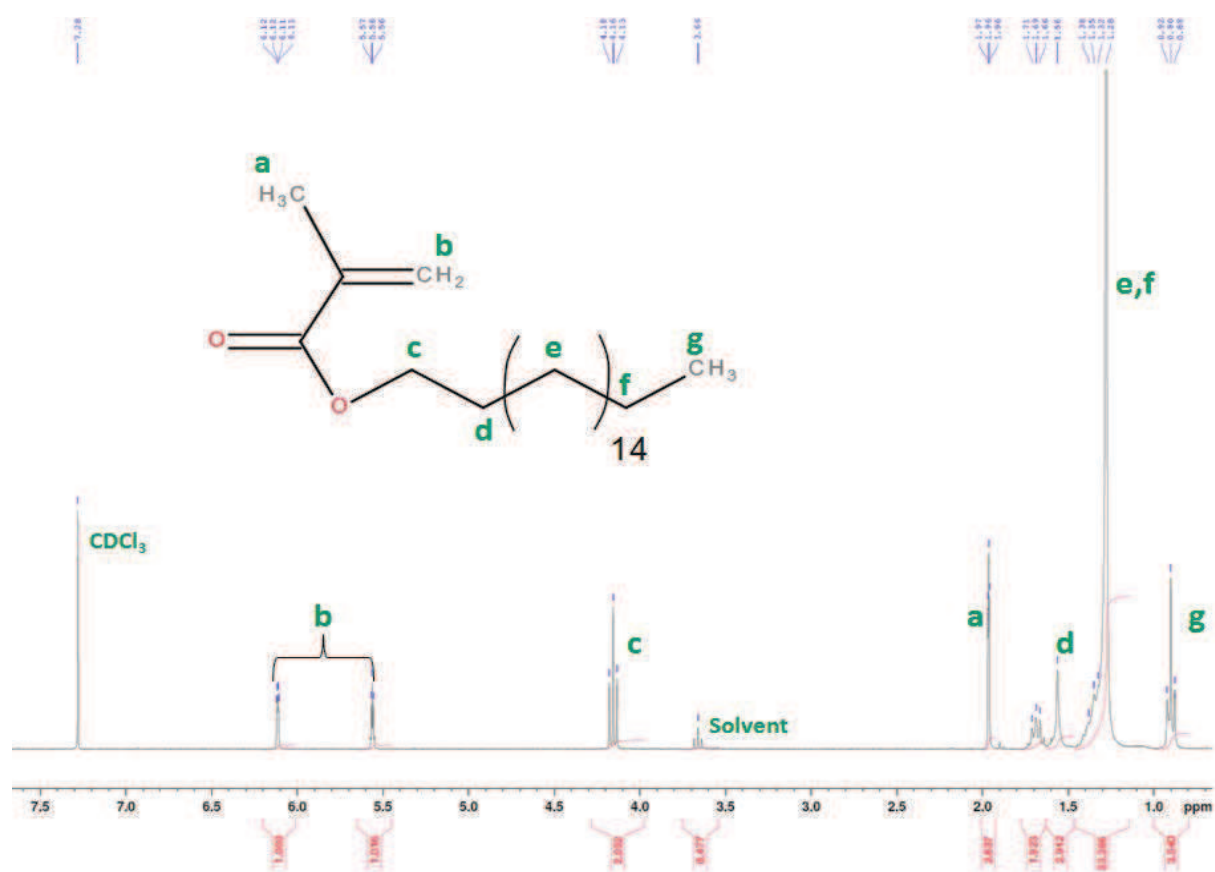
Figure – 4.2: ^{1}HNMR of Octadecyl Methacrylate

In the second stage, methyl methacrylate (MMA) was polymerized using RAFT polymerization technique. This technique offers an effective route for controlled radical polymerization due to its applicability to varied monomers, good control over molecular weight, narrow polydispersity[25]. With a careful selection of the transfer agent having an optimum transfer constant (C_{tr}), it is even possible to

obtain complex macromolecular architectures[26,27] without much hassle. The key component of this technique is the transfer agent, specifically termed as RAFT agent which is usually a thiocarbonylthio compound (Figure – 4.3). The nature of groups "Z" and "R" in a RAFT agent are governed by the type of monomer to be polymerized, polymerization conditions and the desired functionalities of the final product.
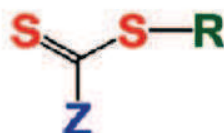
Figure – 4.3: General chemical structure of thiocarbonylthio compound

In general, the nature of Z group primarily affects the stability of the S=C bond and the stability of the $P_n – S – C\bullet$ (Z) $– S – P_m$ radical adduct, thus indirectly affecting the position of and rates of the elementary reactions in the initiation step and the overall main-equilibrium reactions (Figure – 5.4).

Initialization:
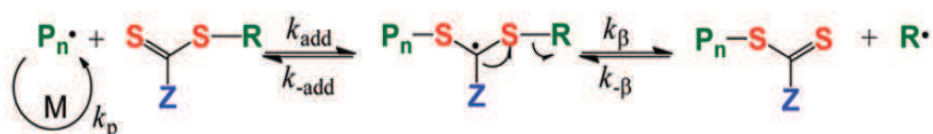
Reinitiation:
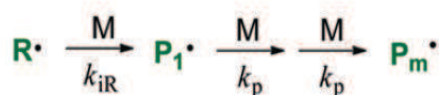
Main equilibrium:
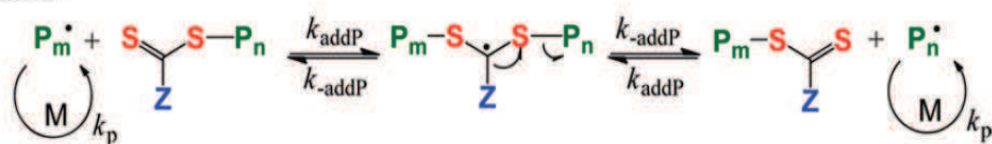
Figure – 4.4: The main-equilibrium reactions of Reversible Addition Fragmentation Transfer Polymerization

A Z group bearing electron withdrawing component in it, is the preferred choice for improved transfer constant but this can also have implications for side reactions[28]. Meanwhile, the R group must be a good hemolytic leaving group in comparison to $P_n\bullet$ so as to favor the right hand side of the initiation

step, but reactive enough to reinitiate a new polymer chain[28]. The sensitivity of these two groups towards the monomer and the temperature to be employed for the polymerization further affects the proper selection[29].
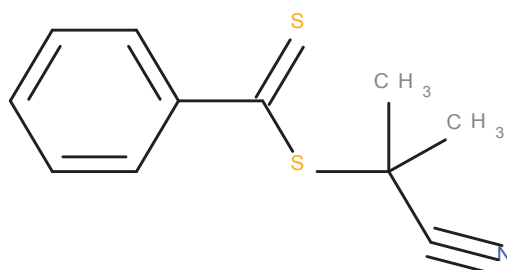
Figure – 4.5: Chemical structure of 2-Cyano-2-propyl benzodithioate

In the present case, a dithioester was employed for the polymerization of MMA as a RAFT agent. This dithioester; 2-Cyano-2-propyl benzodithioate (Figure – 4.5) is an efficient transfer agent for the polymerization of MMA with well established kinetics[29].
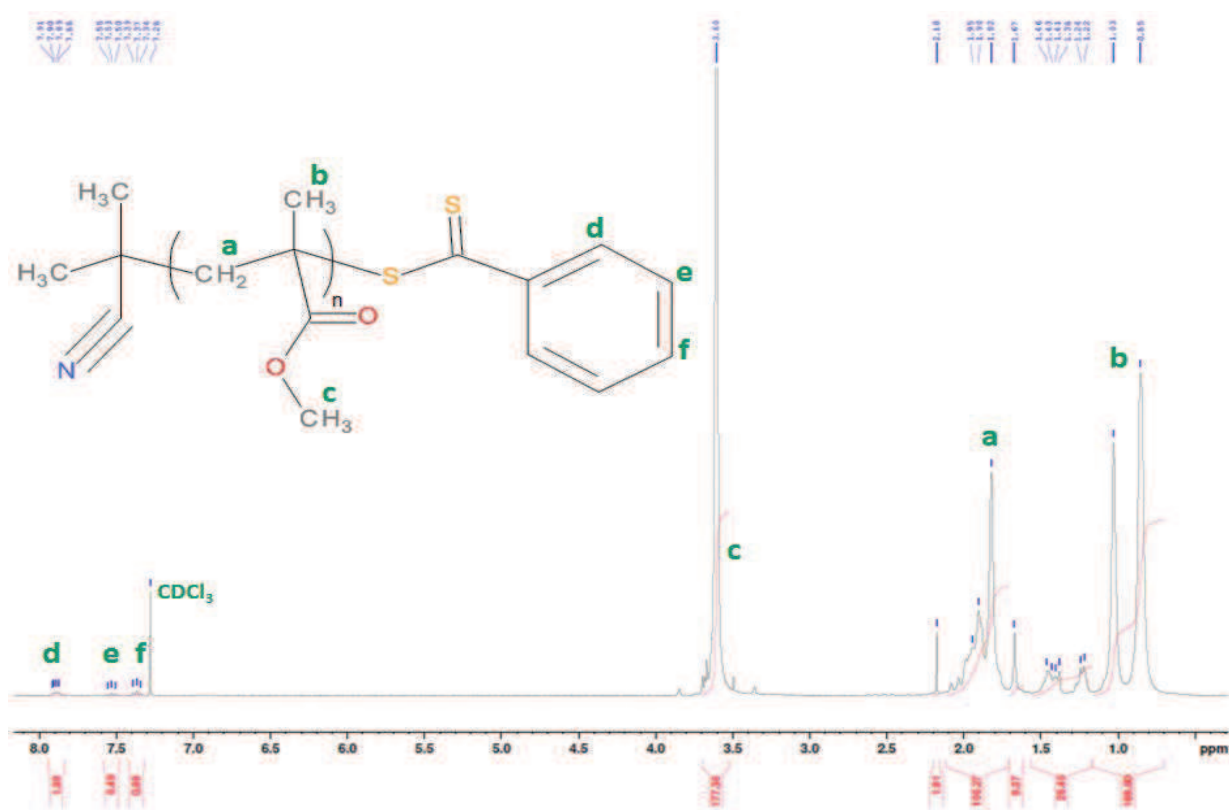
Figure – 4.6: ^{1}HNMR of Poly(methyl methacrylate) prepared via RAFT polymerization

The polymerization was conducted at 70°C in dried toluene for a degree of polymerization (DP) value of 60 to obtain a PMMA macroinitiator with a molecular weight of 7700 g/mol, verified by ^{1}HNMR (Figure – 4.6) and PDI value of 1.15, calculated using size exclusion chromatography analysis. This pale red color PMMA would serve as the RAFT macroinitiator for the polymerization of the octadecyl methyacrylate monomer, synthesized in the first stage.

The copolymerization of octadecyl methacrylate was conducted at 80°C with PMMA RAFT macroinitiator in toluene, for various degree of polymerization (DP) values. The values of Ln([Mo]/[M]) obtained for different DPs reveal a linear dependence (Figure – 4.7) over the time signifying a controlled copolymerization persisted throughout the reaction time. It also means that the number of propagating species remained almost constant during the polymerization duration.
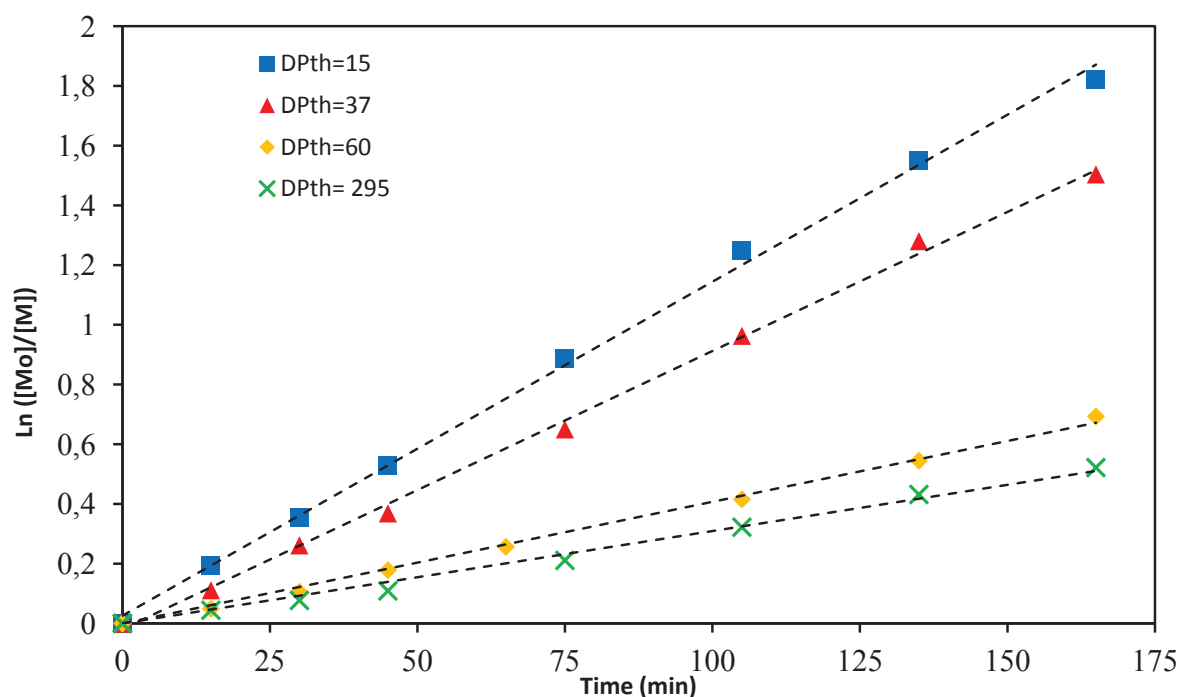
Figure – 4.7: Variation of Ln([M$_{o}$]/[M]) as a function of time for different degree of polymerization values

The evolution of molecular weights also showed a linear evolution with respect to % conversion (Figure – 4.8). As it can be seen, a very high molecular weight was obtained for a given conversion value for DP = 295. As the DP value decreases, a significant decrease is observed in the increase of molecular weight. A higher DP (for example: 295) signifies higher amount of the monomer concentration thus more monomer molecules are available to further react with the propagating chains.
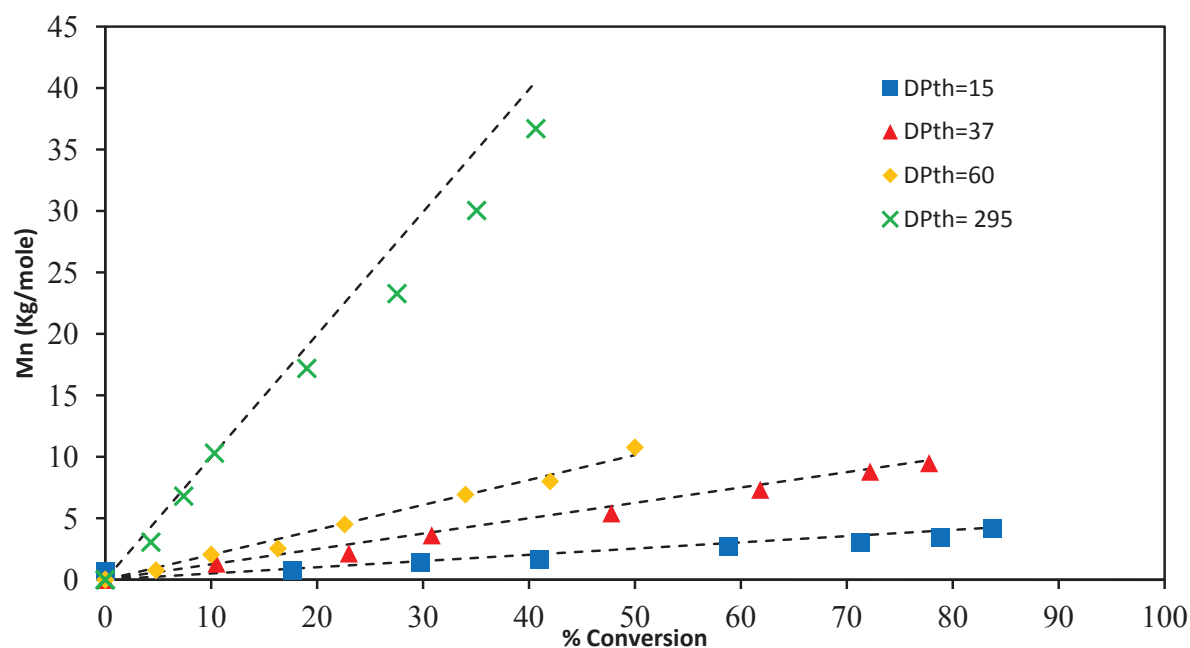
Figure – 4.8: Evolution of molecular weight with % conversion for different degree of polymerization values
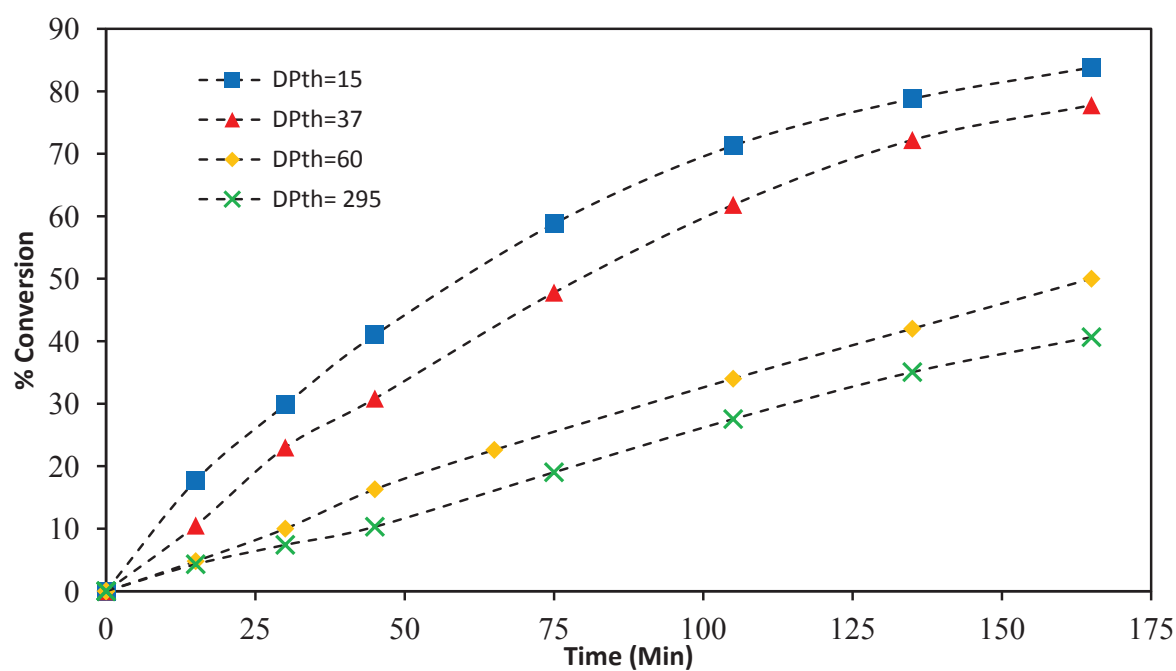
Figure – 4.9: Evolution of % conversion with time for different theoretical degree of polymerization values

A cursory look at the evolution of % conversion with respect to copolymerization time (Figure – 4.9) shows a linear dependence in case of DP = 60 and DP = 295. However, a lower DPs, the conversion follows 2nd degree polynomial tendency. This difference stems from the fact that as copolymerization

proceeds, lesser monomer is available for further reaction. This decreases the overall rate of copolymerization and is more pronounced in case of DP = 15 in comparison to DP = 37.
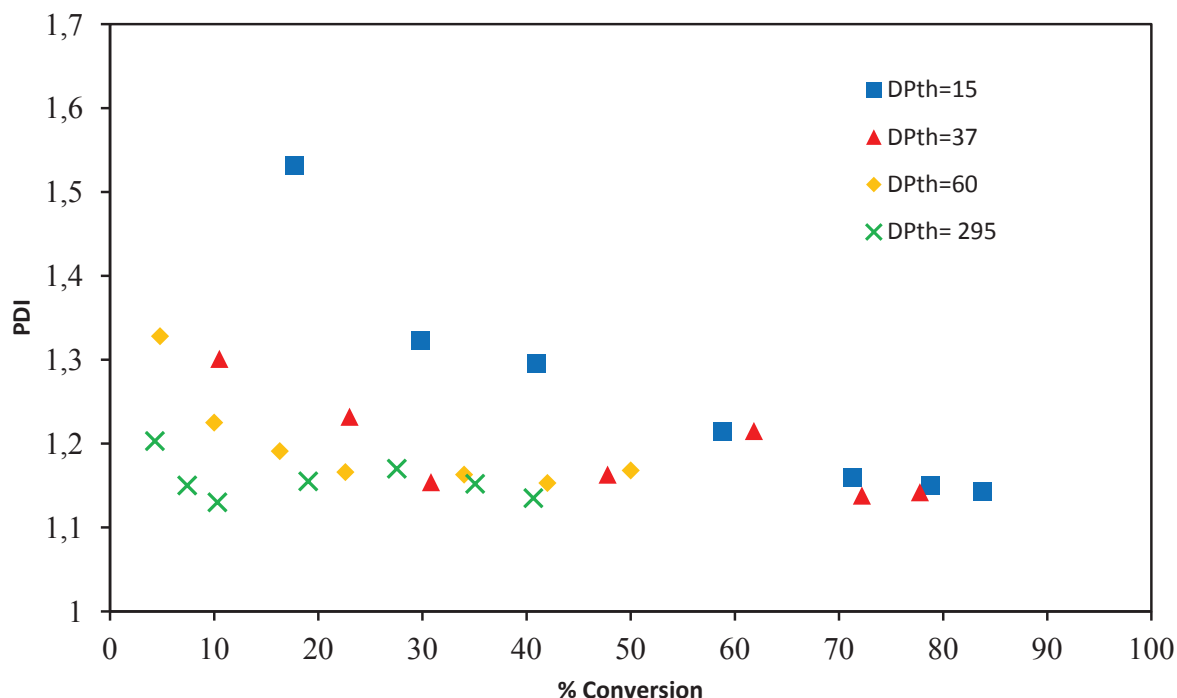
Figure – 4.10: Variation of polydispersity index with respect to % conversion for different degree of polymerization values

Lastly, the polydispersity index (PDI) of the obtained copolymer revealed that higher DP values resulted in lowest PDI with DP = 295 showing between 1.21 – 1.15 (Figure – 4.10). In general, a PDI close to 1.15 was achieved with higher % conversion for all DP values.
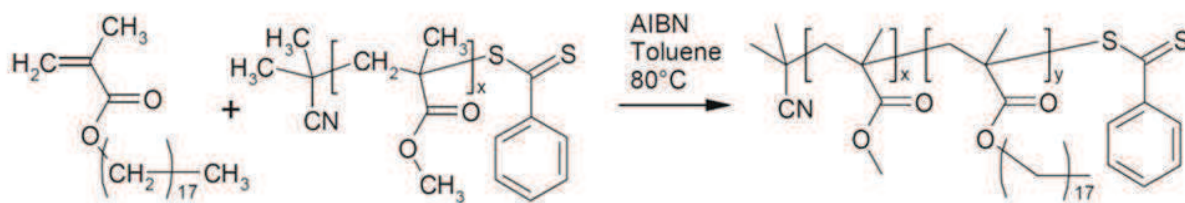
Figure – 4.11: General reaction for the polymerization of octadecyl methacrylate with PMMA macroinitiator

Finally, the copolymer (PMMA – b – PODMA) was synthesized (Figure – 4.11) with an optimum theoretical DP =100 at 80°C for a reaction time of 150 minutes to obtain a molecular weight M_n,PODMA =13500 g/mol (^{1}HNMR); M_n,PODMA – b – PMMA =21200 g/mol (^{1}HNMR) (Figure – 4.12) and a PDI value of 1.12 as determined by size exclusion chromatography.
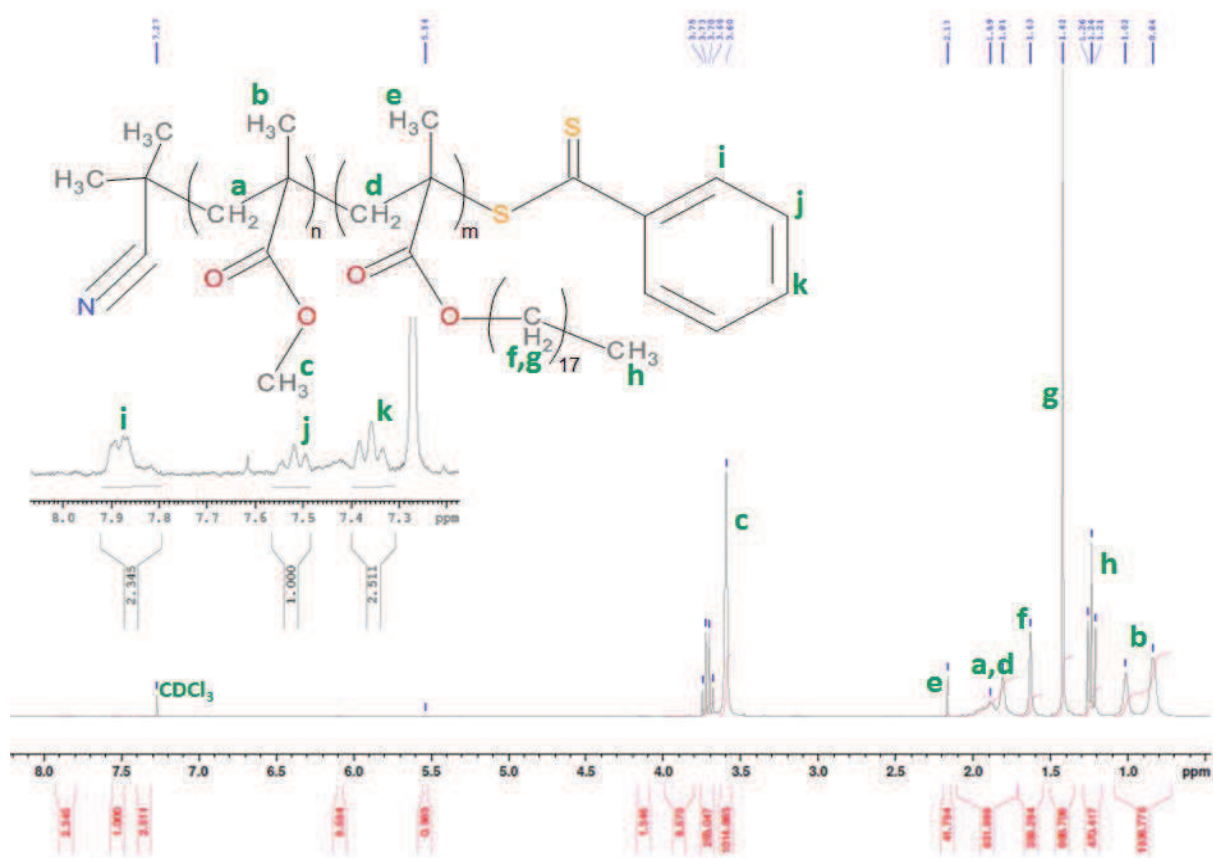
Figure – 4.12: ¹HNMR of Poly(methyl methacrylate)-b-Poly(octadecyl methacrylate)

4.2 MICELLES PREPARATION AND THEIR SELF-ASSEMBLY

The classification of block copolymer micelles can be done on the basis of the type of intermolecular forces segregating the core segment from the aqueous milieu. The first category is represented by amphiphilic micelles (hydrophobic interactions), second by polyion complex micelles (electrostatic interactions) and third represented by micelles emanating from metal complexation[30]. Generally, when the hydrophilic segment exceeds the core block in length, resulting micelle is spherical in shape. By increasing the length of the core segment beyond that of the corona-forming chains, one may generate various non-spherical structures including rods and lamellae[31]. In the present case, the copolymer contains 65 % PODMA which is much more hydrophobic than 35 % PMMA block. To obtain spherical micelles from the copolymer, it was first dissolved in THF followed by slow addition of cyclohexane which is a good solvent for PODMA but a poor one for PMMA. As the concentration of cyclohexane increases more and more, the PMMA part is forced into forming the core while PODMA block forms the corona. For a mixture of cyclohexane and THF (9/1; vol%) and concentration of (3.5

mg/ml), the micelles' hydrodynamic diameter was found to be 35 nm at 25°C (Figure – 4.13) as determined using Photon Cross Correlation Spectroscopy (PCCS).
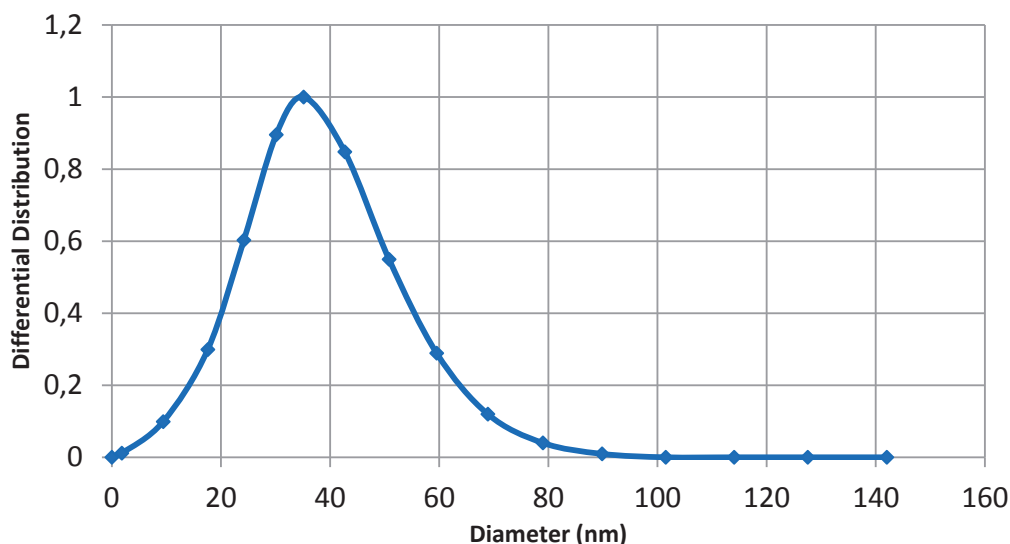
Figure – 4.13: Hydrodynamic diameter of PMMA-b-PODMA copolymer micelles as determined by PCCS

For the assembly of micelles, first a film of PMMA, made from uncontrolled free radical polymerization, was coated onto a thoroughly cleaned Silicon wafer using spin coating. The wafer was then partially dipped into the micellar solution of PMMA-*b*-PODMA for 1 hour, after which the coated wafer was thoroughly rinsed with fresh cyclohexane to remove the physically adsorbed micelles. Once dry, the wafer with two different surface characteristics was characterized by Atomic Force Microscopy (AFM) and contact angle measurement (CA).

A compact assembly of micelles with an average micelle diameter of 15 nm was observed with no long-range ordering on the immersed part of the wafer (Figure – 4.14 a,c). When examining the Z height at both extremity of the blue line drawn in the figure, a difference of about 13 nm was found which is in agreement with a single micelle monolayer height (Figure – 4.14b). The peak observed at the transition corresponds to a "pyramid" of 3 micelle layers. A possible reason for this can be attributed to the slight evaporation of the solvent over the experiment time, creating a flux of micelles at the solvent meniscus thus increasing their local concentration.
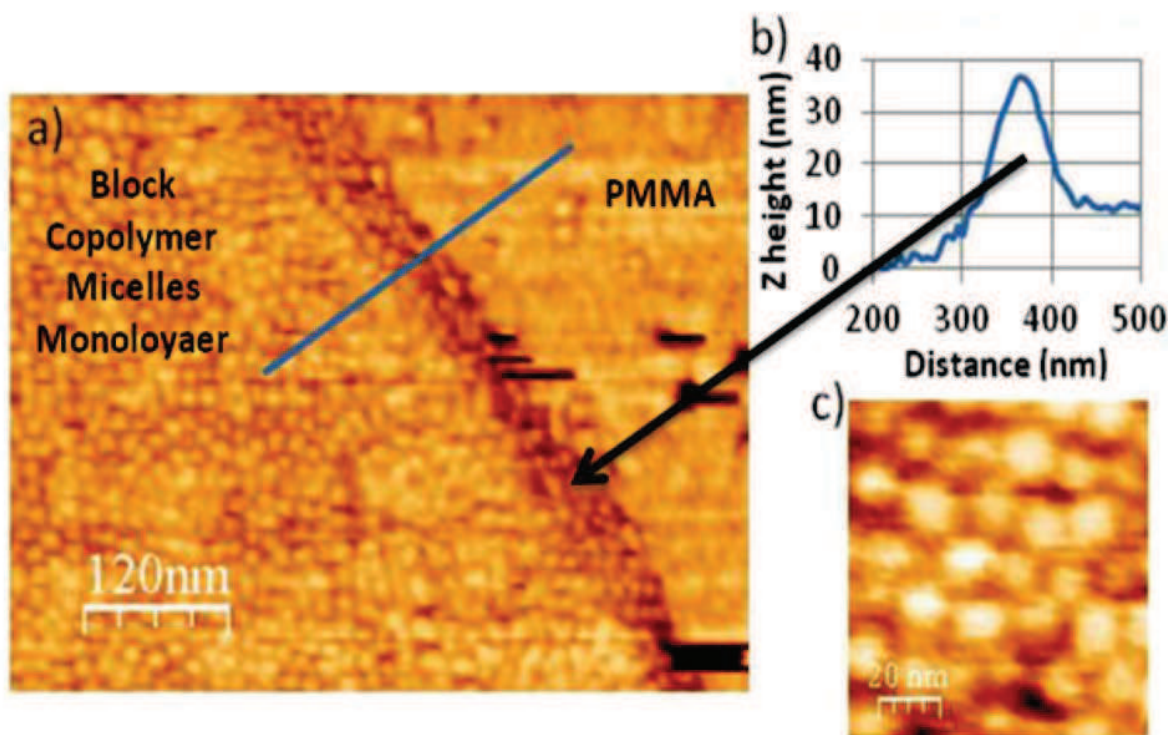
Figure – 4.14: Atomic Force Microscopy images of PMMA-b-PODMA coating over PMMA substrate; a) The blue line indicates the direction of change in the surface modification, b) Variation of height along the blue line from right to left in first image, c) Higher resolution image of the copolymer micelles' assembly

The contact angle measurements gave a value of 75±2° for the virgin PMMA film however after functionalization with a micelle monolayer, the contact angle increased to a value of 88±2° which is in agreement with the change in the surface properties marked by higher hydrophobicity. Based on these results it can be suggested that when dipped in the micellar solution, the PMMA substrate offers an interface which will be covered by block copolymer unimers. The THF present in the solvent mixture is induces a superficial swelling of the PMMA film coated onto the silicon wafer. Consequently, the PMMA block from the copolymer penetrate the film surface and thus acting as anchor for the block copolymer chain once the interface has dried. This leaves only the PODMA block emanating from the surface which is responsible for higher hydrophobicity of the surface (Figure – 4.15). The newly formed block copolymer interface is now available to welcome the micelles through a zipper-assembly with *n*-octadecyl chains from the micelles and the surface interweaving themselves.
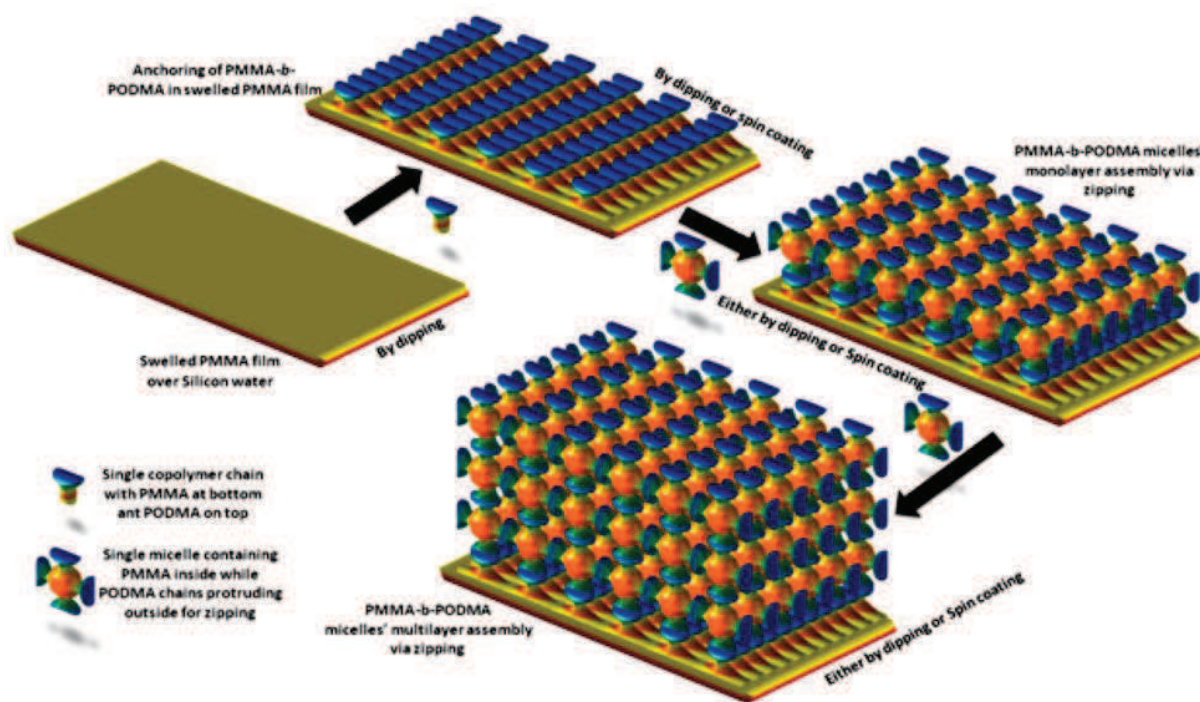
Figure – 4.15: The monolayer and multilayer assembly of PMMA-b-PODMA micelles over PMMA coated silicon substrate. While the anchoring of copolymer chains takes place via the diffusion of PMMA block in the swelled PMMA film matrix, the subsequent zipping process occurs via the interlocking of long pendant chains of PODMA block.

The assembly is further reinforced by inter-micelle zipping along lateral direction, as attested by the observed compact assembly in AFM images. The complete coverage of the PMMA surface is probably due to a continuous reorganization at the interface through an optimization of the PODMA chain interactions. When the immersion route was replaced by spin-coating technique, no anchorage could be promoted with the non-swollen PMMA substrate due to the fast evaporation of the solvent mixture. Hence, the physically adsorbed micelle layers got rinsed off easily when washed with the fresh cyclohexane leaving the PMMA film intact, as observed by AFM and further confirmed with the contact angle value (76±3°).

However, multilayers of micelles were achieved by swelling the PMMA coated silicon wafer into cyclohexane/THF (9/1 vol. %) for 15 min prior to the spin-coating of micellar solution. The contact angle of the coated surface after rinsing was found to be 89±3° and the AFM image obtained showed clear uniform assembly of micelles (Figure – 4.16a). A homogeneous multilayer coating with a thickness of

about 570 nm (~44 layers) and compact micellar morphology was obtained using this strategy (Figure – 4.16b,c).
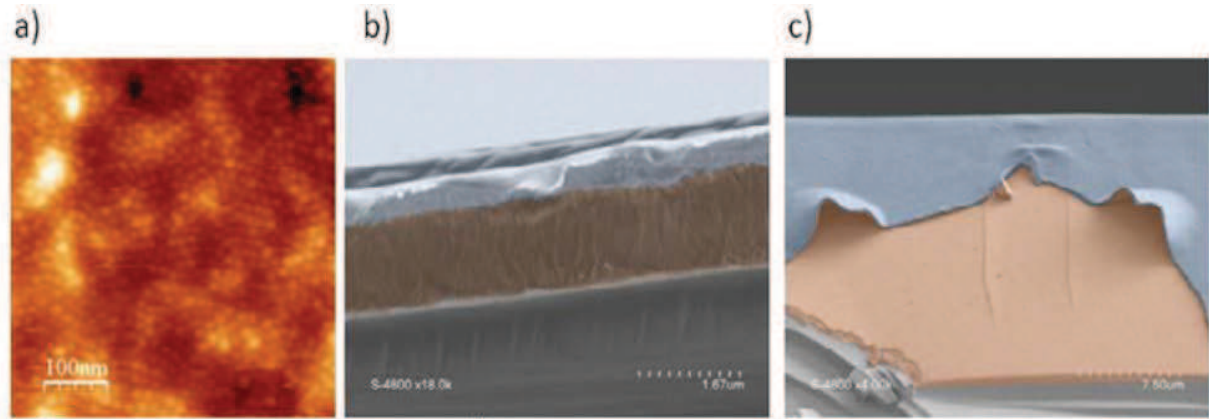
Figure – 4.16: a) Atomic Force Microscopy image of the spin coated multilayer assembly of PMMA-b-PODMA micelles over PMMA film, b)&C) Scanning Electron Microscopy images of the PMMA film (pink color) covered with PMMA-b-PODMA zipper assembly achieved via spin coating.
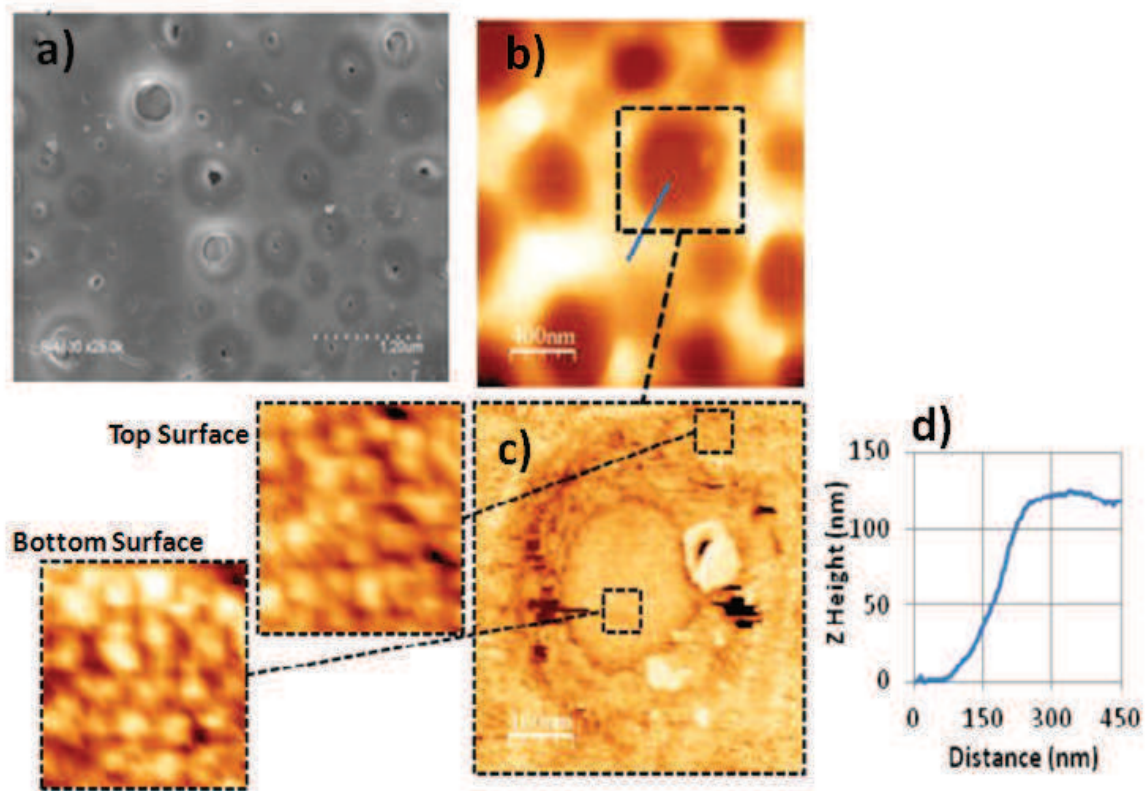
Figure – 4.17: a) Scanning Electron Microscopy images of zipper assembly containing pores, b) Atomic Force Microscopy image of the surface, c) Atomic Force Microscopy image of one such pore (like a crater) having bottom

monolayer of micelles and topmost layer formed via multilayered zipping (the higher resolution image on the left side shows the similarity of micelles in diameter), d) The height variation along the radius of the pore with monolayer center taken as the bottom.

The versatility of this zipping process lies in the simple sequential zipping of a multilayer assembly onto a micelle monolayer (Figure – 4.15). In order to differentiate afterwards the two assembled system, the second zipping stage was carried out in the presence of humid air to induce the formation of pores in accordance with the well-known breath figure method[32]. A micellar solution (2 mg/ml) in cyclohexane/THF (9/1 vol.%) was drop-casted onto a previously zipped monolayer of micelles and let to evaporate to dryness in a casting box at a relative humidity of 70%. In this experiment, the airflow was not used as the objective was not to obtain perfect honeycomb structured morphology but only to produce some perforations across the 2nd assembly layer. The SEM and AFM Images of the surface (Figure – 4.17a,b) showed a randomly perforated multilayered assembly zipped onto a monolayer assembly. The AFM analysis of one such large perforation gave an average diameter of 15 nm for the micelles at bottom of the perforation and the ones on the top of the perforation (Figure – 4.17 c). The height measurement between the two levels gave a total thickness of 120 nm, roughly corresponding to 10 micelle layers (Figure – 5.17 d).

4.3 UNZIPPING OF MICELLE ASSEMBLY AND ITS REVERSIBILITY

The term "zipper-assembly" refers to not only the possibility of zipping but also of unzipping the objects when required in a controlled fashion. The results discussed so far indicate that a good solvent for PODMA like cyclohexane, although capable of dispersing micelles in the solution could not remove the micelle assembly from the surface at room temperature, thanks to the very stable and robust interdigitated *n*-octadecyl chains network. However, if the micelle assembly was heated in cyclohexane at 60°C, a temperature much above the melting point of the PODMA block (~32°C) (Figure – 4.18), the coating was entirely removed (Figure – 4.19) and the micelles were dispersed back in the solvent.
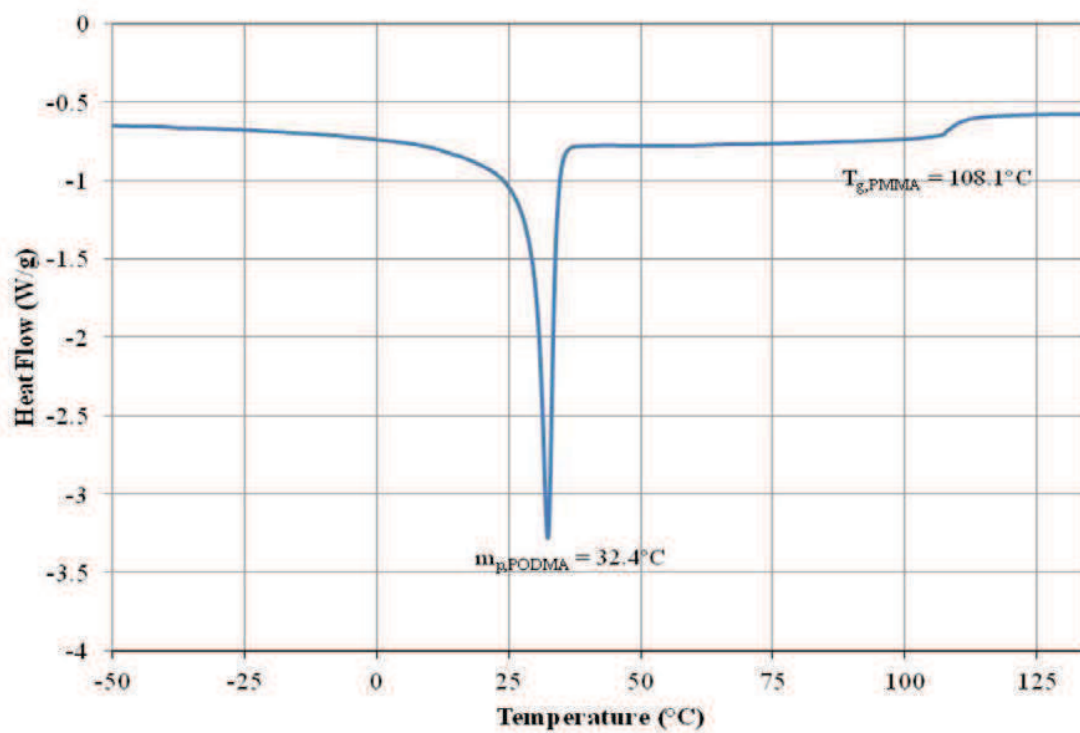
Figure – 4.18: Differential Scanning Calorimetry thermogram for PMMA-b-PODMA copolymer
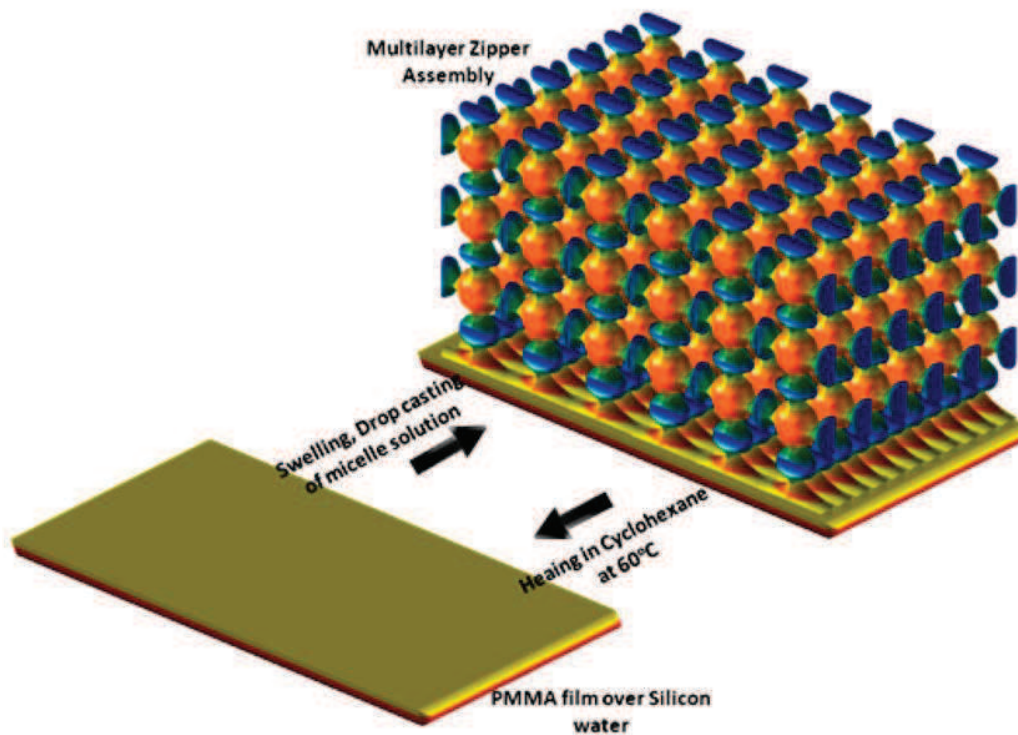
Figure – 4.19: Novel and facile reversibility of Zipper assembly of the copolymer micelles

The presence of the dispersed micelles was detected by PCCS analysis of the solvent bath. As can be seen, the solvent not only contained the original 35 nm micelles but also large aggregates of the micelles giving a much larger value between 200 nm – 400 nm (Figure – 4.20).
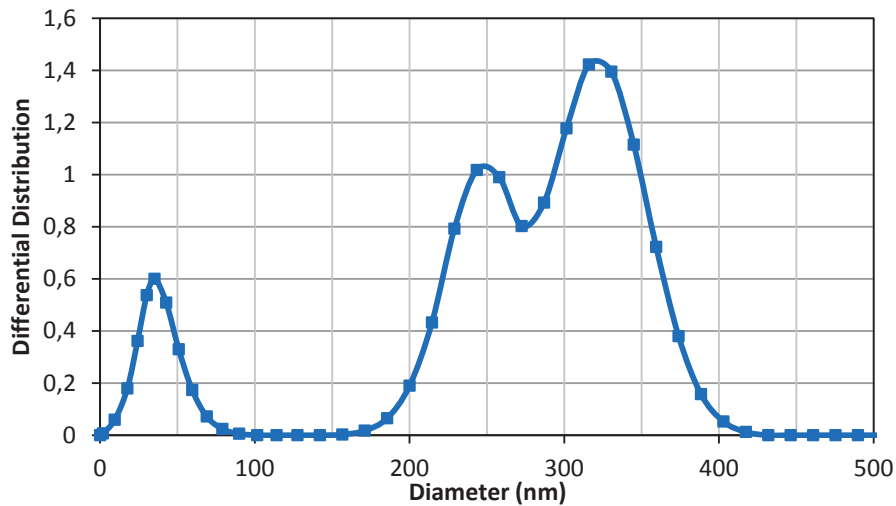
Figure – 4.20: Differential distribution curve obtained for the washed away cyclohexane by Photon Cross Correlation Spectroscopy, showing original micelle distribution as well as aggregates of micelles
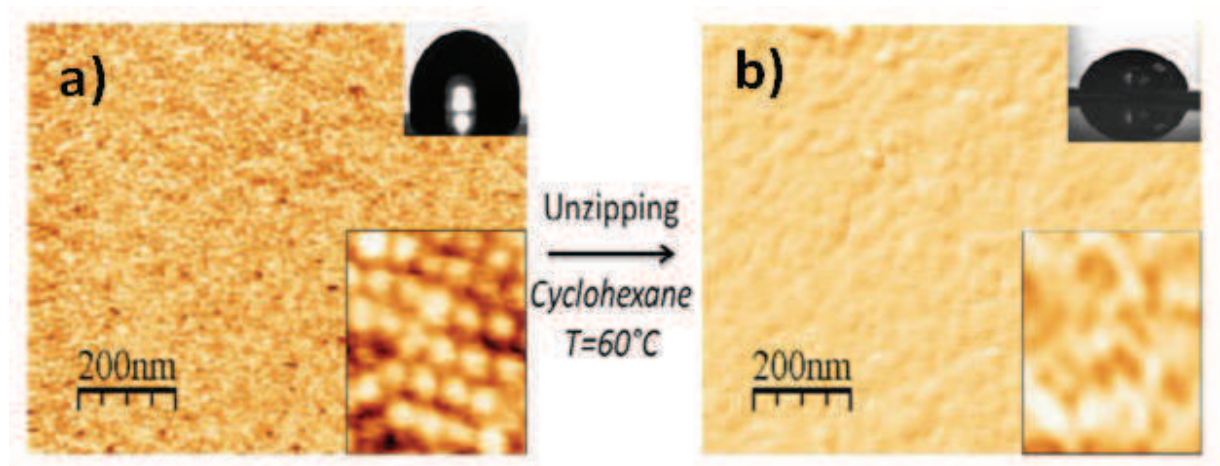
Figure – 4.21: Atomic Force Microscopy of zipper assembly a) before washing, with corresponding water drop having high contact angle, b) after washing into a bath of cyclohexane at 60°C with corresponding water drop showing lower contact angle

The removal of micelles' assembly from the substrate was further verified with AFM images obtained before and after the washing step (Figure – 4.21a,b). As it can be seen, the uniformly ordered

micelles' assembly was totally removed from the surface leaving behind a relatively flat surface devoid of any structural entity.

The contact angle measurements of the washed substrate further pointed towards substantial removal of the micelles' assembly as clearly a decrease in contact angle to a value of 80±2° from PODMA surface (88-89°) was observed (Figure – 4.21a,b inset). However this value is higher than that for virgin PMMA (75°) surface, which indicates that presence of some remaining scattered block copolymer chains still entrapped over the PMMA film. To further substantiate the reversibility of the assembly, 3 cycles of zipping and unzipping of micelles were performed over a PMMA coated silicon surface and the respective contact angle values were obtained. While the coating was performed by drop casting three times over a swelled PMMA film, followed by rinsing with cold cyclohexane; the unzipping process was carried out by leaving the PMMA coated wafer (having zipper assembly) into a bath of cyclohexane heated at 60°C for 30 minutes followed by rinsing with cold cyclohexane. As expected, the values of contact angle showed a zig-zag pattern (Figure – 4.22) which is consistent with the argument that the overall mechanism of the assembly is likely to be a combination of an efficient inter-micelle zipping and a surface anchorage through randomly distributed anchoring points.
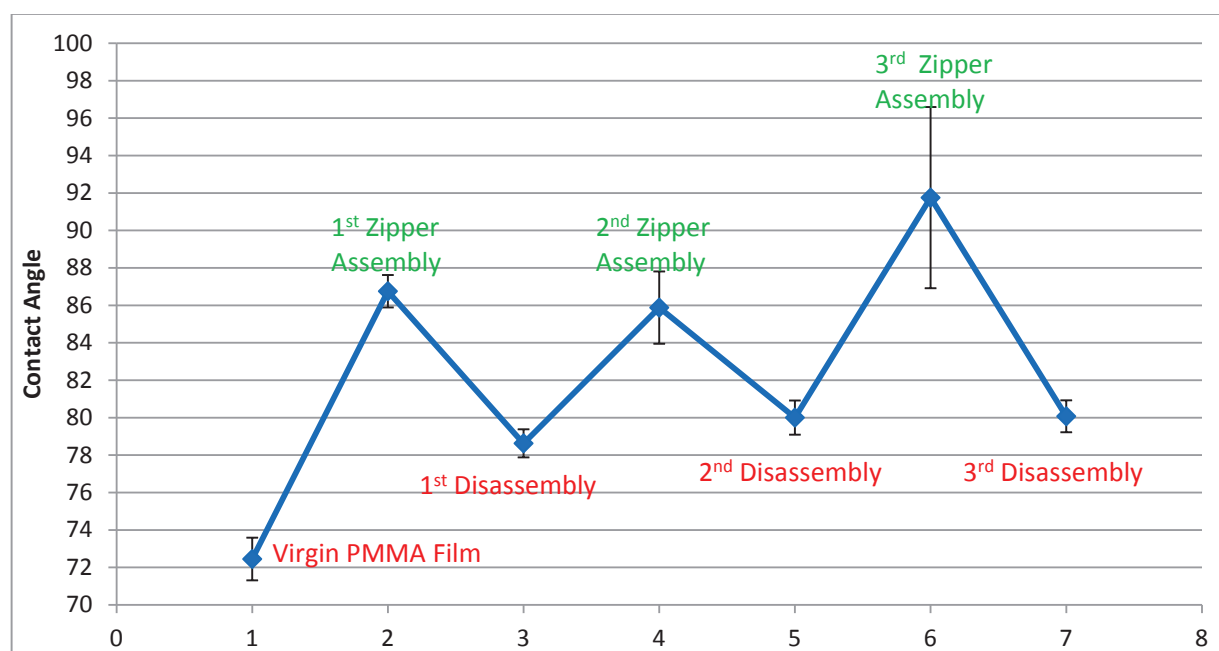
Figure – 4.22: Contact Angle measurements of a PMMA coated silicon wafer after 3 cycles of zipper assembly by drop casting and subsequent disassembly by washing in cyclohexane at 60°C.

4.4 CALORIMETRIC STUDY OF ZIPPED ASSEMBLY

Heating the multilayer micelle assembly in the solid dry state at 60°C for 1 hour, followed by cooling down to 25°C at 1°C min^{-1} led to an increase in the contact angle from 88±2° to 94±2° of the surface. The AFM analysis (Figure – 4.23) of the surface thus obtained showed deformed particles in place of the original micelle spheres.
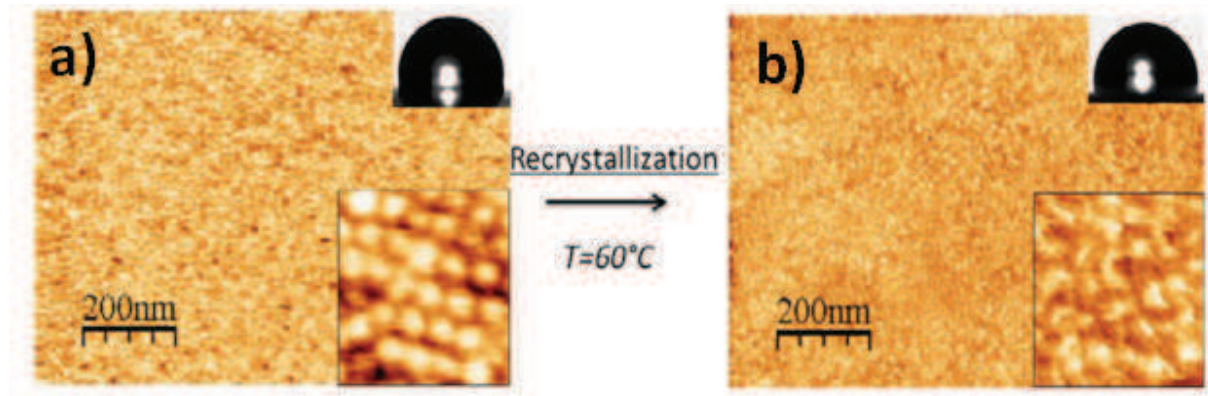
Figure – 4.23: Atomic Force Microscopy and water droplet images (inset) obtained for a) zipper assembly, b) deformed assembly due to melting of PODMA chains in dry state at 60°C followed by recyrstallization.

This deformation can be result increased amount of the crystalline part in between micelle cores. To verify this, differential scanning calorimetry was conducted for block copolymer powder and multilayer micelle assembly and the degree of crystallinity (χc) was calculated from the obtained scans using the following equation:

$$\chi_c = \frac{\Delta H_f}{\Delta H_{f0}}$$ ……….. Eq. (4.1)

where ΔH_f is the enthalpy of fusion of *n*-octadecyl methacrylate in the copolymer and ΔH_{f0} is the enthalpy of fusion of a crystal for alkyl side-chain polymers taken equal to ΔH_{f0}=219.8 J/g[33]. To maintain the overall morphology of the multilayer assembly, the scans were stopped at 90°C, before the glass transition temperature of PMMA is reached. A clear decrease in crystallinity from 17.6 % to 13.5 % was observed (Table – 4.1) when comparing the 1st heating scans of the block copolymer powder and the multilayer micelle assembly. The spherical shape of micelles, like any curved surfaces is known to reduce the contact area required for the zipping and consequently decreasing the overall crystallization[23] also. As expected from the observed deformed particles, the 2nd heating scan of the micelle assembly revealed an increase of χ_c to 17.1%, which stems due to the minimization of curved interfaces caused by heating and relative reorganization of PODMA pendant chains.

	Heating Cycle	ΔH_f (J/g)	χ_c	n_c
PMMA – *b* – PODMA powder	1	37.8	0.176	4.3
	2	36.3	0.165	4.0
PMMA – *b* – PODMA multilayer assembly	1	29.6	0.135	3.3
	2	37.6	0.171	4.1

Table – 4.1: Enthalpy of fusion and degree of crystallinity calculated from thermograms obtained for the copolymer powder and assembled coating from the Differential Scanning Calorimetry

The number of side chain CH_2 groups (n_c) involved in crystallization process was calculated using the following equation:

$$n_c = \frac{\Delta H_f}{\Delta H_{CH2}} \qquad\qquad .... \text{ Eq. (4.2)}$$

where, ΔH is the average melting enthalpy per CH_2 unit for *n*-alkanes (ΔH_{CH2} = 3.07 kJmol^{-1})[34]. Using the above equation, the number of methylene groups involved was found to be around 4, representing 22% of the total methylene units, in agreement with the range 4.7 – 6.9 reported for pure PODMA[34].

4.5 IMPLICATIONS FOR BEING A SELF-HEALING COATING

Given the fact that it is possible to alter the organization of the micelle assembly without changing the overall morphology by heating at 60°C, we strongly believe that the discussed system has the potential to show self-healing ability in case of surface damage. Although not completely autonomous due to application of temperature but a situation can envisioned where a minor surface cut or abrasion is erased or healed by heating the coated substrate at 50°C – 60°C. At this temperature, the pendant long chains of PODMA shall reorganize themselves thus filling the space created by the damage. Furthermore, a porous superstructure can also be prepared by such block copolymer micelles by creating pores into their assembly using methods such as breadth figure method.

4.6 CONCLUSION

In this chapter, we have explored the possibility of using macromolecular zipper to reversibly assemble micelles into 2D and 3D coatings. The zipper effect was observed from the efficient networked interdigitation of pendant long chains of PODMA. First a 2D monolayer was zipped to a PMMA substrate through a one pot strategy comprising of surface functionalization with anchoring points followed by a

stable zipping of the micelles. Multilayer micelles' assemblies were also obtained by increasing the micelle concentration through the solvent evaporation. The system showed impressive reversibility as proved by simple wash-off step carried out in cyclohexane. The reorganization of PODMA block upon heating while conserving the overall morphology further presents an oppourtunity to obtain a temperature mediated self-healing coating system. The aforementioned concept of zipping-assembly of micelles combines a self-assembly stage following "classical" rules and a reversible lock-in of the global morphology through a zipper mechanism.

REFERENCES

1   Zhao, B. & Brittain, W. J. Polymer brushes: surface-immobilized macromolecules. *Progress in Polymer Science* **25**, doi:10.1016/s0079-6700(00)00012-5 (2000).

2   Yoshida, T. *et al.* Electrodeposition of Inorganic/Organic Hybrid Thin Films. *Advanced Functional Materials* **19**, doi:10.1002/adfm.200700188 (2009).

3   Marichy, C., Bechelany, M. & Pinna, N. Atomic Layer Deposition of Nanostructured Materials for Energy and Environmental Applications. *Advanced Materials* **24**, doi:10.1002/adma.201104129 (2012).

4   Hiller, J., Mendelsohn, J. D. & Rubner, M. F. Reversibly erasable nanoporous anti-reflection coatings from polyelectrolyte multilayers. *Nature Materials* **1**, doi:10.1038/nmat719 (2002).

5   de Vos, W. M., de Keizer, A., Stuart, M. A. C. & Kleijn, J. M. Thin polymer films as sacrificial layers for easier cleaning. *Colloids and Surfaces a-Physicochemical and Engineering Aspects* **358**, doi:10.1016/j.colsurfa.2009.12.022 (2010).

6   Tyagi, P. *et al.* Dynamic Interactive Membranes with Pressure-Driven Tunable Porosity and Self-Healing Ability. *Angewandte Chemie-International Edition* **51**, 7166-7170, doi:10.1002/anie.201201686 (2012).

7   Ariga, K. *et al.* Challenges and breakthroughs in recent research on self-assembly. *Science and Technology of Advanced Materials* **9**, doi:10.1088/1468-6996/9/1/014109 (2008).

8   Moulin, E., Cormosw, G. & Giuseppone, N. Dynamic combinatorial chemistry as a tool for the design of functional materials and devices. *Chemical Society Reviews* **41**, doi:10.1039/c1cs15185a (2012).

9   Quemener, D. *et al.* Free-Standing Nanomaterials from Block Copolymer Self-Assembly. *Macromolecules* **43**, doi:10.1021/ma100809v (2010).

10   Landschulz, W. H., Johnson, P. F. & McKnight, S. L. The leucine zipper - a hypothetical structure common to a new class of dna-binding proteins. *Science* **240**, doi:10.1126/science.3289117 (1988).

11   Oshea, E. K., Klemm, J. D., Kim, P. S. & Alber, T. X-ray structure of the gcn4 leucine zipper, a 2-stranded, parallel coiled coil. *Science* **254**, doi:10.1126/science.1948029 (1991).

12   Landon, P. B. *et al.* DNA Zipper-Based Tweezers. *Langmuir* **28**, doi:10.1021/la201267e (2012).

13   Zhang, X., Bera, T., Liang, W. & Fang, J. Longitudinal Zipping/Unzipping of Self-Assembled Organic Tubes. *Journal of Physical Chemistry B* **115**, doi:10.1021/jp2064276 (2011).

14   Kim, H. W. *et al.* One-Dimensional Molecular Zippers. *Journal of the American Chemical Society* **133**, doi:10.1021/ja2031486 (2011).

15   Porus, M. *et al.* Zipper and Layer-by-Layer Assemblies of Artificial Photosystems Analyzed by Combining Optical and Piezoelectric Surface Techniques. *Langmuir* **27**, doi:10.1021/la2007815 (2011).

16   Zeng, J. *et al.* Interplay of Olefin Metathesis and Multiple Hydrogen Bonding Interactions: Covalently Cross-linked Zippers. *Organic Letters* **13**, doi:10.1021/ol201282d (2011).

17   Li, S., Ge, Y., Piletsky, S. A. & Turner, A. P. F. A Zipper-Like On/Off-Switchable Molecularly Imprinted Polymer. *Advanced Functional Materials* **21**, doi:10.1002/adfm.201100593 (2011).

18   Goldburt, E., Shvartsman, F., Fishman, S. & Krongauz, V. Intramolecular interactions in photochromic spiropyran merocyanine polymers. *Macromolecules* **17**, doi:10.1021/ma00136a020 (1984).

19   Wismontskiknittel, T. & Krongauz, V. Self-assembling of spiropyran polymers by zipper crystallization. *Macromolecules* **18**, doi:10.1021/ma00153a009 (1985).

20   de Vos, W. M., Meijer, G., de Keizer, A., Stuart, M. A. C. & Kleijn, J. M. Charge-driven and reversible assembly of ultra-dense polymer brushes: formation and antifouling properties of a zipper brush. *Soft Matter* **6**, doi:10.1039/b926017j (2010).

21   Whitesides, G. M. & Grzybowski, B. Self-assembly at all scales. *Science* **295**, doi:10.1126/science.1070821 (2002).

22   Qin, S. H., Matyjaszewski, K., Xu, H. & Sheiko, S. S. Synthesis and visualization of densely grafted molecular brushes with crystallizable poly(octadecyl methacrylate) block segments. *Macromolecules* **36**, doi:10.1021/ma021472w (2003).

23   Gitsas, A., Floudas, G., Butt, H. J., Pakula, T. & Matyjaszewski, K. Effects of Nanoscale Confinement and Pressure on the Dynamics of pODMA-b-ptBA-b-pODMA Triblock Copolymers. *Macromolecules* **43**, doi:10.1021/ma902639g (2010).

24   Moad, G., Rizzardo, E. & Thang, S. H. Radical addition-fragmentation chemistry in polymer synthesis. *Polymer* **49**, doi:10.1016/j.polymer.2007.11.020 (2008).

25   Moad, G. *et al.* Living free radical polymerization with reversible addition-fragmentation chain transfer (the life of RAFT). *Polymer International* **49**, doi:10.1002/1097-0126(200009)49:9<993::aid-pi506>3.0.co;2-6 (2000).

26   Quinn, J. F., Chaplin, R. P. & Davis, T. P. Facile synthesis of comb, star, and graft polymers via reversible addition-fragmentation chain transfer (RAFT) polymerization. *Journal of Polymer Science Part a-Polymer Chemistry* **40**, doi:10.1002/pola.10369 (2002).

27   Stenzel-Rosenbaum, M., Davis, T. P., Chen, V. & Fane, A. G. Star-polymer synthesis via radical reversible addition-fragmentation chain-transfer polymerization. *Journal of Polymer Science Part a-Polymer Chemistry* **39**, doi:10.1002/pola.1256 (2001).

28   Keddie, D. J., Moad, G., Rizzardo, E. & Thang, S. H. RAFT Agent Design and Synthesis. *Macromolecules* **45**, doi:10.1021/ma300410v (2012).

29   Benaglia, M., Rizzardo, E., Alberti, A. & Guerra, M. Searching for more effective agents and conditions for the RAFT polymerization of MMA: Influence of dithioester substituents, solvent, and temperature. *Macromolecules* **38**, doi:10.1021/ma0480650 (2005).

30   Nishiyama, N. *et al.* Novel cisplatin-incorporated polymeric micelles can eradicate solid tumors in mice. *Cancer Research* **63** (2003).

31   Zhang, L. F. & Eisenberg, A. Multiple morphologies of crew-cut aggregates of polystyrene-b-poly(acrylic acid) block-copolymers. *Science* **268**, doi:10.1126/science.268.5218.1728 (1995).

32   Bunz, U. H. F. Breath figures as a dynamic templating method for polymers and nanomaterials. *Advanced Materials* **18**, doi:10.1002/adma.200501131 (2006).

33   Jiang, Y., Xue, J., Zhu, X. Y. & Yan, D. Y. pH Stimulated Preparation of Polyrotaxane Based on Reversible Covalent Bond in Solution. *Chemical Journal of Chinese Universities-Chinese* **29**, 2558-2562 (2008).

34   Shang, S., Huang, S. J. & Weiss, R. A. Synthesis and characterization of itaconic anhydride and stearyl methacrylate copolymers. *Polymer* **50**, doi:10.1016/j.polymer.2009.05.012 (2009).

5. NANO-GEL BASED SELF-HEALING SYSTEM

In this chapter we have presented a new concept which is under research for the moment. Taking a cue from the monomer laden microcapsule based self-healing approach[1]; we have planned to replace the monomer by a rapidly healing nano-gel will be encapsulated in a hydrophobic shell and dispersed into the membrane. In an event of crack formation, the breakage of the microcapsule's wall will lead the water to contact the gel. This would cause a rapid expansion of the nano-gel however due to its inherent crosslinked structure; it should be able to maintain its structural integrity. Furthermore, being higly hydrophilic, the gel is expected to show good adhesive properties and thereby check the growth of the crack.
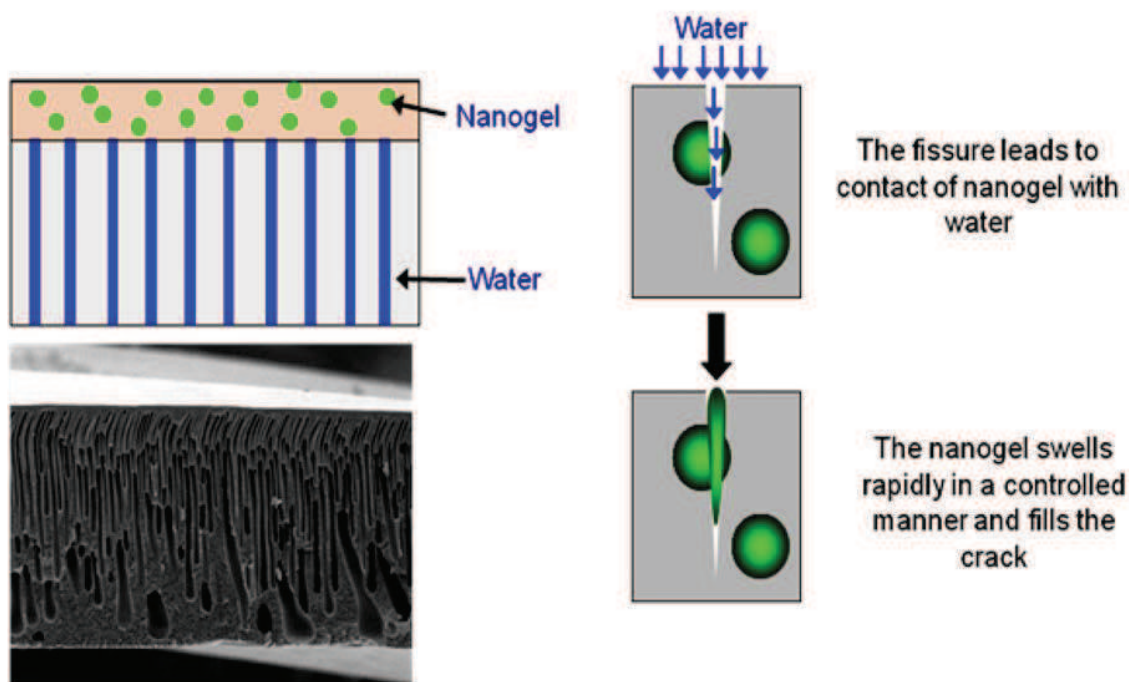
Figure – 5.1: Embedding of encapsulated nano-gel in the active layer of a membrane. Concept of self-healing by using rapid swelling and adhesiveness of the nano-gel in a membrane.

5.1 BACKGROUND STUDY

The concept of nano-gel based self-healing system is based on an earlier preliminary work carried out in the lab by coworker, in which partially crosslinked hydrogels were prepared and their swelling characteristics were studied. The hydrogels were prepared from RAFT mediated controlled radical copolymerization of 2-hyrdoxyethyl methacrylate (HEMA) and Poly(ethylene glycol) dimethacrylate (PEGMA). In the first step, the hydrogels were prepared in the bulk form to study the effect of PEGMA chain length on the swelling rate. The obtained hydrogels showed rapid swelling characteristics with observable dependence upon the molecular weight of PEGMA which acts as a crosslinker of the gel (Figure – 5.1).
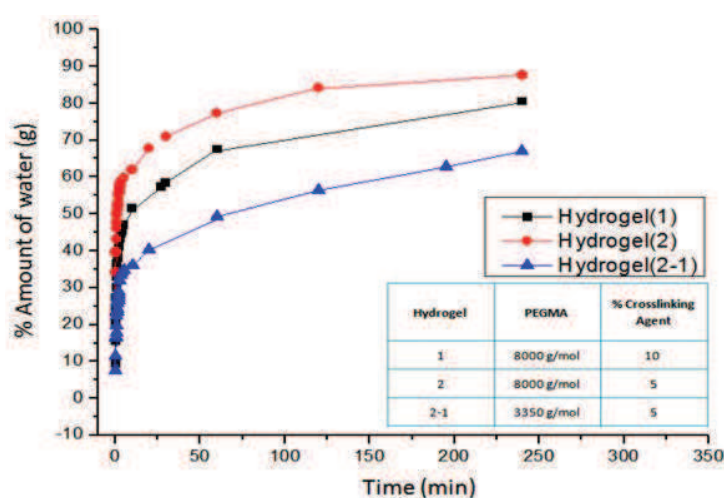
Figure – 5.1: Swelling ration of different hydrogels prepared and the corresponding crosslinking agent with %.
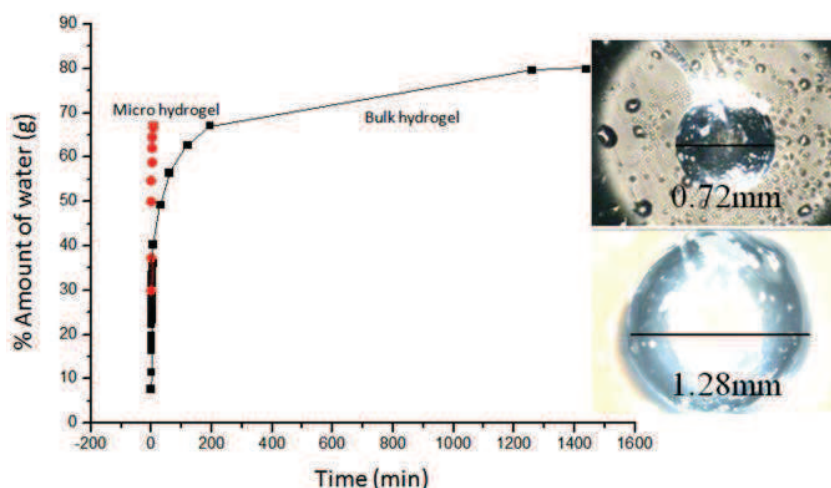
Figure – 5.2: Swelling ratio of micro hydrogel compared with bulk hydrogel. Optical photos of dry micro hydrogel and swelled micro hydrogel

In order to be dispersed into a material, the hydrogel must be prepared as microparticles. To achieve this, inverse suspension technique was utilized which allowed to obtain hydrogel particles having a broad size distribution but average diameter lesser than 1 µm. When the swelling curves are compared with that of bulk hydrogel, the micro hydrogel demonstrated a very high rate of swelling, reaching 70 % water uptake within few minutes as compared to bulk hydrogel which took more almost 200 minutes to gain the same amount of water (Figure – 5.2).

The above findings points that the as the size of hydrogel particles is reduced, their overall swelling characteristics is amplified several folds. In order to further reduce the size of the hydrgels, inverse miniemulsion technique was used, which further reduced average particle size to 300 nm (Figure – 5.3). However, further decrease in the size could not be reached in spite of varying different parameters like surfactant amount, ultrasonication time, temperature, etc. Additionally, the size of the particles gradually increased over time leading to eventual coagualation. However as expected, the reduced sized particles showed even faster swelling than suspension prepared particles (Figure – 5.4).
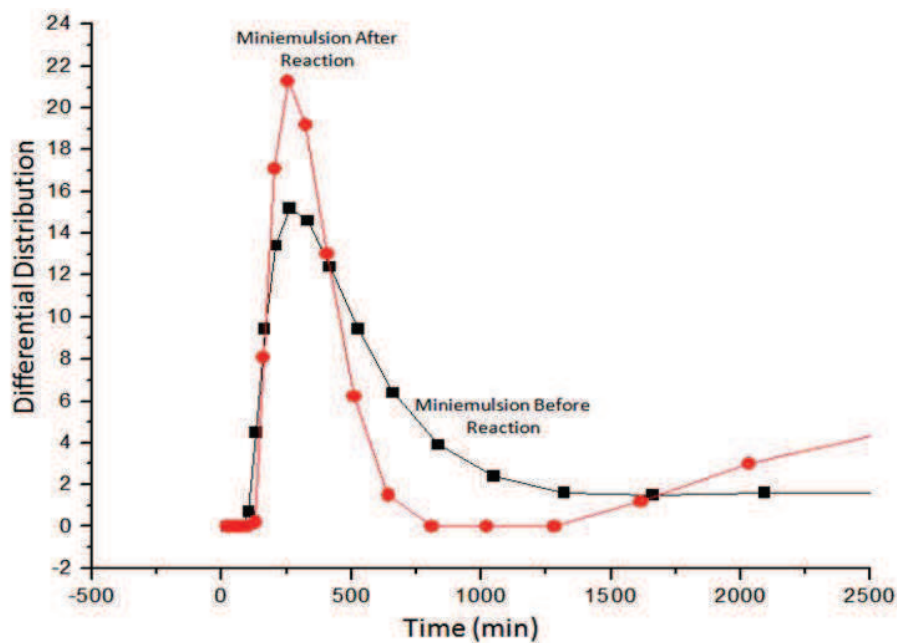
Figure – 5.3: Size distribution of nano hydrogel prepared using miniemulsion technique.
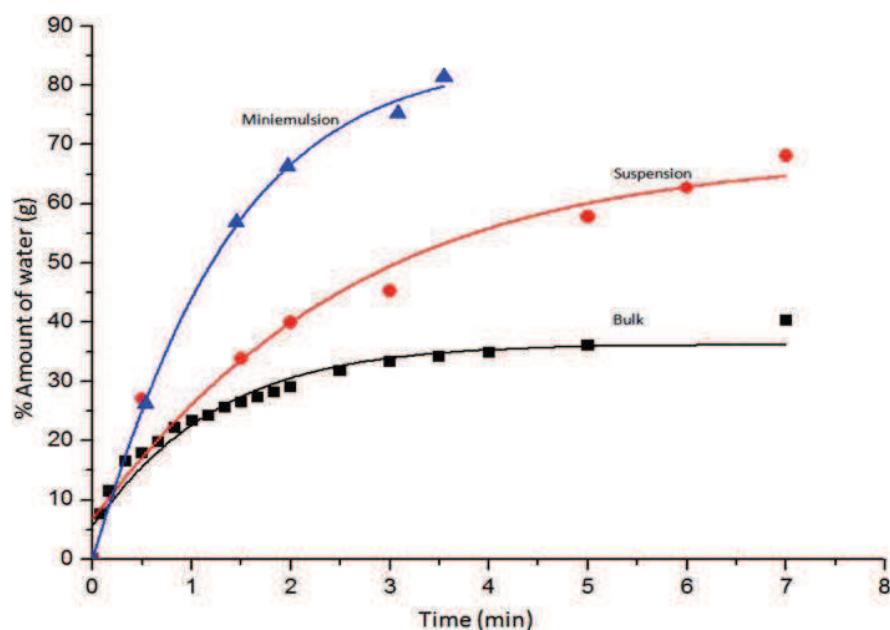
Figure – 5.4: Size distribution of nano hydrogel prepared using miniemulsion technique.

5.2 DESIGN CONSIDERATIONS FOR NANO-GEL

The results obtained from the previous study gave an important result that as the size of hydrogels decreases, their rate of water uptake increases manifold. Although the miniemulsion provides an effective route towards the achievement of smaller particles, it also presents the problem of high level of contamination with reaction formulation species like surfactant. Moreover, in the present case, the emulsion prepared nano-gel particles were found to be unstable over longer duration of time. Hence, it was decided to prepare the nano-gel from a partially cross-linked star copolymer *via* "core first" route. The route involves the extension of arms from a synthesized multifunctional initiator *via* further addition of monomers. To achieve better control over the molecular weight and thus the size of the particle, "Reversible Addition Fragmentation Transfer"[2-4] (RAFT) mediated controlled radical polymerization (CRP) was chosen. However, star polymers have traditionally been prepared *via* other CRP methods like "Atomic Transfer Reaction Polymerization"[5-8] (ATRP) and "Nitroxide Mediated Polymerization"[9-12] (NMP). When using RAFT polymerization, it provides two routes to prepare star polymers. First is the "Z – approach" where the Z group of the RAFT agent is connected to the core molecule or the "R – approach" where the R group of the RAFT agent is connected. Both options present merits and demerits. The "Z – approach" provide a relatively monomodal polymer since the Z group at which the equilibrium takes place, is tethered to the core molecule thus preventing its coupling with another radical species. However, it is often problematic to reach high molecular weight with this

approach since the propagating radical species have rapidly diminishing access to dithioester moiety which is difficult to reach in high-molecular weight scenario, thus affecting the effective chain transfer mechanism. On the other hand, the "R – approach" isn't bounded by such limitation however due the connection of the R-group moiety to the core, the core itself carries radical(s) which can lead to coupling reactions between two or more such cores and thus seriously affecting the polymerization process. The situation worsens as the time increases and a very broad molecular weight distribution (due to coupling of various cores) is obtained. Hence, it is often desirable to stop the polymerization at very lower conversions and in diluted conditions.

In the present case, we attempted to prepare the core-RAFT molecule with "R – approach". The basic idea was to couple a RAFT agent with a tetrafunctional molecule like Pentaerythritol *via* esterification reaction in mild conditions so as not to affect the RAFT agent.

5.3 SYNTHESIS OF CORE-RAFT MOLECULE

To synthesize the core-RAFT molecule, we chose the following two compounds (Figure – 5.6) whose esterification reaction would lead to the desired tetra functional transfer agent. The first compound is a tetra functional alcohol also known as pentaerythritol and commonly used as precursor to prepare complex architectures like dendrimers and other polyfunctional compounds. The RAFT agent, 4-Cyano-4-(phenylcarbonothioylthio)pentanoic acid to be esterified with pentaerythritol contains carboxylic group funcationality. It was decided to perform steglich esterification of the above two compounds in the presence of a dicyclohexylcabodiimide (DCC) catalyzed by 4- dimethylaminopyridine (DMAP). The reaction takes place readily at room temperature in a non-polar solvent like dichloromethane. However the use of DCC produces a significant amount of dicyclohexyl urea as a side product which complicates the work-up process.

Pentaerythritol   4-Cyano-4-(phenylcarbonothioylthio)pentanoic acid
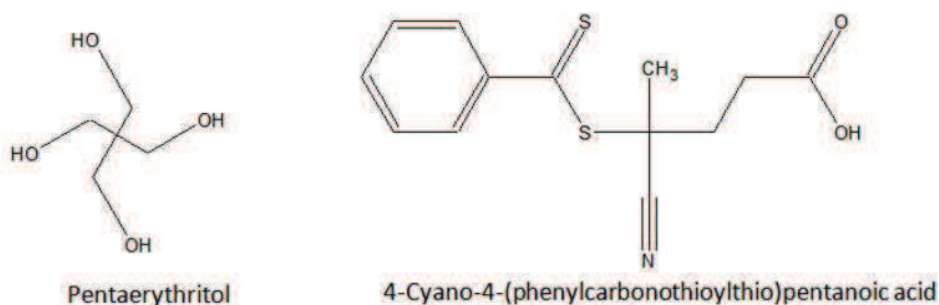
Figure – 5.6: Chemical structures of pentaerythritol and RAFT agent to synthesis core molecule.

In a typical process, the two compounds (RAFT agent and pentaerythritol) were reacted in distilled and dry dichloromethane in the presence of DCC and DMAP. However, the reaction did not take place since the pentaertythriol is insoluble in dichloromethane. Other solvents like chloroform, tetrahydrofuran were also used however due to solubility issues, no reaction took place. Finally the being soluble in dimethylformamide (DMF), it was reacted with the RAFT agent however after few minutes of reaction, the reaction contents' color was found to be changed from pink to deep orange. This color change signified the degradation of the RAFT agent. Due to these reasons, this route was discarded and another approach was taken.

In a changed strategy, it was decided to use click chemistry to combine the two molecules by synthesizing respective azide and alkyne derivatives. Hence in the first step, pentaerythritol was first transformed into more soluble chlorine derivative (2-(2-chloroacetyl)oxyethyl 2-chloroacetate) (Figure – 5.7). To achieve this, the alcohol was dissolved in distilled DMF and chloroacetyl chloride was added dropwise to the reaction mixture in nitrogen atmosphere. Once the addition of the acid chloride was over, the reaction content was heated at 50°C for 24 hours, after which the reaction was stopped by quenching in ice bath. After the suitable work up procedure, pale white color powder was obtained and its ^{1}HNMR (Figure – 5.8), were obtained to verify the structure.
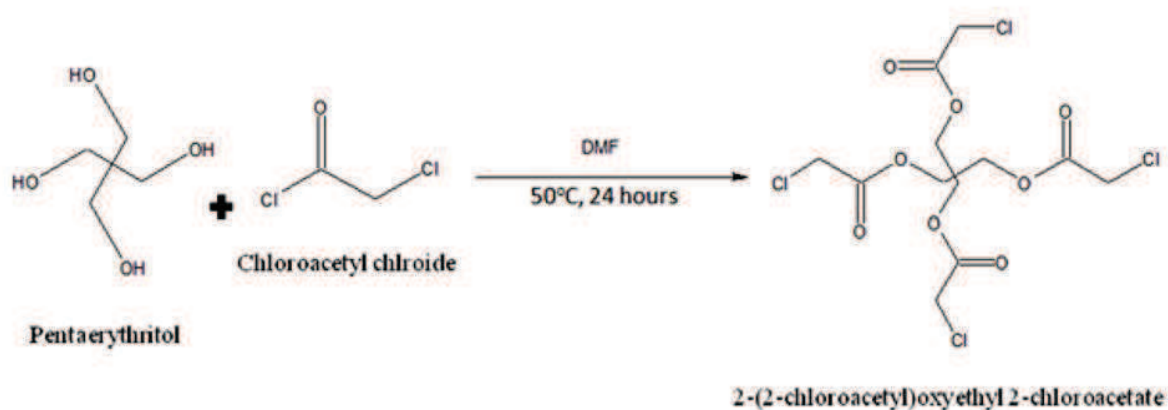
Figure – 5.7: General reaction for the synthesis of chloride derivative of pentaerythritol.

Figure – 5.8 1HNMR spectra obtained for 2-(2-chloroacetyl)oxyethyl 2-chloroacetate

In the second step, the chlorine derivative transformed into azide derivative (2-(2-azidoacetyl)oxyethyl 2-azidoacetate) (Figure – 5.9) by dissolving it in acetone (dried) and refluxing at 55°C with excess of sodium azide for 24 hours. After which, the acetone was removed by evaporation and the same work up process was used to obtain a deep brown viscous liquid. The product's structure was verified using ^{1}HNMR (Figure – 5.10) and Fourier Transform Infra-Red spectroscopy (FTIR) spectra (Figure – 5.11).

Figure – 5.9: General reaction for the synthesis of azide derivative of 2-(2-azidoacetyl)oxyethyl 2-azidoacetate.

131

Figure – 5.10: 1HNMR spectra obtained for 2-(2-azidoacetyl)oxyethyl 2-azidoacetate
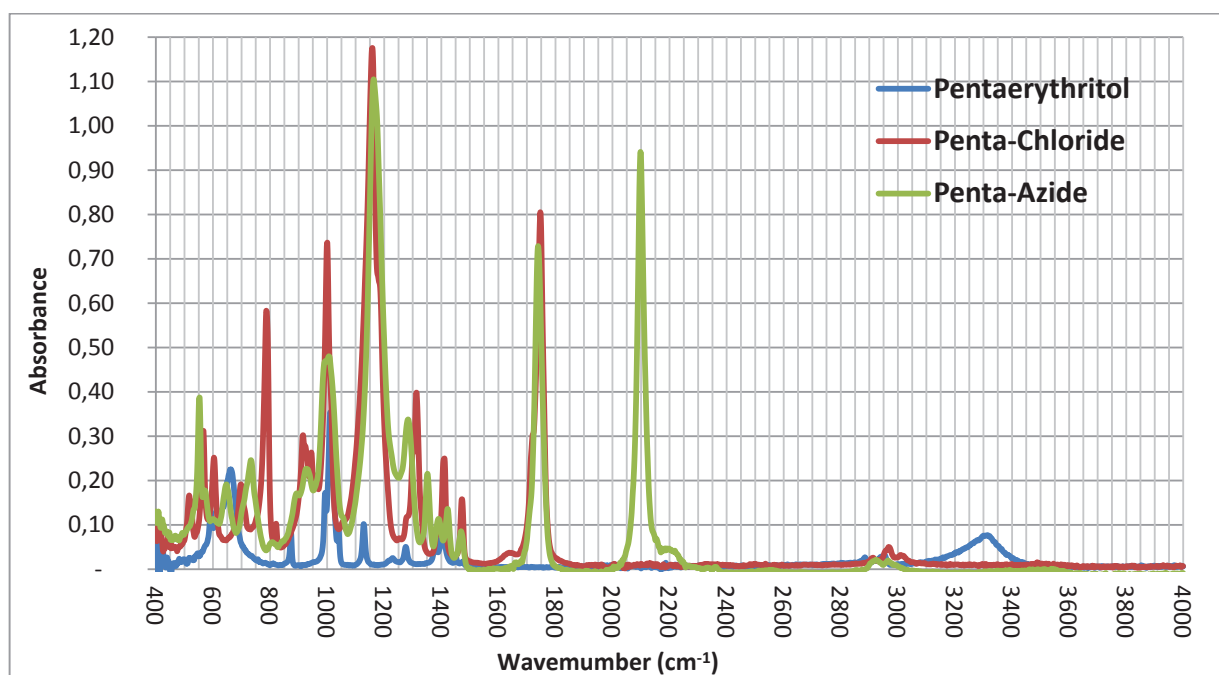
Figure – 5.11: ATR-FTIR spectra obtained for Pentaerythritol, 2-(2-chloroacetyl)oxyethyl 2-chloroacetate and 2-(2-azidoacetyl)oxyethyl 2-azidoacetate showing C=O stretch for 2-(2-chloroacetyl)oxyethyl 2-chloroacetate and 2-(2-azidoacetyl)oxyethyl 2-azidoacetate and C-N$_3$ stretch for 2-(2-azidoacetyl)oxyethyl 2-azidoacetate

In the third step of the strategy, the RAFT agent was esterified in distilled dichloromethane with Propargyl alcohol in the presence of *N*-(3-Dimethylaminopropyl)-*N'*-ethylcarbodiimide hydrochloride (EDC) and DMAP at 0°C for a period of 15 hours (Figure – 5.12). After 15 hours, the reaction content was filtered to remove the urea formed. The red color filtrate thus obtained was concentrated and after the work up process, a deep red colored viscous liquid was obtained. The structure of esterification product was verified with ^{1}HNMR (Figure – 5.13).
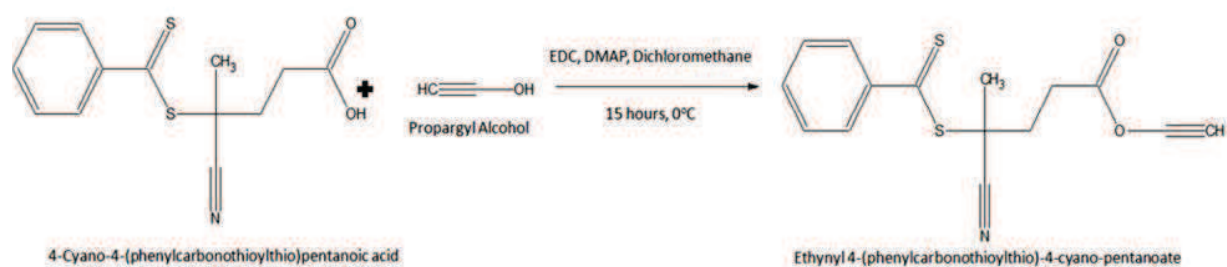
Figure – 5.12: Synthesis of alkyne derivative of RAFT agent via esterification reaction
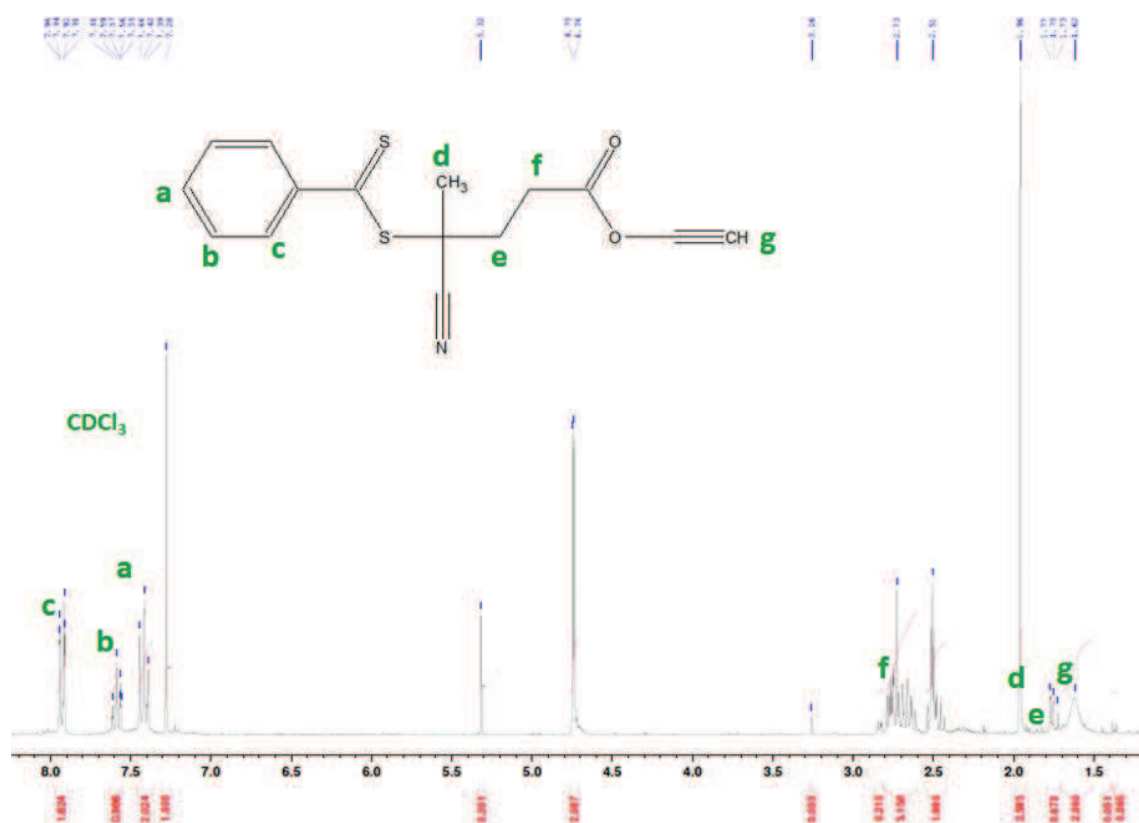
Figure – 5.13: 1HNMR spectra obtained for Ethynyl 4-(phenylcarbonothioylthio)-4-cyano-pentanoate

The ^{1}HNMR spectrum obtained for the esterification product of RAFT agent showed persistant impurities despite purifying over silica gel chromatography. With the obtained spectrum, it is difficult to ascertain the peak signal for two methylene proton groups as well as lone proton of alkyne group.

Nevertheless, we carried on with the same product to be reacted with the azide derivative of pentaerythritol. For this, around 4.5 eq. moles of ethynyl 4-(phenylcarbonothioylthio)-4-cyano-pentanoate was reacted with 1 eq. moles of 2-(2-azidoacetyl)oxyethyl 2-azidoacetate in the presence of copper sulfate pentahydrate and sodium ascorbate. DMF was used as a solvent (Figure – 5.14). The reaction was spontaneous as the color of the *vial* changed to deep red. After 1 hour, the reaction contents were passed through a short alumina column, followed by the work up process, giving deep brownish red color viscous product.
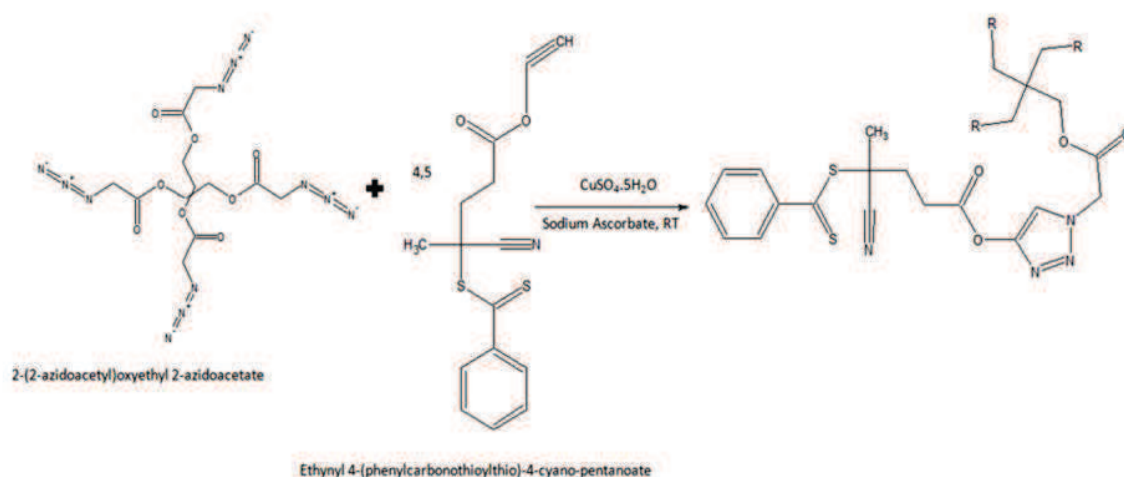
Figure – 5.14: Click chemistry reaction for the coupling of ester derivative of RAFT with tetra azide derivative of pentaerythritol. For clarity, the rest of the three groups have been omitted and represented by R.

The analysis of ^{1}HNMR of the product indicates the presence of unreacted azide derivative in the product which resulted to presence of large number of peaks. At this moment it seems that better purification procedure is required to obtain the core molecule in the good yield and purity.

5.4 CONCLUSION

Very preliminary results have been presented about the concept of nano-gel based self-healing system. Based on the finding of an earlier work, we established the fact that as the size of the nano-gel increases, its rate of swelling increases rapidly with time. Although with miniemulsion, we were able to

decrease the size till 300 nm, the system remained unstable and perpetual increase in particle size was observed. Hence to circumvent this problem, we decided to a 4-arm star polymer using "core first approach having sufficiently molecular weight and hydroxyl units to be able to crosslink and make a gel but at dimensions lesser than 100 nm. As a first step for this, we have attempted to prepare the core molecule by combing the RAFT molecule with a tetrafunctional compound. We tried room temperature esterification of RAFT with the tetrafunctional molecule in dichloromethane, however the transfer agent was degraded. In view of this, we decided to use click chemistry in order achieve a better pathway albeit long. The 1HNMR of the final core molecule shows several peaks due to impurities hence at this moment it is inconclusive to say about the final yield as well as purity content of the precursor molecule.

REFERENCES

1   White, S. R. *et al.* Autonomic healing of polymer composites. *Nature* **409**, 794-797, doi:10.1038/35057232 (2001).

2   Moad, G. *et al.* Living free radical polymerization with reversible addition-fragmentation chain transfer (the life of RAFT). *Polymer International* **49**, doi:10.1002/1097-0126(200009)49:9<993::aid-pi506>3.0.co;2-6 (2000).

3   Moad, G., Rizzardo, E. & Thang, S. H. Radical addition-fragmentation chemistry in polymer synthesis. *Polymer* **49**, doi:10.1016/j.polymer.2007.11.020 (2008).

4   Mayadunne, R. T. A., Jeffery, J., Moad, G. & Rizzardo, E. Living free radical polymerization with reversible addition-fragmentation chain transfer (RAFT polymerization): Approaches to star polymers. *Macromolecules* **36**, doi:10.1021/ma021219w (2003).

5   Matyjaszewski, K. & Tsarevsky, N. V. Nanostructured functional materials prepared by atom transfer radical polymerization. *Nature Chemistry* **1**, doi:10.1038/nchem.257 (2009).

6   Matyjaszewski, K., Miller, P. J., Pyun, J., Kickelbick, G. & Diamanti, S. Synthesis and characterization of star polymers with varying arm number, length, and composition from organic and hybrid inorganic/organic multifunctional initiators. *Macromolecules* **32**, doi:10.1021/ma9904823 (1999).

7   Angot, S., Murthy, K. S., Taton, D. & Gnanou, Y. Atom transfer radical polymerization of styrene using a novel octafunctional initiator: Synthesis of well-defined polystyrene stars. *Macromolecules* **31**, doi:10.1021/ma980712y (1998).

8   Gao, H. & Matyjaszewski, K. Synthesis of star polymers by a combination of ATRP and the "click" coupling method. *Macromolecules* **39**, doi:10.1021/ma060926c (2006).

9   Bosman, A. W., Vestberg, R., Heumann, A., Frechet, J. M. J. & Hawker, C. J. A modular approach toward functionalized three-dimensional macromolecules: From synthetic concepts to practical applications. *Journal of the American Chemical Society* **125**, doi:10.1021/ja028392s (2003).

10   Hawker, C. J. *et al.* ''Living'' free radical polymerization of macromonomers: Preparation of well defined graft copolymers. *Macromolecular Chemistry and Physics* **198**, doi:10.1002/macp.1997.021980112 (1997).

11   Pasquale, A. J. & Long, T. E. Synthesis of star-shaped polystyrenes via nitroxide-mediated stable free-radical polymerization. *Journal of Polymer Science Part a-Polymer Chemistry* **39**, doi:10.1002/1099-0518(20010101)39:1<216::aid-pola240>3.0.co;2-z (2001).

12   Hawker, C. J., Barclay, G. G., Orellana, A., Dao, J. & Devonport, W. Initiating systems for nitroxide-mediated ''living'' free radical polymerizations: Synthesis and evaluation. *Macromolecules* **29**, doi:10.1021/ma951905d (1996).

6. GENERAL CONCLUSIONS

T he objective of this thesis was to develop and bring self-healing capability to the membranes, which had largely been confined to solid materials like composites or gels so far. As the advances are made in chemistry every day, more and more functionalities are emerging having potential to impart the self-mending capability to a material. To impart this capability to a membrane, the principal constraint was to not to affect the main purpose of a membrane, i.e. its filtration behavior. The current methods of acquiring self-healing in a material though novel cannot be applied to prepare a membrane or more specifically a porous material in a straight forward way because of their application environment. Hence, a new and different strategy was used to approach the problem which resulted in successful development of a self-healing membrane.

In the first part of this work, we prepared a nanomaterial based on the in situ 3-dimensional self-assembly of triblock copolymer micelles. The copolymer, PSAN–*b*–PEO–*b*–PSAN was synthesized in collaboration with another research group with optimized molecular weight and ratio of PEO and PSAN. When dissolved in a selective mixture of DMF/Toluene solvents and spin coated onto silicon wafer, a 1.3 μm film could be obtained which was essentially an in-situ self-assembly of copolymer micelles having average diameter of 50 nm as observed with Atomic Force Microscopy. Despite having very low thickness, the nanomaterial showed decent structural robustness to be able to withstand usual handling procedures. The interstitial volume generated between the micelles imparted the film certain degree of porosity so as to be used as a membrane for water permeation. The constituting micelles of the membrane were held together by the copolymer chains running in between micelles' core however due to absence of any covalent bonding, these chains were able to dislocate easily thereby imparting a certain dynamism to the membrane. It is this inherent dynamic nature based on which the porosity of the membrane was found to be variable as a function of water pressure applied orthogonally onto the surface of membrane. The porosity change was found to be a direct result of morphology change (deformation of micelles) however the interesting fact about this change was its complete reversibility till a certain pressure value thus giving a pressure tunable porosity to the membrane. The tunable porosity was successfully demonstrated when from mixture of poly(ethylene glycol)s, selective separation was achieved as a function of pressure. Another result of the dynamic nature was the self-

healing ability shown by the membrane when a perforation several times larger than former's thickness was found to be healed completely at certain pressure. Similar to porosity, the healing was found to be strongly dependent upon the applied water pressure. Although factors like extent of perforation and duration of pressure application were also important but the only requirement of pressure as a driving force for achievement of self-healing, essentially make this an autonomous self-healing porous material. For a given size of perforation, a pressure range was obtained, within which only the healing was observed. From the Scanning Electron Microscopy images obtained for healed membranes, scar formations were observed. This leads to the following postulation that in case of a perforation, it dislocates the bridges between the micelles and separates them which ultimately disrupt natural equilibrium of the micelles. However when pressure is applied on the membrane in aqueous medium, the micelles are forced to come back to their original position. This provides an opportunity to the micelles on the opposite side of the perforation to reestablish the dislocated bridges and restore the original equilibrium. We further noted that although 100 % healing was achieved at certain pressure, but the reestablishment of bridges is always random, which explains the observed scar formation. This work represents the first such attempt to prepare a self-healing porous material which not only exhibits an autonomous self-healing but also an easily tunable porosity.

In the second part of this work, we studied the translocation of nano-objects through the aforementioned self-healing membrane. The motivation was to demonstrate the application of tunable porosity and self-healing as a tool to achieve the translocation of much bigger size nanoparticles (NPs) than the membrane pore, in diffusion mode which in case of a biological membrane leaves behind severe perforations. Out of four class of nano-objects (mixture of PEGs, protein, poly(styrene) NPs and Silica NPs), only the PEGs were found to retained completely despite being lowest in molecular weight and size. The translocation of poly(styrene) NPs was found to be much pronounced than that of silica NPs which suffered due to their different surface nature and relatively larger stiffer structure. The deformable nature of poly(styrene) NPs helped them to translocate across easily or even fuse together inside the membrane. The dynamic nature of the membrane ensured that the cavity during the translocation of nano-objects (PS or silica) was closed immediately after their passage, as no perforations were found in case of poly(styrene). In case of silica, the perforations were found to be partially healed but only on the surface the probable reason for which can be the entrapment of high number of NPs inside the membrane. Through this work, we experimentally demonstrated that the size of the NP, its shape, its surface nature, the external force govern the translocation behavior across a dynamic membrane. To the best of our knowledge the findings are first to be exhibited by a reasonably robust

dynamic synthetic membrane, which are otherwise been shown only with unstable and fragile lipid membranes.

In the third part of the work, we moved from dynamically bridged micelles to a new kind of micelles' assembly where the micelles were held together by virtue of interdigitation of long pendant chains of one of the blocks of the copolymer. The block copolymer synthesized in this work PMMA–*b*–PODMA diblock copolymer having higher content of poly(octadecyl methacrylate) (PODMA). The copolymer formed micelles in selective mixture of Tetrahydrofuran/Cyclohexane. Monolayer and multilayer assemblies were obtained from the micelles's solution over poly(methyl methacrylate) by simple dipping, drop casting and spin coating methods. The micelles arranged themselves in orderly fashion by virtue of so called "zipper effect" brought by the interlocking of long pendant chains of PODMA. The novelty of the work is further highlighted by the fact that the assembly could be removed very easily by washing the coated substrate in cyclohexane at 60°C which would "unzip" the zipped chains without affecting the overall micelle structure. Once removed, the assemblies could again be formed by any of the aforementioned methods. This "zipper" strategy provides a relatively easier, faster route towards the modification of surfaces in a relatively inexpensive way. We strongly believe that room temperature locking and interlocking of these pendant chains could serve as a method to create a self-healing coating albeit *via* temperature application. Moreover, given the methods available for creating pores into a surface, even a porous material can be achieved consisting of such interdigitated micelles as building blocks.

In the final part of the work, we provided glimpse of our attempt to explore another strategy to prepare self-healing membranes. Taking a cue from the microcapsules based self-healing concept, we decided to replace the encapsulated monomer with a cross-linked nanogel having high swelling characteristics but at the same time enough structural integrity as well as adhesiveness. For its realization, it was decided to prepare a 4 – arm star copolymer consisting random blocks of poly(2-hydroxy ethyl methacrylate) and mono-functionalized poly(ethylene glycol methacrylate) responsible for crosslinking of the gel but at the same time providing enough flexibility. For the moment, we have only been able to prepare the required 4 – arm "Reversible Addition Fragmentation Transfer" agent. Once, the polymerization conditions are optimized with this RAFT agent, we hope to proceed towards the preparation of the nanogel and study its swelling characteristics.

7. PERSPECTIVES

Being the first such attempt to develop such kind of membranes, there is a large scope for further exploration and improvement in each of the work discussed in this manuscript.

In the first part, although the system presents unique properties of tunable porosity and self-healing, it still suffers from certain constraints like inability to increase the thickness of the membrane beyond 1.3 μm which would help to study the mechanical properties of the membrane using conventional technique like Dynamic Mechanical Analysis (DMA) as well as rheological properties. Also, to further reinforce the postulation that indeed the gradual movement pendant copolymer chain bridges is responsible for the healing phenomenon, the PSAN block of the copolymer can be functionalized with photo-crosslinkable group like Coumarin. A membrane prepared from this slightly modified copolymer can then be cross-linked by UV-Visible radiation in order to completely arrest the movement of dynamic bridges and same perforation – water flux measurements can be carried out. If the healing mechanism is indeed based on the movement of dynamic copolymer chain bridges, then it can be imagined that due to crosslinking of the core of the micelles, the chains would be permanently attached thus unable to dislocate. In this situation, a perforation will not be healed at all. Another aspect that can be explored will be the effect of temperature on the porosity changes as well as healing characteristics since the all the results shown on this membrane are based on the experiments carried out at room temperature. Finally, the PSAN block of the micelles can be changed with another polymer like poly(methyl methacrylate) and the resulting characteristics can be matched.

In the second part, we observed difficulties regarding the quantitative analysis of retentates and permeates containing silica nanoparticles by Photon Cross Correlation Spectroscopy. The problem lies with tendency of silica NPs to form aggregates and alter the measurements. Hence, instead of using simple NPs, may be florescent group functionalized silica NPs can be used, which can be analyzed via florescence microscopy easily. Furthermore, this can also help to map the entrapped NPs inside the transparent membrane. Coming back to the translocation of these NPs, in this work the filtration experiments were carried out only till 1 bar. Perhaps it will be interesting to carry out filtration of silica SP2 NPs at higher pressures to verify the response of global retention % and obtain the minimum

possible retention. Lastly, translocation should be carried with even smaller silica NPs (comparable to poly(styrene) ones) at same concentration in order to better correlate the results. Similarly, larger poly(styrene) NPs should be prepared in order to examine the role of surface nature *vs.* size *vs.* structural characteristics of the NPs. Even stiffer NPs than silica, like that of Titanium dioxide or Gold can be explored to completely understand the role of various parameters. Finally, these experiments can also be carried out with the membrane having crosslinked core in order to conclusively prove the role of structural dynamism of the membrane.

In the third part, we couldn't develop a true membrane from the copolymer hence this can be considered as the first objective to how achieve a porous superstructure from thousands of such zipped micelles' layers. Being very thin, it was difficult to explore the mechanical response of the assembly. Currently, experiments are underway where the thin PMMA films coated with such multilayer assembly will be tested on a DMA instrument. Surface indentation measurements can also be utilized to get an estimation of hardness of the coating and eventually the membrane. Preliminary experiments are underway to verify the thermally simulated self-healing of the coating at different temperatures. Once the healing is established, there can be whole series of experiments involving DMA, rheological tests of healed and un-healed specimens at different temperatures and other conditions.

For the final part, as it has been indicated to be largely incomplete except the synthesis of the precursor RAFT agent, hence there are lot of experiments need to be done. The foremost ones being to validate the idea of crack retardation and its closure by a soft matter like gel at microns level followed by perpetual decrease in size till nano level.

EXPERIMENTAL…

8. MATERIALS & METHODS

This chapter is dedicated to the experimental part of this thesis. The various materials and methods have been classified according to their corresponding chapters.

8.1 SELF-HEALING DYNAMIC INTERACTIVE MEMBRANE

8.1.1 Membrane Film Preparation

The Membrane films were prepared from a 100 mg·ml^{-1} DMF (Sigma-Aldrich, > 99.6%)/ Toluene (Sigma-Aldrich, > 99.8 %) solution of the triblock copolymer P(Sty$_{319}$-*co*-AN$_{262}$)-*b*-PEO$_{795}$-b-P(Sty$_{319}$-*co*-AN$_{262}$). To prevent any external contaminations including atmospheric water, dried solvents (with oven dried molecular sieves) were added through a syringe fitted with a PTFE filter (Millipore®) with a pore diameter of 0.45 µm. The polymer solution was then homogenized under magnetic stirring for 5 days. Silicon wafers of 25 cm^2 area were used for the spin-coating as a substrate. In order to obtain a clean surface, wafers were dipped in a 2 vol % of cleaning surfactant solution (RBS35, Chemical products®) under ultrasounds for 2 hours. The wafers were then washed and rinsed with ultrapure water (MilliQ®) followed by dipping into heptane (Carlo Erra Reagents®, 99.5 %) filled beaker under ultrasounds at 20 % intensity. The spin coater was first purged under argon at a pressure of 3 bars for 10 min in order to minimize the presence of water. Each silicon wafer was directly transferred from heptane beaker to spin coater and dried under argon before deposition. The polymer solution was transferred into a syringe fitted with PTFE filter (pore diameter – 5 µm). About 20 drops of the polymer solution deposited onto the center of the silicon wafer held tight by vacuum into the spin coater. The spin coater was turned on to have the wafer rotated at 2000 rpm for 180 s with a speed ramp of 50 rpm.s^{-2}. After three minutes, each wafer was removed from the spin coater and under vacuum for 1 day in order to obtain complete drying. After 24 hours, the coated Si wafers were then immersed into a petri-dish filled with ultrapure water at 25°C for 6 hours. After 6 hours, the detached membrane films were supplanted carefully onto a non-woven polyester fabric. As an alternative to the surfactant assisted cleaning process, piranha solution can also be used. Although potentially hazardous, this route is advantageous due to lesser dipping time involved, no need of ultrasound treatment and better surface cleaning.

8.1.2 Fluid Flow Resistance Measurements

To carry out the fluid flow resistance measurements, first membrane films supplanted over the non-woven fabric were cut with area section of 4.1 cm^2 in accordance with a 10 ml filtration cell (Amicon®) dimensions (Figure – 8.1a). The experimental set-up for the measurements (Figure – 8.1b) consists of a dead-end filtration cell containing the membrane. Water is supplied to the cell under pressure from a reservoir which is in turn maintained at the pressure by compressed air inlet. The pressure can be regulated using the attached manometer. The filtration cell consists of a small outlet from which the permeated water is collected into a very light weight plastic recipient. The recipient itself is kept onto a weighing balance which in turn is connected to the computer to monitor the gain in the mass of recipient. The software was used to register the mass gain as function of time. The water permeation experiments were conducted at various pressure drops by regulating the compressed air inlet and following the water flux through encased membrane films over time. The experiments were ended once an equilibrium state was reached.
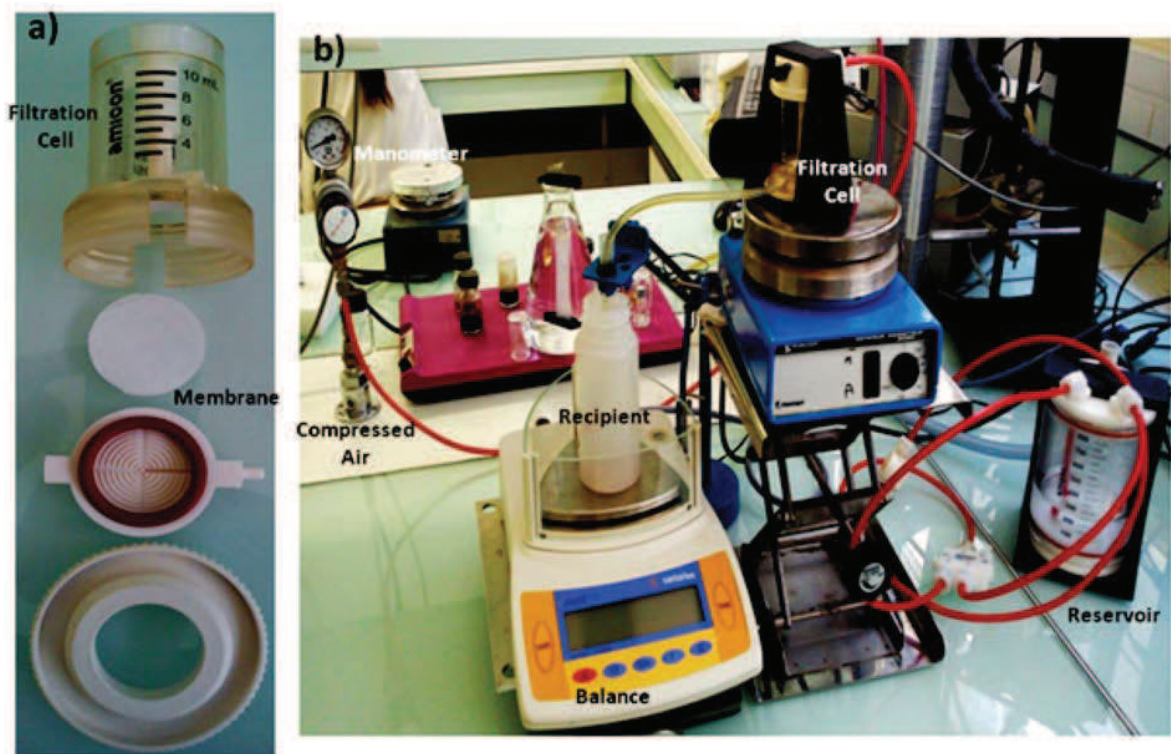
Figure – 8.1: Images of a) Exploded view of Filtration cell along with membrane supported over non-woven fabric, b) Experimental set up for water permeation and translocation experiments.

8.1.3 PEG Filtration Measurements

The Poly(ethylene glycol) (PEG) feed solution was prepared by weighing 0.25 g each of different PEGs (400 Da, 1450 Da, 4600 Da, 10 KDa and 35 KDa) (Sigma-Aldrich®, 99.5 %) and dissolving in ultrapure water to obtain a $1g.l^{-1}$ solution, stirred overnight. This solution was filled into the reservoir of the setup described above and a small glass vial was attached to the outlet of the cell containing the membrane. Approximately 2 ml of permeates were collected after certain interval of time successively at a given pressure difference.

8.1.4 Self-Healing Measurements

After being subjected to water pressure a first time to measure the flux evolution as a reference using the above discussed set-up, the pressure was relieved and each membrane film was carefully removed along with its non-woven substrate from the filtration cell. The removed membrane was then transferred onto humid silicon water. A single perforation was created in the hydrated membrane using a solid body needle having tip diameter of 110 μm (Figure – 8.2a, b). The needle was put into contact with the assembly of membrane film/polyester fabric, piercing till the silicon surface so as to obtain better reproducibility in terms of perforation diameter. After the perforation, the membrane/fabric assembly was again encased into the filtration cell and water permeation test were resumed. The whole process of disembarking of membrane, perforation and its re-embarking was accomplished with five minutes to minimize the effects of the developed pressure change.

Figure – 8.2: Scanning Electron Microscopy images of, a-b) Tip of the needle to make perforation in the films.

8.1.5 Atomic Force Microscopy

The AFM images were obtained with Dimension 3100 -Veeco Instruments®. This system of near-field microscopy used for high r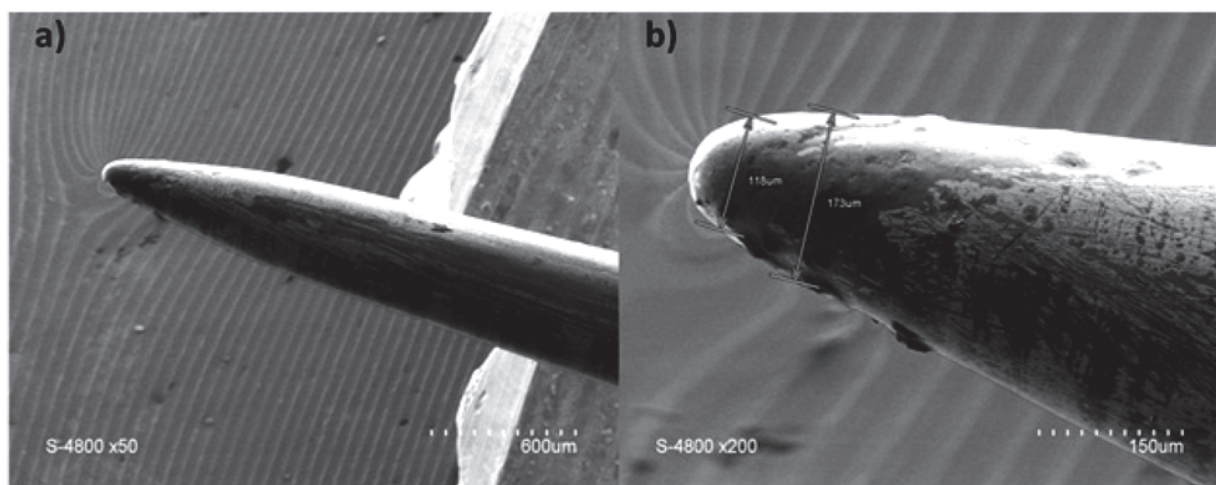esolution imagery was controlled by the Nanoscope IIIA quadrex software. All analyses were carried out in tapping mode allowing the capture of topographic images in repulsive mode. The tips used in this study were needles with force modulation provided by Nanosensors (Pointprobe plus - Silicon SPM sensor, with a resonance frequency of about 60 kHz and K=2 N/m). To analyze the morphology change due to pressure after water permeation at a given pressure, the membrane was removed together with the nonwoven fabric and dried in a closed chamber in the presence of silica gel (oven dried) for 24 hours. Once dry, the membranes were separated from the fabric and manually transferred onto Silicon wafers before AFM analysis.

8.1.6 Scanning Electron Microscopy

The SEM images were obtained using a Hitachi® S-4800 instrument operating at a spatial resolution of 1.5 nm at 15 kV of energy. The samples were dried in a closed chamber in the presence of silica gel (oven dried) and analyzed without metallization. To obtain 3-Dimensional images, images of the samples taken at different angles and were processed using Alicona® MeX software for 3D color rendering.

8.2 TRANSLOCATION ACROSS A SELF-HEALING MEMBRANE

8.2.1 Membrane Film Preparation

The membrane films were prepared according to the aforementioned procedure.

8.2.2 Silica Nanoparticles Synthesis

The synthesis of silica particles was carried out using a modified Stober process[1]. The procedure involves the hydrolysis and condensation of triethyl orthosilicate (TEOS) (Sigma-Aldrich®, > 99.9 %) in isopropanol (Sigma-Aldrich®, > 99.99 %)in the presence of ammonium hydroxide. In a general procedure, a 100 ml ultrasonically cleaned round bottom flask (RB) was taken and certain amount of ultrapure water (MilliQ®), Ammonium hydroxide solution (Sigma-Aldrich®, > 99.99 %) and Isopropanol were mixed using a clean magnetic stirrer for 5 minutes. The RB was closed using a rubber septum and the temperature was maintained at 20°C followed by the addition of a precalculated quantity of TEOS in dropwise manner by using a calibrated syringe. The transparent solution mixture gradually became opaque by the end of

addition of TEOS due to formation of silica suspension in the RB. In case of series SP1, the system was kept on stirring at 20°C for 5 hours after which, the particles were separated from liquid via centrifugation (12000 rpm, 15 min). The particles were washed 4 times with ultrapure water and ethanol (Sigma-Aldrich®, >99.5 %) successively followed by vacuum assisted overnight drying at 150°C. In case of series SP2, after the addition of TEOS, ultrasonic probe (Amplitude: 40%; Pulse: 5 min on 10 min off) was used for a period of 1 hour 30 minutes followed by aforementioned washing procedure for SP1 series. The application of ultrasonic probe increases temperature hence to maintain the temperature of the RB, an ice bath was used.

The quantity of all the components of the reaction mixture was taken in terms of volume and the relative concentrations of the reactants were according to the following relation:

$$[NH_3] = 0.81[TEOS]), [H_2O] = 6.25[TEOS]$$

The value of [TEOS] was taken to be 0.22 M[1], calculated by taking the final concentration of TEOS in the reaction mixture. The following Table – 8.1 presents the concentrations and amount of reactants used for the synthesis of two series of silica particles used in this work.

Silica Particles	Isopropanol	TEOS		NH$_3$; NH$_4$OH		H$_2$O		Temperature ^{o}C	Distribution
	ml	moles	ml	moles	ml	moles	ml		
SP1	28.5	0.0135	3	0.01088	0.73	0.0839	1.5	20	Bimodal
SP2	58	0.0224	5	0.01814	1.2	0.1399	2.5	20	Bimodal

Table – 8.1: Amount of reactants used in the synthesis of silica nanoparticles.

8.2.3 Scanning Electron Microscopy

The SEM instrumentation and its specifications are the same as mentioned in the first section. However all the samples excluding the membrane with translocated Poly(styrene) particles, were metalized for 6 minutes prior to analysis. All samples were dried according to the process previously mentioned.

8.2.4 Atomic Force Microscopy

The AFM instrumentation and its specifications remains the same as mentioned in the first section. The membranes with absorbed BSA protein molecules were detached from non-woven fabric and then placed delicately onto small Silicon wafers for analysis. To avoid the sample contamination and distortion, the drying was carried out in the same manner as described before.

8.2.5 Concentration Calibration for Poly(styrene) & Silica Nanoparticles

Since the membranes were susceptible to clogging due to possible high concentration of nanoparticles hence optimum concentrations for both Polystyrene and Silica nanoparticles by obtaining the calibration curves using Photon Cross Correlation Spectroscopy (PCCS) (Nanophox®).

In case of Polystyrene, a mother solution of Poly(styrene) latex beads (Sigma-Aldrich®, 10 wt %, 10148 M.W.) was prepared in ultrapure water (0.1146 g in 20 g water). A small part of this solution taken in crown glass vial and analyzed using PCCS to obtain the particle size distribution curve and the corresponding average intensity value (Kcps; Kilo Counts Per Second). The remaining solution was then subsequently diluted with ultrapure water (MilliQ®) and analyzed using PCCS to obtain the average intensity values (Table – 8.2).

S.No.	Amount of Mother Solution taken (g)	Amount of Water Added (g)	Amount of Poly(styrene) (g)	Concentration (g/ml) X 10^{-8}	Average Kcps
1	5.01*	5.0047	4.53916E-08	0.45325	17.95
2	5.06**	5.0025	1.81204E-07	1.80078	33.75
3	0.025	10.2454	7.16221E-07	6.97365	56.5
4	0.0509	10.18	1.45823E-06	14.2532	129.45
5	0.0999	9.9992	2.86202E-06	28.3394	259.2
6	0.2001	10.0511	5.73263E-06	55.9216	481.45
7	0.3011	10.039	8.62617E-06	83.4245	497.45
8	0.4021	10.0519	1.15197E-05	110.194	959.1
9	0.5007	10.0154	1.43445E-05	136.405	1299.7

*Tablee – 8.2: The absolute concentrations of poly(styrene) nanoparticles solutions with their corresponding Kcps values as obtained from Photon Cross Correlation Spectroscopy to obtain concentration calibration curve. ** means 5.06 g of solution was taken from solution no. 3, * denotes that 5.01 g of solution was taken from solution no. 2.*

In case of silica, the mother solution was prepared starting with 0.0012 g of silica dispersed into 4.0036 g of ultrapure water. For a uniform homogeneous solution, the vial containing the

solution was ultrasonicated for 15 minutes before being analyzed using PCCS. The ultrasonication step extends the time window in which PCCS measurements can be performed effectively before the silica nanoparticles settles at the bottom of the vial. The situation gets less pronounced as the concentration decreases with further dilutions. However the ultrasonication step was performed for each diluted solution (Table – 8.3).

SP1		SP2	
Concentration (g/ml) X 10^{-5}	Average Kcps	Concentration (g/ml) x 10^{-5}	Average Kcps
30	926,69	7	223.94
9.86	289,47	3.48	103.91
0.934	33,45	1.78	66
		1.46	52
		0.843	47.45

Tablee – 8.3: The absolute concentrations of silica nanoparticles (SP1 & SP2) solutions with their corresponding Kcps values as obtained from Photon Cross Correlation Spectroscopy to obtain the concentration calibration curve.

8.2.6 Preparation of Feed Solutions of Nano-Objects for Translocation

The Poly(ethylene glycol) (PEG) feed solution was prepared by weighing 0.25 g each of different PEGs (35 KDa, 100 KDa, 200 KDa and 400 KDa) (Sigma-Aldrich®, 99.5 %) and dissolving in ultrapure water to obtain a 1g.L^{-1} solution. This feed solution was first analyzed in terms of refractive index using refractive index detector (Water® 2440) of Gel Permeation Chromatography technique (Waters Corporation®).

The Bovine Serum Albumin (BSA, Aldrich, >96%) solution was prepared at a concentration of 1.5 mg.ml^{-1} in Phosphate buffered saline solution. The feed solution was analyzed by UV-Vis Spectrometry at a wavelength 280 nm. The concentration could then be estimated from the following calibration curve.

An aqueous solution of Polystyrene particles (0.1146 g in 20 g of water) was further diluted with 200 ml of ultrapure water and the resulting solution was used as feed solution for Polystyrene translocation.

For both series of silica particles, two 100 ml solutions were prepared containing 0.0024 g of SP1 and SP2 silica particles respectively. Both the solutions were ultrasonicated for 1 hour.

8.2.7 Translocation Experiments

The membranes were first compressed to their maximum by performing water permeation experiments using the experimental set-up described in the first section. After 2 hours of permeation test, the filtration cell was disconnected from the water reservoir. It was filled with 10 ml of the feed solution (For example: PEGs solution or PS solution) and connected directly to compressed air supply. The whole process was executed very quickly so as to avoid the decompression of the membrane due to release of pressure. Additionally, to keep the feed solution homogeneous inside the cell, magnetic stirring was started at 300 rpm. At the outlet of the filtration cell, a small vial was attached to obtain 1.5 ml permeate at each pressure drop value. Once the requisite amount of permeate was collected, the experiment was stopped and the retentate sample was obtained from the remaining solution in the filtration cell.

In case of PEGs, the collected permeates and retentates were first filtered using PTFE filter (Millipore®; 0.45 µm) before passing for GPC analysis.

In case of BSA, the collected permeates and retentates were filtered and analyzed by the UV-Visible spectrometer to obtain the corresponding absorbance values.

In case of Polystyrene and Silica nanoparticles, the collected permeates and retentates were also filtered using PTFE filters (Millipore®; 2µm) before being analyzed using PCCS. The vial was ultrasonicated for 15 minutes before being introduced into the instrument. The duration of analysis for each sample was kept at 60 minutes per scan at 25°C. Three such scans were conducted for each sample. The theoretical model for the correlation was chosen to be NNLS.

8.3 BLOCK COPOLYMER MICELLES' ZIPPER ASSEMBLY

8.3.1 Synthesis of Octadecyl Methacrylate

In a dried two neck round bottom flask (RB), 15.0 g (0,0554 moles) 1-octadecanol was taken along with a magnet. It was stirred at 500 rpm in 120 ml freshly distlilled Tetrahydrofuran (THF) (Carlo Erra Reagents®, >99.7 %). On one neck of the RB, a dropping funnel containing 30 ml of distilled THF was connected having provision for outlet for nitrogen, which was introduced at a brisk rate from the second neck. After 30 minutes of complete dissolution, about 16ml (0,111 moles)

Triethylamine (TEA) (Sigma-Aldrich®, >99.99%) was added via a syringe. The mixture was blended for further 15 minutes at 25°C after which 11 ml (0,111 moles) Methacrylolyl chloride (Sigma-Aldrich®, >99.9 %) was added to the dropping funnel via a syringe. The nitrogen flow was stopped and the chloride/THF mixture was then introduced into the RB in a slow drop by drop manner while maintaining the temperature at 25°C. The content of the RB soon became densely white as more and more chloride reacted with the alcohol. The system was kept on stirring for 24 hours after which, 5 ml of Methanol (Sigma-Aldrich®, 99.8%) was added via a syringe to the RB and to react with any unreacted Methacrylolyl Chloride. After 10 minutes, the content of the RB was filtered over a sintered glass filter (porosity 3) to obtain a yellow color liquid filtrate and white color salt residue. The filtrate was concentrated over a rotavapor and the concentrated solution was precipitated into a mixture (50/50 by volume) of ultrapure water and ethanol kept in ice bath. The pale white precipitate thus obtained was separated from the rest of the solution via filtration over a sintered glass filter (porosity 3) followed by room temperature vacuum drying. The solid thus obtained was then re-dissolved in minimum amount of Cyclohexane (Carlo Erra Reagent®, 99.5 %) and cooled at $-$80°C for 5 hours after which, the solid content was allowed to slowly anneal at room temperature. The crystallized Octadecyl Methacrylate (ODMA) remained in solid form while the Cyclohexane became liquid. The majority of the solvent was removed via simple decantation while the rest was removed by employing strong tertiary vacuum at room temperature to obtain a pale white colored waxy solid. The product was weighted (13.3412 g) and stocked at -5°C in an air tight bottle, to be used for further reactions.

8.3.2 Synthesis of PMMA by Uncontrolled Radical Polymerization

Methyl Methyacrylate (MMA) (Sigma-Aldrich®, 99.9 %) was passed over a short alumina column to remove the inhibitor and 10 g (9.988 x 10^{-2} moles) of this purified MMA was sealed in a dried Schlenk tube containing 0.1 g (6.09 x 10^{-4} moles) of Azobisisobutyonitrile (AIBN) (Sigm-Aldrich®, 98 %) (recyrstallized from methanol). The mixture was given four freeze-pump-thaw cycles to remove oxygen completely and placed in a constant temperature oil bath at 70°C for 70 minutes. The system was quenched in liquid nitrogen to stop further polymerization and then annealed at room temperature. The flask was connected to rotary evaporator to evaporate any remaining MMA followed by addition of 30 ml dichloromethane (Sigma-Aldrich®, >99 %) to dissolve the gel overnight. The viscous solution thus obtained was then precipitated 2 times in cold methanol,

filtered over sintered glass filter (porosity 3) and vacuum dried at 60°C for 48 hours to obtain white colored polymer.

8.3.3 Synthesis of PMMA by Controlled Radical Polymerization

Purified MMA (10 g, 0.1 moles), 2-cyano-2-propyl benzodithioate (CPDB) RAFT agent (0.231 g, 1.04 x 10^{-3} moles) (Sigma-Aldrich®, > 97 %) and AIBN (33.8 mg, 0.21 x 10^{-3} moles) (recrystallized from Methanol) were solubilized in 5 ml of freshly distilled Toluene (Sigma-Aldrich®, > ab99.7 %) and sealed in a dry Schlenk tube. Four freeze-pump-thaw cycles were used to remove residual oxygen. The solution was then placed in a constant temperature oil bath at 70°C for 150 min, after which it was quenched in liquid nitrogen to stop the polymerization. The polymer solution was precipitated twice as a pink powder (PMMA macroinitiator) in cold methanol, filtered and dried at room temperature over tertiary vacuum for 48 hours.

8.3.4 Synthesis of PODMA-*b*-PMMA Copolymer

The above synthesized PMMA macro RAFT chain transfer agent (1.87 g, 0.24 x 10^{-3} moles), *n*-octadecyl methacrylate (8 g, 23.6 x 10^{-3} moles) and AIBN (8 mg, 0.049 x 10^{-3} mol) were solubilized in 16 ml of freshly distilled toluene and sealed in a dry Schlenk tube. Four freeze-pump- thaw cycles were employed to remove any residual oxygen. The solution was then placed in a constant temperature oil bath at 80°C for 150 min, after which it was quenched in liquid nitrogen to stop the polymerization. The polymer solution was precipitated in cold methanol. The recovered white solid was then further purified in order to remove unreacted *n*-octadecyl methacrylate. The solid was dissolved in 100 mL of cyclohexane and methanol was added dropwise until turbidity appeared. After one night of decantation, the milky phase was recovered and dried under tertiary vacuum 48 hours at room temperature to obtain a light pink colored powder.

8.3.5 Proton Nuclear Magnetic Resonance Spectroscopy (H^{1}NMR)

The proton NMR spectra were obtained by preparing samples in deuterated chloroform, CDCl$_3$ (Euros®) and analyzed on 300 MHz Bruker® AV300 instrument with TopSpin v2.1 software. All the spectra were obtained at 25°C with 64 scans per sample.

8.3.6 Self-Assembly of Copolymer Micelles

To prepare the monolayer assembly of the micelles, first a substrate layer of uncontrolled PMMA was spin coated over thoroughly cleaned Silicon wafer using spin coating. 1 g PMMA was dissolved in 3 ml Dicholoromethane in a small vial and the resulting solution was coated onto the Silicon wafer dried under argon atmosphere in the spin coater. The spin rate was kept at 1000 rpm for 3 minutes to obtain 1.3 μm thick substrate film. The coated substrate thus obtained was immersed in small beaker a 10 ml micellar solution of PMMA-*b*-PODMA (3.5 g.ml^{-1} in THF/Cyclohexane, 1/9 vol.%) for 1 hour followed by rinsing with Cyclohexane. The coated surface thus obtained was dried and further analyzed.

To prepare multilayer assembly, the PMMA coated wafer was first swelled in 20 ml mixture of THF/Cyclohexane (1/9, vol.%) for 15 minutes. The swelled PMMA coated wafer was taken out quickly, put into spin coater and the micellar solution of PMMA-*b*-PODMA (3.5 g.ml^{-1}) was coated under argon atmosphere.

8.3.7 Contact Angle Measurements

The contact angle measurements were conducted by drop sessile methond on lab made apparatus equipped with a light source, a stage to put the substrate to be analyzed, a light source and a CCD camera. A 10 μl water drop was dropped onto the sample surface by using a 50 μl syringe stationed above the stage. All measurements were done at room temperature and the images acquired were analyzed using ImageJ® software and the contact angles were determined by interpolation method using DropSnake® plugin. The values reported represent average of 5 measurements.

8.3.8 Atomic Force Microscopy

The AFM instrumentation and its specifications remains the same as mentioned in the first section of this chapter.

8.3.9 Scanning Electron Microscopy

The SEM instrumentation and its specifications are the same as mentioned in the first section. The samples were metalized for 6 minutes before the analysis.

8.4 NANO-GEL BASED SELF-HEALING SYSTEM

8.4.1 Synthesis Of 2-(2-chloroacetyl)oxyethyl 2-chloroacetate

In a 250 ml two neck round bottom flask (RB), 5 g of lyophilized Pentaerythritol (Sigma – Aldrich®, > 99 %)was taken along with a stirrer and dissolved in 60 ml of freshly distilled dimethylformamide (DMF). The system was closed with septums with one neck for nitrogen outlet while other acting as outlet. The solution was kept on stirring for 30 minutes until complete dissolution of pentaerythritol. After that, 13.5 ml of chlroacetyl chloride (Sigma – Aldrich®, > 99 %) was taken into a syringe and added to the solution in the RB in a drop by drop manner. Once all the acid chloride was added, the temperature of the solution was increased to 50°C slowly by putting into an oil bath. The solution was allowed to undergo stirring for 24 hours after which it was cooled into an ice bath and then the DMF was evaporated at 60°C. Once most of the DMF was evaporated, the resulted dark brown colored solid was dissolved in 100 ml of dichloromethane and washed with 200 ml of water 3 times. The organic phase was collected, dried over MgSO$_4$ (Sigma – Aldrich®, > 99.5 %), filtered and finally concentrated at 40°C to obtain pale white colored crystals. DMF was taken as solvent due to easy solubility of pentaerytritol in it, its high boiling point as well as its ability to trap the liberated protons in the reaction thus inhibiting the formation of hydrochloric acid. The final yield of the reaction was 86 % with sufficient degree of purity.

8.4.2 Synthesis Of 2-(2-azidoacetyl)oxyethyl 2-azidoacetate

To synthesize the azide derivative of 2-(2-azidoacetyl)oxyethyl 2-azidoacetate, 4.96 g of 2-(2-chloroacetyl)oxyethyl 2-chloroacetate and 18.02 g of sodium azide (sigma – Aldrich®)were dissolved in 100 ml of distilled acetone (Sigma – Aldrich®, > 99.5 %) in a 250 ml single neck RB, equipped with a condenser on it. The system was allowed to reflux at 55°C for 24 hours. After 24 hours, the refluxing was stopped, acetone was dried and the resulting concentrate was again dissolved in 100 ml dichloromethane. The solution was washed with 200 ml of ultrapure water (MilliQ®) 4 times and the organic phase was collected, dried over MgSO4, filtered and concentrated to give a viscous, honey colored liquid. The yield of the reaction was approximately 94 %.

8.4.2 Synthesis Of Ethynyl – 4 – (phenylcarbonothioylthio) – 4 – cyano pentoate

3 g of 4-Cyano-4-(phenylcarbonothioylthio)pentanoic acid (Sigma-Aldrich®, > 97 %) was dissolved in freshly distilled 50 ml of dichloromethane in a 100 ml two neck R.B. The system was maintained at 0°C and nitrogen flow was maintained in the system. To this 0.9 g of propargyl alcohol (Sigma-Aldrich®, 99 %)

was added followed by addition of 0.56 g of 4- dimethylaminopyridine (DMAP) (Sigma-Aldrich®, > 99 %) and 0.04 g of *N*-(3-Dimethylaminopropyl)-*N*'-ethylcarbodiimide hydrochloride (EDC) (Sigma-Aldrich®, > 99 %) at 0°C. The system was allowed to react for 15 hours at constant temperature of 25°C. After 15 hours, the solution was filtered, and the filterate was diluted with 10 ml of dichloromethane and subsequently washed with 100 ml of ultrapure water 4 times. The aqueous phase was collected, dried over MgSO$_4$, filtered and then again concentrated. The product was further passed through a silica column with the eluent mixture of ethyl acetate/cyclohexane (30/70). The deep red fraction was collected and concentrated to obtain a deep red colored compound.

8.4.3 Coupling Of Ethynyl – 4 – (phenylcarbonothioylthio) – 4 – cyano pentoate With 2-(2-azidoacetyl)oxyethyl 2-azidoacetate Using Click Chemistry

In a small 10 ml glass vial, 0.9 g of propargyl functionalized RAFT agent was taken along with 0.31 g of 2-(2-azidoacetyl)oxyethyl 2-azidoacetate dissolved in 3 ml of DMF. To this solution, a 2 ml aqueous solution containing 0.057 g of Sodium Ascorbate was added followed quickly by the addition of 2ml aqueous solution of 0.036 g of copper sulfate pentahydrate. The mixture quickly turned from deep red to deep brown. It was allowed to undergo for 1 hour at room temperature followed by passing over a short alumina column to remove the copper. The rest of the filtrate was diluted with little dichloromethane and washed with ultrapure water. The aqueous phase was collected, dried, filtered and finally concentrated to obtain a deep red colored viscous compound.

8.4.4 Nuclear Proton Magnetic Resonance (¹HNMR)Spectrsoscpy

The proton NMR spectra were obtained by preparing samples in deuterated chloroform and the parameters were same as mentioned before in the previous section.

REFERENCES

1   Wang, X.-D. *et al.* Preparation of spherical silica particles by Stober process with high concentration of tetra-ethyl-orthosilicate. *Journal of Colloid and Interface Science* **341**, doi:10.1016/j.jcis.2009.09.018 (2010).

ELABORATION OF SELF-HEALING POLYMERIC MEMBRANES

The objective of this thesis is to develop such kind of polymeric membranes which can repair themselves autonomously in an event of damage. Such damage in a membrane, if left undetected can pose serious health issues in some of the intended applications. In the first approach, a dynamic polymeric membrane based on ABA type triblock copolymer micelles has been prepared. The block "A" is represented by mechanically robust poly(styrene-co-acrylonitrile) copolymer while block "B" by relatively soft and flexible poly(ethylene oxide). When pressure is applied to the membrane, its morphology can be fine-tuned thanks to the compressible nature of micelles as well as intermicellar dynamic bridges. A range of porosities are accessible which can be regulated by pressure and thereby controlling the filtration performance. The same dynamic nature has also been utilized to display an effective pressure driven autonomous healing. The efficiency of healing process has been found to be dependent on the extent of damage, pressure value and time duration of application of pressure. Using the self-healing property of above membrane, "Direct Mode Translocation" of nanoparticles has also been studied. Four different classes of nanoparticles were used with varied intrinsic and extrinsic properties. The findings of the work prove that the size, shape and surface characteristics of the nanoparticles as well as the applied force govern the translocation process. In a second approach, a 2D and 3D reversible coating based on the self-assembly of micelles of diblock copolymer consisting of poly(methyl methacrylate) (PMMA) and poly(n-octadecyl methacrylate) (PODMA) blocks have been developed. The assembly of micelles is accomplished via so called "Zipper" effect, thanks to the long pendant chains of PODMA block. The same "zipper" effect plays the role of removing the coating easily by washing in a selective solvent, thus giving the ability to alter the surface of substrate for many times in reversible manner. The room temperature crystallization of PODMA block provides huge implications for a thermally assisted self-healing coating without affecting the global micelle morphology. Finally, another approach has been conceptualized in which self-healing occurs via encapsulated nano-gel dispersed within a membrane. The nano-gel is based on a partially crosslinked hydrophilic star shaped block copolymer which has to be synthesized by "Reversible Addition-Fragmentation Transfer" (RAFT)

polymerization technique. The synthesis of a 4- arm RAFT agent for polymerization has been accomplished however; a substantial amount of work is still needed to validate the synthetic route towards the nano-gel synthesis as well as its further application for the self-healing process.

ELABORATION DES MEMBRANES POLYMERES AUTO-REPARABLES

L'objectif de cette thèse est d'élaborer et de développer un type de membranes polymère qui peuvent se réparer de manière autonome en cas de fissures. Si elles ne sont pas détectées, ces fissures peuvent poser des problèmes notamment pour des applications médicales. Dans une première partie, une membrane polymère dynamique à base de micelles de copolymère tribloc ABA a été préparée. Le bloc "A" est représenté par le poly (styrene-co-acrylonitrile), copolymère bloc mécaniquement robuste, et un bloc "B" relativement mou et souple le poly (oxyde d'éthylène). Lorsqu'une pression est appliquée à la membrane, sa morphologie peut être ajustée grâce à la nature compressible des micelles, ainsi que les ponts dynamiques intermicellaires. Une gamme de porosités accessible peut être régulée par la pression et de manière à contrôler la performance de filtration. La même nature dynamique a également été utilisée pour montrer une réparation autonome entrainée par la pression. L'efficacité du processus de réparation dépend de la taille des fissures, de la valeur de pression et de la durée d'application de la pression. En utilisant la propriété d'auto-réparation de la membrane ci-dessus, le processus «Direct Mode Translocation » de nanoparticules a également été étudié. Quatre classes différentes de nanoparticules ont été utilisées avec diverses propriétés intrinsèques et extrinsèques. Les conclusions de ces travaux prouvent que les caractéristiques de taille, de forme et de surface des nanoparticules ainsi que la force exercée régissent le processus de translocation. Dans une seconde partie, un revêtement 2D et 3D réversible basé sur l'auto-assemblage de micelles de copolymère dibloc constitué d'un poly (methyl methacrylate) (PMMA) et du poly (n-octadecyl methacrylate) (PODMA) blocs a été développé. L'assemblage de micelles est réalisé par l'effet "Zipper", grâce aux longues chaînes pendantes du bloc PODMA. Le même effet "Zipper" permet d'enlever facilement le revêtement par lavage dans un solvant sélectif, donnant ainsi la possibilité de modifier la surface d'un substrat plusieurs fois de manière réversible. La cristallisation à température ambiante du bloc PODMA offre la possibilité d'avoir un revêtement auto-réparable thermiquement sans affecter la morphologie globale des micelles. Enfin, une dernière partie a été conceptualisée, dans laquelle l'auto-réparation se fait par «nano-gel» encapsulés et dispersés dans une membrane. Le « nano-gel » est à base d'un

copolymère hydrophile en forme d'une étoile partiellement réticulée et qui doit être synthétisée par la technique de "Reversible Addition-Fragmentation Transfer" (RAFT) polymérisation. La synthèse d'un agent RAFT avec 4 bras pour la polymérisation a été accomplie, cependant, des travaux sont encore nécessaires pour valider la voie de synthèse vers la synthèse de « nano-gel » ainsi que son application pour le processus d'auto-réparation.